ALL-SOLID-STATE FEMTOSECOND CR:LISAF AND CR:LISGAF LASERS

Matthew Peter Critten

A Thesis Submitted for the Degree of PhD
at the
University of St Andrews

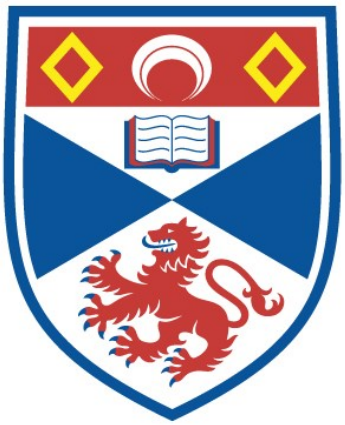

1997

All-solid-state Femtosecond Cr:LiSAF and Cr:LiSGaF Lasers

Thesis submitted for the degree of

Doctor of Philosophy

to the

University of St. Andrews

by

Matthew Peter Critten, B.Sc., A.R.C.S.

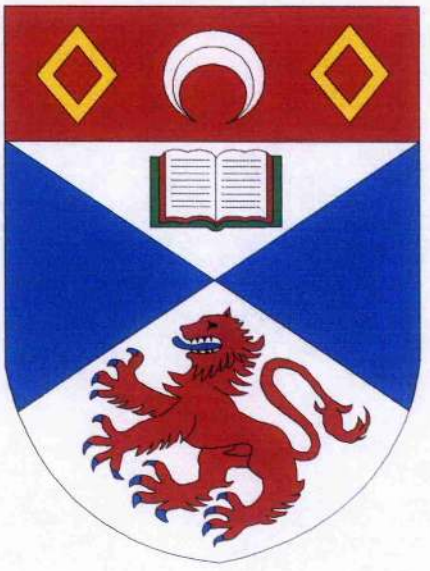

The J. F. Allen Physics Research Laboratories
Department of Physics and Astronomy
University of St. Andrews
North Haugh
St. Andrews
Scotland KY16 9SS

December, 1996

TH c240

Declarations

I, Matthew Peter Critten, hereby certify that this thesis, which is approximately sixty thousand words in length, has been written by me, that it is the record of work carried out by me and that it has not been submitted in any previous application for a higher degree.

date signature of candidate

27/12/96

I was admitted as a research student and as a candidate for the degree of Doctor of Philosophy in October, 1993; the higher study for which this is a record was carried out at the University of St. Andrews between 1993 and 1996.

date signature of candidate

27/12/96

I hereby certify that the candidate has fulfilled the conditions of the Resolution and Regulations appropriate for the degree of Doctor of Philosophy in the University of St. Andrews and that the candidate is qualified to submit this thesis in application for that degree.

date signature of supervisor

27/12/96

In submitting this thesis to the University of St. Andrews I understand that I am giving permission for it to be made available for use in accordance with the regulations of the University Library for the time being in force, subject to any copyright vested in the work not being affected thereby. I also understand that the title and abstract will be published, and that a copy of the work may be made and supplied to any *bona fide* library or research worker.

date signature of candidate

27/12/96

- Maybe. Who cares? Perhaps I'm old and tired, but I always think that the chances of finding out what really is going on are so absurdly remote that the only thing to do is to say hang the sense of it and just keep yourself occupied... What does it matter? Science has achieved some wonderful things of course, but I'd far rather be happy than right any day.

- And are you?

- No. That's where it all falls down of course.

Douglas Adams, *The Hitch-Hiker's Guide to the Galaxy*

Abstract

This thesis describes the development of all-solid-state self-modelocked Cr:LiSAF and Cr:LiSGaF lasers. Diode-pumped colquiriite lasers compare favourably with mainframe-pumped Ti:sapphire lasers, but the conflicting requirements of self-modelocking and pumping by broad-area diodes can cause problems. Two alternatives were investigated.

Firstly, high Cr^{3+} doping permitted pumping in the Cr:LiSAF green absorption trough. Frequency-doubled Nd:YLF and Nd:YAG minilasers offer high-power, diffraction-limited beams in the green. The 'green problem' plagued both minilasers, however, and an Ar-ion pump laser was therefore also used. A laser utilising a 10%-doped AR-coated Cr:LiSAF crystal produced 30 mW output power at 320 mW pump, and 90 fs pulses at 859 nm and 86 MHz repetition rate. The self-modelocking threshold was 280 mW. A laser utilising a 22%-doped Brewster-angled crystal produced 120 mW output power at 1.1 W pump, and 72 fs pulses at 76 mW output. The self-modelocking threshold was 360 mW. 160 mW output was obtained by pumping the crystal at both ends to overcome thermal problems.

Secondly, factors affecting CW and self-modelocking thresholds were considered; in particular, the effects of waist size, beam brightness, cavity configuration and intracavity dispersion. A Cr:LiSAF laser, pumped by a self-injection-locked diode, produced sub-100-fs pulses for just 73 mW pump. Its tuning curve was modulated by birefringence effects. The excellent free-running noise properties of the laser permitted a sub-picosecond streak camera evaluation.

Two low-threshold lasers utilising low-loss Cr:LiSGaF were also developed. 87 fs pulses at 11.5 mW output power were produced from a Z-cavity laser for 170 mW pump. A laser utilising a compact 'retroreflector' three-mirror cavity produced 84-fs pulses at 173 MHz repetition rate for 116 mW pump. Subsequent optimisation led to the production of sub-100-fs pulses for 40 mW pump, with self-modelocked operation demonstrated at pump powers as low as 21 mW.

Preface

The layout of this thesis is as follows.

In Chapter 1, I introduce basic concepts that are relevant to ultrashort-pulse laser systems in general.

In Chapter 2, I report novel self-modelocked Cr:LiSAF lasers, based on highly doped crystals, that are pumped in the green spectral region. In the course of this chapter, I also discuss vibronic laser materials, in particular Cr:LiSAF, and describe the techniques of self-modelocking and dispersion compensation. Two frequency-doubled minilasers are described in some detail because, although they were not developed by the author, they were used as pump sources for the Cr:LiSAF systems described.

In Chapter 3, I consider factors that affect the power required to self-modelock a laser. I derive an expression for (a) the CW threshold of a laser in which both the pump and cavity modes are focused Gaussian beams, and (b) the overlap efficiency between a Gaussian cavity beam and a non-diffraction-limited pump beam. I also consider briefly the effects of beam focusing on nonlinear lensing. Self-injection-locking of broad-area semiconductor lasers is then described. I next outline the model of self-modelocking developed by Cerullo, Magni and de Silvestri, and present two new simple analytical expressions that predict the optimum cavity configuration for self-modelocked operation, eliminating the need for Cerullo's graphical approach. The soliton model of pulse propagation is then described, and consideration is given to its implications for the power required to sustain a pulse of a particular duration, and the effects of third-order dispersion on this power.

In Chapter 4, I describe the development and performance of a novel self-modelocked Cr:LiSAF laser system in which the ideas of Chapter 3 are applied to produce self-modelocked operation at remarkably low pump powers.

In Chapter 5, I describe the development and performance of two low-threshold self-modelocked Cr:LiSGaF lasers, the second of which is based around a novel three-mirror resonator. I investigate the hard- and soft-aperture modelocking of

three-mirror lasers by applying the Magni model of self-modelocking in astigmatic resonators.

Chapter 6 contains general conclusions and a discussion of possible future developments.

In Appendix B, I present a novel geometric optics model of resonator stability based around the propagation of plane- and spherical-waves through pairs of lenses. The model provides simple, intuitive means of deriving expressions for the stability limits of four-mirror resonators and for distinguishing the high misalignment sensitivity (HMS) stability region from the low misalignment sensitivity (LMS) stability region.

Table of Contents

1. Introduction

1.1 Ultrashort Light Pulses

In popular science, the laser is often presented as an object of wonder that can generate a mathematical abstraction: a monochromatic, continuous, coherent and parallel beam of light. Real lasers are far more interesting of course. Phenomena such as spectral hole burning, Q-switching, finite coherence lengths and far-from-diffraction-limited beams are just a few examples of the refusal of nature to make anything quite so simple. This thesis is concerned with a branch of photonics in which monochromatic and continuous laser operation is deliberately abandoned in favour of lasers that oscillate over bandwidths of a few terahertz (10^{12} Hz) and produce pulses of light that last for only tens of femtoseconds (10^{-15} s).

In many fields of research ultrashort pulses are far more useful than monochromatic beams. Ultrashort pulses can be very precise tools, delivering large instantaneous powers on time scales that are much shorter than the time scales of many electronic processes in biology, chemistry and materials science. The instantaneous powers involved can be very large indeed. If pulses of one hundred femtoseconds duration are generated every ten nanoseconds then the peak power of each pulse will be of the order of one hundred thousand times larger than the average power of the pulse train. These high peak powers can be used to excite nonlinearities that are too weak to be significant in experiments utilising continuous beams. Indeed, ultrashort-pulses themselves are evolved by positive feedback from continuous signals in lasers that are designed to exploit nonlinear effects.

1.1.1 Applications for Ultrashort Light Pulses

Applications for these ultrashort light pulses are to be found in all branches of photoscience[1]. Many applications take the form of pump-probe experiments. In these experiments a 'pump' pulse prepares a sample by exciting it to higher energy states and then a 'probe' pulse is used to investigate the sample's subsequent behaviour. In femtochemistry, for example, these techniques permit chemical

reactions in gas phase/molecular beams to be followed in real-time[2]. First of all, the pump pulse excites reactants to a transition state. This state decays to the final reaction products on time-scales of between 10 fs and 1 ps. At some point during that decay, the probe pulse further excites the transition state (or products) to a state that can be easily detected by monitoring fluorescence, ion counts or some other suitable signal. By varying the delay between the creation of the transition state and the arrival of the probe pulse it is possible to resolve the course of the reaction with time.

Pump-probe techniques have been used to study the rotational and vibrational motion of the excited states of molecular iodine[3] and the photodissociation of I-CN[4] and Bi-Bi[5]. Similar procedures are used in the study of chemical reactions in solutions[6]. Molecular structure can be studied using ultrafast electron-diffraction, a technique that utilises both ultrashort optical pulses and ultrashort electron pulses[7,8]. In life-chemistry, the dynamics of internal motions in proteins can also be studied in pump-probe experiments[9]; and in photobiology, the primary event in vision, cis-trans isomerisation of rhodopsin, has been studied with 35 fs pump pulses at 500 nm and 10 fs probe pulses at 500 nm and 620 nm[10].

In semiconductor physics, the development of high-speed electronic and optoelectronic devices requires an understanding of the dynamical properties of electrons in semiconductors on femtosecond and picosecond time scales. Electronic devices are incapable of investigating phenomena on these time scales, since they are themselves limited by the dynamical properties of electrons. Optical methods offer resolutions of the order of 10 fs, together with perturbation, sensitivity and temporal jitter properties that are much superior to those of electronic systems[11]. Pump-probe techniques have been used to study the time-resolved saturation of the optical absorption of the semiconductors GaAs[12] and AlGaAs[13]. Luminescence spectroscopy has been used to study radiative recombinations in GaAs and InP. Resolutions of the order of 500 fs were achieved by sum-frequency mixing the luminescence resulting from a probe pulse with a gating pulse of known intensity and duration[14]. Electronic devices can also be studied with ultrashort electronic signals that are generated from ultrashort light pulses via high-speed photoconductors[15].

Femtosecond pulses can be amplified to intensities of 10^{18} W cm^{-1} [16-19] by using the technique of Chirped Pulse Amplification (CPA)[20]. Pulses of such high intensities can be used in the generation of extreme ultraviolet (XUV) and X-ray pulses. This can be achieved by focusing the pulse onto a dense solid or liquid target to form a dense plasma that emits XUV or X-rays through black-body radiation, Bremsstrahlung, or inner-shell recombination[21]. Focusing onto the surface of a solid metallic target results in a strong density gradient, and electrons driven back and forth across this gradient experience a strongly anharmonic motion and emit light at higher harmonics[22,23]. Another alternative is high-harmonic generation in gases, which is a particularly attractive technique because the generated emission is coherent and confined to a small solid angle; the 143rd harmonic (7.4 nm) of a Nd laser has been generated by this technique[24]. Finally, because transitions in the X-ray region typically have upper-state lifetimes of a few femtoseconds, amplified femtosecond pulses could potentially be used to pump x-ray lasers[21].

These examples alone demonstrate the diversity of applications that exist for ultrashort light pulses.

1.1.2 The Self-modelocked Ti:sapphire Laser

The ultrashort-pulse laser systems described in Chapters 2 to 5 of this thesis are self-modelocked lasers producing pulses of durations of the order of 100 fs that are tunable between 830 nm and 870 nm at repetition rates of about 80 MHz. These operating specifications place the lasers in a market that has been dominated in recent years by the self-modelocked titanium-doped sapphire (Ti^{3+}:sapphire) laser[25].

Ti:sapphire lasers are, in general, pumped by mainframe argon ion (Ar^+ ion) lasers. As Table 1.1 shows, Ar^+ ion lasers are inefficient, bulky and they require a three-phase power supply and high-pressure water cooling. Maintenance costs make them expensive laser sources. Because of these disadvantages, recent research has focused on gain media similar to Ti:sapphire that can be pumped by broad-area semiconductor lasers. Broad-area semiconductor lasers are far smaller, more efficient and more reliable than ion lasers, and they have zero maintenance costs and require only a mains power supply and, at the worst, mains water cooling.

Property	20 W Ar^+ Ion Laser	0.5 W Broad-area AlGaInP Laser Diode
Size	~ 80000 cm^3 + power supply	~ 500 cm^3 + power supply
Electrical to optical efficiency	~ 0.1%	~ 25 %
Initial cost	~£60000 (£3000/W)	~£2000 (£4000/W)
Maintenance cost	£20000/year	Nil
Running costs	Three-phase mains electricity (15000 W) + high pressure water	Domestic mains electricity (~2 W)
Lifetime	~ 2000 hours/tube	10000 hours

TABLE 1.1 *Approximate specifications of Ar^+ ion lasers and broad-area AlGaInP diode lasers.*

Semiconductor lasers also have noise properties that are superior to those of mainframe ion lasers. The gain media used in the work described in this thesis, Cr:LiSAF and Cr:LiSGaF, have been widely identified as practical semiconductor-laser-pumped complements to the Ti:sapphire laser system.

1.2 Techniques for Generating Ultrashort Light Pulses

1.2.1 The Ideal CW Laser

The light inside a laser cavity circulates for many round trips, and if the intracavity field does not reproduce itself exactly after each round trip destructive interference will inevitably occur. Consequently, a laser can only operate at the discrete frequencies at which the field's round-trip phase shift is an integer multiple of 2π, namely a comb of frequencies spaced by

$$\Delta\nu = \frac{c}{P},$$

EQUATION 1.1

where P is the round-trip optical path length of the laser cavity and c is the speed of light. The gain seen by the longitudinal modes corresponding to these allowed frequencies is determined by the gain profile of the laser transition (Figure 1.1).

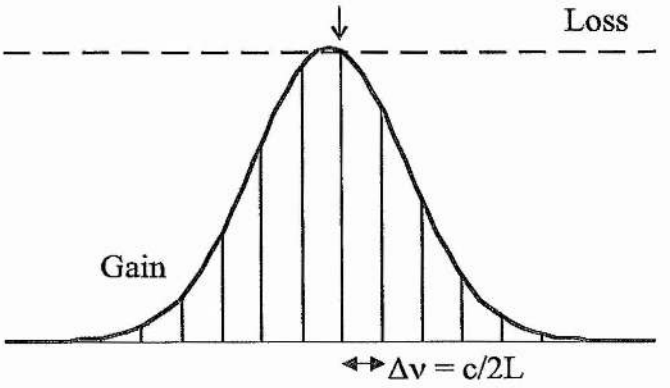

FIGURE 1.1 *Longitudinal modes and the laser gain profile. In an ideal narrow-band laser, only one mode will see sufficient gain to match the cavity loss and thereby oscillate.*

In steady-state operation, the intracavity field in a laser must experience equal gain and loss over every round trip. In an ideal laser, the longitudinal mode nearest to the peak of the gain curve will see more gain during the build-up of laser oscillation than the other modes. The gain will saturate when it equals the round-trip loss seen by this mode. All other modes will therefore see less gain than the mode nearest the peak and hence they will see a net round-trip loss and will not oscillate. An ideal laser will therefore emit continuous-wave (CW) light at a single longitudinal mode frequency. (This argument applies to homogeneously-broadened transitions. An inhomogeneously-broadened transition can be viewed as a superposition of many independent homogeneously-broadened oscillators. As these oscillators are independent, each one will saturate at the gain which allows the mode nearest its peak to oscillate and so there will be many modes oscillating across the inhomogeneously-broadened linewidth.)

1.2.2 Pulse Generation

In real laser materials, the peak of the gain curve will be comparatively flat and so many adjacent, closely-spaced modes will be able to oscillate. In general, these modes will be oscillating with phases that are more or less random and independent of each other[26]. A random amplitude and phase structure in the spectral domain leads to a randomly fluctuating output in the time domain, as shown in Figure 1.2(a). The sum of many such randomly fluctuating profiles is a uniform, continuous output[27]. However, if many longitudinal modes oscillate with a fixed phase relationship then the resultant output will be a regular sequence of pulses, as shown in Figure 1.2(b). Modelocking is the process of forcing a laser to operate with many modes that have a fixed phase relationship. Multi-mode operation is achieved in an ideal laser by increasing the loss seen by the line-centre CW mode and consequently allowing the gain in the laser to build to a level where additional modes reach their oscillation threshold. Modulation of the gain or loss of the laser at the inter-mode separation frequency introduces a loss to the CW mode and forces neighbouring modes to oscillate with a fixed phase relationship, producing pulses.

The conditions required for modelocking can also be deduced by considering the behaviour of the intracavity field in the time domain. A laser will modelock when its cavity is aligned so that the gain required by ultrashort pulses is less than that required by a CW field. Pulses will then be built up from a CW field because noise fluctuations that repeat with the period of the applied modulation will be amplified until the gain is saturated at the lower level required by ultrashort pulses. The most obvious way to contrive that pulsed operation requires less round-trip gain than a CW field is to ensure that a CW field sees more loss than a pulse. Ensuring that a pulse makes more efficient use of the available gain has the same effect, however, and this latter approach can be exploited in synchronously-pumped and soft-aperture self-modelocked lasers, as will be explained in Section 2.3.4.2.

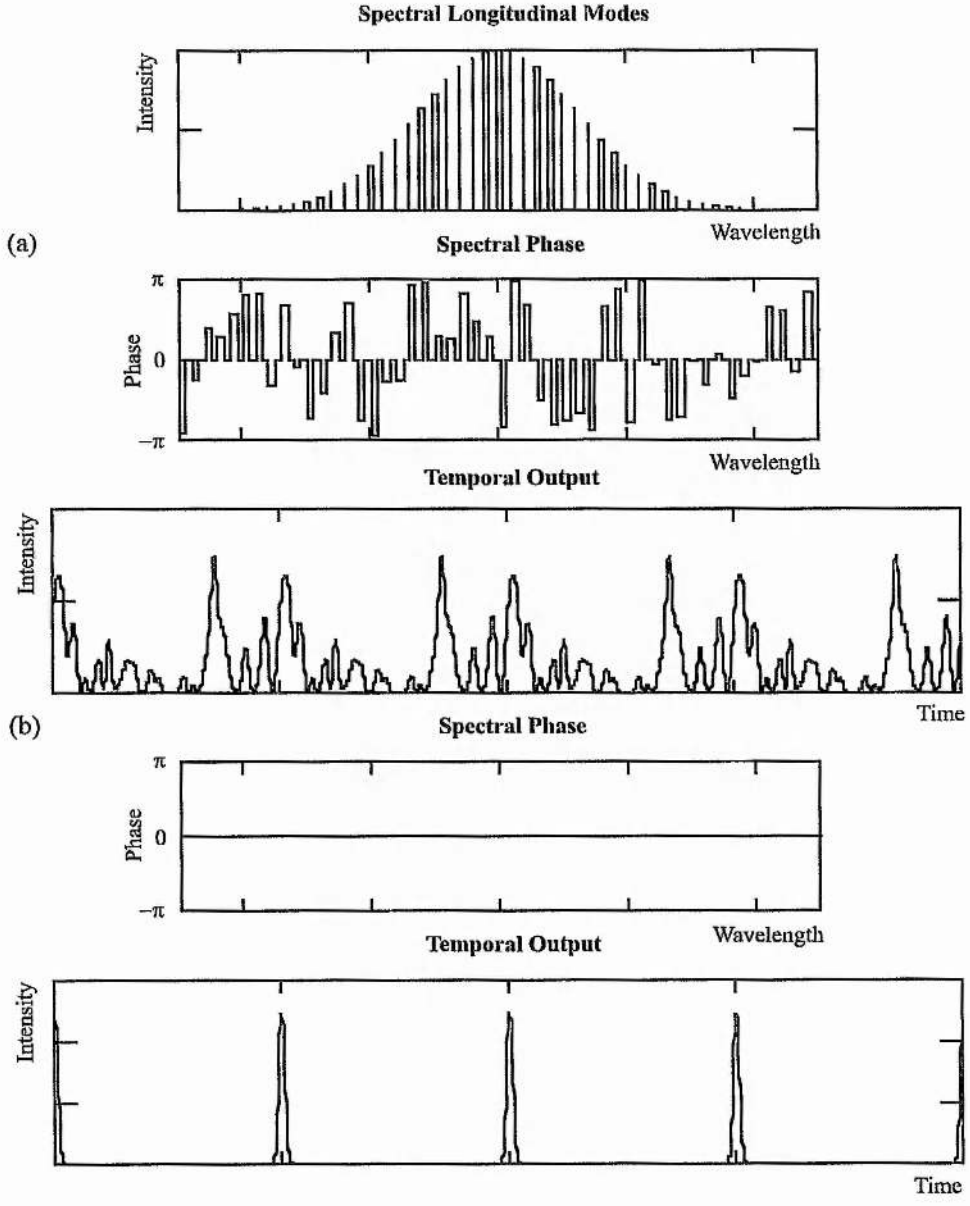

FIGURE 1.2 *Calculated effect of longitudinal mode phase relationships on laser output for a Gaussian gain profile: (a) many longitudinal modes oscillating with random phases lead to a randomly fluctuating periodic output (the superposition of many such states leads to a uniform, continuous output); (b) many longitudinal modes oscillating with a fixed phase relationship lead to a regular sequence of pulses.*

The techniques by which the modulation of the laser field is achieved are generally divided into two categories. Active modulation (Section 1.2.4) is the periodic perturbation of the cavity gain or loss at a frequency determined by some external driving signal. "Passive" modulation (Section 1.2.5) is the modulation of the cavity gain or loss by the laser field itself through a process known as self-amplitude

modulation (SAM). Firstly, however, and for completeness, I will briefly describe two cruder methods of generating pulses, namely gain-switching and Q-switching.

1.2.3 Gain-switching and Q-switching

The gain in a laser will saturate when it compensates for the round-trip resonator losses (Section 1.2.1): a condition of positive feedback is then achieved and laser oscillation results. If, however, the laser is turned on very quickly, by unblocking the cavity or by using a fast-rise-time chopped pump, for example, then a large population inversion will be generated in a very short space of time. Many modes can then oscillate simultaneously and the light field undergoes damped oscillations until the steady state is reached. Such relaxation oscillations (or electron-photon resonance) can be exploited in the generation of primitive high power pulse sequences via a technique known as gain switching[28].

Another crude method of producing pulses is by Q-switching[29]. In a Q-switched laser the population inversion in the gain medium is first allowed to build up by ensuring that there is no feedback in the laser cavity (and hence little stimulated emission); this can be achieved, for example, by obscuring one cavity mirror. In this condition the laser is a lossy, or low-Q, resonator. If feedback is then suddenly introduced into the cavity by uncovering the end mirror, the laser becomes a high-Q resonator. All of the energy stored in the inverted population is released more or less simultaneously in a high-energy output pulse. This process differs from modelocking because Q-switching involves the switching on and off of laser oscillation. In a modelocked laser, on the other hand, the laser modes are continuously oscillating, but their amplitude and phase relationships ensure that they interfere with each other in such a way that they result in a stream of pulses.

1.2.4 Active Modelocking

In an actively modelocked laser the gain or loss is modulated at a frequency determined by some external source. Modulation at a frequency equal to the frequency separation of the longitudinal modes of a resonator results in each mode acquiring modulation sidebands, and these sidebands coincide in frequency with the

frequencies of the modes' nearest neighbours. If the mode at the peak of the gain is represented in the form

$$E(t) = E_0 \cos(\omega_0 t).$$

EQUATION 1.2

then modulation at a frequency ω_m and of amplitude E_m leads to

$$E'(t) = E(t)\left[1 + \frac{E_m}{E_0}\cos(\omega_m t)\right]$$

EQUATION 1.3

where $\frac{E_m}{E_0}$ is the modulation depth. $E'(t)$ can be rewritten

$$E'(t) = E_0 \cos(\omega_0 t) + \frac{E_m}{2}\cos[(\omega_0 - \omega_m)t] + \frac{E_m}{2}\cos[(\omega_0 + \omega_m)t]$$

EQUATION 1.4

If ω_m is equal to the frequency separation of the intracavity modes then power is transferred from the central mode to its neighbours, and from the neighbours to their neighbours. This has the effect of fixing all the mode amplitude and phase relationships, and results in a periodic stream of discrete pulses.

1.2.4.1 Amplitude Modulation.

Amplitude modulation and phase modulation are two common methods of modulating the intracavity field of a laser. An important example of an amplitude modulator is the acousto-optic modulator, which consists of a piezo-electric transducer attached to a quartz block. Driving the transducer with a sine wave results in the generation of an acoustic standing wave in the quartz which depends upon the magnitude of the driving signal[30]. The acoustic standing wave changes the local refractive index of the quartz and produces an optical diffraction grating. An acousto-optic modulator therefore introduces a loss to a cavity that is controlled by the variation of the driving signal. Since the loss is a minimum when the driving signal is zero, loss modulation occurs at twice the driving frequency; thus if the modulator is driven at half the cavity frequency, the modulation will be at the

intermode-separation frequency, as required. Acousto-optic active modelocking produces pulses which are typically of durations of the order of 50 ps - 100 ps, with the expected full width half maximum duration τ_p given by[31]

$$\tau_p = \left(\frac{2\sqrt{2}\ln 2}{\pi^2}\right)^{\frac{1}{2}}\left(\frac{g}{\Delta_m}\right)^{\frac{1}{4}}\left(\frac{1}{f_m \nu_a}\right)^{\frac{1}{2}}$$

EQUATION 1.5

where g the round-trip gain, ν_a is the atomic linewidth, Δ_m is the modulation strength and f_m is the modulation frequency.

Another form of amplitude modulation is gain modulation. Semiconductor diode lasers can be actively modelocked by adding a small modulated component to an injection current which would otherwise keep them just below threshold. Current modulation at the cavity frequency of a diode laser is difficult to achieve because of the very small cavity length of the diode. A common solution to this problem is to extend the effective cavity length by using an external mirror in conjunction with a diode in which the intrinsic facet reflection has been eliminated by, for example, an anti-reflection coating[32,33].

An extreme form of gain modulation is synchronous-pulse pumping. If the laser gain medium is pumped by a series of pulses at an integer multiple of the cavity repetition rate then pulsed operation will in general be favoured over CW operation. Synchronous pumping is, however, most suitable for laser systems employing gain media with upper-state life-times significantly shorter than the round-trip time of the laser cavity. This ensures that the population inversion does not persist for long enough after each pump pulse to support a CW field.

Synchronous pumping has been applied to a variety of systems; for example, dye lasers pumped by modelocked Ar^+ or Nd:YAG lasers[34-36] , colour-centre lasers pumped by Kr^+ or Nd:YAG lasers[37,38], and fibre-Raman lasers[39,40]. Synchronously-pumped optical parametric oscillators (OPOs)[41], although operating on an entirely different physical principle (three-wave mixing), also produce ultrashort pulses by much the same mechanism: the 'pump' pulses which sustain the 'signal' and 'idler' fields are introduced to the nonlinear crystal at the OPO cavity repetition rate. The

OPO fields see a pulsed 'gain' and so they are amplified into a train of pulses of picosecond[42] or femtosecond[43] durations.

1.2.4.2 Phase Modulation

The other active modelocking technique is phase modulation, and the most common phase modulator is the electro-optic modulator. Electro-optic modulators introduce a periodic cavity loss by exploiting the Pöckels effect[44]. In electro-optic modelocking, the intracavity field of the laser is phase-shifted as it passes through a Pöckels cell driven by a RF signal with a period of half the cavity repetition period. The rate of change of this phase-shift corresponds to a frequency-shift of the carrier field. Two pulse sequences are generated in the temporal domain, each synchronised to the regions of zero rate of change of phase shift (i.e., the two points of zero frequency shift). Phase modulators have been successfully applied, for example, to doped-fibre laser systems[45,46], and pulse durations of < 20 ps have been demonstrated[47]. An electro-optic modulator has also recently been used in a regenerative configuration to initiate pulses of 21 fs duration in a self-modelocked Ti:sapphire laser[48]. One potential drawback of phase-modulation techniques is that the two pulse sequences that are generated are independent of each other and will in general have different characteristics.

1.2.5 Passive Modelocking

Whilst active modelocking can be conveniently described in both the temporal and spectral domains, passive modelocking mechanisms are usually better described in the temporal domain. It is conventional to divide passive modelocking techniques into two categories: slow saturable absorber modelocking and fast saturable absorber modelocking. However, first I will consider regenerative modelocking, which does not fit easily into either category.

1.2.5.1 Regenerative Modelocking

Regenerative modelocking[49] employs the hardware of active modelocking (e.g. an acousto-optic modulator) but it is a passive technique because the driving signal is derived from the laser field itself. In regenerative modelocking, the power in the

longitudinal modes of a laser are monitored on a fast photodiode and this signal is filtered, amplified and used to drive a modulator. Any changes in cavity length due to environmental fluctuations are reflected in a change in the modulator drive frequency, eliminating cavity/drive frequency mismatches. In common with all passive modelocking techniques, regenerative modelocking must be initiated by some signal already present at the cavity repetition frequency. However, the magnitude of the signal required for regenerative modelocking is much lower than that required for other modelocking techniques, and the beating that occurs between adjacent longitudinal cavity modes is usually sufficient. As this technique is more-or-less self-starting, it is often used as a means of initiating other passive mechanisms such as self-modelocking (also called Kerr-lens-modelocking).

1.2.5.2 Slow Saturable Absorber Modelocking

A pulse circulating in a laser cavity containing a slow saturable absorber can be shortened by a combination of absorption saturation and gain saturation. These effects persist for time periods that are long compared with the duration of the pulse; hence the effects are 'slow'. The leading edge of the pulse is attenuated by the absorbing action of the absorber, but this absorption saturates when the pulse envelope intensity reaches a certain level. As the saturation persists for a time longer than the pulse duration, the remainder of the pulse passes without significant absorption. However, the high intensities at the peak of the pulse saturate the gain of the laser medium, and this reduces the gain seen by the trailing edge of the pulse. Thus absorption on the leading edge of the pulse and gain saturation on the trailing edge tend to act in combination to shorten the pulse.

The first laser to produce sub-100 fs pulses at high repetition rates of ~100 MHz was a colliding-pulse-modelocked (CPM) dye laser[50]. This was a ring laser in which two counter-propagating pulses collided in a fluid jet consisting of a solution of 3,3'-diethyloxadicarbocyanine iodide (DODCI) that acted as a slow saturable absorber. A rhodamine 6 G (Rh6G) dye jet provided gain and gain saturation, as mentioned above. Although pulse durations of ~20 fs were achieved[51,52], CPM lasers offer only low power outputs ($\leq$ 10 mW) because of the loss introduced into the laser by the absorber. They are also limited in tunability by the small net

bandwidths of the absorber and gain dye combination. Continuum generation via laser-amplifier systems has permitted the generation of pulses tunable over 200 nm-1.6 μm[53], but the pulse to pulse amplitude fluctuations of the amplified pump pulses were of the order of 15 % and the systems had low repetition rates of ≤ 8 kHz.

Although many lasers are now available that offer performances far superior to that of CPM dye lasers, the CPM technique is still finding applications in semiconductor diode lasers[54,55]. In CPM diode lasers, the waveguide consists of two forward-biased gain regions sandwiching a reverse-biased absorber region. These devices offer sub-picosecond pulses at ultrahigh repetition rates (~350 GHz) and a monolithic CPM diode laser has been demonstrated[56]. 'Bow-tie' geometries with flared gain regions have been employed to increase the average output powers from CPM diode lasers[57,58].

1.2.5.3 Fast Saturable Absorber and Fast Saturable Gain Modelocking

A fast saturable absorber acts as an instantaneous intensity-dependent loss mechanism in a laser cavity. The loss seen by any part of the pulse depends only on its instantaneous intensity, in contrast to the slow saturable absorber case, in which saturation is achieved by the integrated effect of a significant fraction of the pulse profile. Because the instantaneous intensity of the pulse alters itself, the effect is known as self amplitude modulation (SAM).

Most of the absorbing dyes used to modelock tunable laser systems have long recovery times, of the order of a few hundred picoseconds, but SAM can be achieved by the use of a number of so-called artificial fast-saturable absorbers. The technique of additive-pulse, or coupled-cavity, modelocking (APM or CCM) was a significant development in the history of ultrashort pulse sources. The first APM/CCM laser was the 'soliton' laser[59]. This consisted of a synchronously pumped KCl:Tl^0(1) colour-centre laser that was coupled to an anomalously dispersive optical fibre in an external cavity. Synchronous pumping alone produced pulses of 8 ps, but when the external cavity length was an integral multiple of the main cavity length, pulses as short as 50 fs[60] were obtained. The synchronous-pumping was shown to be acting only as an initiation mechanism for what was

otherwise passive modelocking[61,62] by a fast-saturable gain. This reduction in pulse duration was originally interpreted as being due to soliton-like shaping of the pulse in the external cavity (hence the name soliton laser). Numerical modelling suggested, however, that pulse-shortening would also be possible if an optical fibre with non-soliton-supporting, normal dispersion was used[63], and this was subsequently confirmed experimentally[64-67]. Theoretical modelling suggested that the pulse-shortening was due to interference between pulses in the main cavity and those returning from the fibre[68,69]. The nonlinearity of the fibre resulted in an intensity-dependent phase shift as the pulse traversed the coupled cavity, and, consequently, the coupled cavity was behaving like an etalon with an intensity-dependent thickness. If the cavity was properly adjusted, the reflectivity seen at the coupling mirror by the wings of a pulse in the main cavity was reduced relative to that seen by the peak, and pulse shortening resulted.

Additive-pulse modelocked systems offer many advantages over CPM dye lasers: higher powers, wider tunability, higher stability and the elimination of the complexity and hazards related to the use of laser dyes. Colour-centre lifetimes can be limited, however, and colour-centre crystals such as KCl:Tl^0(1) and NaCl:OH^- require special handling conditions and cryogenic cooling[70]. APM/CCM operation has now been demonstrated in lasers based on many gain media that do not suffer from these problems, including Ti:sapphire[71,72], Nd:YAG[73], Nd:YLF[74], Nd:glass[75] and Cr:forsterite[76].

The principal disadvantage of the APM/CCM approach is that the interferometric matching of two cavities demands very accurate initial cavity alignment and active stabilisation during operation. Also, although pulses as short as 90 fs were obtained from a CCM Ti:sapphire laser[77], group-velocity dispersion compensation was required in both the master cavity and the cavity containing the fibre in order to achieve this. The complexity and increased alignment sensitivity that resulted from this negated some of the advantages that Ti:sapphire offered over colour-centre systems. These problems were eliminated, however, with the demonstration of 'self-modelocking' in a single-cavity Ti:sapphire laser exploiting the nonlinear response of the gain medium itself rather than that of a fibre in an external cavity[25].

Self-modelocking, also known as Kerr-lens modelocking, will be discussed in detail in subsequent chapters of this thesis.

1.3 The Behaviour of Ultrashort Light Pulses

As explained in Section 1.2.1, the natural gain curve of an ideal laser transition will permit the oscillation of only the longitudinal mode nearest to line-centre. A CW broadband laser such as Ti:sapphire will, however, typically operate on randomly phased modes oscillating across a bandwidth of the order of hundreds of MHz. Modelocking mechanisms can be employed to permit other modes to oscillate and to lock the phases of all the oscillating modes. Self amplitude modulation, for example, enables modes to oscillate across a bandwidth of hundreds of GHz, corresponding to transform-limited pulses of a few picoseconds at 850 nm. However, for pulses below this duration SAM acts as only a stabilising mechanism and pulse durations are determined by other physical effects. The dominant mechanism in determining pulse durations in the sub-picosecond regime is a soliton-like interplay between group-velocity dispersion and self phase modulation resulting from the Kerr nonlinearity of the laser crystal. These effects can be exploited to give pulses of sub-100 fs durations with bandwidths of more than 3 THz. The major limitations to pulse shortening in the sub-100 fs domain are perturbative effects associated with the break-down of this soliton-like behaviour and with higher-order dispersion[78]. Compensation of third-order dispersion (TOD) can lead to the generation of pulses with durations of the order of 10 fs (32 THz). Generation of pulses below ~8 fs is hampered by the effects of fourth-order dispersion and gain dispersion, and also by damage problems resulting from high peak intensities.

A full consideration of the phenomena associated with pulse propagation in dispersive and nonlinear media can be found in *Nonlinear Fiber Optics* by G. P. Agrawal[79]. The effects that are most relevant to this thesis will be summarised in Sections 1.3.1 and 1.3.2.

1.3.1 Group Velocity Dispersion

In a typical self-modelocked laser, two effects will dominate the behaviour of a pulse established by self-amplitude modulation: dispersive effects resulting from the linear response of intracavity dielectrics to the pulse E-field and intensity-dependent effects resulting from the nonlinear response of intracavity dielectrics to the pulse E-field. An interplay between these two effects determines the temporal profile of the steady-state pulse circulating in the cavity.

The response of a dielectric medium to an applied electric field **E** can be described by the relationship[80].

$$\mathbf{P} = \varepsilon_0\left(\chi^{(1)}\cdot\mathbf{E} + \chi^{(2)}\mathbf{:EE} + \chi^{(3)}\mathbf{:EEE} + \ldots\right),$$

EQUATION 1.6

where **P** is the induced polarisation, ε_0 is the permittivity of the vacuum and $\chi^{(j)}$ is the jth order susceptibility. A pulse propagating in a centrosymmetric crystal is influenced by the first and third terms in this expansion: the frequency dependence of the linear susceptibility $\chi^{(1)}$ leads to dispersive effects and the intensity dependence of the third term $\chi^{(3)}|\mathbf{E}|^2$ leads to self-focusing and self-phase modulation. The second term in the expansion relates to effects such as second-harmonic generation, sum- and difference-frequency generation and optical parametric amplification. It is zero in centrosymmetric crystals. The refractive index $n(\omega)$ is related to $\chi^{(1)}$ by

$$n(\omega) = 1 + \frac{1}{2}\mathrm{Re}[\chi^{(1)}(\omega)];$$

EQUATION 1.7

and the frequency dependence of the wavenumber $\beta(\omega)$ is given by

$$\beta(\omega) = \frac{n(\omega)\cdot\omega}{c}.$$

EQUATION 1.8

At frequencies well away from the electronic resonances of the dielectric, the frequency dependence of n is described by the Sellmeier equation

$$n^2(\omega) = 1 + \sum_{j=1}^{m} \frac{B_j \omega_j^{\,2}}{\omega_j^{\,2} - \omega^2},$$

EQUATION 1.9

where ω_j is the frequency and B_j is the strength of the jth resonance, the summation being over all contributing resonances[81]. It is conventional to expand $\beta(\omega)$ about the centre frequency ω_0:-

$$\beta(\omega) = \beta_0 + \beta_1(\omega - \omega_0) + \frac{1}{2}\beta_2(\omega - \omega_0)^2 + \frac{1}{6}\beta_3(\omega - \omega_0)^3 + \ldots,$$

EQUATION 1.10

where

$$\begin{aligned}
\beta_m &= \left(\frac{d^m\beta}{d\omega^m}\right)_{\omega=\omega_0} \\
&= \frac{\omega n}{c} && \text{for } m = 0 \\
&= \frac{1}{c}\left(n + \omega\frac{dn}{d\omega}\right) && \text{for } m = 1 \\
&= \frac{1}{c}\left(2\frac{dn}{d\omega} + \omega\frac{d^2n}{d\omega^2}\right) && \text{for } m = 2.
\end{aligned}$$

EQUATION 1.11

It is interesting to note that, for $m \geq 2$, β_m can be written in the general form

$$\beta_m = \frac{1}{c}\left(m\frac{d^{m-1}n}{d\omega^{m-1}} + \omega\frac{d^m n}{d\omega^m}\right) \quad \text{for } m \geq 2.$$

EQUATION 1.12

The behaviour of pulses propagating in a dispersive medium can be explained by the influence of the terms in this expansion. Table 1.2 shows the physical phenomena to which each term is linked.

Term in Taylor expansion	Physical parameter
$\beta_0 = n \cdot \frac{\omega}{c}$	Phase velocity $v_\phi = \frac{\omega_0}{\beta_0}$
$\beta_1 = \frac{1}{c}\left(n + \omega \frac{dn}{d\omega}\right)$	Group velocity $v_g = \frac{1}{\beta_1}$
$\beta_2 = \frac{1}{c}\left(2\frac{dn}{d\omega} + \omega \frac{d^2n}{d\omega^2}\right)$	Group velocity dispersion (GVD) $\beta_2 = \frac{d}{d\omega}\left(\frac{1}{v_g}\right)$ Dispersion parameter $D = -\frac{2\pi c}{\lambda^2}\beta_2$
$\beta_3 = \frac{1}{c}\left(3\frac{d^2n}{d\omega^2} + \omega \frac{d^3n}{d\omega^3}\right)$	Third order dispersion (TOD) $\beta_3 = \frac{d(GVD)}{d\omega}$

TABLE 1.2 *Physical phenomena associated with terms in the Taylor expansion of $\beta(\omega)$.*

The behaviour of the envelope of a propagating pulse is governed primarily by β_2, the group velocity dispersion (GVD). The precise effect of GVD will depend upon several factors: the sign of the GVD; the shape of the pulse envelope; and the sign of any frequency chirp present in the pulse, as will be discussed shortly. The pulses produced in self-modelocked lasers can, in general, be assumed to be of the form[82]

$$U(t) = \operatorname{sech}\left(\frac{t}{T_0}\right)\exp\left(-\frac{iC}{2}\frac{t^2}{T_0^2}\right),$$

EQUATION 1.13

where C is a frequency chirp parameter and T_0 is the pulse half-width at the 1/*e*-intensity point (related to the full-width at the half-maximum intensity point by $T_{FWHM} = 2\ln\left(1+\sqrt{2}\right)T_0$). This hyperbolic-secant pulse-shape describes a fundamental soliton in an optical fibre; the conditions under which it is legitimate to deduce the behaviour of a pulse circulating in a laser cavity from the behaviour of a soliton propagating down a fibre will be considered in Chapter 3. Figure 1.3

shows an unchirped and a heavily-chirped hyperbolic-secant pulse. Since $\omega = \frac{d\phi}{dt}$, a phase chirp that is quadratic in time introduces a linear frequency sweep across the pulse: 'positive', or 'up' chirp implies that the leading edge of the pulse is red-shifted and the trailing edge blue-shifted; 'negative' or 'down' chirp implies the reverse.

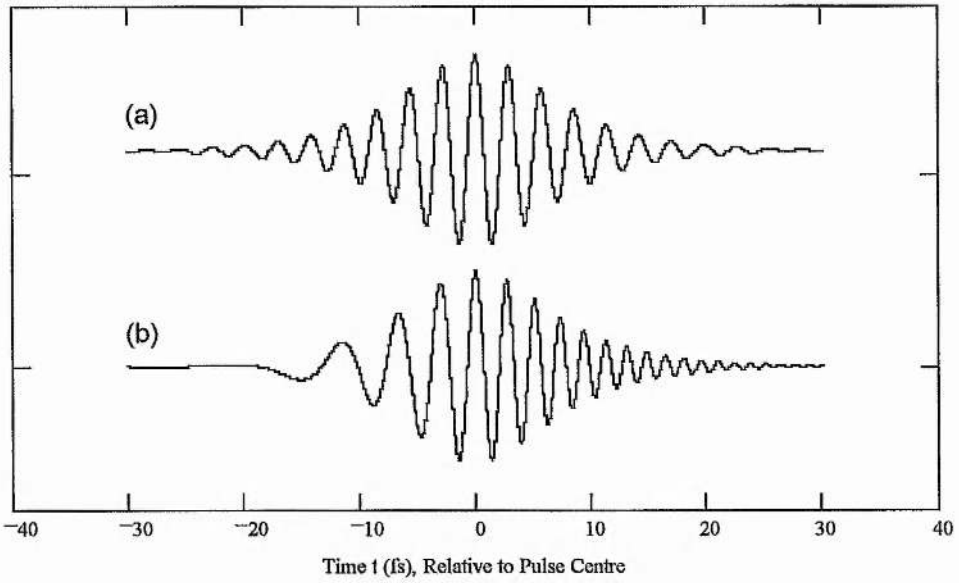

FIGURE 1.3 *Hyperbolic-secant pulses (T_{FWHM} =10 fs, λ=850 nm): (a) chirp parameter C = 0 and (b) C = +3.3.*

The duration and chirp of a pulse will change as the pulse propagates in the presence of GVD. The nature of this change for various propagation regimes is summarised in Figure 1.4. (These curves were obtained for a Gaussian pulse profile, but the qualitative effects are the same for hyperbolic-secant pulses). Positive β_2 is generally referred to as 'positive' or 'normal' dispersion; negative β_2 is generally referred to as 'negative' or 'anomalous' dispersion.

In the sub-100 fs regime, pulse duration can be limited by the broadening and destabilising effects of third-order and, in the sub-10 fs regime, higher-order dispersion. Third-order dispersion effects will be considered in more detail in Chapter 3.

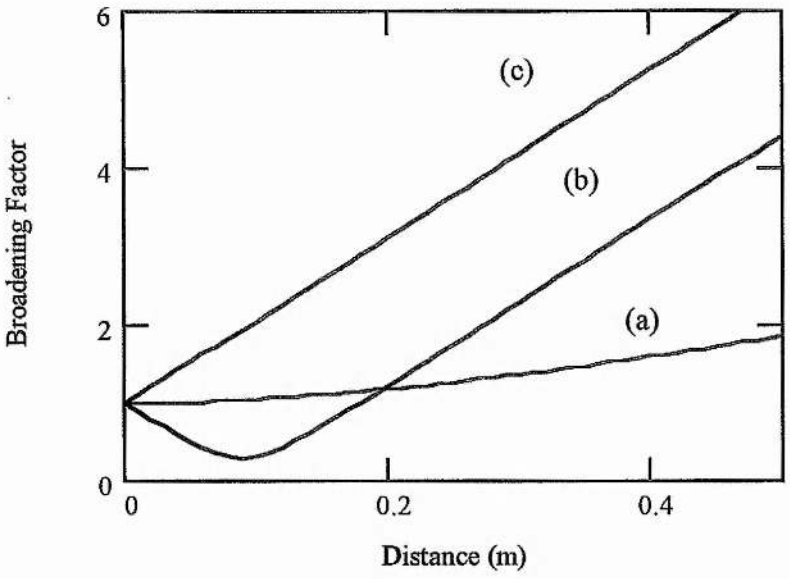

FIGURE 1.4 *Pulse broadening with propagation through a dispersive medium: (a) C=0, β_2 =-100 fs^2, (b) C=+3.3, β_2=-100 fs^2, (c) C=-3.3, β_2=-100 fs^2. For β_2=+100 fs^2, (b) and (c) would be interchanged.*

1.3.2 Nonlinear Optical Behaviour

1.3.2.1 Self Phase-modulation

When a light field is incident on a dielectric medium, the induced polarisation **P** can be written as $\mathbf{P} = \mathbf{P}_L + \mathbf{P}_{NL}$ where $\mathbf{P}_L$ is the linear component and $\mathbf{P}_{NL}$ is the nonlinear component due to the applied electric field **E**. $\mathbf{P}_{NL}$ is dominated by the contribution[83]

$$\mathbf{P}_{NL} = \varepsilon_0 \left(\frac{3}{4} \chi^{(3)}_{xxxx} |\mathbf{E}|^2 \right) \mathbf{E} .$$

EQUATION 1.14

The refractive index is written

$$\tilde{n} = n + n_2 |\mathbf{E}|^2 ,$$

EQUATION 1.15

where $n_2 = \frac{3}{8n}\mathrm{Re}\left(\chi^{(3)}_{xxxx}\right)$ is defined as the nonlinear-index coefficient[84]. A pulse propagating a distance L in such a nonlinear medium will experience a phase shift, $\Delta\phi$, across its profile given by

$$\Delta\phi = \exp\left[-\frac{2\pi i\tilde{n}L}{\lambda}\right]$$
$$= \exp\left[\frac{2\pi inL}{\lambda}\right]\exp\left[\frac{2\pi in_2|E|^2L}{\lambda}\right]$$

EQUATION 1.16

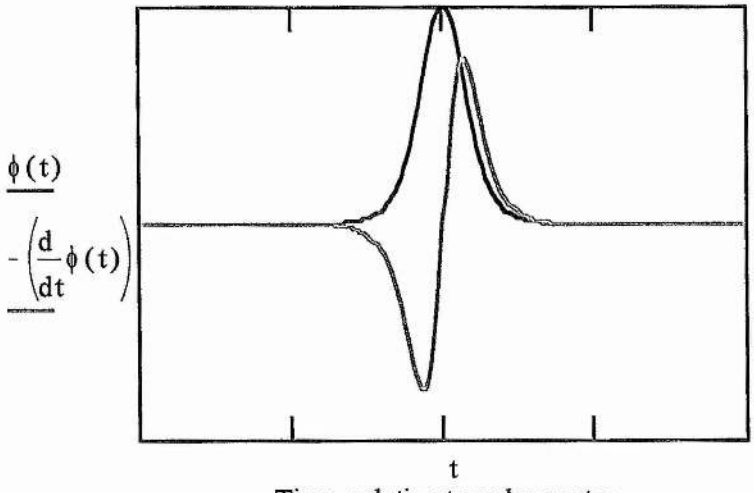

FIGURE 1.5 *The phase shift* $\phi(t)$ *and the frequency shift* $-\left(\frac{d}{dt}\phi(t)\right)$ *seen across a hyperbolic-secant pulse.*

Because the optical intensity $I = \sqrt{\frac{\varepsilon}{\mu}}|E|^2$, the phase shift experienced by each part of the pulse depends upon the instantaneous intensity of the pulse envelope. Figure 1.5 shows the phase shift that would be seen by a hyperbolic-secant pulse. Note that the frequency shift across the centre of the pulse is linear up-chirp; i.e., the frequency shift that would have been produced if an unchirped pulse passed through dielectric material of positive dispersion. In a self-modelocked laser, competition between the effects of self-phase modulation and real negative dispersion results in pulses with little chirp.

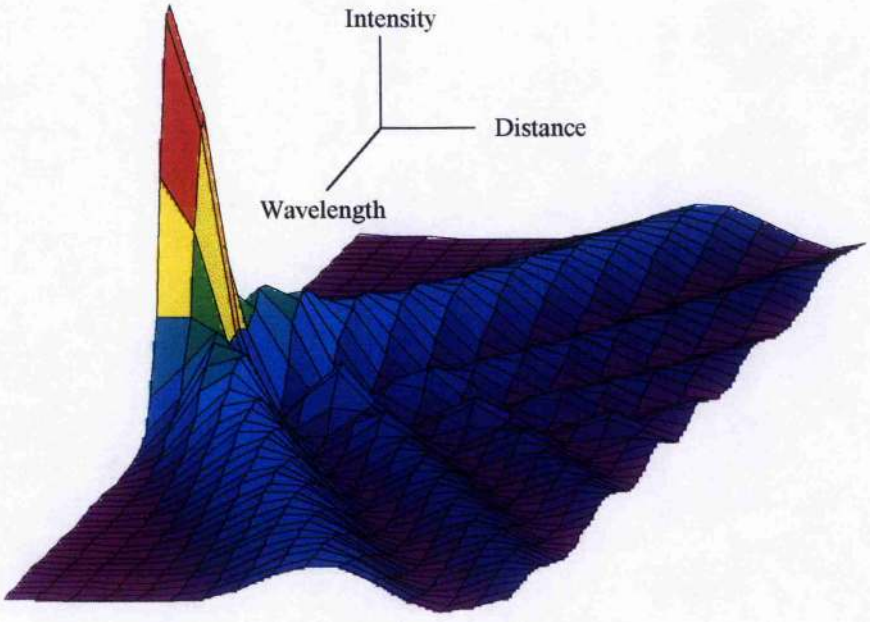

FIGURE 1.6 *The effects of SPM on the spectrum of an initially unchirped hyperbolic-secant pulse as it propagates through a nonlinear medium.*

Self-phase modulation and dispersion can also act to shorten pulses during pulse evolution. The varying phase shift produced across the temporal profile of a pulse by SPM corresponds to a broadening and modulation of the pulse spectrum (Figure 1.6). If negative dispersion removes the quasi-positive chirp from the temporal profile, the broadened spectrum results in a pulse that is shorter than that initially affected by the SPM. In reality, for a given net cavity dispersion and pulse peak power, an intracavity pulse will quickly evolve to a temporal and spectral profile which remains constant for many round trips; i.e., the pulse behaves like a fundamental soliton.

1.3.2.2 Self-focusing

The intensity-dependent refractive index that is responsible for SPM can also result in self-focusing, which is another important effect in self-modelocked lasers. The optical field inside a laser resonator will, in general, have an approximately Gaussian cross-section. Since the centre of the beam is of a higher intensity than the wings it will experience a larger phase shift, and so the beam's phase fronts will

become concave and the beam will be focused. A non-linear medium can therefore act as an intensity-dependent lens within a laser resonator. This property is exploited in self-modelocked lasers: the cavity is arranged so that the intracavity field sees a higher loss or a lower gain without a lens than with one. Consequently, a high peak intensity, strongly-lensing pulse is preferred to a CW field.

1.4 Characterising Ultrashort Light Pulses

1.4.1 Characterising the Pulse in the Temporal Domain

Several devices were used to characterise the ultrashort light pulses produced by the lasers discussed in this thesis. The average power of the pulses was measured using a linear-response silicon photodiode and Hameg 20 MHz HM203-6 or HP50603B oscilloscope. However, this system had an maximum frequency resolution of the order of a few MHz, which was not sufficiently sensitive to resolve a pulse train in which pulses were separated by 12 ns. A fast silicon photodiode and Tektronix 7904 oscilloscope system was therefore used, with an overall maximum resolution of the order of 500 MHz. This could resolve individual pulses within the pulse train but was unable to resolve the pulse profile or duration. A streak camera offered a resolution of ~1 ps [see Chapter 4], but that was still not sufficiently high. Ultimately, femtosecond resolution was achieved by using a second-harmonic generation (SHG) autocorrelator.

1.4.1.1 The Second-order Autocorrelator

A scheme to measure ultrashort light pulses to femtosecond accuracies by using second-harmonic generation was first demonstrated in the mid 1960s[85].An autocorrelator is able to achieve femtosecond accuracy by converting the measurement of a very short period of time into the measurement of a distance that is easily within the range of laboratory instruments. This is achievable because, for example, a 100 fs pulse is 30 μm long.

The laboratory implementation of a collinear Type I SHG autocorrelator is depicted in Figure 1.7.

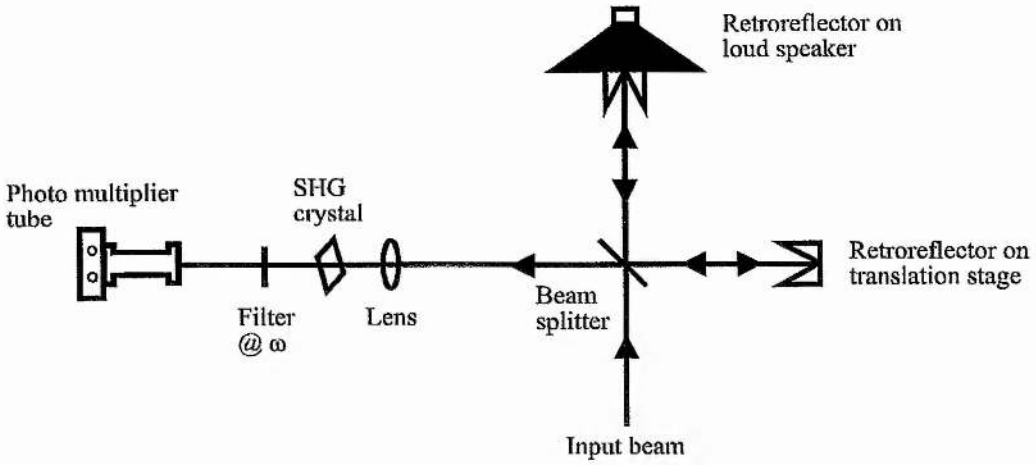

FIGURE 1.7 *A schematic of the SHG autocorrelator.*

Output pulses from the laser traverse a Michelson-type optical delay arrangement, one arm of which consists of a retroreflector mounted on a loudspeaker driven at ~20 Hz. The length of this arm is varied by the vibrating loudspeaker but the other arm is of a fixed length. The pulses from each arm are recombined at the beam-splitter, and the time delay between the pulses varies with the oscillation of the speaker. After re-combination, the pulses pass into a nonlinear crystal, such as KDP, cut for Type I second-harmonic generation[86]. The generated second-harmonic light passes through a filter (which blocks unconverted fundamental light) and is monitored by a photomultiplier tube. The resultant electrical signal, integrated over a period of time much longer than the pulse duration, is a function of the degree of overlap between the pulses from each arm of the interferometer.

The temporal pulse data recorded by the autocorrelator can either be the 'interferometric' second-order autocorrelation function or the time average of $g_2(\tau)$, the 'intensity' autocorrelation function $G_2(\tau)$[87]. The interferometric autocorrelation of a pulse, defined by the real electric field $E(t) = \xi(t)\cos[\omega t + \phi(t)]$, is given by

$$g_2(\tau) = \frac{\int_{-\infty}^{\infty} \left| [E(t) + E(t-\tau)]^2 \right|^2 dt}{2\int_{-\infty}^{\infty} E^4(t)dt}$$

which can be expanded to give

$$g_2(\tau) = 1 + \frac{2\int_{-\infty}^{\infty} E^3(t)E(t+\tau)dt + 2\int_{-\infty}^{\infty} E(t)E^3(t+\tau)dt + 3\int_{-\infty}^{\infty} E^2(t)E^2(t+\tau)dt}{\int_{-\infty}^{\infty} E^4(t)dt},$$

EQUATION 1.17

giving a maximum peak-to-background ratio of 8 to 1.

The time average of $g_2(\tau)$, the 'intensity' autocorrelation function $G_2(\tau)$, is given by

$$G_2(\tau) = 1 + 2\frac{\int_{-\infty}^{\infty} I(t)I(t-\tau)dt}{\int_{-\infty}^{\infty} I^2(t)dt},$$

EQUATION 1.18

where $I(t) = \xi^2(t)$, and the maximum peak-to-background ratio is 3 to 1.

If the time response of the photomultiplier tube and oscilloscope system is slow compared with the length of an optical cycle then the intensity autocorrelation $G_2(\tau)$ will be recorded. If the system is impedance-matched, on the other hand, this low-pass filter is eliminated and the interferometric autocorrelation $g_2(\tau)$ is obtained.

The parameter τ in Equation 1.17 and Equation 1.18 corresponds to the varying delay of the loudspeaker arm of the interferometer. Calibration of the autocorrelator is achieved by translating the retroreflector by a known distance and calculating the temporal delay to which that distance corresponds.

The intensity autocorrelation function is used to measure the duration of the laser pulses. It is can also give some information about the extent to which the laser is modelocked. Some calculated intensity autocorrelation functions are shown in Figure 1.8 for the laser operating under various conditions. Figure 1.8(a) shows the autocorrelation of a CW signal. This autocorrelation consists of a coherence spike on a constant background, with a signal:background ratio of 3:2. The spike occurs when there is zero delay between the arms of the autocorrelator and results from

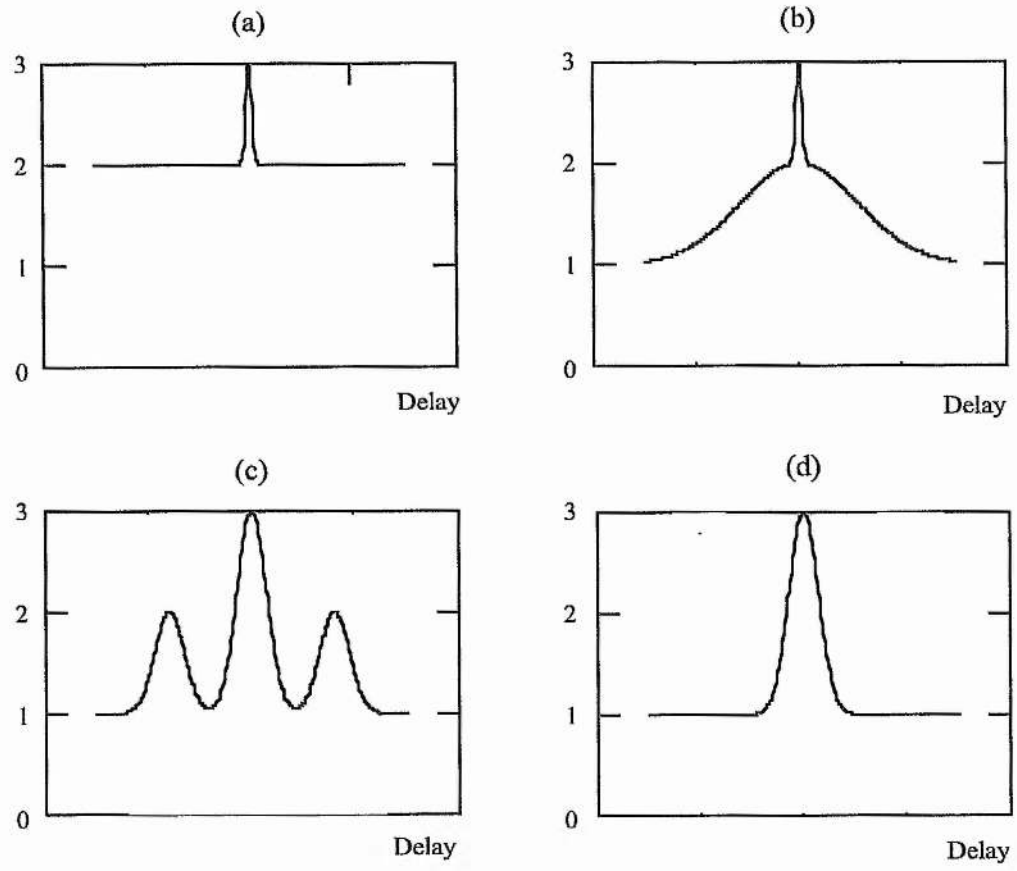

FIGURE 1.8 *Calculated intensity autocorrelation profiles for laser outputs corresponding to various operating conditions: (a) CW operation; (b) a noise burst with 100% modulation; (c) double pulsing; (d) fully modelocked operation.*

constructive interference over the coherence time of the CW light. Figure 1.8(b) shows a noise burst with 100% modulation. Again, this autocorrelation features the coherence spike that is characteristic of random noise, this time superimposed on a broad pedestal, the width of which is related to the duration of the noise burst. Figure 1.8(c) shows double pulsing, a common phenomenon in modelocked lasers. Figure 1.8(d) shows fully modelocked operation, with a 3:1 contrast ratio indicating that all of the oscillating bandwidth is fully phase-locked.

The width of the autocorrelation shown in Figure 1.8(d) is related to the duration of the pulse from which it is derived by the relationship

$$\tau_{FWHM}^{pulse} = \frac{\tau_{FWHM}^{autocorrelation}}{k}.$$

EQUATION 1.19

The magnitude of the constant 'k' depends upon the precise shape of the pulse being measured.

Autocorrelations provide only a partial analysis of the temporal properties of ultrashort pulses. In particular, autocorrelations are always symmetric, and it is necessary to assume a pulse shape in order to calculate the pulse duration. One must then calculate the duration-bandwidth product ($\Delta\tau^{pulse}_{FWHM}\Delta\nu_{FWHM}$) that results from this calculated duration to see if it is consistent with the assumed pulse-shape. Values of k are given in Table 1.3.

Pulse shape	**k**	$\Delta\tau^{pulse}_{FWHM}\Delta\nu_{FWHM}$
Gaussian	1.414	0.4413
$Sech^2$	1.543	0.3148

TABLE 1.3 *Values of the constant 'k' in Equation 1.19 for two pulse shapes, together with the corresponding transform-limited duration-bandwidth products*[87].

Chirped pulses will have duration-bandwidth products larger than those given in the table and, consequently, there is the potential for ambiguity in calculated values. However, by comparing autocorrelations calculated from the assumed pulse shape with those obtained in the lab, and by checking duration-bandwidth products, a reasonable degree of accuracy can usually be achieved. A further check is provided by monitoring the interferometric autocorrelation function $g_2(\tau)$, which gives an indication of the presence of chirp in the pulse. Figure 1.9 shows calculated interferometric autocorrelations for transform-limited and increasingly-chirped pulses. Note that the interferometric autocorrelation has a contrast ratio of 8:1. The front and rear of a frequency-chirped pulse are not coherent with each other and do not interfere; consequently, the interferometric autocorrelation collapses to the intensity autocorrelation over these parts of the pulse. Temporal calibration can be achieved directly from the interferometric autocorrelation, as the separation of each fringe corresponds to one optical cycle at the centre frequency of the pulse (2.8 fs at 850 nm).

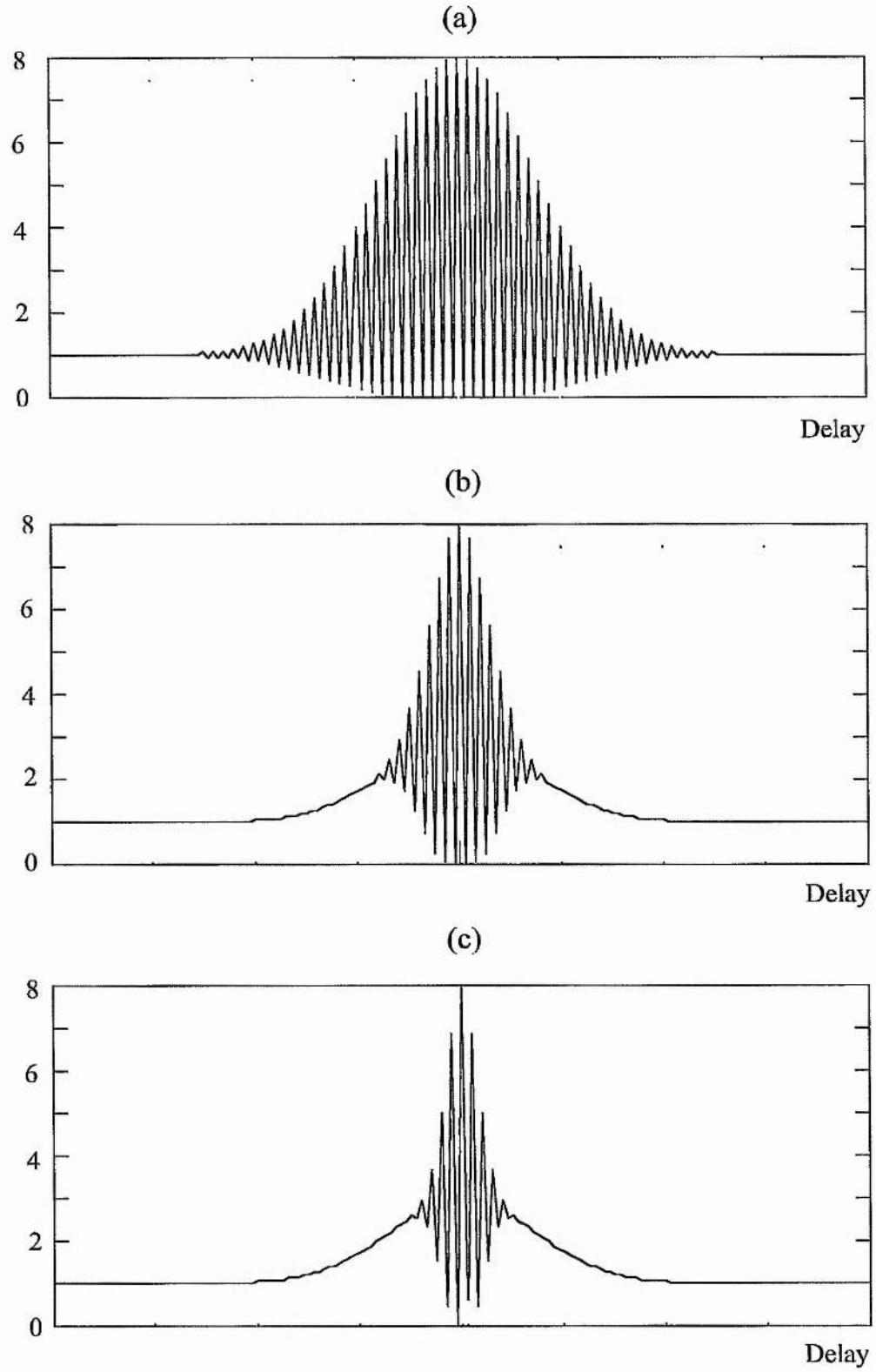

FIGURE 1.9 *Calculated interferometric autocorrelations of (a) a transform-limited sech^2 pulse, (b) a pulse with a chirp of $C = +1$ and (c) a pulse with a chirp of $C = +2$.*

1.4.2 Monitoring the Pulse in the Spectral Domain

Optical pulse spectra provide information that complements the information that can be deduced from temporal measurements. In the first place, the bandwidth of a pulse must be measured in order to calculate $\Delta\tau_{FWHM}^{pulse}\Delta\nu_{FWHM}$. In addition to this, the pulse spectrum can indicate, for example, the presence of CW background radiation through the appearance of a spike at the CW frequency, or indicate the presence of multiple pulses within the cavity through the appearance of a modulation.

Two devices were used during the course of this work to monitor pulse power spectra. A fibre-coupled Anritsu Wiltron MS96A optical spectrum analyser (OSA) was used to obtain pulse spectra to a resolution of 0.1 nm - 0.5 nm. The OSA is essentially a digitally-calibrated scanning monochromator. Real-time monitoring was achieved with the use of an Applied Photophysics monochromator in combination with a linear charge-coupled-device (CCD) array, giving a resolution of 0.1 nm. The output slit of the monochromator was opened to allow the full angular width of the pulse spectrum out of the device, and this light was incident on the CCD, with the CCD output being monitored on an oscilloscope.

In addition to the optical spectrum, the radio frequency (RF) power spectrum of the laser output gives valuable information about the pulse train. Firstly, beating between the longitudinal modes of the CW laser enables the calculation of cavity length to be made to a far higher degree of accuracy than is possible by direct measurement; cavity length is an important parameter when using a regeneratively-initiated modelocking system. The RF spectrum also provides a convenient means of checking that regenerative modelocking is maintained during optimisation of the laser for self-modelocking. Finally, the RF spectrum provides information on the noise properties of the laser output: a comparison of the RF spectral power at a high harmonic with that of the fundamental permits the extraction of the power spectrum of the phase noise or timing jitter; i.e., the long-term uncertainty in the time of arrival of future pulses in a pulse sequence [see Chapter 4]. Throughout this work, the fast silicon photodiode of the regenerative-initiation circuit was used

in conjunction with an HP70000 System RF spectrum analyser to monitor the RF spectrum of the pulse train.

1.4.3 Other Pulse Characterisation Techniques

A pulse can be characterised with a reasonable degree of accuracy by the measurement of its autocorrelations and spectrum. Given an assumed shape, the duration of a pulse can be calculated and an interferometric autocorrelation can be used to make some estimate of the degree of frequency chirp present. Various researchers have recently made progress, however, in the development of techniques that permit the full characterisation of the electric field associated with a pulse. Such techniques have many potential applications: for example, one - known as Frequency-Resolved Optical Gating (FROG) - has already led to important insights into the mechanisms that shape pulses in the sub-10 fs regime[88].

In most of the methods that have been developed, a short segment of the pulse is sampled by a nonlinear optical element that acts as a time gate[89-94]. The two most successful recent pulse characterisation techniques FROG[92,93] and Frequency-Domain Phase Measurement (FDPM)[91]. In FROG, a pulse passes through a nonlinear autocorrelator, such as a second-harmonic generation (SHG) autocorrelator, and then through a spectrometer. A spectrogram is recorded, and the original pulse can be reconstructed from this by iteration. In FDPM, the measurements are reversed: a portion of the pulse is first passed through a spectrometer and then spectrally resolved components of the pulse are cross-correlated with the pulse itself in a SHG crystal. A sonogram is measured and the original pulse is again reconstructed by iteration. Both of these methods rely on a nonlinear element such as a SHG crystal, but Wong and Walmsley have pointed out that the full characterisation of a pulse is possible from purely linear measurements[95]. The important point is that all linear pulse characterisation techniques must include at least one time-stationary filter (such as a spectrometer) and one time non-stationary filter, which will usually be a frequency-stationary filter. Both FROG and FDPM rely on amplitude frequency-stationary filters, and these methods are nonlinear because nonlinear crystals are the only devices currently available with temporal responses that are fast enough to be used in the

amplitude gating of femtosecond pulses. Walmsley and Wong point out, however, that linear frequency-stationary filters are readily available in the form of phase-only devices. The Time-Frequency Converter[96] and the Spectral Shearing Interferometer[97] utilise electro-optic phase modulators as phase-only frequency-stationary filters. The advantage of these linear techniques is that the original pulse can be fully reconstructed by analytical, rather than iterative, methods[95,98]. Another important method developed by Mysyrowicz and co-workers utilises a Kerr medium as a nonlinear filter[99].

The diversity of these techniques gives some idea of the magnitude of the recent surge of interest in the full characterisation of ultrashort optical pulses. Whilst none of the techniques were used in the work described in this thesis, it is anticipated that they will become important tools in the characterisation of ultrashort pulses in the near future.

1.5 Concluding Remarks

In this chapter I have introduced some important aspects of the field of ultrashort light pulse generation. I have briefly described some of the applications of ultrashort pulses; the various techniques that can be used to generate them; their behaviour in dispersive and nonlinear media; and methods that can be used to characterise their temporal and spectral profiles. These ideas form the background material necessary for the work that will be described in subsequent chapters.

This thesis is concerned with the generation of ultrashort pulses from all-solid-state Cr:LiSAF systems. The systems described in the next chapter are self-modelocked Cr:LiSAF lasers pumped by frequency-doubled minilasers operating in the green spectral region. This novel pumping scheme is made possible by the use of LiSAF crystals doped with 10 % - 22 % Cr^{3+}. Minilasers provide relatively high pump powers in beams of high optical quality, and this permitted the construction of a Cr:LiSAF system that produced sub-100 fs pulses at output powers that are only now being matched by directly diode-pumped systems.

The system described in Chapters 3 and 4 is a low-threshold laser pumped directly by a self-injection-locked broad-area diode. Chapter 3 builds on the ideas

introduced in this chapter to discuss the factors that affect the pump power required for self-modelocked operation. Chapter 4 describes the implementation of these ideas in a Cr:LiSAF laser that produced sub-100 fs pulses for just 73 mW of pump power.

Chapter 5 describes the development of the latest systems that are being constructed to provide self-modelocked operation at still lower pump powers from compact resonator geometries. In Chapter 6, general conclusions are drawn, the future of Cr:LiSAF lasers is discussed and some novel all-solid-state ultrashort-pulse systems are proposed.

---

[1] See, for example, W. Kaiser, ed., *Ultrashort Laser Pulses and Applications*, Springer-Verlag, New York (1988)

[2] M. Gruebele and A. H. Zewail in *Physics Today*, p24 May 1990

[3] M. Dantus, R. Bowman, A. H. Zewail, Nature **343**, 737 (1990)

[4] M. J. Rosker, M. Dantus and A. H. Zewail, J. Chem. Phys. **89**, 6113 (1988)

[5] J. H. Glownia, J. A. Misewich, P. P. Sorokin, J. Chem. Phys. **92**, 3335 (1990)

[6] G. R. Fleming and P. G. Wolynes in *Physics Today*, p36 May 1990

[7] M. Dantus, S. B. Kim, J. C. Williamson, A. H. Zewail J. Phys. Chem. **98**, 2782 (1994)

[8] A. H. Zewail, J. C. Williamson, J. Phys. Chem. **98**, 2766 (1994)

[9] A. Migus, A. Antonetti, J. Etchepare, D. Hulin and A. Orszag, J. Opt. Soc. Am. B **2**, 584 (1985)

[10] Q. Wang, R. W. Schoenlein, L. A. Peteanu, R. A. Mathies, C. V. Shank, Science **266**, 422 (1994)

[11] D. H. Auston in *Physics Today*, p46, February 1990

[12] P. C. Becker, H. L. Fragnito, C. H. Brito Cruz, J. Shah, R. L. Fork, J. E. Cunningham, J. E. Henry, C. V. Shank, Appl. Phys. Lett. **53**, 2089 (1988)

[13] W.-Z. Lin, R. W. Schoenlein, J. G. Fujimoto, E. P. Ippen, IEEE J. Quantum Electron. **24**, 267 (1988)

[14] J. Shah, B. Deveaud, T. C. Damen, W.-T. Tsang, A. C. Gossard and P. Lugli, Phys. Rev. Lett. **59**, 222 (1987)

[15] D. H. Auston, in *Ultrashort Laser Pulses and Applications* ,W. Kaiser, ed., Springer-Verlag, New York (1988), p183

[16] C. P. J. Barty, C. L. Gordon and B. E. Lemoff, Opt. Lett. **19**, 1442 (1994)

[17] J. Zhou, C-P Huang, C. Shi, M. M. Murnane, and H. Kapteyn, Opt. Lett. **19**, 126 (1994)

[18] W. E. White, A. Sullivan, D. F. Proce, J. Bonlie and R. Stewart, in *Technical Digest of Conference on Lasers and Electro-Optics* (Optical Society of America, Washington, D. C., 1995), Paper CPD45-1

[19] C. Le Blanc, G. Grillon, J. P. Chambaret, A. Migus and A. Antonetti, Opt. Lett **18**, 140 (1993)

[20] P. Maine, D. Strickland, P. Bado, M. Pessot and G. Mourou, IEEE J. Quantum Electron **24**, 398 (1988)

[21] A. Mysyrowicz, in *Laser Sources and Applications SUSSP47* ed. A. Miller and D. M. Finlayson (IOP, London,1995)

[22] G. Fracas, C. Toth, D. Moustaizis, N. Papadogiannis, C. Fotakis, Phys. Rev. A **46**, 3605 (1992)

[23] D. von der Linde, T. Engers, G. Genke, P. Agostini, G. Grillon, E. Nibbering, A. Mysyrowicz and A. Antonetti, Phys. Rev. A **52**, 25 (1995)

[24] M. D. Perry and G. Mourou, Science **264**, 917 (1994)

[25] D. E. Spence, P. N. Kean and W. Sibbett, Opt. Lett. **16**, 42 (1991)

[26] V. I. Malyshev, A. V. Masalov and A. A. Sychev, JETP Lett. **11**, 215 (1970)

[27] D. J. Bradley and G. H. New, Proc. IEEE **62**, 313 (1974)

[28] See, for example, W. Koechner, in Solid-state Laser Engineering, 4th Edn., (Springer-Verlag, Berlin, 1996) p110

[29] See A. E. Siegman in *Lasers*, University Science Books, California (1986), Chapter 26

[30] A. Yariv in Quantum Electronics, 3rd Edn. (Wiley, New York, 1989) p327

[31] A. E. Siegman in *Lasers*, University Science Books, California (1986), p1067

[32] D. J. Bradley, M. B. Holbrook and W. E. Sleat, IEEE J. Quantum Electron **17**, 658 (1981)

[33] J. Chen, W. Sibbett and J. I. Vukusic, Electron Lett. **18**, 426 (1982)

[34] C. K. Chan and S. O. Sari, Appl. Phys. Lett. **25**, 403 (1974)

[35] J. Kuhl, H. Klingenberg, and D. von der Linde, Appl. Phys. **18**, 279 (1979)

[36] A. M. Johnson and W. M. Simpson, Opt. Lett. **8**, 554 (1979)

[37] L. F. Mollenauer in *Handbook of Lasers* (eds M. L. Stich and M. Bass), Vol. 4, Amsterdam, North-Holland (1985), Chapter 2

[38] N. Langford, K. Smith and W. Sibbett, Opt. Lett. **12**, 817 (1987)

[39] R. H. Stolen, Fibre Integr. Opt. **3**, 21 (1980)

[40] J. D. Kafka, D. F, Head and T. Baer in *Ultrafast Phenomena V* (eds. G. R. Fleming and A. E. Siegman), Springer Series in Chemical Physics 46, Springer, New York, p. 51 (1986)

[41] K. Burneika, M. Ignatavicius, V. Kabelka, A. Piskarskas and A. Stabinis, IEEE J. Quantum Electron. **QE-8**, 574 (1972)

[42] A. Nebel, C. Fallnich, R. Beigang and R. Wallenstein, J. Opt. Soc. Am. B **10**, 2195 (1993)

[43] D. C. Edelstein, E. S. Wachman and C. L. Tang, Appl. Phys. Lett. **54**, 1728 (1989)

[44] A. E. Siegman in *Lasers*, University Science Books, California (1986), p980

[45] G. Geister and R. Ulrich, Opt. Commun. **68**, 187 (1988)

[46] D. C. Hanna, A. Kazer, M. W. Philips *et al.* , Electron. Lett. **25**, 95 (1989)

[47] J. B. Schlager, Y. Yamabayashi, D. L. Franzer and R. I. Juneau, IEEE Phot. Tech. Lett. **1**, 264 (1989)

[48] W. P. Grice and I. A. Walmsley, Opt. Lett. **20**, 1553 (1995)

[49] G. R. Huggett, Appl. Phys. Lett. **13**, 186 (1968)

[50] R. L. Fork, B. I. Greene and C. V. Shank, Appl. Phys. Lett. **38**, 671 (1981)

[51] J. A. Valdmanis, R. L. Fork and J. P. Gordon, Opt. Lett. **10**, 131 (1985)

[52] A. Finch, G. Chen, W. Sleat and W. Sibbett, J. Mod. Opt. **35**, 345 (1988)

[53] R. L. Fork, C. V. Shank, C. Hirlimann, R. Yen and W. J. Tomlinson, Opt. Lett. **8**, 1 (1983)

[54] Y-K Chen and C. W. Ming, IEEE J. Quantum Electron. **28**, 2177 (1992)

[55] D. J. Derickson *et al*, IEEE J. Quantum Electron. **28**, 2186 (1992)

[56] Wu *et al*, in *Ultrafast Phenomena VIII* (Springer-Verlag, Berlin, 1993) p211

[57] G. Eisenstein, R. S. Tucker, U. Koren and S. K. Korothy, IEEE J. Quantum Electron. **22**, 142 (1986)

[58] Y. K. Chen and M. C. Wu, IEEE J. Quantum Electron. **28**, 2176 (1992)

[59] L.F. Mollenauer and R. H. Stolen, Opt. Lett. **9**, 13 (1984)

[60] F. M. Mitschke and L. F. Mollenauer, Opt. Lett. **12**, 407 (1987)

[61] F. M. Mitschke and L. F. Mollenauer, IEEE J. Quantum Electron. **QE-22**, 2242 (1986)

[62] J. F. Pinto, C. P. Yakymyshyn and C. R. Pollock, Opt. Lett. **13**, 383 (1988)

[63] K. J. Blow and D. Wood, J. Opt. Soc. Am. B **5**, 629 (1988)

[64] P. N. Kean, R. S. Grant, D. W. Crust, X. Zhu, D. Burns and W. Sibbett, in *Technical Digest of Conference on Lasers and Electro-Optics* (Optical Society of America, Washington, D. C., 1988), Paper PD7

[65] P. N. Kean, X. Zhu, D. W. Crust, R. S. Grant, N. Langford and W. Sibbett, Opt. Lett. **14**, 39 (1989)

[66] K. J. Blow, D. S. Forrester and B. P. Nelson in *Ultrafast Phenomena IV* (Springer-Verlag, Berlin, 1988), p 67

[67] K. J. Blow and B. P. Nelson, Opt. Lett. **13**, 1026 (1988)

[68] J. Mark, L. Y. Liu, K. L. Hall, H. A. Haus and E. P. Ippen, Opt. Lett. **14**, 48 (1989)

[69] F. Oullette and M. Piche, Opt. Comm. **60**, 99 (1986)

[70] C. P. Yakymyshyn, J. F. Pinto and C. R. Pollock, Opt. Lett. **14**, 621 (1989)

[71] P. M. W. French, J. A. R. Williams and J. R. Taylor, Opt. Lett. **14**, 686 (1989)

[72] J. Goodberlet, J. Wang,J. G. Fujimoto and P. A. Schulz, Opt. Lett. **14**,1125 (1989)

[73] L. Y. Liu, J. M. Huxley, E. P. Ippen and H. A. Haus, Opt. Lett. **15**, 553 (1990)

[74] C. Spielmann, F. Krausz, E. Wintner and A. J. Schmidt in *Digest of the Topical Meeting on Ultrafast Phenomena* (Optical Society of America, Washington, D. C., 1990), paper PD10

[75] J. K. Chee, E. C. Cheung, M. N. Kong and J. M. Liu in *Digest of the Topical Meeting on Ultrafast Phenomena* (Optical Society of America, Washington, D. C., 1990), paper MA2

[76] A. Sennaroglu, T. J. Carrig and C. R. Pollock, Opt. Lett. **17**, 553 (1992)

[77] D. E. Spence and W. Sibbett, J. Opt. Soc. Am. B **8**, 2053 (1991)

[78] C. Spielmann, P. F. Curley, T. Brabec and F. Krausz, IEEE J. Quantum Electron. **30**, 1100 (1994)

[79] G. P. Agrawal, in *Nonlinear Fiber Optics* (Academic Press, London, 1995)

[80] Ref. 79, p15

[81] Ref. 79, p7

[82] Ref. 79, p69

[83] Ref. 79, p39

[84] Ref. 79, p40

[85] H. P. Weber, J. Appl. Phys. **38**, 2231 (1967)

[86] A. Yariv in Quantum Electronics, 3rd Edn. (Wiley, New York, 1989) Chapter 16

[87] J.-C. M. Diels, J. J. Fontaine, I. C. McMichael and F. Simoni, Appl. Opt. **24**, 1270 (1985)

[88] G. Taft, A. Rundquist, H. Kapteyn and M. Murnane, Opt. Lett 7, 743 (1995)

[89] C. Yan and J.-C. Diels, J. Opt. Soc. Am. B **8**, 1259 (1991)

[90] K. Naganuma, K. Mogi and H. Yamada, IEEE J. Quantum. Electron. **25**, 1225 (1989)

[91] J. L. A. Chilla and O. E. Martinez, IEEE J. Quantum Electron. **27**, 1228 (1991)

[92] D. J. Kane and R. Trebino, IEEE J. Quantum Electron. **29**, 571 (1993)

[93] R. Trebino and D. J. Kane, J. Opt. Soc. Am. A **10**, 1101 (1993)

[94] J. Paye, M. Ramaswamy, J. G. Fujimoto and E. P. Ippen, Opt. Lett. **18**, 1946 (1993)

[95] V. Wong and I. A. Walmsley, J. Opt. Soc. Am. B **12**, 1491 (1995)

[96] M. T. Kauffmann, W. C. Bantai, A. A. Godil and D. M. Bloom, Appl. Phys. Lett. **64**, 270 (1994)

[97] V. Wong and I. A. Walmsley, Opt. Lett. **19**, 287 (1994)

[98] M. Beck, M. G. Raymer, I. A. Walmsley and V. Wong, Opt. Lett. **18**, 2041 (1993)

[99] B. S. Prade, J. M. Schins, E. T. J. Nibbering, M. A. Franco and A. Mysyrowicz, Opt. Comm. **113**, 79 (1994)

2. All-solid-state Self-modelocked Cr:LiSAF Lasers Pumped in the Green Absorption Trough

2.1 Introduction

Self-modelocking has now been demonstrated in several materials (see Table 2.1 for some examples) but the commercial self-modelocked laser market is dominated by lasers based on the Ti^{3+}-doped sapphire (Ti:sapphire). Ti:sapphire can be grown relatively easily, and it has a spectral linewidth capable of supporting pulses of sub-10-fs duration, a relatively large laser gain cross-section, exceptional mechanical strength and a high thermal damage threshold. The principal disadvantage of Ti:sapphire lasers is the need for pumping by mainframe Ar^+ ion lasers. These devices are expensive, bulky and have considerable electrical and cooling requirements. An all-solid-state (or 'holosteric') system would offer a cheaper, more reliable, more efficient and considerably more compact source of ultrashort pulses. Recently, self-modelocked operation of a Ti:sapphire laser pumped by a frequency-doubled diode-pumped Nd:YLF laser has been demonstrated[1]. This development has sparked renewed interest in Ti:sapphire as a gain crystal candidate for all-solid-state systems, and commercial minilaser-pumped devices are now becoming available[2].

In this chapter, two all-solid-state laser systems are described that are based on the gain material Cr^{3+}:$LiSrAlF_6$ (Cr:LiSAF). Cr:LiSAF is a vibronic gain medium, and the first section of this chapter is an introduction to vibronic gain media in general, and to Cr:LiSAF in particular. The rest of the chapter is devoted to a description of two Cr:LiSAF lasers that share the novel feature that they are pumped by frequency-doubled minilasers operating in the green spectral region. This region corresponds to a *minimum* in the absorption spectrum of Cr:LiSAF. The frequency-doubled minilaser pump sources were developed at the University of St. Andrews by C. Yelland and J. Hong, but they are described in some detail in this

chapter because they form integral parts of the novel femtosecond Cr:LiSAF laser systems described in this chapter.

Material	Pump band λ (μm)	Emission cross-section σ (10^{-19} cm^2)	Upper-state lifetime τ (μs)	Fluores-cence peak (μm)	Tuning range (μm)	στ (10^{-19} cm^2 μs)
Ti^{3+}:sapphire	0.45-0.6	3.8	3.2	0.78	660-1180	12.2
Cr^{4+}:forsterite	0.85-1.2	1.1	15	1.0	1167-1345	16.5
Cr^{4+}:YAG	0.88-1.1	8.0	4	1.4	1300-1600	32.0
Cr^{3+}:LiSAF	0.40-0.75	0.48	67	0.83	760-920	32.2
Cr^{3+}:LiCAF	0.35-0.75	0.12	170	0.78	720-840	20.4

TABLE 2.1 *Spectroscopic properties of some gain materials that have been used in self-modelocked lasers*[3-6]. *N.B.: Laser linewidth and threshold pump power are both inversely proportional to στ.*

2.2 Cr:LiSAF

2.2.1 Vibronic Gain Media

The first laser ever demonstrated was solid-state. It used a ruby (Cr^{3+} doped sapphire - Cr:Al_2O_3) gain crystal, but it had only a narrow linewidth and was essentially non-tunable[7]. Vibronic lasers are a class of widely-tunable solid-state lasers. Solid-state gain materials are made by doping crystalline (or glassy) host media with 'activator' ions, usually ions from the rare-earth or transition-metal regions of the Periodic Table. Although lasing occurs between the electronic energy levels of the these dopant ions, the host material is also very important in determining the laser characteristics of a particular crystal because it determines the relative positions of the electronic energy levels.

Vibronic laser materials have large linewidths because the electrons of their active ions and vibrational modes in their host media interact with each other (hence *vibronic*, from *electronic* and *vibrational*). Cr^{3+} doped LiSAF (Lithium Strontium Aluminium Fluoride - Cr^{3+}:$LiSrAlF_6$), for example, shows broad tunability and has supported pulses as short as 18 fs[8], even though its active ion is the same as that of ruby.

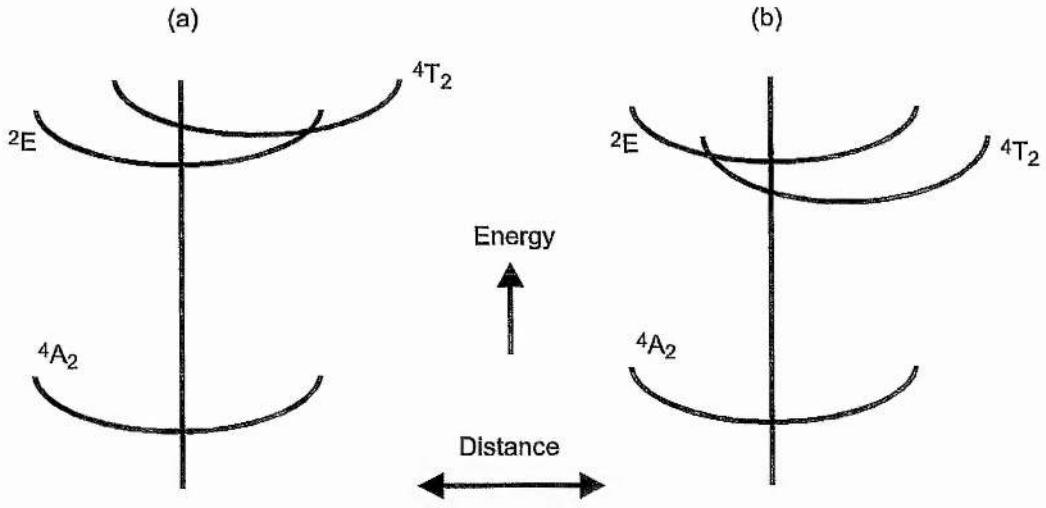

FIGURE 2.1 *Simplified configuration co-ordinate diagrams for Cr3+ in (a) ruby and (b) LiSAF*

The differing effects of sapphire and LiSAF hosts on the energy levels of active Cr^{3+} ions are illustrated in simplified form in Figure 2.1. These sketches are configuration co-ordinate diagrams: they represent the combined energies of the electrons of the active ions and the vibrations of the lattice. The principal difference between ruby and Cr:LiSAF is the position of the $^4T_2$ energy level in each host. The relative position of the $^4A_2$ and ^2E electronic states depends upon a spin-orbit interaction among the Cr^{3+} ion's electrons and is therefore largely independent of the host medium[9]. The position of the $^4T_2$ level, on the other hand, depends strongly on the size of the crystal field at the site of the laser ion. This field is much stronger in ruby than it is in Cr:LiSAF and so there is a difference in the position of this level in the two hosts. LiSAF is a 'low-field host'.

Ruby is a three-level laser material. Light is absorbed in the transition $^4A_2 \rightarrow {}^4T_2$, electrons in the $^4T_2$ level quickly relax to the ^2E level and lasing occurs on the ^2E

$\rightarrow {}^4A_2$ transition. The wavelength of the emitted light is constant regardless of the vibrational state of the host lattice - that is, regardless of position on the ^2E parabola of Figure 2.1 - because the separation of points on the ^2E and $^4A_2$ parabolas is constant across the parabolas. The laser transition in ruby therefore has a small linewidth.

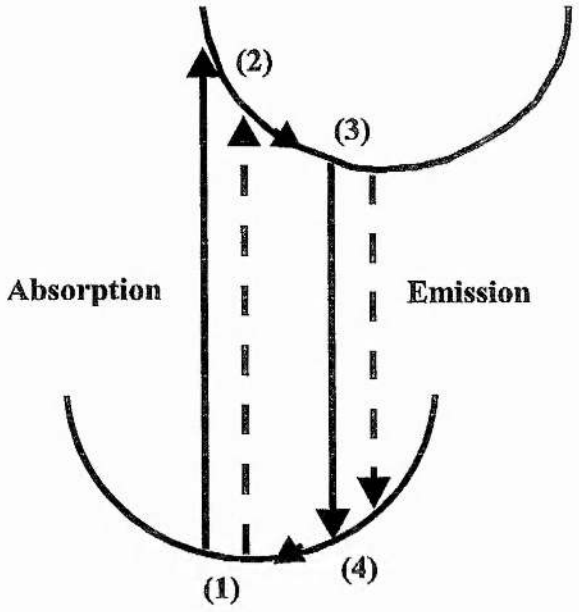

FIGURE 2.2 *The four-level cycle of a Cr:LiSAF laser: (1) excitation of ions in the electronic ground state by pump photons; (2) relaxation of the lattice by the emission of phonons; (3) relaxation of ions to the electronic ground state by emission of photons in the laser transition; and (4) relaxation of the lattice to the vibrational ground state by the emission of phonons.*

In Cr:LiSAF pumping can again occur on the $^4A_2 \rightarrow {}^4T_2$ line, but laser action is on the $^4T_2 \rightarrow {}^4A_2$ transition. At normal temperatures, the ions of the host lattice are undergoing relatively small vibrations about their equilibrium position near the bottom of the $^4A_2$ parabola. Because the $^4T_2$ parabola has been displaced by the LiSAF crystal field relative to its position in ruby, pumping now excites electrons into high lattice vibrational energy states, far out along the parabola (see Figure 2.2). Thus the laser material is excited both electronically and vibrationally. Firstly the lattice relaxes radiatively, emitting its energy in the form of phonons, and then the ions relax to the electronic ground state in the lasing transition. However, the medium is then in an excited vibrational state once again, and so phonons are emitted to return the system to its overall electronic and vibrational ground state.

Cr:LiSAF is thus a four-level laser. Because the energy gap between the two levels of the laser transition varies across the parabolas, the wavelength of the laser light is spread over a comparatively large range. The laser transition in Cr:LiSAF thus extends over a large bandwidth.

2.2.2 Vibronic Laser Materials

Lasers based upon transition metal ions[10] and colour centres[11] operating on vibronic transitions were demonstrated in the early days of lasers. It was not until the late 1970's, following the demonstration of laser operation in Cr^{3+}:Alexandrite[12] and F_A colour centres[13], that significant research effort began to concentrate on the investigation of tunable solid-state gain media. Unfortunately, few of the systems subsequently demonstrated were entirely free from problems such as difficulties with crystal growth, low quantum efficiencies or strong excited state absorption (ESA)[14]. ESA is parasitic absorption occurring when the laser or pump transition energy of a crystal happens to be equal to the energy of another transition. A search for an ESA-free laser material led to the demonstration of the first Ti^{3+}:sapphire laser in 1982[15]. Ti:sapphire is free from ESA because Ti^{3+} has only one valence electron, found in the 3d shell, and the energy required to take the electron out of this shell is much larger than the energies of the pump or laser transitions.

Cr:LiCAF[16] and Cr:LiSAF[17] are members of the colquiriite family of Cr^{3+} doped fluorides. They have attracted increasing attention as alternatives to Ti:sapphire as gain media in self-modelocked lasers. These materials exhibit a tuning range similar to that of Ti:sapphire but also have several properties which facilitate their direct pumping by diode lasers[18]. They have absorption bands in the red spectral region that are coincident with the emission bands of potential semiconductor pump sources, such as GaInP/AlGaInP diode lasers, and are broad enough to make temperature tuning and stabilisation of such pump lasers unnecessary. They have relatively long upper-state life-times, and very high Cr^{3+} doping levels are possible without degradation of the crystal quality[19]. (The absorption peak of Ti:sapphire is in the green spectral region, which makes it unsuitable for direct diode-pumping). The rate of change of refractive index with temperature is negative in LiSAF and

LiCAF, lessening the likelihood of thermal lensing problems. Against these positive points, however, are the fracture toughness and thermal performance of LiSAF/LiCAF, which are significantly poorer than those of Ti:sapphire, resulting in an increased likelihood of mechanical failure at high pump powers.

Cr:LiSAF has attracted more attention as a laser crystal than Cr:LiCAF. Cr:LiSAF's tuning range is broader than Cr:LiCAF's (780 nm to 1060 nm vs. 720 nm to 840 nm) and Cr:LiSAF has absorption and emission cross-sections that are four times larger. (In fact, Cr:LiSAF's cross-section-lifetime ($\sigma\tau$) product is the highest of any Cr^{3+} doped laser material). However, LiSAF does have poorer mechanical and thermo-optical properties than LiCAF; ESA is significant in Cr:LiSAF (but not in Cr:LiCAF[20]); and multiphonon processes offer significant alternative decay routes from the upper lasing level of Cr:LiSAF at temperatures above 69 °C (compared with 255 °C for Cr:LiCAF).

2.2.3 Growth and Properties of Cr:LiSAF

Compared with other transition-metal ions, Cr^{3+} ions can, in general, be incorporated into host materials quite easily[21]. The Cr^{3+} ion is relatively resistant to both oxidation and reduction and this allows flexibility in the choice of host material and in the atmosphere under which crystals are grown. In addition to this, Cr^{3+} impurity ions will, in general, exclusively occupy octahedral sites in materials in which other crystallographic sites are also present. This means that all of the Cr^{3+} ions in any particular host will experience similar crystal fields, and they will consequently all behave with similar spectroscopic properties.

Crystals of Cr:LiSAF are generally grown by the Czochralski technique[22]. Crystals of CrF, LiF, SrF and AlF are crushed together to form a homogeneous mass or, alternatively, pre-prepared powders can be used. The mixture is then melted in a crucible. Crushing or powdering is a necessary first step in the growth of Cr:LiSAF because there is only a small temperature difference between the top and bottom of the melt and this makes mixing by convection currents inefficient[23]. Crystal growth is initiated by touching the melted mixture with a rotating seed crystal which is gradually pulled away from the surface of the melt as the melt is cooled. Crystals of

Cr:LiSAF exhibiting losses of less than 0.1% loss per cm can be routinely grown by this technique[24].

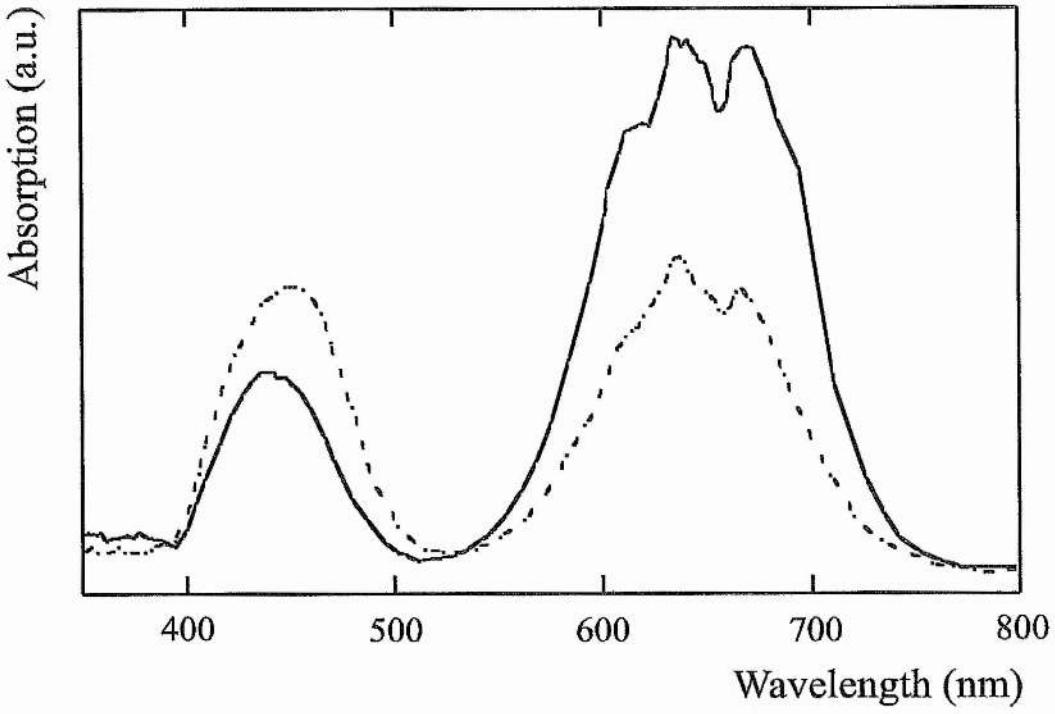

FIGURE 2.3 *Spectra of the absorption in Cr:LiSAF of light that has its E-field polarised parallel (p-polarised - solid line) and perpendicular (s-polarised - dashed line) to the crystal c-axis.*

Spectra of the absorption in Cr:LiSAF of π- and σ-polarised radiation are shown in Figure 2.3. The spectra show two broad absorption bands, one in the blue spectral region and one in the red. The band centred around 450 nm results from the excitation of Cr^{3+} ions from the $^4A_2$ energy level to a $^4T_1$a energy level (not shown on Figure 2.1) above the $^4T_2$ upper laser level; the excited ions quickly relax to the upper laser level. The band centred around 670 nm results from the direct excitation of electrons from the $^4A_2$ energy level into a vibrationally-excited state of the $^4T_2$ energy level, as discussed in Section 2.2.1. The work described in this chapter focuses attention on the region between these two absorption bands. Cr:LiSAF lasers are described that were pumped at wavelengths between 514 nm and 532 nm.

It is clear from Figure 2.3 that absorption in the green is very low compared with the absorption peaks at 450 nm and 670 nm. Pumping in the absorption trough in the green spectral region was made possible because LiSAF can be doped with very high levels of Cr^{3+} ions[19]. A close-up of the absorption of π-polarised light at wavelengths between 450 nm and 550 nm is shown in Figure 2.4.

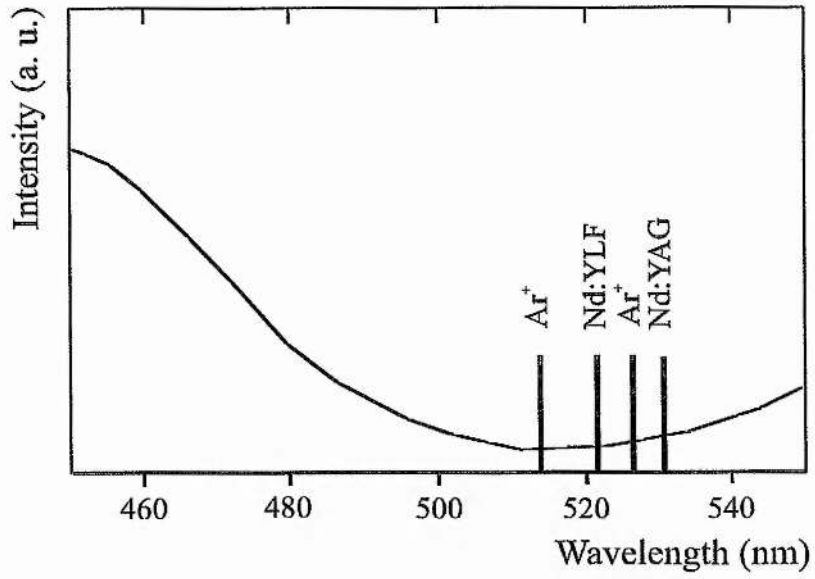

FIGURE 2.4 *Absorption spectrum of Cr:LiSAF from 450 nm to 550 nm (π-polarisation). Also shown are the operating wavelengths of frequency-doubled Nd:YAG and Nd:YLF lasers, and two green Ar^+ laser lines.*

The emission spectrum of π-polarised light from Cr:LiSAF is shown in Figure 2.5. Emission occurs on the vibronically-broadened $^4T_2$-$^4A_2$ transitions. The Cr:LiSAF emission band covers a significant fraction of the emission band of Ti:sapphire (660 nm - 1180 nm) and this is one reason that Cr:LiSAF has attracted attention as a gain medium. However, a comparison of Figure 2.3 and Figure 2.5 shows that there is only a small overlap between the absorption and emission bands of Cr:LiSAF. Ti:sapphire, on the other hand, exhibits a significant residual absorption between 800 nm and 850 nm that is due to the presence of Ti^{3+}-Ti^{4+} pairs within the laser crystal.

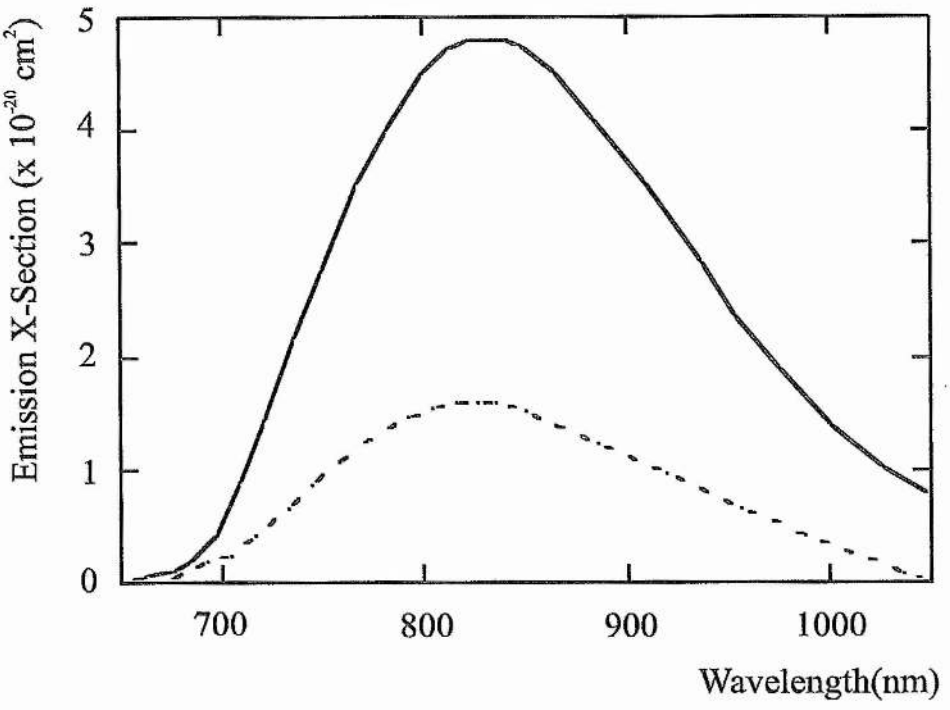

FIGURE 2.5 *The emission spectrum of π-polarised (solid line) and σ-polarised (dashed line) light from Cr:LiSAF.*

A full summary of the known thermo-optic constants, thermo-mechanical constants and the optical and laser properties of Cr:LiSAF and the other colquiriites Cr:LiSGaF, Cr:LiCAF and Cr:LiCGaF is given in Appendix A.

2.2.4 Progress Towards an All-solid-state Self-modelocked Cr:LiSAF Laser

The first Cr:LiSAF laser[17] was pumped by a mainframe Kr^+ laser. Attention soon focused on the development of devices pumped by semiconductor lasers operating at around 670 nm[25,26]. Continuous pulsed operation was demonstrated shortly afterwards in actively mode-locked 647 nm Kr+ laser pumped[27] and self-modelocked 476 nm Ar^+ laser pumped[28] systems. Pulses as short as 33 fs were produced by a 488 nm Ar^+ laser pumped passively mode-locked system utilising a saturable absorber[29]

Initially, diode-pumped self-modelocked devices proved difficult to engineer. This was because the rapid divergence of broad-area semiconductor laser output beams

meant that careful attention had to be paid to the pump optics in order to avoid wasting much of the available pump energy through poor cavity/pump mode matching. Cr:LiSAF suffers from significant thermal problems, including damage, lensing and thermally-induced non-radiative decay routes, and so it is important that as little pump light as possible is dissipated as heat in the crystal. Pulses of hundreds of picoseconds duration were produced from diode-pumped systems[30-32], but a sub-100 fs laser utilising an A-FPSA as a saturable absorber was also demonstrated[33].

An alternative approach to constructing an all-solid-state, self-modelocked Cr:LiSAF laser utilised the superior beam quality of frequency-doubled Nd:YLF minilasers operating at 659 nm[34]. This pumping scheme had none of the problems associated with direct pumping by diodes at that time, and produced 160 fs pulses in a purely-self-modelocked operating regime. At St. Andrews we also followed the minilaser route. The system of reference 34 operated on the weak 1320 nm line of Nd:YLF, frequency-doubled to coincide with the red absorption peak of the Cr:LiSAF absorption spectrum. Our system utilised the strong 1047 nm line frequency-doubled to 523 nm, coincident with the trough of the Cr:LiSAF absorption curve. Pumping at this wavelength was made possible by the use of a highly doped crystal, an approach paralleling the 752 nm IR 'wing-pumping' scheme proposed previously which utilised AlGaAs laser diode arrays[19]. Nd-based minilasers frequency-doubled into the green offer the same high beam quality as their red cousins, and are also established and highly developed lasers in their own right.

2.3 Cr:LiSAF Lasers Pumped in the Green Absorption Trough

2.3.1 Ti:sapphire and Cr:LiSAF

Unlike Cr:LiSAF, Ti:sapphire has a broad absorption band in the blue-green spectral region, and Ti:sapphire lasers are usually pumped by Ar^+ ion lasers operating between 488 nm and 514 nm. Modelocked Ti:sapphire lasers pumped by arc-lamp-pumped, frequency-doubled Nd:YLF and Nd:YAG minilasers were demonstrated in the early 1990s[35,36], but progress towards all-solid-state

modelocked systems was for a long time hampered by a combination of the high pump-power thresholds of self-modelocked lasers and the limited output powers available from frequency-doubled minilasers, compared with mainframe Ar^+ lasers. Giant-pulse, all-solid-state Ti:sapphire lasers were developed that were pumped by frequency-doubled, Q-switched Nd:YAG[37] and frequency-doubled, modelocked and Q-switched Nd:YLF lasers[38,39], and a CW all-solid-state Ti:sapphire laser with a threshold of just 200 mW was demonstrated in 1991[40]. Eventually, in 1993, a self-modelocked all-solid-state Ti:sapphire laser was demonstrated at St Andrews University[41], but this device, with a CW threshold of 400 mW and a modelocking threshold of 500 mW, was operating near the limit of the output power of the available frequency-doubled Nd:YLF pump laser. At 700 mW pump power, the device produced 110 fs pulses at 20 mW average output power.

As Table 2.1 shows, Cr:LiSAF has a $\sigma\tau$ product that is almost three times larger than that of Ti:sapphire. The CW threshold of a laser is inversely proportional to the $\sigma\tau$ product of its gain medium. Consequently, an approximately three-fold reduction in CW threshold would be expected when Ti:sapphire is replaced by Cr:LiSAF as the gain medium in a laser, and the 400 mW threshold should thus be reduced to ~150 mW. This would mean that the laser could be pumped ~250 mW above threshold, and this excess pump power should then be available to produce increased output power from the modelocked laser.

The only problem associated with the direct substitution of Cr:LiSAF for Ti:sapphire in a frequency-doubled minilaser-pumped system is the weak absorption of Cr:LiSAF in the green spectral region. This can be overcome by using crystals doped with high levels of Cr^{3+}. Two self-modelocked Cr:LiSAF systems were developed at St. Andrews that were pumped by frequency-doubled green minilasers. A brief introduction to the minilasers will be given in this chapter, but for a detailed account the interested reader should consult Ref. 42. One of the self-modelocked lasers was based on a 10%-doped AR-coated Cr:LiSAF crystal that was pumped by a frequency-doubled Nd:YLF ring laser and the other was based on a 22%-doped Brewster-angled crystal that was pumped by a frequency-doubled Nd:YAG laser. Ti:sapphire crystals are typically doped at ~0.1 % (residual absorption by Ti^{3+}-Ti^{4+} pairs prevents doping at significantly higher levels).

2.3.2 The First Green-pumped Cr:LiSAF System

In this section I will give a brief introduction to frequency-doubled minilasers and then describe the Nd:YLF minilaser used to pump a Cr:LiSAF laser. Next I will describe the Cr:LiSAF laser itself, and I will then discuss the principles of self-modelocking and dispersion compensation. Finally I will describe the self-modelocked operation of the first green-pumped Cr:LiSAF laser developed at St. Andrews.

2.3.2.1 Frequency-doubled Nd-based Minilasers and the 'Green Problem'

The development of frequency-doubled Nd-based minilasers has been dominated by the need to overcome the so-called 'green-problem'. In order to achieve the intensities required for efficient frequency-doubling it is necessary to resonantly enhance the fundamental laser field. An obvious way to achieve this is to place the frequency-doubling crystal within the resonator of the laser that is generating the fundamental field; the first frequency-doubled minilasers utilised the nonlinear crystals MgO:$LiNbO_3$ [43] and KTP [44] in this kind of intracavity geometry. However, Baer[44] observed that intracavity-doubled CW Nd:YAG lasers exhibit longitudinal-mode instabilities and large fluctuations in output amplitude. This undesirable behaviour was attributed to the coupling of the longitudinal modes of the laser by sum-frequency generation in the frequency-doubling crystal: this is the 'green problem'. Nonlinear crystals cut for intracavity doubling will, in general, have phase-matching bandwidths that are large enough to simultaneously phase-match both frequency-doubling and sum-frequency mixing. Sum-frequency mixing of adjacent longitudinal modes is a nonlinear coupling, and this leads to large temporal amplitude fluctuations in the laser output.

The 'green problem' can be avoided by using an external resonant cavity[45,46] for doubling but this requires a stable, single frequency source of the fundamental radiation and active stabilisation of the external cavity. An approach that has been more widely adopted has been to construct intracavity-doubled lasers that operate on a single longitudinal mode. It is difficult to achieve single-frequency operation in an intracavity-doubled laser because, in addition to the problem of spatial hole-burning associated with standing-wave resonators, a single oscillating mode sees a

nonlinear loss as a result of the doubling process. This means that the population inversion required to sustain oscillation of this mode is usually increased to the point where many other modes near the peak of the laser gain curve see enough gain to oscillate.

Several methods have been tried to eliminate this problem: the addition of an intracavity etalon can be used to introduce losses at frequencies other than the frequency of the peak of the gain curve; the length of the cavity can be reduced until only one longitudinal mode is within the oscillating bandwidth of the laser[47]; or a coupled-cavity scheme can be employed to produce a frequency-dependent output coupler[48]. All of these approaches become less effective at higher pump powers, however, because as the pump power is increased more discrimination is needed between the loss of the desired mode and that of its neighbours. Output powers are, in general, limited to a few milliwatts.

One method of producing stable green light at higher output powers relies on the control of the polarisation properties of the laser resonator. Oka and Kubota[49] observed that the unwanted sum-frequency mixing could occur between the polarisation modes of a resonator as well as between the longitudinal modes. They also showed, however, that the polarisation modes of a laser containing a Type II doubling crystal could be de-coupled by the insertion of a quarter-wave plate orientated with its fast axis angled at 45° to the optical axes of the doubling crystal. Used in conjunction with an etalon that suppressed multiple longitudinal mode operation, this scheme enabled the construction of a laser generating 3.5 W of stable green light[50]. Yelland *et al.* built a similar device at St. Andrews University that was used as a pump source for Cr:LiSAF and will be described in Section 2.3.3.

Despite the high output powers achieved from these lasers, frequency-doubled operation was sensitive to the losses introduced by the intracavity elements and stable, high power operation could be difficult to achieve. An alternative way to achieve single-frequency operation is to build a laser based on a ring cavity[51]: a unidirectional ring tends to run on a single longitudinal mode as spatial hole burning does not occur because of the travelling-wave nature of the intracavity field. The pump source used to pump the Cr:LiSAF laser described in Section

2.3.2.3 was a diode-laser pumped, intracavity doubled CW ring laser based on Nd:YLF.

2.3.2.2 The Nd:YLF Pump Laser

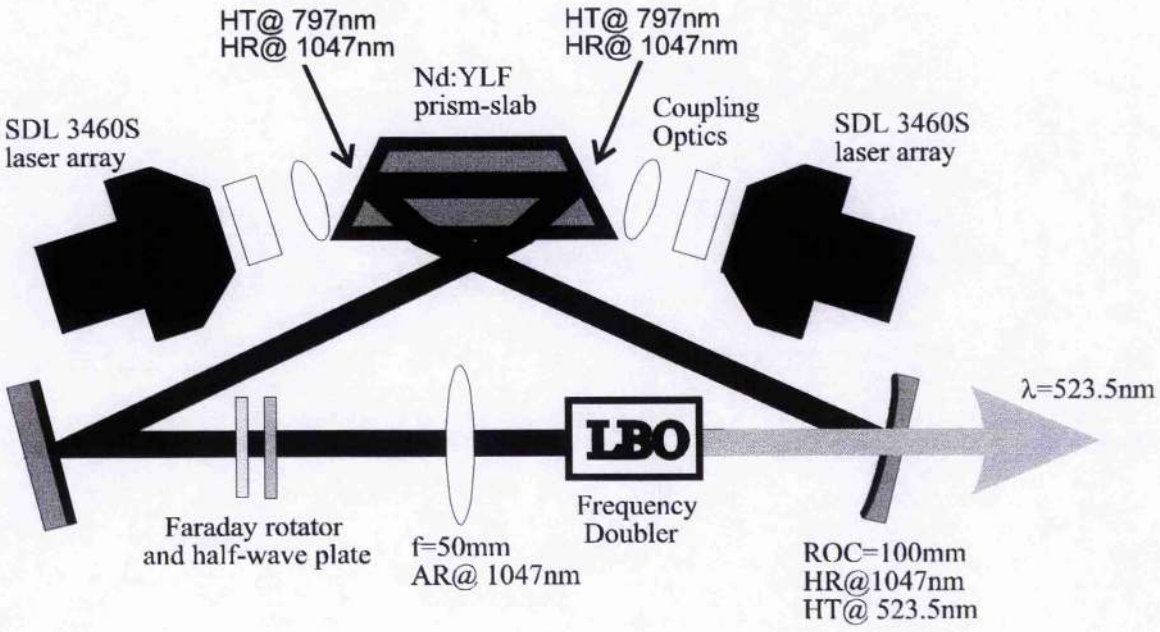

FIGURE 2.6 *A schematic diagram of the diode-pumped, intracavity-doubled CW Nd:YLF ring laser (HR - high reflection coating, AR - anti-reflection coating, HT - high transmission coating).*

Nd:YLF has several properties that have led to its acceptance as a possible rival to Nd:YAG as a gain medium in diode-pumped solid-state lasers[52]. Its principal emission wavelength of 1047 nm is close to that of Nd:YAG, and its main absorption lines at 792 nm, 797 nm and 806 nm fall well into the output range of high-power AlGaAs laser diodes (780 nm - 860 nm). Its fluorescence lifetime is twice that of Nd:YAG, leading to twice the energy storage for the same pump power (which is important for Q-switched devices). Its thermal conductivity is relatively large, and its natural birefringence overwhelms thermally-induced birefringence which, in isotropic media, leads to the formation of radial and tangential thermal lenses of different focal lengths[53,54]. It also exhibits intrinsically weaker thermal lensing because $\frac{dn}{dt}$ is smaller and also negative[54]. However, the thermo-mechanical properties of YLF are not as good as those of YAG: it has a

low hardness, which can make mounting difficult, and a low thermal fracture limit, which restricts its use in high-pump power schemes. (Optical, mechanical and thermal properties of Nd:YLF are listed in Table 2.2 on page 60).

A 'green minilaser' based on a Nd:YLF/LBO ring cavity was developed by Hong, Yelland and Sibbett at the University of St. Andrews, and this device was used to pump both the first all-solid-state femtosecond Ti:sapphire laser to be demonstrated[41] and the novel all-solid-state Cr:LiSAF laser described below. This green minilaser is illustrated schematically in Figure 2.6.

The Nd:YLF crystal was an 18 mm long, truncated-prism shaped slab, the ends of which were anti-reflection (AR) coated for 797 nm light and coated for high reflectivity (HR) for 1047 nm light. The slab was pumped by Spectra Diode Laboratories 3460S CW AlGaAs linear diode-laser bars operating at 797 nm. Each bar consisted of forty-eight 100 μm emitting apertures, which were separated by 200 μm (centre-centre), and each bar was capable of emitting up to 20 W for 27 A drive current, with a slope of 0.92 W/A. The diodes were temperature-tuned to operate at the main Nd:YLF absorption wavelength of 797 nm; this was achieved by cooling the bars to 18 °C by using a Marlow DT-1089 thermoelectric cooler mounted on a water-cooled copper heat sink. The output from each diode bar was focused into the Nd:YLF slab through a cylindrical lens of 5 mm focal length and a spherical lens of 8.5 mm focal length.

The intracavity Faraday rotator and half-wave plate ensured unidirectional operation of the Nd:YLF laser beam. Single longitudinal mode output powers of up to 2.2 W through a 5% output coupler were achieved at 1047 nm in TEM_{00} beam, for 10 W total pump power.

For intracavity doubling, the intracavity mode was focused using a 50 mm focal length lens to a 50 μm waist in a lithium triborate LiB_3O_5 (LBO)[55] crystal. The LBO crystal was 25 mm long and its faces were AR-coated for 1047 nm and 523.5 nm. The crystal was cut for Type I non-critical phase-matching (non-critical phase-matching results in a large acceptance angle and zero pump-signal walk-off, and so long crystals can be used for high conversion efficiencies - for a comprehensive treatment of the nonlinear optics of crystals see, for example, Ref. 56). The LBO

crystal was mounted inside a temperature-stabilised oven which was heated to the SHG phase-matching temperature of 150 °C. For a total pump power of 10 W, single-longitudinal mode outputs of up to 1 W were achieved at 532.5 nm in a TEM_{00} beam.

Unfortunately, there were several problems associated with this pump laser. The loss experienced by the fundamental longitudinal mode by the SHG process brought the laser gain up to the level where several adjacent modes were near to their oscillation threshold. The temperature stabilisation of the LBO oven was not effective enough to eliminate the effects of environmental disturbances and these also led to multiple longitudinal mode operation of the Nd:YLF laser and hence to a resurgence of the green problem. Furthermore, the low thermal fracture limit of YLF prevented the diode bar pump lasers from being driven at anything like their maximum current. Poor heat sinking meant that pump powers in excess of 5 W per bar resulted in catastrophic damage of the Nd:YLF crystal.

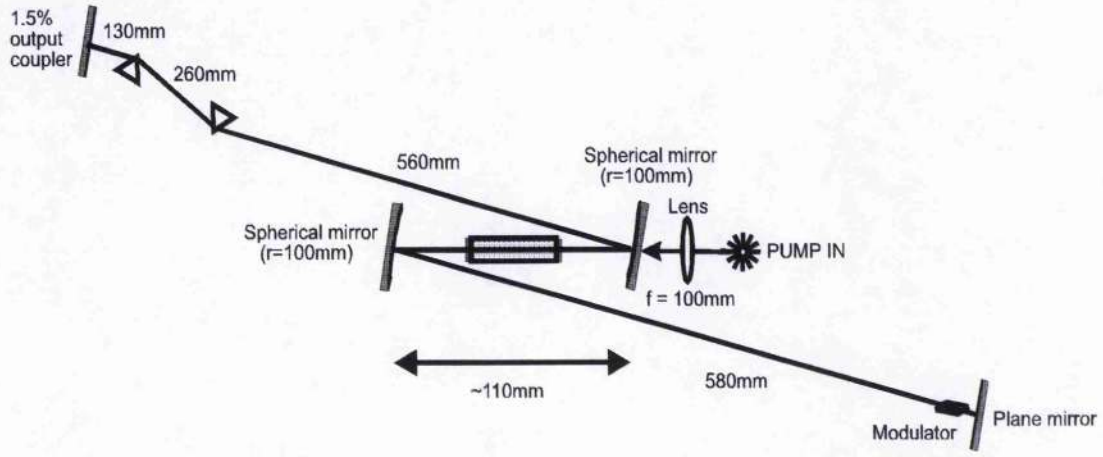

FIGURE 2.7 *The Cr:LiSAF laser used in the experiments with the frequency-doubled Nd:YLF laser.*

2.3.2.3 The Cr:LiSAF Laser

The Cr:LiSAF laser shown in Figure 2.7 was pumped by both the Nd:YLF pump laser described above and a mainframe Ar^+ ion laser operating at 528 nm. The laser was initially modelocked using the Ar^+ ion laser and then light from the frequency-doubled minilaser was passed through a telescope (used to match the spot sizes of

the two pump lasers) and then steered into the laser along the path of the Ar^+ ion beam.

A 100 mm focal length convex lens was used to couple the pump light into the laser. The Cr:LiSAF cavity was a standard four-mirror cavity based around an AR-coated Cr:LiSAF crystal. The crystal was 12 mm long and 10 % doped with Cr^{3+}. This gave 73 % absorption of the light incident on the crystal. The crystal was AR coated for 850 nm light.

The cavity mirrors were coated HR for 850 nm light and AR for 670 nm light (670 nm is the output wavelength of AlGaInP diode lasers). The overall power-transfer efficiency from the pump laser to absorption in the crystal was 65 %. The cavity end-mirror in the arm containing the prisms provided an output coupling of 1.5 % at 850 nm. The mirrors in the folding section had a radius of curvature of 100 mm. The use of an AR-coated crystal rather than a Brewster-angled crystal meant that the angle of incidence of the intracavity beam at the folding mirrors had to be minimised for optimum operation (see Chapter 3). In this laser, this angle was limited by the crystal itself to ~3 °. The arm containing the prisms was 950 mm long and the arm containing the modulator was 580 mm long. The overall cavity repetition frequency was 91.5 MHz.

In the next section I will describe the self-modelocked operation of this Cr:LiSAF laser. I will also take the opportunity to discuss the technique of self-modelocking itself, and to consider the problem of dispersion compensation.

2.3.2.4 Self-modelocking

2.3.2.4.1 Regenerative modelocking

A Brimrose Corporation Brimrose model FQM442 acousto-optic (AO) modulator, based on a 12 mm long Brewster-angled block of quartz, was placed near to the HR cavity end-mirror in the arm that did not contain the prisms (see Figure 2.7). The AO modulator was used to introduce a periodic loss modulation into the CW intracavity field. The modulator was initially driven by the output from a Marconi Instruments Model 2019 signal generator. The driving frequency was set at 43 MHz and the cavity length was adjusted until the second-harmonic of the cavity

mode-beating signal was seen on a RF spectrum analyser to coincide with the second harmonic of the AO modelocking signal at 172 MHz.

Although active AO modelocking can be used to assist the initiation of self-modelocking, in general, environmental disturbances lead to changes in the length of the laser cavity, and hence to a mismatch between the AO drive signal and the cavity repetition frequency. To counter this effect, the AO modulator was driven regeneratively. In regenerative modelocking[57] the modulator is driven by circuitry such as that shown in Figure 2.8[58]. A fraction of the laser output is directed onto a photodiode and output from this diode is filtered by a 172 MHz bandpass filter with a bandwidth of approximately 10 MHz. This signal is then amplified with a hybrid RF amplifier and then passed through a 'divide-by-four' circuit. The resultant 43 MHz signal, after filtering and amplification, is used to drive the AO modulator. The driving frequency of the AO modulator is thus derived from a repetitive signal that is directly linked to the laser resonator: this ensures that the modulation frequency is referenced to the cavity frequency even if there are perturbations in the cavity period.

This regenerative modulation helps to initiate pulse generation by acting as a form

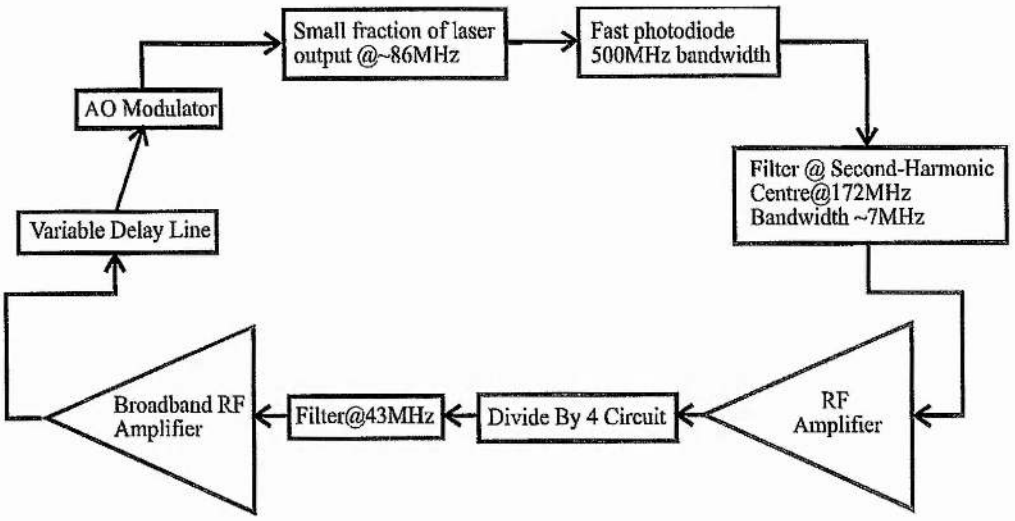

FIGURE 2.8 *A schematic illustration of the circuitry used for regenerative modelocking. The variable delay line enables the phase of the applied modulator signal to be matched to that of the circulating intracavity pulse.*

of 'passive' AO modelocking. This leads to pulses of the order of 40 ps duration

which have significantly higher peak powers than the CW field and are therefore more able to exploit intracavity Kerr lensing. Once self-modelocking occurs and pulses are established in the laser cavity, the regenerative scheme can also act as a stabilising mechanism because although the loss it introduces is essentially constant over the duration of a pulse, the loss modulation does help to suppress the oscillation of CW light *between* pulses.

2.3.2.4.2 Self-modelocking.

The demonstration by Spence, Kean and Sibbett in 1990 of ultrashort-pulse generation in a single Ti:sapphire cavity[59] led to speculation as to the mechanisms behind this 'self-modelocking'. Piché first suggested that self-modelocking could be explained by considering the effects of self-focusing on the intracavity beam profile[60].

Herrmann divides the action of self-modelocking into three distinct phenomena[61]. Firstly, there is straight-forward 'hard-aperture' self-modelocking[62,63]. In this operating regime, an induced Kerr lens in the laser gain medium can result in a decrease in the size of the laser beam at an intracavity slit. This means that the peak of a pulse will see less loss at the slit than the lower-intensity wings of the pulse or the CW field because it will induce a strong Kerr lens. Pulsed operation will therefore be preferred in the laser. However, self-modelocking can also be achieved without an intracavity aperture[64,65]. In this second form of self-modelocking, an induced Kerr lens results in an improved overlap between the cavity mode and the pump beam. This leads to an intracavity-power dependent gain which again favours pulsed operation over CW radiation. The third phenomenon involved in self-modelocking is 'gain guiding'[66], a redistribution of the intracavity optical field. If the beam used to pump a laser crystal has a Gaussian profile then the intracavity radiation will have a profile different from that produced by a uniform pump. The gain profile of the pump causes a transverse redistribution of the radiation in the cavity mode, and it consequently causes a change in the shape of the beam throughout the resonator. Gain guiding therefore affects self-modelocking whether or not there is a hard intracavity aperture.

The Cr:LiSAF system to be described in Chapters 3 and 4 was designed for optimised modelocking with a computer model that dealt exclusively with the effects of hard-aperture modelocking. Although the predictions of this model resulted in a system that performed extremely well, the laser's behaviour suggested that intensity-dependent beam overlap and gain guiding were also important phenomena in its self-modelocked operation. The Cr:LiSAF lasers described in this chapter were modelocked without the use of additional 'hard' apertures and so self-modelocking relied upon intensity-dependent beam overlap and gain-guiding effects. Modelling of both types of laser predicts that self-modelocking is most easily achieved when a laser is operating near to the edge of one of its stability zones[67].

2.3.2.4.3 Dispersion Compensation.

Self-amplitude modulation through Kerr lensing will, in general, lead to the formation of pulses of durations of the order of a few picoseconds in the absence of any intracavity elements other than the gain crystal. To generate pulses of shorter durations than this, it is necessary to compensate for the effects of intracavity group-velocity dispersion (GVD). In general, the shortest duration

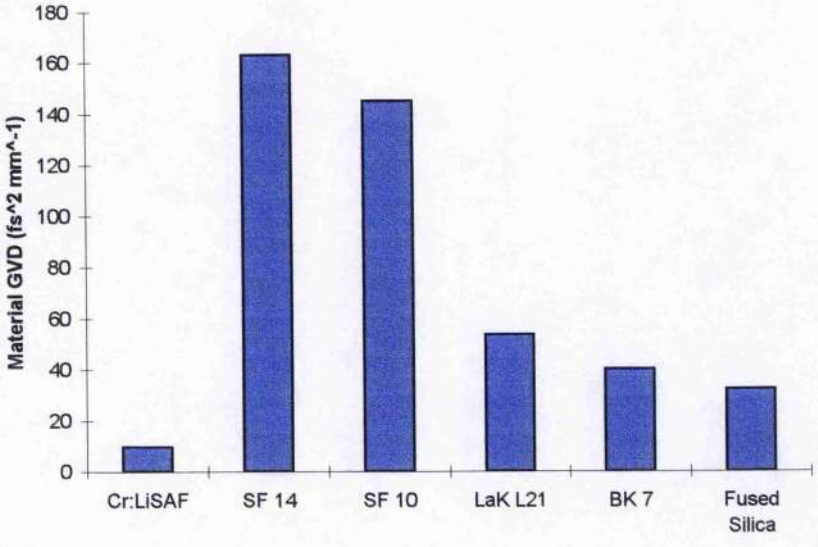

FIGURE 2.9 *Material GVD in various optical materials.*

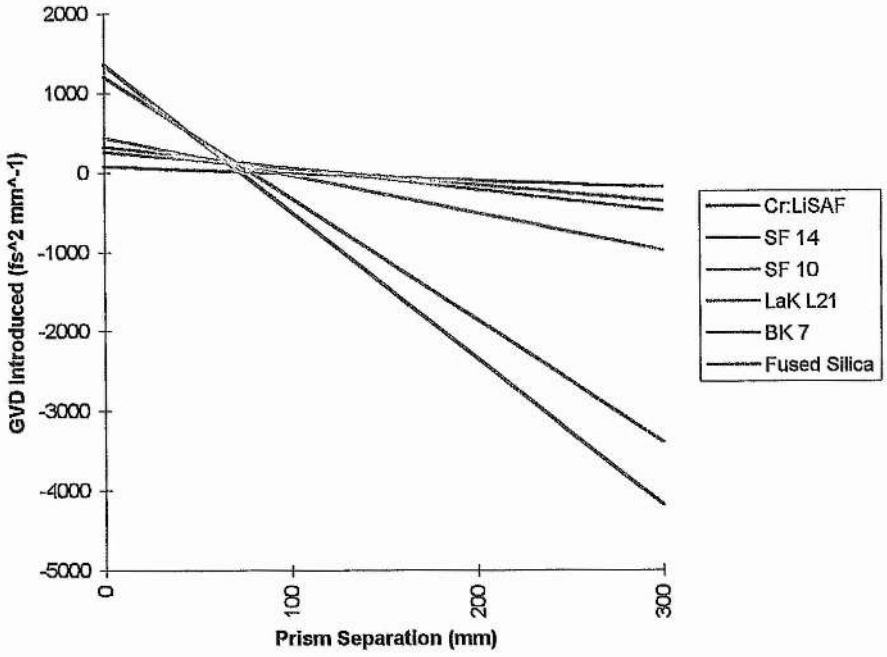

FIGURE 2.10 *Refractive GVD for prism pairs made of various optical materials. Note that the refractive GVD results from both propagation between the prism pair and propagation through 2 mm of material in each prism.*

pulses will be generated when the net intracavity GVD is negative, and of the order of a few hundred femtoseconds squared. A net negative GVD is required to balance the pseudo-positive-GVD effects of SPM (Chapter 1, Section 1.3.2.1) or - more accurately - to support the propagation of solitonic pulses (Chapter 3, Section 3.5).

The GVD in a cavity designed for regeneratively initiated self-modelocking has three principal origins: the laser crystal, the quartz AO modulator and the prism pair which is introduced to provide negative GVD to balance the positive GVD of the other two. The prism pair contributes to the net GVD both through material dispersion and through refractive dispersion resulting from the different path lengths seen by different wavelengths as they propagate between the intracavity prisms. GVD is given by the general expression[68]

$$\frac{d^2\phi}{d\omega^2} = \frac{\lambda^3}{2\pi c^2}\frac{d^2P}{d\lambda^2}$$

EQUATION 2.1

where ϕ is the optical phase shift, P is the optical path length seen by light of wavelength λ. In material dispersion, P is simply the physical path length times the material refractive index n; the material GVD per mm of various optical materials is shown in Figure 2.9.

In refractive dispersion, the second derivative of optical path length with wavelength is given by

$$\frac{d^2P}{d\lambda^2} \cong 4\left[\frac{d^2n}{d\lambda^2} + \left(2n - \frac{1}{n^3}\right)\left(\frac{dn}{d\lambda}\right)^2\right]L_p \sin(\beta) - 8\left(\frac{dn}{d\lambda}\right)^2 L_p \cos(\beta)$$

EQUATION 2.2

where L_p is the prism separation, $\cos(\beta) \cong 1$ and $L_p\sin(\beta) \cong 2$ mm[69]. A plot of refractive GVD versus prism separation is shown in Figure 2.10.

Figure 2.11 shows the contribution of various intracavity elements to the net round-trip GVD in the self-modelocked Cr:LiSAF laser cavity. The negative GVD

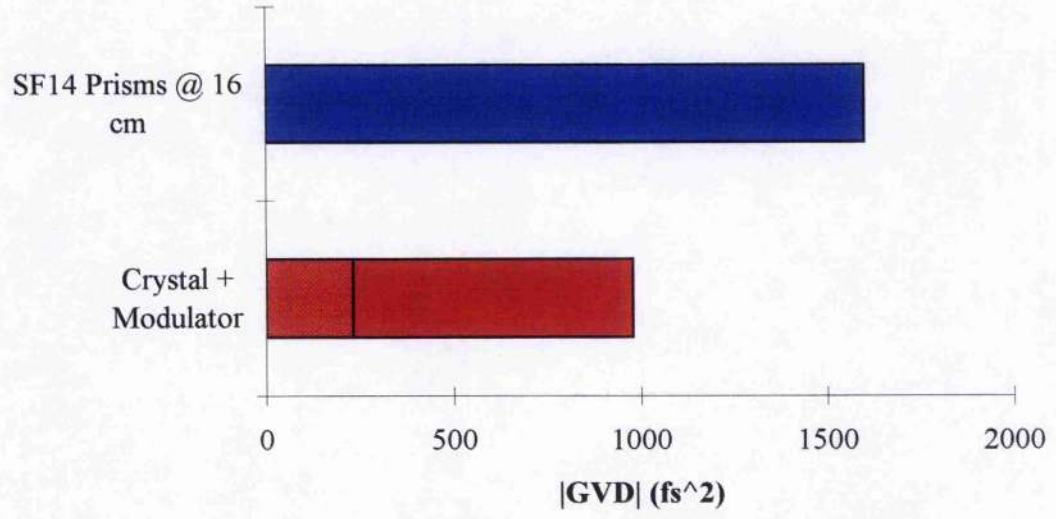

FIGURE 2.11 *Contributions to the round-trip (double-pass) GVD seen by a pulse. Upper bar: negative GVD due to SF 14 prism pair separated by 16 cm. Lower bar: positive GVD due to 12 mm Cr:LiSAF crystal and 11.6 mm quartz modulator.*

contribution of the SF14 prisms is shown for a prism separation of 16 cm, which is the smallest separation for which pulsed operation could be achieved. It is assumed that at this separation the intracavity beam passed through the tips of the prisms; i.e., that the beam did not pass through any excess glass over and above the 2 mm assumed in the Gordon and Fork model[69]. The net GVD in the cavity was -650 fs^2. This was the negative dispersion that was required to balance the SPM generated inside the Cr:LiSAF crystal by the 90 fs, 230 kW peak intracavity power (30 mW average output power) pulses produced by the laser.

2.3.2.4.4 Modelocked Performance.

The Cr:LiSAF laser had a threshold absorbed pump power level of 105 mW (150 mW incident) when operated with a 1.5 % output coupler and its slope efficiency (power out x 100/power in) was 8 %, giving 65 mW at 1 W pump. When self-

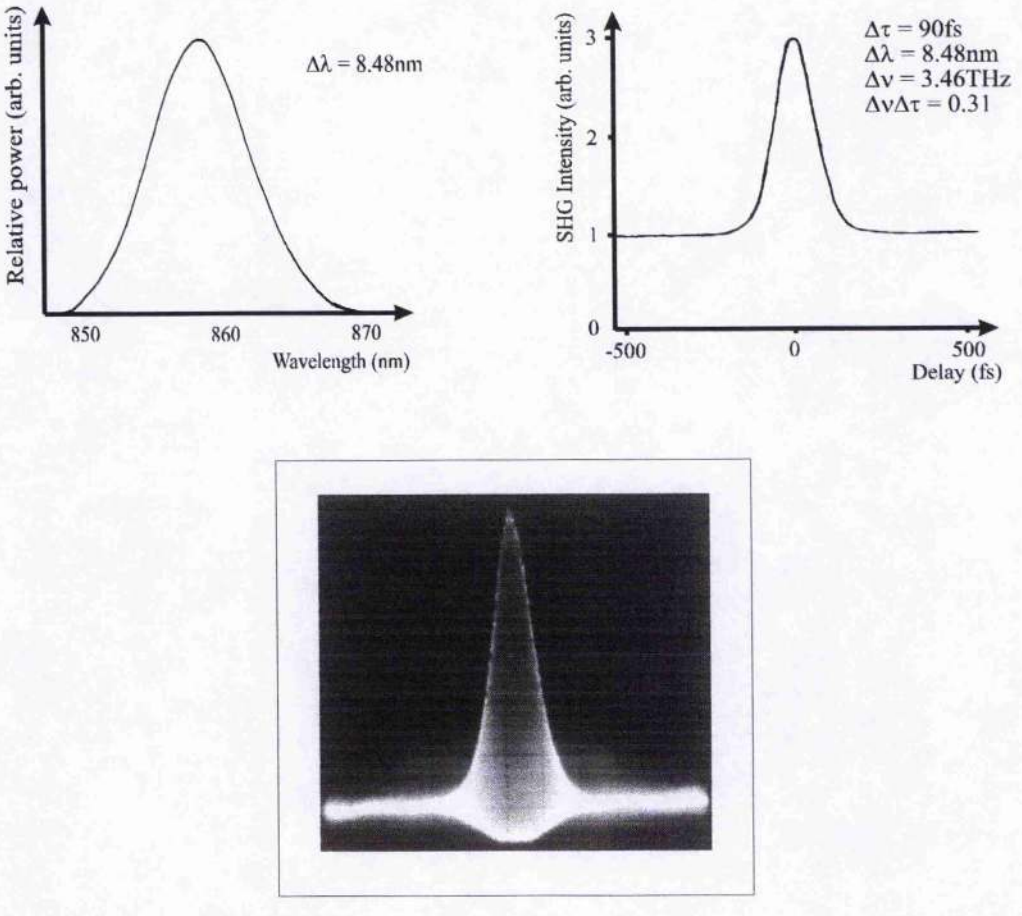

FIGURE 2.12 *Intensity and interferometric autocorrelations and pulse spectrum from the Cr:LiSAF laser based on the AR-coated crystal.*

modelocked, the laser produced 90 fs pulses at 859 nm at a repetition rate of 86 MHz (see Figure 2.12); the average output power was 30 mW at 320 mW pump power (460 mW incident). Intensity and interferometric autocorrelations and a pulse spectrum are shown in Figure 2.12. The pulse bandwidth was 8.5 nm, corresponding to a bandwidth-duration product $\Delta\nu\Delta\tau$ of ~0.31 and implying that the pulses were transform-limited for a $sech^2$ intensity profile. Self-modelocked operation was achieved for absorbed pump powers as low as 280 mW (400 mW incident).

As described in Section 2.3.2, several problems were experienced with the Nd:YLF laser that was used to pump this system. For practical purposes, the Nd:YLF pump laser was able to provide ~ 500 mW of single-mode light for periods of tens of minutes at a time before re-optimisation was required. Self-modelocked operation proved extremely difficult to achieve with this pump source operating so close to the threshold for laser modelocking at 400 mW incident power. However, modelocked operation under Ar^+ ion pumping showed that pumping Cr:LiSAF in its green absorption trough was a viable technique that had the potential to produce all-solid-state modelocked operation at output powers comparable with or superior to those obtainable from directly-diode-pumped devices.

Subsequent work with lasers utilising AR-coated crystals has shown that, whilst they had a lower threshold than lasers utilising Brewster-angled crystals (See Chapters 3 and 4), the losses associated with the AR-coatings result in a lower slope efficiency[70]. Thus, whilst AR coatings are to be preferred in systems where the available pump power is limited, higher-power systems should employ Brewster-angled rods.

2.3.3 The Second Green-pumped Cr:LiSAF System

I will now describe the second green-pumped Cr:LiSAF developed at St. Andrews University. I will introduce Nd:YAG and describe the Nd:YAG pump laser, and then describe the Cr:LiSAF laser itself and its modelocked operation. Finally, I will discuss the thermal problems that limit the performance of Cr:LiSAF at high pump power.

2.3.3.1 The Nd:YAG Pump Laser

The low thermal fracture limit of Nd:YLF meant that the ring laser described in the preceding section was limited to a pump power of ~ 10 W and therefore an output power of ~1 W in the green. Attention therefore returned to Nd:YAG. The development by Liu *et al* of a longitudinally diode-pumped CW laser offering 3.5 W of green light[71], based on Oka and Kubota's work[49], led to consideration of the control of the green problem by the decoupling of polarisation eigenmodes.

Nd:YAG is the most successful solid-state laser material to date[73]: it combines high gain, low threshold and good optical quality with strength and hardness. It has relatively broad pump bands at 750 nm and 810 nm that again make it suitable for pumping by high-power AlGaAs diode lasers, and, although its fluorescence lifetime is half that of Nd:YLF, it is otherwise superior to Nd:YLF at high pump

	Nd:YAG	Nd:YLF
Lasing wavelength (nm)	1064	1053 (σ) 1047 (π)
Fluorescence Lifetime (μs)	230	480
Stimulated emission cross-section (cm^{-2})	6.5×10^{-19}	1.8×10^{-19} (π) 1.2×10^{-19} (σ)
Strength ($N\ m^{-2}$)		3.3×10^{7}
Thermal conductivity ($W\ cm^{-1}\ K^{-1}$)	0.14	0.06
Thermal expansion coefficient ($°C^{-1}$)	[100] orientation: 8.2×10^{-6} [110] orientation: 7.7×10^{-6} [111] orientation: 7.8×10^{-6}	a-axis: 13×10^{-6} c-axis: 8×10^{-6}
Melting point (°C)	1970	825

TABLE 2.2 *Some physical and optical properties of Nd:YAG and Nd:YLF*[72].

powers because of its hardness, thermal conductivity and the relatively isotropic nature of its thermal expansion (although this leads to problems with thermally induced birefringence). The principal emission line in Nd:YAG is at 1064 nm, and it can therefore be frequency-doubled into the green at 532 nm. Some physical properties of Nd:YAG are listed in Table 2.2.

The Nd:YAG laser used to pump the Cr:LiSAF laser described in this section was developed by Yelland and Sibbett[74] at the University of St. Andrews and is shown in schematic form in Figure 2.13.

The laser was pumped by two fibre-coupled 20 W diode-laser arrays (OptoPower Corporation). The fibre bundles were combined into a single bundle from which the output was coupled into a single 600 μm, 0.37 N.A. AR-coated fibre. The output from this multimode delivery fibre was focused into the crystal through a

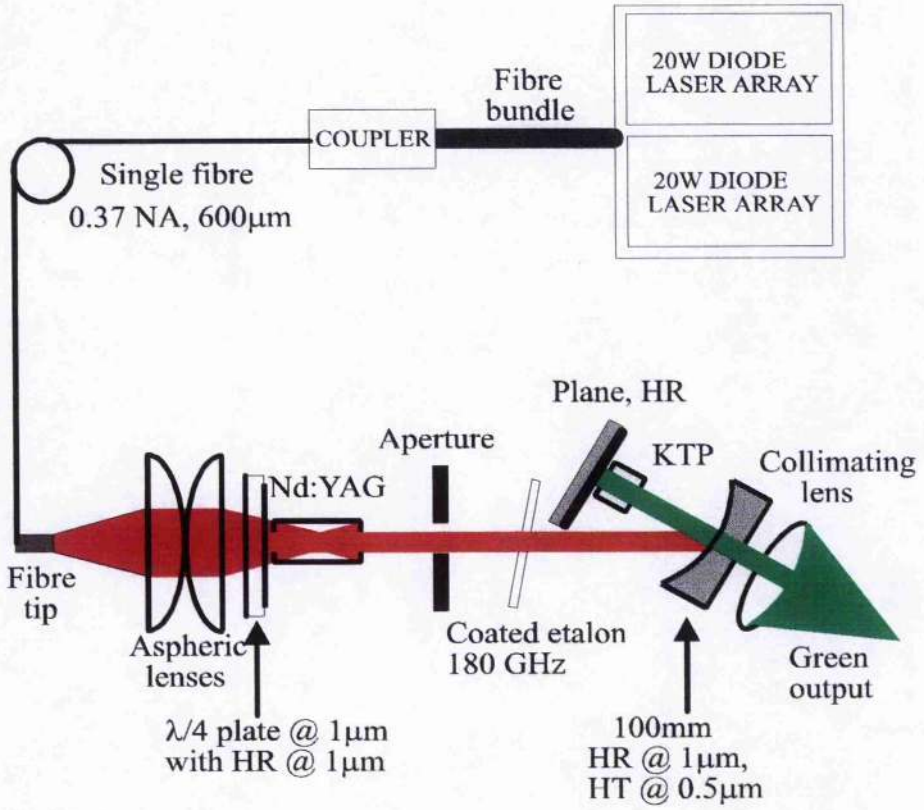

FIGURE 2.13 *The fibre-coupled diode-pumped frequency-doubled Nd:YAG laser used to pump the Cr:LiSAF laser described below.*

thin mirror-$\lambda/4$ substrate via a 8.5 mm focal length pump lens. The pump source was capable of delivering up to 25 W at 808 nm - 811 nm.

The Nd:YAG laser was a simple three-mirror cavity, consisting of two plane end mirrors and a folding mirror of 100 mm radius of curvature. The mirrors were HR coated at 1064 nm and AR coated at 532 nm. The Nd:YAG crystal was 8 mm in length and intracavity doubling was achieved in a 5 mm KTP crystal cut for type II noncritical phase-matching. The intracavity quarter-wave plate was orientated at 45° with respect to the o- and e-axes of the KTP crystal, thus decoupling the polarisation modes of the laser in the sum-frequency mixing process, as explained by Oka and Kubota[49]. The two polarisation modes were separated by 450 MHz because of the difference in path length for the two polarisations in the KTP crystal.

The Nd:YAG laser produced up to 4 W of single-longitudinal-mode light at 532 nm but its operation was somewhat unreliable. Although the use of a correctly-orientated quarter-wave plate decoupled the two eigenpolarisations associated with each longitudinal mode, it was still necessary to ensure that the laser operated on only one longitudinal mode. This proved somewhat difficult to achieve because the laser was very sensitive to perturbations in its environment. Even when single longitudinal mode operation was achieved, any vibrations or other disturbances in the laboratory would cause the laser to revert to a fluctuating mode pattern and hence a very noisy temporal output which made modelocking the Cr:LiSAF laser impossible. In general, single longitudinal operation of the Nd:YAG laser could only be maintained for periods of about ten minutes at a time before significant re-optimisation was required. Covering the laser cavity to reduce air currents may help to alleviate these problems. The problem of amplitude fluctuations was the only significant difference between the operation of the Cr:LiSAF laser when it was pumped by the frequency-doubled Nd:YAG laser and its operation when it was pumped by the mainframe Ar^+ ion laser.

2.3.3.2 The Cr:LiSAF Laser

The Cr:LiSAF laser used in this experiment is shown in Figure 2.14. The cavity was similar to that used in the experiments with the frequency-doubled Nd:YLF

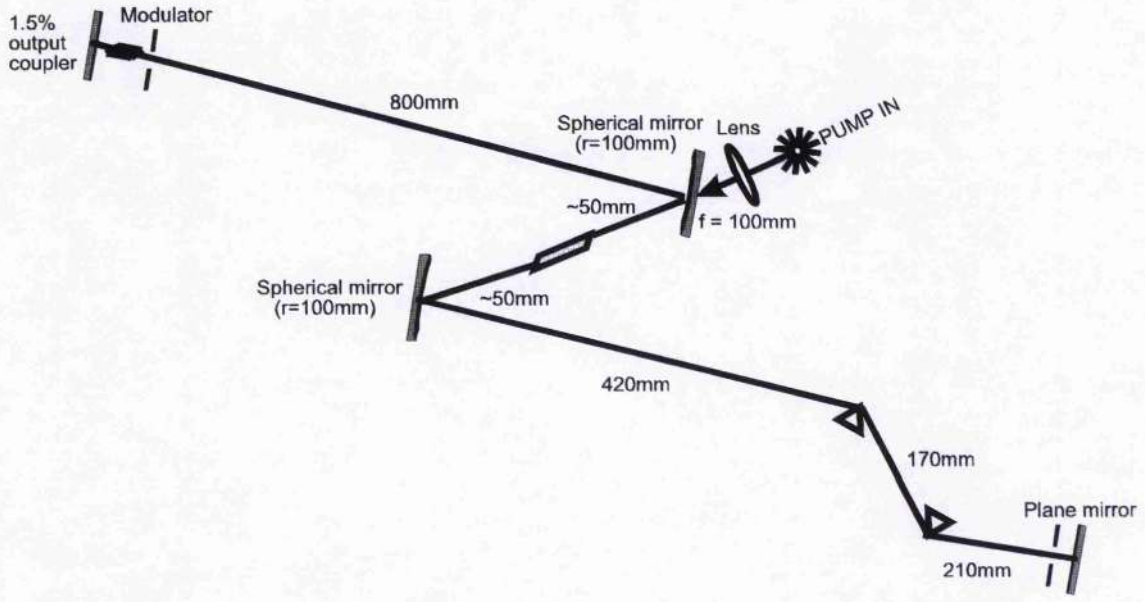

FIGURE 2.14 *The Cr:LiSAF laser used in the experiments with the frequency-doubled Nd:YAG laser.*

ring laser. The gain crystal in this case was a 14 mm, Brewster-angled crystal, doped with 22 % Cr^{3+}; this crystal absorbed 95 % of the pump light incident on its surface. The cavity arms were both 80 cm long, and the angle of incidence of the intracavity beam on the folding mirrors was increased to 12° to balance the astigmatism introduced by the Brewster-angled crystal.

The CW laser threshold was 153 mW absorbed power (170 mW incident), and the laser gave over 120 mW of output power through a 1.5 % output coupler at 1.2 W pump. Modelocked operation was achieved with both Ar^+-ion laser pumping and minilaser pumping, at a pump threshold of 360 mW (400 mW incident). The laser gave 72 fs pulses at 76 mW output power for 1.1 W of pump power (1.2 W incident). Intensity and interferometric autocorrelations and a pulse spectrum are shown in Figure 2.15. The minimum prism separation for which pulsing was achieved was 17 cm, corresponding to a residual net GVD of -760 fs^2.

The pulse bandwidth was 16 nm, implying a bandwidth-duration product $\Delta\nu\Delta\tau$ of 0.47. This is significantly larger than the bandwidth-limited value of 0.315 for $sech^2$ pulses. The reason for this anomaly is not clear. It could be attributed partly to the slight asymmetry seen in the pulse spectrum in Figure 2.15, which in turn is probably due to the effects of intracavity third-order dispersion (Section 3.5.2).

The interferometric autocorrelation shows a slight thickening in the wings which may be attributable to excessive intracavity SPM, suggesting that the intracavity power was too high for stable soliton-like pulse shaping. A higher output coupler would eliminate this effect.

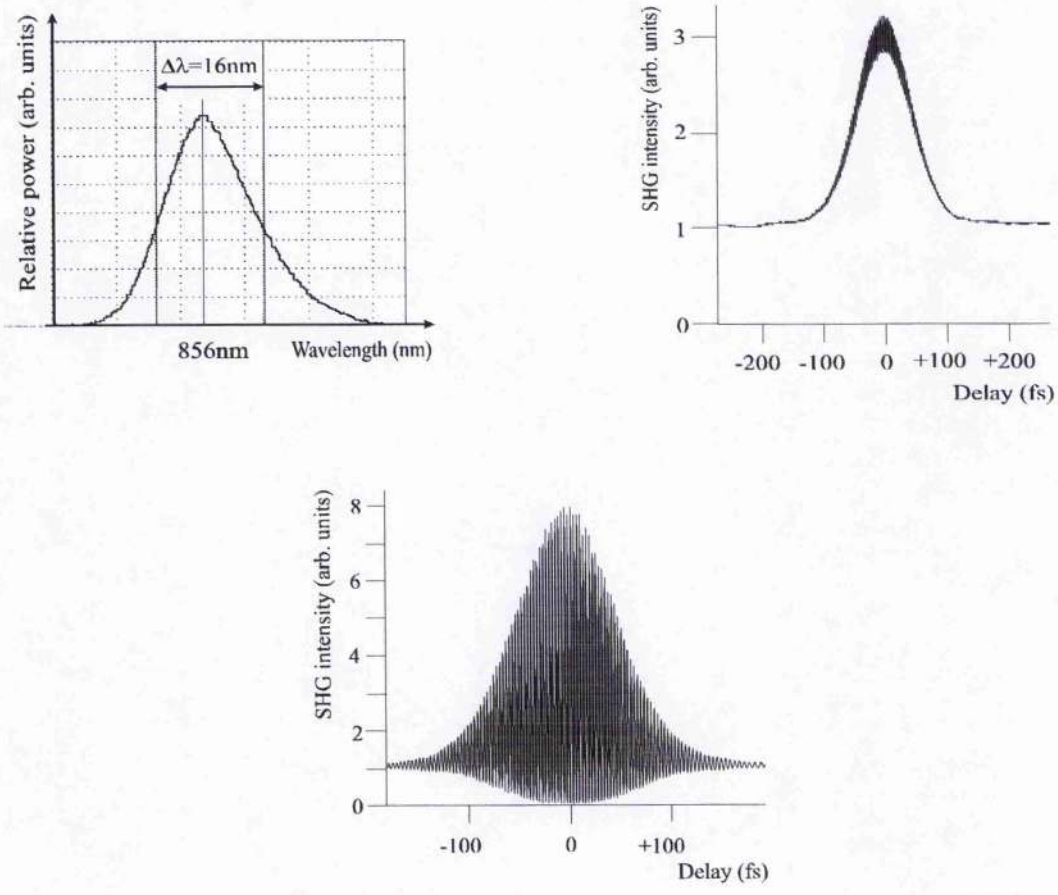

FIGURE 2.15 *Intensity and interferometric autocorrelations ($\Delta\tau_p$ = 72 fs) and pulse spectrum (λ_p = 856 nm, $\Delta\lambda$ = 16 nm) from the Cr:LiSAF laser based on the Brewster-angled crystal. The bandwidth-duration product was $\Delta\nu\Delta\tau_p$ = 0.47.*

2.3.3.3 Thermal Problems

In the past, the development of Cr:LiSAF lasers was hampered by thermal problems that were attributed to the effects of excess crystal heating resulting from the inefficient use of non-diffraction-limited beams[75]. The laser described in this section also suffered from thermal problems, even though it was pumped by a

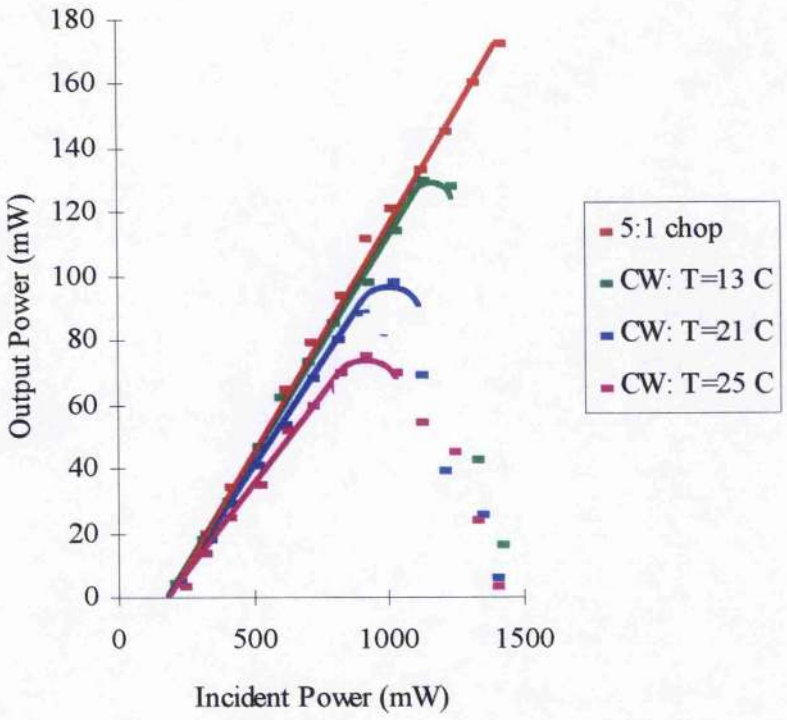

FIGURE 2.16 *Power-transfer characteristics of the Cr:LiSAF laser for a chopped pump beam and for CW operation at various heat-sink temperatures.*

diffraction-limited beam from either an Ar^+ ion laser or a frequency-doubled Nd:YAG laser. These problems only became significant at relatively high pump powers, however.

The Cr:LiSAF crystal was mounted on a heat-sink controlled by a Peltier-effect cooler. The laser power transfer characteristics are shown in Figure 2.16 for various heat-sink temperatures. Even when the crystal was cooled to 13 °C, the output power suffered from thermally induced rolloff at incident pump powers greater than ~1.2 W.

This phenomenon has been attributed to the depopulation of the upper laser level in Cr:LiSAF by thermally-excited non-radiative decay routes[76]. This can be explained with the configuration co-ordinate diagram of Figure 2.17. At sufficiently high thermal excitation energies, electrons in the $^4T_2$ level can tunnel into highly excited states of the $^4A_2$ ground state. This provides an alternative route

for depopulation of the upper laser level, and consequently leads to a reduction in the upper-state lifetime of the Cr^{3+} ions. The upper-state lifetime $\tau(T)$ is given by

$$\frac{1}{\tau(T)} = \frac{1}{\tau_R} + \frac{1}{\tau^0_{NR}} \exp\left(-\frac{\Delta E}{kT}\right)$$

EQUATION 2.3

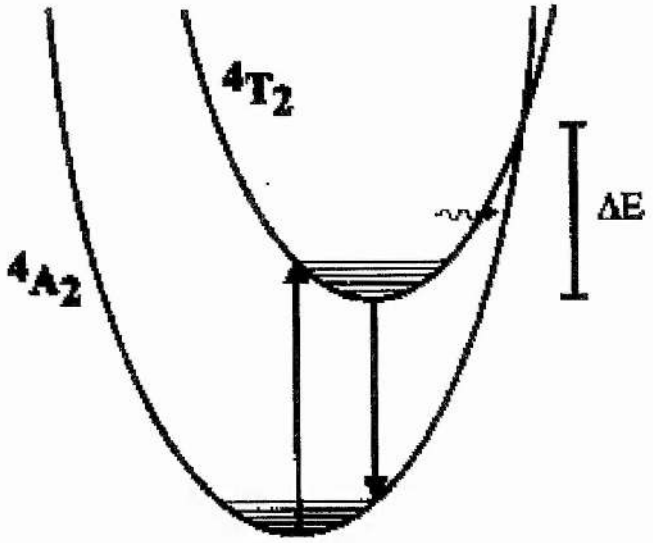

FIGURE 2.17 *Configuration co-ordinate diagram showing the mechanism behind non-radiative decay in vibronic gain media.*

where the first term relates to the (constant) radiative lifetime and the second term relates to the non-radiative lifetime contribution. ΔE and τ^0_{NR} are constants, with ΔE corresponding to the energy difference between the vibrational ground-state energy of the $^4T_2$ level and the energy at which the $^4T_2$ and the $^4A_2$ levels cross. The temperature at which non-radiative processes begin to dominate can be quantified by determining the temperature at which the upper-state lifetime drops to half of its value at low temperatures; i.e.,

$$T_{1/2} = \frac{\Delta E}{k \ln\left(\frac{\tau_R}{\tau^0_{NR}}\right)}.$$

EQUATION 2.4

The value of $T_{1/2}$ is just 69 °C in Cr:LiSAF. Table 2.3 shows equivalent data for the laser materials Cr:LiSCAF, Cr:LiCAF and Ti:sapphire.

Material	τ_R (μs at 77 K)	$T_{1/2}$ (K)	$T_{1/2}$ (°C)	τ^0_{NR} 10^{-14} s^{-1}	ΔE (cm^{-1})
Cr:LiSAF	64	342	69	2.4	5125
Cr:LiSCAF	80	348	75	17	4791
Cr:LiCAF	190	528	255	1.3	8532
Ti:sapphire	3.85	378	105		

TABLE 2.3 *Parameters giving the temperature dependence of the fluorescence lifetime of various laser materials*[76,77].

Cooling the Cr:LiSAF crystal to even lower temperatures would, of course, permit pumping at higher powers, but a practical temperature limit was reached in the laboratory because cooling below 13 °C resulted in condensation forming on the crystal facets. The use of a nitrogen purge would eliminate this problem, but would also rather defeat the object of having a compact and practical all-solid-state laser system. Another problem was that serious damage was caused to the laser crystal when it was pumped at powers in excess of ~ 1.2 W. This probably resulted from particles of dust accumulating on the crystal facet and acting as absorption centres. Similar damage problems were experienced with the AR-coated crystal used previously. Of the materials shown in Table 2.3, Cr:LiCAF seems to be the most promising alternative to Cr:LiSAF as far as its thermal performance is concerned, but further improvement to its optical quality is required.

The problems associated with pumping at higher powers can be alleviated to a certain extent by pumping the Brewster rod from both ends, thus spreading out the thermal load. This was accomplished with Ar^+-ion pumping by splitting the power of the beam into two with a dielectric beam splitter. In this pumping scheme, and with a 3% output-coupler, the Cr:LiSAF laser had a CW threshold of 150 mW

from each pump beam and produced 160 mW of output power for 1.3 W total pump power when the crystal was cooled to 16 °C. The maximum output power obtainable from the Ar^+-ion laser when it was operating on its 528 nm line was 1.3 W, but if the above figures are extrapolated, and we assume that a total pump power of 2 W can be applied before thermal problems prevent lasing, it would suggest that powers of up to 270 mW could be obtained from a Cr:LiSAF system that was simultaneously pumped from both ends. The Nd:YAG laser was not sufficiently stable at 1.3 W for a trial of this beam-splitting approach to be made.

2.4 Concluding Remarks

2.4.1 A Summary of the Chapter

Following a brief review of vibronic gain media in general, and Cr:LiSAF in particular, this chapter has concentrated on two Cr:LiSAF lasers that were pumped by frequency-doubled minilasers operating in the green spectral region. This region corresponds to a trough the absorption spectrum of colquiriite crystals. This novel approach to the development of an all-solid-state Cr:LiSAF system was made possible by the use of LiSAF crystals doped with up to 22 % Cr^{3+}. The green-pumping approach offers potential advantages over direct diode pumping because frequency-doubled minilasers offer diffraction-limited beams at several watts of output power, greatly exceeding that available from AlGaInP semiconductor lasers with good beam quality.

The first system described utilised an AR-coated LiSAF crystal doped with 10 % Cr^{3+}. It was pumped first by an Ar^+ ion mainframe laser and then by a frequency-doubled Nd:YLF ring minilaser. The laser produced transform-limited 90 fs pulses at 859 nm at a repetition rate of 86 MHz. The average output power was 30 mW at 320 mW absorbed pump power and self-modelocked operation was achieved for pump powers as low as 280 mW. Minilaser-pumped operation was impeded by two problems associated with the pump laser. Firstly, the minilaser was prone to multimode operation that resulted in a fluctuating green output and, secondly, its output power was limited to ~ 1 W because of the low thermal fracture power of the Nd:YLF laser crystal. The AR coatings of the crystal caused feedback into the

ring laser, decreased the laser slope efficiency and were susceptible to damage at high pump powers. However, this system demonstrated that the green-pumping of highly doped Cr:LiSAF was a viable approach to building an all-solid-state femtosecond Cr:LiSAF laser.

The second system described incorporated a Brewster-angled crystal doped with 22 % Cr^{3+} and was pumped firstly by an Ar^{+} ion mainframe laser and then by a frequency-doubled Nd:YAG minilaser. The only significant difference in the operation of the Cr:LiSAF laser with each of these pumps was that under minilaser pumping, the Cr:LiSAF laser suffered from periodic bursts of amplitude fluctuations, caused by the 'green problem' in the pump laser. In CW operation, the laser gave over 120 mW of output power through a 1.5 % output coupler when pumped by 1.1 W absorbed power. When modelocked, it produced 72 fs pulses at 76 mW average output power. At incident pump powers greater than ~1.2 W, the laser suffered from thermally induced roll-off in output power that was attributed to non-radiative decay routes from the upper laser level. 160 mW of average output power was obtained by pumping the Cr:LiSAF laser from both ends, through a better distribution of the thermal load. Cr:LiCAF crystals may be a better alternative to Cr:LiSAF as far as thermal performance is concerned but, to date, the optical quality of Cr:LiSAF is superior.

The work described in this chapter demonstrates that green-pumping of Cr:LiSAF is a viable alternative to direct-diode pumping and, significantly, the second green-pumped system described above produced femtosecond pulses at output powers that are only now being matched by directly diode-pumped systems. The principal problem that hindered work on both systems was the 'green problem' that plagued the frequency-doubled minilaser pump sources. Recently, two minilaser systems have become commercially available that are not affected by the green problem. The 'Millennia' from Spectra Physics Lasers Inc. solves the green problem by allowing many (>100) longitudinal modes to oscillate at once[78]. Whilst a few coupled longitudinal modes result in a wildly fluctuating output, the variations due to many longitudinal modes average out, and a steady output results[79,80]; in the Millennia, this output has less than 0.1 % rms noise in over 6 W of 532 nm light. The Millennia itself is based on Nd: yttrium vanadate ($Nd:YVO_4$)[81,82], but a

similar system has been demonstrated that is based on Nd:YAG[83]. The doubling crystal in both cases is LBO.

A second system based on Nd:vanadate and LBO has been developed by Coherent Laser Group[84]. The 'Verdi' is a ring laser that utilises a birefringent filter and provides over 8.5 W of single-frequency 532 nm light, again with less than 0.1 % rms noise.

The main advantage green-pumped Cr:LiSAF offers over green-pumped Ti:sapphire is its significantly lower threshold; Cr:LiSAF lasers self-modelock reliably at about 0.5 W pump, whereas Ti:sapphire lasers require closer to 1 W for reliable operation. For pump powers over about 2 W this difference becomes much less significant, and the thermal properties of Cr:LiSAF begin to count against it. Nevertheless, this work has demonstrated the viability of 'green-trough' pumping, and Cr:LiSAF is still a suitable gain crystal for lasers pumped by lower-power frequency-doubled minilasers such as the 1 W 'Greenline 1000' from Edinburgh Instruments. In addition to this, an alternative crystal such as Cr:LiCAF may still be able to rival Ti:sapphire if crystals of a suitably high optical quality can be grown.

2.4.2 More Recent Developments in Cr:LiSAF lasers

Minilaser-pumped lasers, whether based on Cr:LiSAF, Cr:LiCAF or Ti:sapphire, are all relatively expensive devices because the minilaser pumps are themselves pumped by expensive diode arrays. Since the work described in this chapter was completed, significant progress has been made in the development of self-modelocked Cr:LiSAF laser systems that are pumped directly by broad-area semiconductor lasers. Dymott and Ferguson developed the first such system[85], and they subsequently demonstrated a device that generated over 40 mW of output power[86]. Facoz *et al* reported a device that exhibited self-starting diode-pumped self-modelocked operation[87]. A self-modelocked system pumped by a diode master oscillator power amplifier (MOPA) has been demonstrated that gave 45 mW of output power[88], and a MOPA-pumped device modelocked by a saturable Bragg reflector has produced 70 fs pulses at 100 mW output power. A directly-diode-pumped device modelocked with an anti-resonant Fabry-Perot saturable absorber

(A-FPSA) has produced 98 fs pulses at 50 mW, and CW powers of up to 140 mW[89], and a self-modelocked Cr:LiSAF laser has produced pulses as short as 18 fs[8]. Finally, Coherent Laser Group have recently announced that a 100 mW, 100 fs Cr:LiSAF laser will be commercially available in the near future.

All of these systems rely on components, such as A-FPSAs, saturable Bragg reflectors, MOPAs or simply broad-area semiconductor lasers, that may be cheap compared with frequency-doubled minilasers but still form a significant fraction of the overall cost of each system. The system described in the next two chapters of this thesis, however, opens up the prospect of an all-solid-state, self-modelocked laser pumped by a single, narrow-stripe semiconductor laser. Such a device would be a remarkably simple and inexpensive ultrashort-pulse laser system.

---

[1] K. Lamb, D. E. Spence, J. Hong, C. Yelland and W. Sibbett, Paper CW13 in *Conference on Lasers and Electro-Optics*, **8**, 1994 OSA Technical Digest Series (Optical Society of America, Washington, D.C., 1994), pp 235-236

[2] See, for example, references 78 and 84

[3] S. A. Payne, L. L. Chase, H. W. Newkirk, L. K. Smith and W. F. Krupke, IEEE J. Quantum Electron. **24**, 2243 (1988)

[4] J. Hecht, Laser Focus World **28**, No. 10 p.93 (1992)

[5] C. Spielmann, P. F. Curley, T. Brabec and F. Krausz, IEEE J. Quantum Electron. **30**, 1100 (1994)

[6] F. Krausz, M. E. Fermann, T. Brabec, P. F. Curley, M. Hofer, M. H. Ober, C. Spielmann, E. Wintner and A. J. Schmidt, IEEE J. Quantum Electron. **28** 2097 (1992)

[7] T. H. Maiman, Nature **187**, 493 (1960)

[8] M. J. P. Dymott and A. I. Ferguson, in *Conference on Lasers and Electro-Optics*, Vol. 15 of 1995 OSA Technical Digest Series (Optical Society of America, Washington, D. C., 1995), Paper CWM1

[9] P. F. Moulton, Proc. IEEE **80**, 340 (1992)

[10] L. F. Johnson, R. E. Dietz and H. J. Guggenheim, Phys. Rev. Lett. **11**, 318 (1963)

[11] B. Fritz and U. Menke, Solid St. Commun. **3**, 61 (1965)

[12] J. C. Walling, H. P. Jenson, R. C. Morris, E. W. O'Dell and O. G. Peterson, Opt. Lett **4**, 182 (1979)

[13] L. F. Mollenauer and D. H. Olson, Appl. Phys. Lett. **24**, 1557 (1967)

[14] P. F. Moulton, Proc. IEEE **80**, 340 (1992)

[15] P. F. Moulton, J. Opt. Soc. Am. B **3**, 125 (1986)

[16] S. A. Payne, L. L. Chase, H. W. Newkirk, L. K. Smith and W. F. Krupt, IEEE J. Quantum Electron. **24**, 2243 (1988)

[17] S. A. Payne, L. L. Chase, L. K. Smith, W. L. Kway and H. W. Newkirk, J. Appl. Phys **66**, 1051 (1989)

[18] M. D. Perry, S. A. Payne, T. Ditmire, R. Beach, G. J. Quarles, W. Ignatuk, R. Olson and J. Weston, Laser Focus World, p.85 Sept. 1993.

[19] S. A. Payne, W. F. Krupke, L. K. Smith, W. L. Kway, L. Davis DeLoach and J. B. Tassano, IEEE J. Quantum Electron. **28**, 1188 (1992)

[20] H. W. H. Lee, S. A. Payne and L. L. Case, Phys. Rev. B **39**, 8907 (1989)

[21] J. A. Cairn, in *Tuneable Solid-State Lasers*, (Ed. P. Hammerling, A. B. Budgor and A. Pinto) Springer-Verlag, Berlin (1985)

[22] G. A. Keig, J. Cryst. Growth **2**, 236 (1968)

[23] Personal communication with D. Burns, Institute of Photonics, University of Strathclyde, Wolfson Centre, 106 Rottenrow, Glasgow, G4 0NW, Scotland, UK.

[24] M. D. Perry, S. A. Payne, T. Ditmire, R. Beach, G. J. Quarles, W. Ignatuk, R. Olson and J. Weston, in *Laser Focus World*, September 1993

[25] R. Scheps, J. F. Myers, H. B. Serreze, A. Rosenberg, R. C. Morris and M. Long, Opt. Lett. **16**, 820 (1991)

[26] Q. Zhang, G. J. Dixon, B. H. T. Chai and P. N. Kean, Opt. Lett. **17**, 43 (1992)

[27] A. Miller, P. LiKamWa, B. H. T. Chai and E. W. Van Stryland, Opt. Lett **17**, 195 (1992)

[28] J. M. Evans, D. E. Spence, W. Sibbett, B. H. T. Chai and A. Miller, Opt. Lett. **17**, 1447 (1992)

[29] N. H. Rizvi, P. M. W. French and J. R. Taylor, Opt. Lett **17**, 1605 (1992)

[30] P. M. W. French, R. Mellish, J. R. Taylor, P. J. Delfyett and L. T. Florez, Electron. Lett. **29**, 1262 (1993)

[31] F. Balembois, P. Georges and A. Brun, Opt. Lett. **18**, 1730 (1993)

[32] P. M. W. French, R. Mellish, J. R. Taylor, P. J. Delfyett and L. T. Florez, Opt. Lett. **18**, 1934 (1993)

[33] D. Kopf, K. J. Weingarten, L. Brovelli, M. Kamp and U. Keller, Postdeadline Paper CPD22-1/49 Conference on Lasers and Electro-Optics **8** (1994)

[34] J. R. Lincoln, I. M. Botheroyd, M. J. P. Dymott and A. I. Ferguson, Paper CW12, in *Conference on Lasers and Electro-Optics*, **8**, 1994 OSA Technical Digest Series (Optical Society of America, Washington, D. C., 1994), pp 234-235

[35] F. Krauz, M. E. Fermann, T. Brabec, P. F. Curley, M. Hofer, M. H. Ober, Ch. Spielmann, E. Wintner and A. J. Schmidt, IEEE J. Quantum Electron. **28**, 2097 (1992)

[36] C. W. Siders, E. W. Gaul, M. C. Downer, A. Babin and A. Stephanov, in *Conference on Lasers and Electro-Optics*, 1994 OSA Technical Digest Series (Optical Society of America, Washington, D. C. 1994) Paper CThI10

[37] T. R. Steele, D. C. Gerstenberger, A. Drobshoff and R. W. Wallace, Opt. Lett. **16**, 399 (1991)

[38] G. T. Maker and A. I. Ferguson, Opt. Lett. **15**, 375 (1990)

[39] G. P. A. Malcolm and A. I. Ferguson, Opt. Comm. **82**, 299 (1991)

[40] J. Harrison, A. Finch, D. M. Rines, G. A. Rines and P. F. Moulton, Opt. Lett. **16**, 581 (1991)

[41] K. Lamb, D. E. Spence, J. Hong, C. Yelland and W. Sibbett, Opt. Lett. **19**, 1864 (1994)

[42] C. Yelland, Ph.D. Thesis, University of St. Andrews (1996)

[43] T. Y. Fan, G. J. Dixon and R. L. Byer, Opt. Lett. **11**, 204 (1986)

[44] T. Baer, J. Opt. Soc. Am. B **3**, 1175 (1986)

[45] A. Ashkin, G. D. Boyd, J. M. Dziedzic, IEEE J. Quantum Electron. **2**, 109 (1966)

[46] W. J. Kozlovsky, C. D. Nabors and R. L. Byer, Opt. Lett. **12**, 1014 (1987)

[47] J. J. Zayhowski and A. Mooradian, Opt. Lett. **14**, 24 (1989)

[48] C. Pederson, P. L. Hansen, T. Skettrup and P. Buchhave, Opt. Lett. **20**, 1389 (1995)

[49] M. Oka and S. Kubota, Opt. Lett. **13**, 805 (1988)

[50] L. Y. Liu, M. Oka, W. Wiechmann and S. Kubota, Opt. Lett. **19**, 189 (1994)

[51] A. J. Alfrey, IEEE J. Quantum Electron. **30**, 2350 (1994)

[52] W. Koechner, in *Solid-State Laser Engineering*, Springer-Verlag, Berlin (1996)

[53] J. E. Murray, IEEE J. Quantum Electron. **19**, 488 (1983)

[54] G. Cerullo, S. De Silvestri and V. Magni, Opt. Comm. **93**, 77 (1992)

[55] C. Chen, Y. Wu, A. Jiang, B. Wu, G. You, R. Li and S. Lin, J. Opt. Soc. Am. B 6, 616 (1989)

[56] D. A. Roberts, IEEE J. Quantum Electronics **28**, 2057 (1992)

[57] G. R. Huggett, Appl. Phys. Lett. **13**, 186 (1968)

[58] D. E. Spence, J. M. Evans, W. E. Sleat and W. Sibbett, Opt. Lett. **16**, 1762 (1991)

[59] D. E. Spence, P. N. Kean and W. Sibbett, Opt. Lett. **16**, 42 (1991)

[60] M. Piché, Opt. Comm. **86**, 156 (1991)

[61] J. Herrmann, J. Opt. Soc. Am. B **11**, 498 (1994)

[62] T. Brabec, P. F. Curley, Ch. Spielmann, E. Wintner and A. J. Schmidt, J. Opt. Soc. Am. B **10** 1029 (1993)

[63] V. L. Lashnikov, V. P. Kalosha, V. P. Mikhailov and I. G. Poloyko, J. Opt. Soc. Am. B **12** 462 (1995)

[64] See, for example, Reference 59 above

[65] M. Piché and F. Salin, Opt. Lett. **18**, 1041 (1993)

[66] F. Salin and J. Squier, Opt. Lett **17**, 1352 (1992)

[67] See, for example, D. Georgiev, J. Herrmann and U. Stamm, Opt. Comm. **92**, 368 (1992) and Reference 65 above

[68] G. P. Agrawal, in *Nonlinear Fiber Optics* (Academic Press, London, 1995), p9

[69] R. L. Fork, O. E. Martinez and J. P. Gordon, Opt. Lett. **9**, 150 (1984)

[70] Personal communication with D. Burns, Institute of Photonics, University of Strathclyde, Wolfson Centre, 106 Rottenrow, Glasgow, G4 0NW, Scotland, UK. See also K. Oppo, Ph. D. Thesis, University of St. Andrews (1996).

[71] L. Y. Liu, M. Oka, W. Wiechmann and S. Kubota, Opt. Lett. **19**, 189 (1994)

[72] Adapted from W. Koechner, in *Solid-State Laser Engineering*, Springer-Verlag, Berlin (1996)

[73] W. Koechner, in *Solid-State Laser Engineering*, Springer-Verlag, Berlin (1996), p 48

[74] C. Yelland and W. Sibbett, in *The Twelfth UK National Quantum Electronics Conference Technical Digest*, I.O.P., 1995, Paper 2-4

[75] D. Kopf, K. J. Weingarten, L. R. Broveli, M. Kamp and U. Keller, Opt. Lett **19**, 2143 (1994)

[76] M. Stalder, M. Bass and B. H. T. Chai, J. Opt. Soc. Am. B **9**, 2271 (1992)

[77] P. Albers, E. Stark and G. Huber, J. Opt. Soc. Am. B **3**, 134 (1986)

[78] W. L. Nighan and J. Cole, in *Advanced Solid-State Lasers*, 1996 Paper PD4-1

[79] V. Magni, G. Cerullo, S. De Silvestri, O. Svelto, L. J. Qian, M. Danailov, Opt. Lett. **18**, 2111

[80] G. E. James, E. M. Harrell II, C. Bracikowski, K. Wiesenfeld and R. Roy, Opt. Lett. **15**, 1141 (1990)

[81] J. R. O'Connor, Appl. Phys. Lett. **9**, 407 (1966)

[82] A. W. Tucker, M. Birnbaum, C. L. Fincher, J. Appl. Phys. **78**, 232 (1976)

[83] W. L. Nighan, S. B. Hutchinson, D. Dudley and M. S. Keirstead, in *Conference on Lasers and Electro-Optics*, 1996 OSA Technical Digest Series Volume 9 (Optical Society of America, Washingtom, D. C. 1996) Paper CWN2

[84] M. D. Selker, T. J. Johnston, G. Frangineas, J. L. Nightingale and D. K. Negus, in *Conference on Lasers and Electro-Optics*, 1996 OSA Technical Digest Series Volume 9 (Optical Society of America, Washingtom, D. C. 1996) Paper CPD21-2

[85] M. J. P. Dymott and A. I. Ferguson, Opt. Lett **19**, 1988 (1994)

[86] M. J. P. Dymott and A. I. Ferguson, Opt. Lett **20**, 1157 (1995)

[87] F. Falcoz, F. Balembois, P. Georges and A. Brun, , Opt. Lett **20**, 1874 (1995)

[88] A. Robertson, R. Knappe, K-J Boller and R. Wallenstein, in *1996 Conference on Lasers and Electo-Optics Europe*, (IEEE Catalog number 96TH8161), Paper CWA2

[89] D. Kopf, K. J. Weingarten, L. R. Brovelli, M. Kamp and U. Keller, , Opt. Lett **19**, 2143 (1995)

3. Routes to Self-modelocking at Low Pump Powers

3.1 Introduction

In Chapter 2 the construction and assessment of two minilaser-pumped Cr:LiSAF lasers was described. The laser pumped by a frequency-doubled Nd:YAG laser produced sub-100 fs pulses at output powers higher than those obtained from any contemporary self-modelocked Cr:LiSAF laser. In this Chapter, a system is introduced that approaches the problem of all-solid-state sub-100 fs pulse generation from another novel angle. In the two years since the development of the minilaser-pumped Cr:LiSAF system, directly-diode-pumped systems have improved to the point where Coherent Inc. are promising that a directly diode-pumped Cr:LiSAF laser offering 100 fs pulses at 100 mW will be commercially available early in 1997. Direct diode-pumping is both cheaper and more compact than minilaser pumping, although the powers obtained from directly diode-pumped systems are not, in general, as high. A typical diode-pumped Cr:LiSAF laser is pumped by two 100 μm stripe, 500 mW output power diode lasers. Because broad-area diode laser output beams are not diffraction-limited, extended pump optics schemes are required to couple the pump light into the Cr:LiSAF crystal, and the available pump light is used inefficiently. However, many applications do not require the larger output powers available from systems pumped by broad-area diodes. The system that I introduce in this chapter was designed to produce relatively low average power sub-100 fs pulses, but it could also potentially be pumped by very cheap, low-power, narrow-stripe laser diodes.

A Cr:LiSAF crystal has a relatively high $\sigma\tau$ product (32.2×10^{-19} cm^2 μs^{-1}, compared with 12.2×10^{-19} cm^2 μs^{-1} for Ti:sapphire) and therefore, potentially, a low CW laser threshold. The laser described in the Chapters 3 and 4 exploits this fact together with the routes towards low-threshold self-modelocking described in this chapter. The system is pumped by a single self-injection-locked 100 μm stripe

diode laser, but the reduction in the pump power required for self-modelocking makes pumping by narrow-stripe diode lasers that give diffraction-limited beams a very real possibility. Narrow-stripe diode lasers are much cheaper than broad-area, higher-power devices, costing hundreds rather than thousands of dollars. The present work looks towards a compact laser system offering sub-100 fs pulses at a significantly lower cost than that of similar devices currently available.

In this chapter, I will outline the various factors that affect the power required for self-modelocking in a Cr:LiSAF laser. In Chapter 4, I will describe the physical implementation of these ideas in a diode-pumped, low-threshold self-modelocked laser Cr:LiSAF laser system. The present chapter opens with an investigation into the factors that affect the CW threshold of a laser and the strength of the nonlinear lensing induced in the laser crystal. I next describe the principles of self-injection-locking, which was used to produce a diffraction-limited pump beam whilst the Cr:LiSAF laser threshold was reduced towards a value within the reach of narrow-stripe semiconductor lasers. Next, I will outline the key features of a model of hard-aperture self-modelocking that was developed by Cerullo *et al*[1]. This model is used to provide a laser-design prescription that ensures reliable self-modelocking even at low intracavity powers. Finally, consideration is given to the effects of intracavity dispersion on pump power requirements in ultrashort-pulse systems.

3.2 Factors Affecting CW Threshold and Nonlinear Lensing

3.2.1 Oscillation Threshold For Focused Gaussian Beams

In this section I consider the parameters that affect the oscillation threshold of the four-mirror cavity configurations that are typical for lasers used for ultrashort pulse generation. The intracavity beam is tightly focused in the gain crystal in these lasers, because the gain crystal also serves as the source of the nonlinearity responsible for modelocking. The pump beam must also be tightly focused in order to efficiently transfer its power to the cavity beam.

I shall first derive an expression for the threshold pump power required for CW oscillation in a laser system in which both the pump and cavity modes are focused

Gaussian beams. Alfrey derives an expression that relates pump power to intracavity power in such a laser[2]:-

$$P_p = \frac{(T+\Lambda)h\nu_p\pi^2}{8\sigma\tau\alpha_p \int_0^L \frac{e^{-\alpha_p z}}{w_c^2 w_p^2} Q(z)dz}.$$

EQUATION 3.1

Here z is the axial distance from the crystal face; P_p is the absorbed pump power; T is the output coupling; Λ is the round-trip cavity loss; L is the length of the crystal; α_p is the absorption coefficient at the pump wavelength λ_p; and σ and τ are the emission cross-section and upper-state lifetime, respectively. The pump and cavity mode spot sizes w_p and w_c are given by

$$w_p^2 = w_p^2(z) = w_{p0}^2\left\{1+\frac{(z-z_p)^2\lambda_p^2}{\pi^2 w_{p0}^4 n_p^2}\right\} \qquad w_c^2 = w_c^2(z) = w_{c0}^2\left\{1+\frac{(z-z_c)^2\lambda_c^2}{\pi^2 w_{c0}^4 n_c^2}\right\},$$

EQUATION 3.2

where z_p and z_c are the locations of the waists w_{p0} and w_{c0} of the pump and cavity beams, which experience refractive indices n_p and n_c respectively. Finally Q(z) is given by

$$Q(z) = 2\pi\int_0^\infty \frac{e^{-Ar^2} r dr}{1+Be^{-Dr^2}}$$

EQUATION 3.3

where r is the radial co-ordinate,

$$A = \frac{2\left(w_p^2+w_c^2\right)}{w_p^2 w_c^2}, \qquad B = \frac{4}{\pi w_c^2}\frac{P_c}{I_s} \qquad \text{and} \qquad D = \frac{2}{w_c^2},$$

EQUATION 3.4

where P_c is the intracavity power and I_s is the saturation intensity.

We can deduce a general expression for the threshold of this system from Equation 3.1. At threshold the intracavity field intensity $I_c = \frac{P_c}{\pi w_c^2} << I_s$, and so

$$Q(z) \rightarrow 2\pi \int_0^{\infty} e^{-Ar^2} r dr = \frac{\pi}{2} \frac{w_p^2 w_c^2}{w_p^2 + w_c^2}$$

EQUATION 3.5

Equation 3.1 therefore becomes

$$P_{th} = \frac{(T + \Lambda) h\nu_p \pi}{4\sigma\tau\alpha_p \int_0^L \frac{e^{-\alpha_p z}}{w_p^2 + w_c^2} dz}.$$

EQUATION 3.6

Note that in the special case in which the pump and cavity mode sizes remain constant throughout the gain crystal, P_{th} reduces to the more familiar form[3]

$$P_{th} = \frac{\pi}{4} \frac{h\nu_p}{\sigma\tau} \frac{\left(w_{p0}^2 + w_{c0}^2\right)(T + \Lambda)}{1 - e^{-\alpha_p L}}$$

EQUATION 3.7

3.2.2 Factors Affecting The Oscillation Threshold

Equation 3.6 contains the principal parameters that determine the oscillation threshold of a laser. Firstly, there are materials parameters. Threshold is inversely proportional to the $\sigma\tau$ product of a gain crystal, and this makes the Cr:LiSAF an attractive gain medium for a low-threshold laser. Cr:LiSAF has a $\sigma\tau$ product of 32.2 x 10^{-19} cm^2 μs^{-1}, which compares favourably with the values for Cr:LiCAF (20.4 x 10^{-19} cm^2 μs^{-1}) and Ti:sapphire (12.2 x 10^{-19} cm^2 μs^{-1}). Threshold is also proportional to the energy of the pump photons, which gives diode-pumped Cr:LiSAF and Cr:LiCAF systems (λ_p = 670 nm) another advantage minilaser-pumped Ti:sapphire systems ($\lambda_p \cong$ 530 nm).

In addition to materials parameters, oscillation threshold depends upon factors that vary from laser to laser. The threshold is directly proportional to the round-trip cavity loss (T + Λ). Clearly, a low threshold laser must have small intracavity losses and a very modest output coupling. Finally, the threshold is inversely

proportional to the composite term in Equation 3.6 that depends upon the spatial overlap of the pump and cavity beams, and upon the absorption coefficient:-

$$P_{th} \propto \left(\alpha_p \int_0^L \frac{e^{-\alpha_p z}}{w_p^2 + w_c^2} dz \right)^{-1}$$

EQUATION 3.8

Figure 3.1 shows the variation of threshold with the position of the pump and cavity beam waists in a 10 mm Cr:LiSAF crystal. Minimum threshold is achieved when the beam waists are focused 1.65 mm from the pumped face of the crystal. For the purposes of modelocking, it will be shown later that it is advantageous to

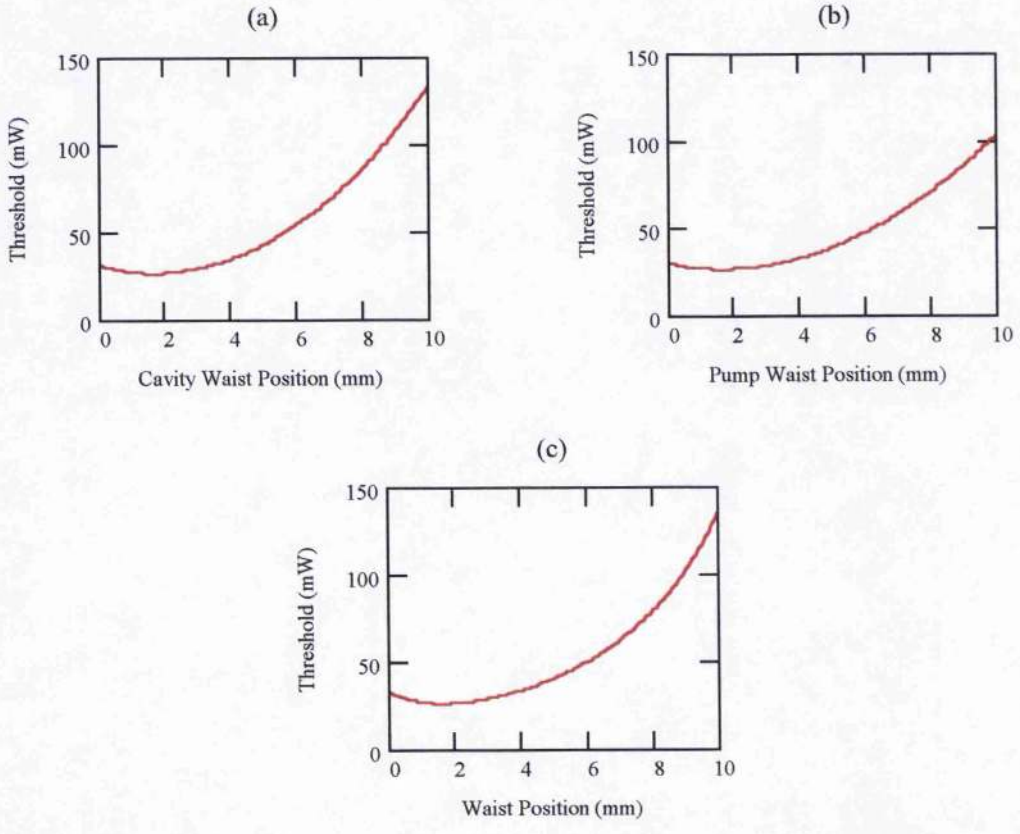

FIGURE 3.1 *Threshold as a function of distance from the pumped crystal face for (a) pump beam waist fixed at 1.65 mm; (b) cavity beam waist fixed at 1.65 mm; and (c) coincident pump and cavity beam waists. The figures were calculated for equal waists of 20 μm; a crystal of length 10 mm, an absorption coefficient of 3.2 cm^{-1} (giving 96% absorption in 1 cm); a refractive index of 1.41; and pump and laser wavelengths of 670 nm and 850 nm, respectively.*

have the intracavity waist focused on the face of the laser rod, and Figure 3.1 shows that the CW threshold is near its minimum value at this point.

Figure 3.2 shows the variation of oscillation threshold with the sizes of the pump and cavity beam waists. In general, tighter focusing of both the pump and the intracavity beams leads to a lower threshold. However, contrary to the predictions of the constant-spot-size model of Equation 3.7, the overlap of the pump and cavity beams is also significant in determining threshold. If either beam is focused significantly more than the other then the increased divergence of the more focused beam leads to a poorer overlap, and hence a higher threshold. The numerical values predicted by Equation 3.6 are in good agreement with the experimentally measured thresholds to be presented in Chapter 4; the values predicted by Equation 3.7 are too small by a factor of two.

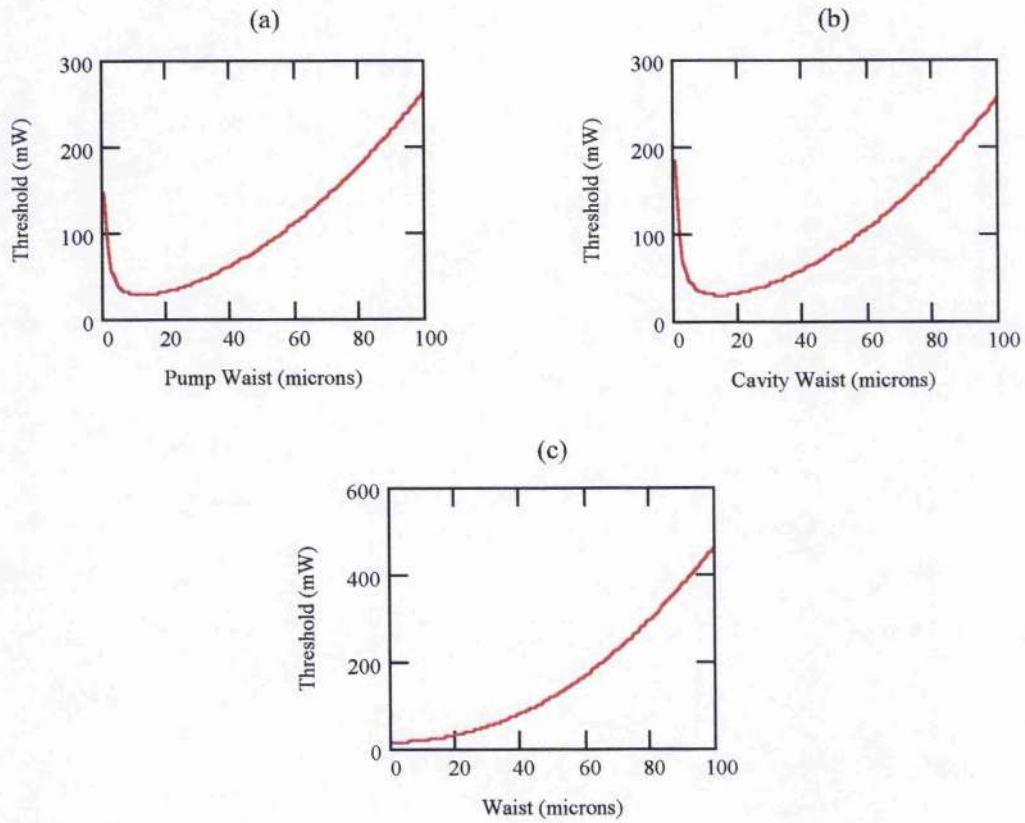

FIGURE 3.2 *The variation of laser threshold with (a) pump beam waist size, given a fixed cavity beam waist of 20 μm; (b) cavity beam waist size, given a fixed pump beam waist of 20 μm; and (c) equal pump and cavity beam waist sizes. These figures were calculated for waists focused on the crystal face, and with other parameters as for Figure 3.1.*

3.2.3 Non-diffraction-limited Pump Beams

3.2.3.1 Overlap Efficiency with Non-diffraction-limited Pump Beams

Beam overlap efficiency becomes particularly important in a laser system in which the pump beam is not diffraction-limited. In the context of this thesis, this particularly means the pump beam from a broad-area semiconductor lasers. The overlap-absorption efficiency η_0 for collimated Gaussian beams can be quantified in the expression[4]

$$\eta_0 = \eta_B \eta_a = \frac{\int_0^\infty g(r) I_B(r) 2\pi r dr}{\int_0^\infty I_B^2(r) 2\pi r dr} \int_0^L \alpha_p e^{-\alpha_p z} dz$$

EQUATION 3.9

where η_B is the overlap efficiency, η_a is the pump absorption efficiency, g(r) is the radial variation of the gain profile in the laser rod and I_B is the intracavity beam profile. This expression reduces to

$$\eta_0 = \eta_B \eta_a = \frac{2w_{c0}^2}{w_{p0}^2 + w_{c0}^2} \cdot \left(1 - e^{-\alpha_p L}\right) \qquad \text{for } w_{p0} > w_{c0}$$

and

$$\eta_0 = \eta_B \eta_a = \left(1 - e^{-\alpha_p L}\right) \qquad \text{for } w_{p0} \le w_{c0}.$$

EQUATION 3.10

In a self-modelocked laser system, the pump and cavity beams are not, in general, collimated; instead, they are usually focused to a waist in the gain crystal. The pump beam from a broad-area diode will also be non-diffraction limited. To calculate the beam-overlap efficiency for a focused Gaussian cavity beam and a focused non-diffraction-limited pump beam, we firstly assume that the pump beam has a top-hat profile. This is a typical beam profile of the output of a semiconductor laser. We also assume that the pump beam half-width spot size propagates as

$$w_p = w_{p0} + \left|z - z_p\right| \tan\left(\frac{\theta}{2}\right),$$

EQUATION 3.11

where θ is the FWHM angular width of the pump beam in the far-field. The top-hat profile of the pump beam means that the gain is given by

$$g(r) = \frac{1}{\pi w_p^2} \qquad \text{for } r < w_{p0}$$

and $$g(r) = 0 \qquad \text{for } r \geq w_{p0}.$$

EQUATION 3.12

The focused Gaussian cavity beam is described by

$$I_B(r,z) = \frac{2}{\pi w_c^2} \exp\left(-2\frac{r^2}{w_c^2}\right),$$

EQUATION 3.13

with $w_c = w_c(z)$ propagating as defined in Equation 3.2.

In general, the focused pump and cavity modes will cross over at some point in the crystal. The pumping efficiencies on each side of the cross-over point must be treated separately. We first calculate the fractions of the total available pump light that are coupled into the cavity mode on each side of the cross-over point. We then add these fractions to find the overall fraction of the available light coupled into the cavity mode.

So,

$$\eta_0 = \eta_{aB} = \eta_{w_p < w_c} + \eta_{w_p > w_c}$$

EQUATION 3.14

Assuming that the pump spot is initially smaller than the cavity spot, and that they cross over at $z = z_x$, we can say

$$\eta_{w_p<w_c} = \int_0^{z_x} \alpha_p e^{-\alpha_p z} dz,$$

EQUATION 3.15

because the overlap efficiency is unity if the pump beam is smaller than the cavity beam (as in Equation 3.10).

Once the pump beam becomes larger than the intracavity beam, the light available to support the intracavity beam, expressed as a fraction of that available from a perfectly matched Gaussian pump beam, is given by

$$\eta_{ndl} = \frac{\int_{z_x}^{L}\int_0^{w_p} \frac{I_B(r,z)}{\pi W_p^2} \alpha_p e^{-\alpha_p z} 2\pi r dr dz}{\int_{z_x}^{L}\int_0^{\infty} I_B^2(r,z) \alpha_p e^{-\alpha_p z} 2\pi r dr dz}$$

EQUATION 3.16

and so,

$$\eta_{w_p>w_c} = \eta_{ndl} \cdot \int_{z_x}^{L} \alpha_p e^{-\alpha_p z} dz$$

EQUATION 3.17

3.2.3.2 Brightness and Non-diffraction-limited Pump Beams

The quality of a semiconductor laser beam can be characterised by its brightness; that is the power it emits per unit cross-sectional area per unit solid angle of divergence. This parameter is constant throughout any lossless optical system. For a broad-area semiconductor laser, the characterisation of brightness reduces to a consideration of the width of the diode emission stripe and the divergence of the output beam in the plane of the stripe. This is equivalent to considering how close the beam divergence is to the diffraction-limit. (N.B., in the plane perpendicular to the stripe, the beam is always approximately diffraction-limited.) Diffraction-limited divergence is defined as the divergence seen by a plane wave at a rectangular aperture; this is given by[5]

$$\theta_{FWHM}^{DL} = 2\sin^{-1}\left(\frac{\beta\lambda}{\pi W}\right)$$

EQUATION 3.18

where W is the width of the aperture, and β is a constant given by the transcendental equation

$$\sin(\beta) = \frac{\beta}{\sqrt{2}},$$

EQUATION 3.19

which can be evaluated graphically to give β = 79.7 degrees. A diffraction-limited beam offers the highest attainable brightness, as non-diffraction-limited beams have larger divergences for the same stripe width.

Figure 3.3 shows the variation of the overlap efficiency η_{aB} with the stripe width of a semiconductor laser. The beam divergence is assumed to be $\theta_{FWHM} = 8°$ from the emitting stripe for all stripe widths (8° is a typical value for broad-area 670 nm AlGaInP lasers). The stripe width is therefore inversely proportional to the pump beam brightness and, as brightness is constant throughout the pump optics, the pump beam divergence in the crystal is related to the divergence from the stripe by

$$\theta = \frac{\theta_{FWHM} W}{2w_{p0}}$$

EQUATION 3.20

The overlap efficiency curve in Figure 3.3 was calculated using Equation 3.14 to Equation 3.19. Figure 3.3 clearly shows that the beam overlap efficiency deteriorates rapidly as the beam departs from being diffraction-limited. Laser threshold is inversely proportional to the beam overlap efficiency[6], and so in order to achieve a low CW threshold it is very important that a high-brightness, diffraction-limited pump beam is used. In particular, broad-area semiconductor lasers, with typical stripe widths of 100 μm, are not suitable as pump sources for low-threshold systems. Narrow-stripe semiconductor lasers, with stripes of ~1 μm, would be ideal because they have the added advantage of low cost but, unfortunately, they offer only low output powers. The technique of self-injection-

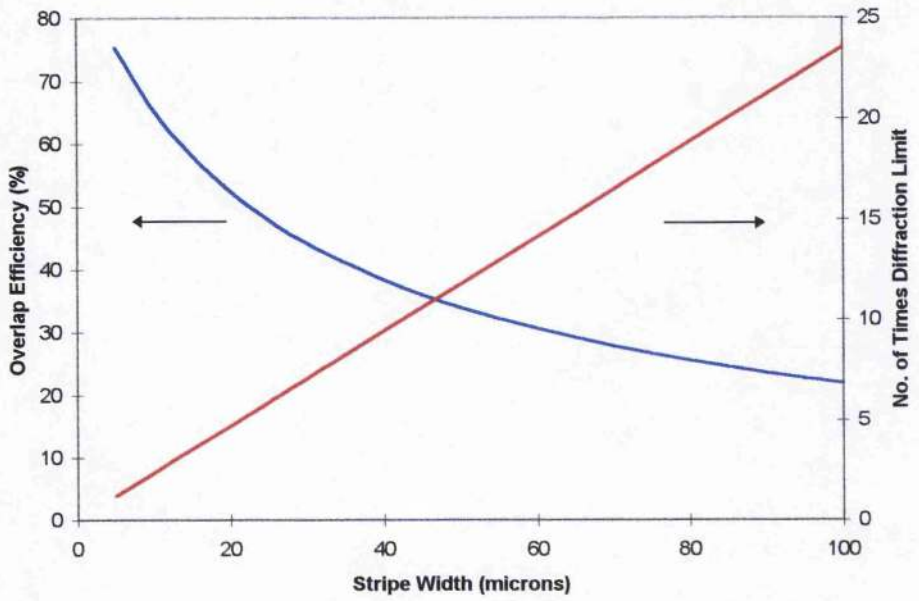

FIGURE 3.3 *Overlap efficiency and beam divergence (as a multiple of the diffraction limited value) as a function of pump laser stripe width. The calculations are made for a constant pump beam divergence of 8 ° from the emitting stripe for all stripe widths. The top-hat pump beam is focused to match a cavity waist size of 20 μm on one end of the crystal, and the pump and cavity wavelengths are 670 nm and 850 nm, respectively. (Other parameters as for Figure 3.1.) The predicted deterioration in overlap efficiency of 20% -30% for a 100 μm stripe is consistent with the difference in thresholds reported in Chapter 4 for self-injection-locked- and broad-area diode-pumped systems.*

locking as a means of obtaining a near-diffraction-limited pump beam will be discussed in Section 3.3.

3.2.4 Factors Affecting Nonlinear Lensing

In Section 3.2.2 I have discussed the importance of the position and size of the pump and cavity beam waists in the determination of a laser's CW threshold. In this section I will briefly discuss the significance of the cavity-beam waist size in the nonlinear lensing experienced by the intracavity beam in the laser crystal. Later, in Section 3.4, I will consider the effects of the position of the cavity-beam waist on the self-modelocking process itself.

A material with a positive nonlinear refractive index n_2 will behave as a distributed lens with a positive intensity-dependent focal length. The power P_k of the lens induced in a thin slice of thickness Δz of such a material is given by[7]

$$P_K = \frac{8 n_2 n_0 P_0}{\pi a w_c^4} \Delta z ,$$

EQUATION 3.21

where n_0 is the linear refractive index, P_0 is the instantaneous peak power and 'a' is a correction factor ($3 < a < 7$) that is required because it is assumed in the derivation of Equation 3.21 that a Gaussian beam induces a quadratic index variation across its profile rather than a Gaussian index variation.

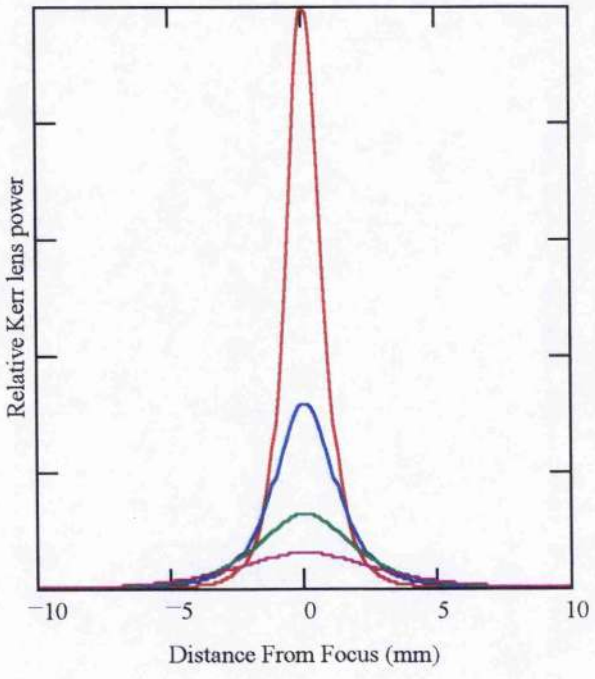

FIGURE 3.4 *The instantaneous-power distribution of the Kerr lens induced in Cr:LiSAF, calculated for a waist of 15 μm (red line), 20 μm (blue line), 25 μm (green line), 30 μm (magenta line). The beam-size distribution is assumed to maintain its linear form (Equation 3.2) throughout the crystal.*

Figure 3.4 shows the instantaneous Kerr-lens power distributions in a 10 mm crystal due to Gaussian beams focused to various waist sizes. Clearly, the w_c^{-4} dependence means that focusing the beam a little more tightly results in far

stronger instantaneous lensing. If we approximate the nonlinear interaction length with the confocal parameter of the Gaussian beams

$$z = \frac{\pi n_0 w_{c0}^2}{\lambda}$$

EQUATION 3.22

then the strength of the lensing varies inversely with the square of the waist size.

It will become clear in Section 3.4 that optimum modelocking is achieved when the Kerr lens induced in a crystal is offset as far from the geometric center of the crystal as possible. Another important parameter, therefore, is the extent to which the lens is localized, rather than distributed, within the crystal. The distance over which the instantaneous Kerr lens power is greater than half of its maximum value is given (from Equation 3.2 and Equation 3.21) by $\sqrt{\sqrt{2}-1}$ (≈ 0.64) times the confocal parameter; this value is plotted as a fraction of the length of a 10 mm crystal against waist size in Figure 3.5. It is apparent from this figure that the induced lens becomes highly localized for tightly-focused waists. The approximation of a single lens rather than a distributed lens becomes increasingly

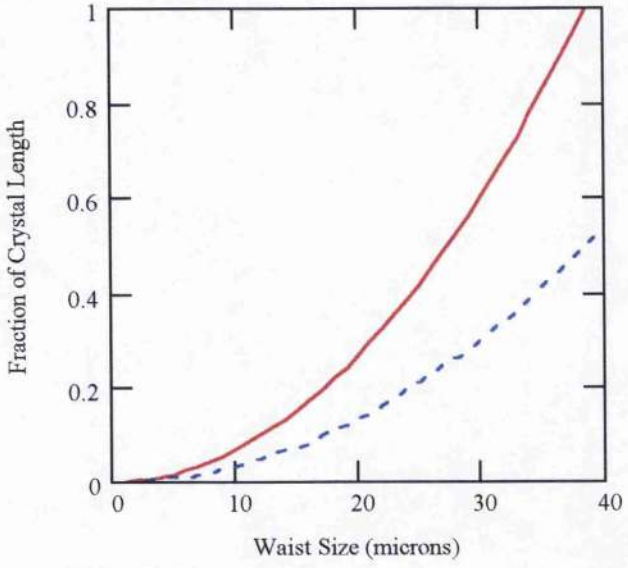

FIGURE 3.5 *The effect of waist size on the fraction of the crystal length for which the power of the induced Kerr lens is greater than half its maximum value. The solid line is for a beam focused at the centre of a 10 mm crystal; the dashed line is for a beam focused at one end of the same crystal.*

more legitimate as the beam is focused more tightly.

3.3 Self-injection-locked Semiconductor Lasers

It is clear from Section 3.2.3 that if low thresholds are to be achieved in a laser, it is essential that it is pumped with a diffraction-limited Gaussian beam. Narrow-stripe diode lasers are available that offer tens of milliwatts in a diffraction-limited beam, but in order to optimise our low-threshold laser it was necessary to have an alternative high-brightness pump source. Our chosen solution to the problem was to use a broad-area semiconductor laser together with a self-injection-locking feed-back scheme. This gave us a compact, source of a medium-power, diffraction-limited beam.

Broad-area diodes typically have lateral stripe dimensions of hundreds of microns. This enables them to produce significantly higher powers than narrow-stripe devices can produce because the larger emission aperture reduces both thermal loading and effects associated with facet defects, that would otherwise cause catastrophic facet damage. Unfortunately, however, the breadth of the stripe also permits multiple lateral modes to oscillate. The far-field mode that results from the superposition of these modes is, in general, a top-hat profile with a typical divergence of ~8-10°, which is about 25 times the diffraction limit. Injection locking can reduce this divergence to near the diffraction limit.

Injection locking is a well-known phenomenon in nonlinear oscillators[8,9], and it is a well-known technique for improving the spectral output characteristics of lasers[10-13]. In the basic injection-locking arrangement[14], the output from a low-power single-longitudinal-mode "master" oscillator is injected into the cavity of a much higher-power "slave" oscillator. If the master oscillator is tuned close to the oscillation frequency of the slave then the injected signal is regeneratively amplified, taking gain from the slave signal until, if tuned closely enough, it extinguishes the slave signal altogether. The injected signal dominates the slave signal because it already has a significant, finite intensity, unlike the slave signal which builds up from low-level random noise (spontaneous emission). The gain in the slave cavity therefore saturates at a lower level for the injected signal than for the slave signal, and so the slave signal does not oscillate.

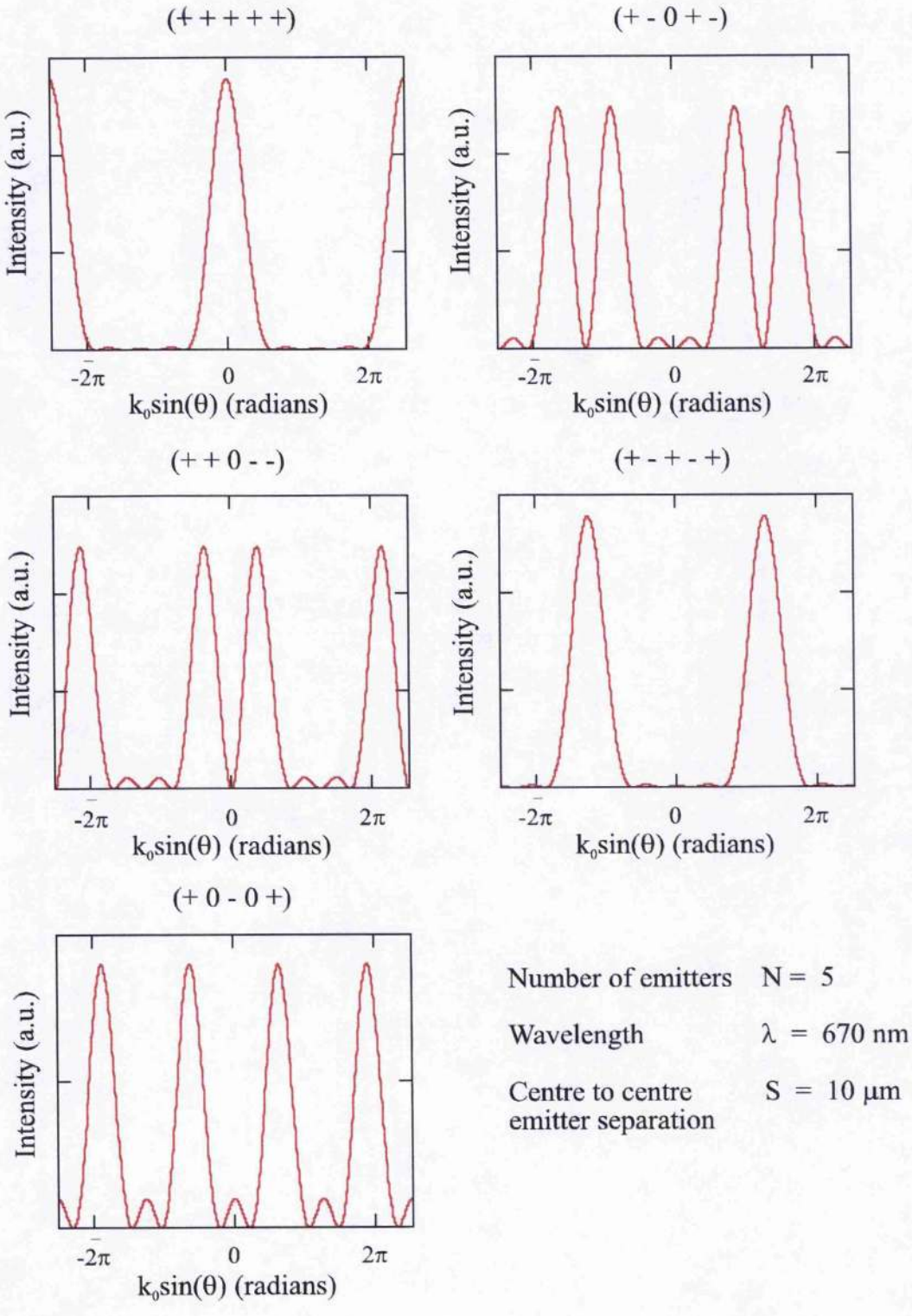

FIGURE 3.6 The grating function of the supermodes of a five stripe array with identical channels and uniform coupling. The symbols in brackets represent the phase relationships of each stripe. The actual far-field patterns are obtained by superimposing the far-field pattern of an individual stripe on these patterns. (After Reference 31)

Injection locking was originally demonstrated in He-Ne lasers[15], and has since been demonstrated in CO_2 lasers[16-18], dye lasers[19-21], excimer lasers[22] and Nd:YAG lasers[23]. Injection locking of semiconductor lasers, which normally oscillate on many longitudinal modes, has been shown to greatly improve the spectral purity of the laser output[10,11,24-30]. As well as locking the frequency of the output of a laser, the injected signal also locks the phase of that output, and it is this property that is particularly important in the *spatial* injection-locking used in this work.

Several models have been used to explain spatial injection locking in semiconductor lasers. In the first to be proposed, the output from a semiconductor laser array was described in terms of 'supermodes', the eigenmodes of the composite-array waveguide[31]. A free-running array of N single-mode emitters can support N supermodes which are distinguished by the phase relationships that exist between the emitters. Each eigenmodal phase relationship corresponds to a distinct far-field pattern, as shown in Figure 3.6. In general, the output from the array will consist of a superposition of these eigenmodes. Injecting a beam into the array can lock the phases of the emitters to alter the composition of this superposition to the combination that most closely matches the injected beam's spatial characteristics[32]. For example, injecting the correct size of beam at the correct off-axis angle could select an output given purely by the (+ - + - +) phase combination in Figure 3.6. In this case, the resultant output would consist of two diffraction-limited lobes, one collinear with the injected beam and one at the equal and opposite angle from the diode axis. Self-injection locking[33], or external-cavity phase-locking[34-37], is achieved by placing a mirror in one of these lobes and feeding it back into the laser.

The supermode description of injection locking provides a good illustration of how injecting a beam or feeding back laser output can improve the spatial characteristics of that output. It also illustrates the sensitivity of the process to injection angle, because it is easy to see that injecting a beam at some angle a little off the angle of one of the output lobes in the (+ - + - +) supermode would begin to excite other supermodes. However, the supermode model does not completely explain the behaviour of injection-locked arrays or broad-area devices. Another model of injection-locking exploits the fact that broad-area devices exhibit their own spatial eigenmodes[38] and simply treats the multiple-stripes of arrays as

perturbations to the broad-area model[38-41]. However, the principle in this approach is still that the injected beam selects the combination of eigenmodes that has spatial characteristics closest to its own.

An alternative description of injection-locking is based on a Fabry-Perot amplifier model[42,43]. In this model the semiconductor laser, be it an array or a broad-stripe device, is regarded as being a simple Fabry-Perot cavity. If a Gaussian beam is injected it bounces around the device, emitting a beam each time it is reflected from the polished front facet (Figure 3.7) of the diode. Each of the emitted Gaussian beams interferes with its neighbours, and, if the injection angle and waist spot-size are chosen correctly, their superposition results in a diffraction-limited lobe in the far-field (Figure 3.8).

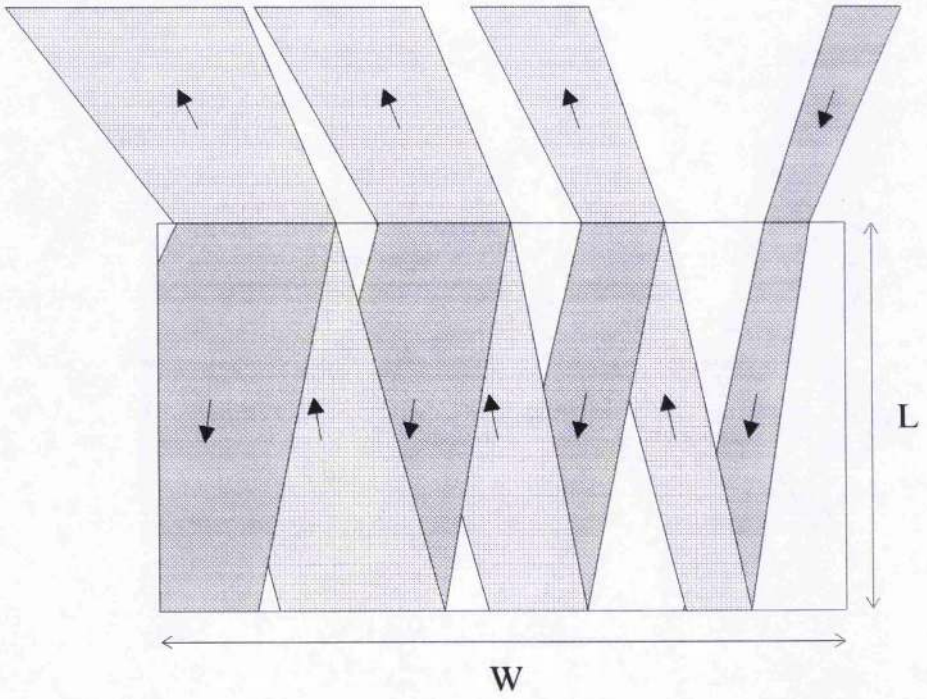

FIGURE 3.7 *The Fabry-Perot model of an injection-locked broad-area laser diode. The injected Gaussian beam is emitted after each pass through the device. The interference between these emitted beams results in a diffraction-limited spike in the far field (see Figure 3.8). (After References 42 and 43)*

In self-injection locking, the injected beam takes the form of spontaneous emission which is fed back into the device from just outside the edge of the far-field free-running laser output. The device again acts as a multiple-pass gain reservoir, with the injected beam competing at all times with the free-running laser output for the

gain available within the device. For full injection-locking, it is necessary to ensure that there is sufficient injected (or fed-back) power to completely saturate the gain and extinguish the free-running mode; unfortunately, the injected power required to do this increases non-linearly with diode drive current[44]. This is a particular problem for self-injection locking, which relies upon feeding back the laser's own output power, which increases linearly with drive current. In practice, it is found that maintaining a diffraction-limited output as the diode drive current is increased requires increasing precision in the positioning and orientation of the feedback mirror. A drive current is eventually reached at which complete suppression of the free-running mode becomes impossible.

Despite this limitation, self-injection locking is significantly simpler than injection-locking, and it offers near-diffraction-limited beams at modest pump powers. As the thrust of the work described in this thesis was towards the development of low-threshold laser systems, only modest pump powers were required and self-injection-locking offers the best compromise between simplicity, beam quality and useful output power.

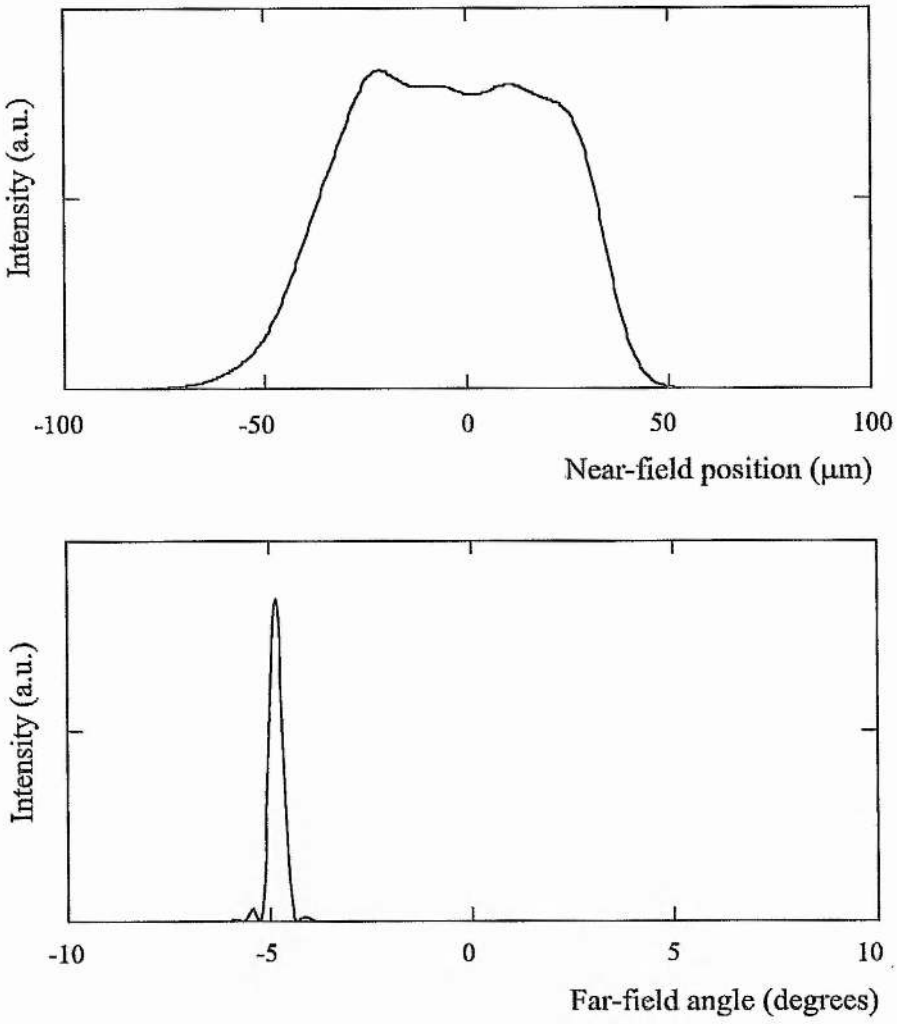

FIGURE 3.8 *Near- and far-field distributions of a L = 300 μm, W = 100 μm, n = 3.6, λ = 670 nm broad-area diode injected at 5 ° with a beam with a 1/e half-width of 12.5 μm focused 5 μm from the right-hand edge of the diode facet. The injected beam makes 6 complete passes through the crystal. (After References 42 and 43)*[45]

3.4 Reliable Self-modelocking - the 'Cerullo' model

Having considered the factors affecting the CW threshold of a four-mirror laser, and the means to obtain a diffraction-limited pump beam to minimise that threshold, I will now consider the factors affecting the ease with which a laser can be modelocked. The greater the propensity a laser has to modelock, the less intracavity power is required in order to modelock it. In this section I will describe a model that predicts how a cavity can be optimised for self-modelocking and, in

Section 3.5, I will consider the factors that affect the power required to sustain pulses of a particular duration once self-modelocking is established.

3.4.1 Theory

Soft-aperture self-modelocking is a complex phenomenon, resulting as it does from a subtle change in the three-dimensional overlap of two laser modes. Most theoretical models of soft-aperture modelocking have concentrated on the mechanisms underlying this process rather than offering a practical guide to laser design. Hard-aperture self-modelocking, on the other hand, is conceptually relatively simple: a Kerr lens in the laser crystal leads to a reduction in the laser mode size at an intracavity slit, and hence a reduction in the round-trip loss. The Kerr lens is intensity dependent, so the high-intensity peak of a pulse experiences less loss than a CW field and the modelocking regime is therefore preferred.

A model developed by Cerullo, Magni and De Silvestri[46-50] has been particularly successful because it offers a clear and precise prescription for building an hard-aperture self-modelocked laser. It is attractive to the experimental laser physicist or engineer because a single equation relates cavity parameters easily measurable in the laboratory to the suitability of the cavity for modelocking.

The theory behind this equation is relatively straightforward and will be outlined briefly here. References 46,47 and 50 should be consulted for the full analysis.

The 'Cerullo' model, as it will be referred to from now on, predicts the change in the intracavity mode size that occurs at the end mirror of a laser as the power inside the laser changes. The problem, therefore, is to relate the mode size at the end mirror to the effects of a Kerr lens produced inside the laser crystal by the intracavity field. Cerullo and co-workers took two approaches towards solving this problem: the first (discussed below) was to represent the Kerr medium as an infinitesimally-thin non-linear slice at the centre of the laser crystal; the second (summarised very briefly in Section 3.4.3 and considered in detail in Chapter 5) was to represent it as a sequence of independent power-dependent lenses distributed throughout the crystal. Both approaches are based on an extension of the ABCD ray-matrix formalism[51] and the aberrationless theory of self-focusing, in

which it is assumed that the intracavity beam maintains a Gaussian profile throughout its propagation in the Kerr medium, but with an altered complex beam parameter q.

In the first approach, the effects of propagation through a nonlinear crystal of effective length d_e are represented by the matrices

$$\begin{pmatrix} 1 & \frac{d_e}{2} \\ 0 & 1 \end{pmatrix} \mathbf{M}_k \begin{pmatrix} 1 & \frac{d_e}{2} \\ 0 & 1 \end{pmatrix}$$

EQUATION 3.23

where the first and last terms each represent power-independent propagation through half of the crystal. The middle term is the power-dependent non-linear matrix

$$\mathbf{M}_k = \frac{1}{\sqrt{1-\gamma}} \begin{pmatrix} 1-\frac{\gamma}{2} & -\frac{d_e\gamma}{4} \\ -\frac{\gamma}{d_e} & 1-\frac{\gamma}{2} \end{pmatrix}$$

EQUATION 3.24

where

$$\gamma = \left[1 + \frac{1}{4} \left(\frac{2\pi w_e^2}{\lambda d_e} - \frac{\lambda d_e}{2\pi w_0^2} \right)^2 \right]^{-1} \frac{P}{P_c}$$

EQUATION 3.25

Here w_e is the intracavity spot size at the centre of the crystal and w_o is the spot size at the beam waist calculated at zero intracavity power. P is the beam power and P_c is the critical power for self-focusing, given by

$$P_c = \frac{c\varepsilon_0\lambda^2}{2\pi n_2}$$

EQUATION 3.26

If $P = P_c$ then a beam with an initially flat wavefront will propagate indefinitely without change in spot size or radius of curvature (a phenomenon known as self-trapping).

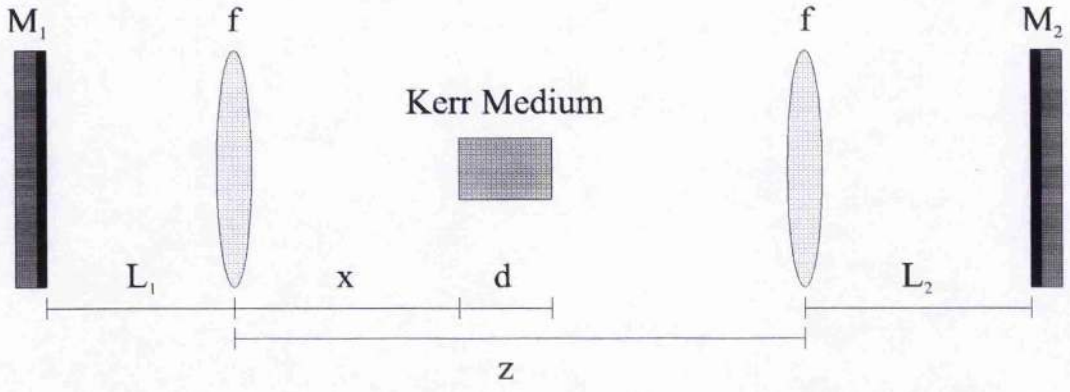

FIGURE 3.9 *A representation of a typical resonator used in self-modelocked lasers: M_1, M_2 - plane mirrors; f - lenses (or curved mirrors).*

A typical cavity used in a self-modelocked laser can be represented in the form shown in Figure 3.9. The curved folding-section mirrors found in a X- or Z-cavity are here represented by lenses with effective focal lengths f. All the matrices that are required to represent this cavity are conventional ABCD matrices, with the exception of $\mathbf{M_k}$, the nonlinear element at the centre of the Kerr medium.

The variation with intracavity power of the size of the laser spot at the cavity end mirror is calculated by using the conventional ABCD matrix method, but treating $\mathbf{M_k}$ as a linear matrix with a fixed value of γ. In this way the variation of the spot size at the cavity mirror can be calculated directly as a function of γ, as can the spot size at the centre of the crystal $w_c(\gamma)$. The location of the beam waist is determined by calculating the beam spot size and beam radius of curvature at one of the folding section mirrors and then calculating how far it is necessary to propagate the beam for the radius of curvature to reach infinity. The spot size at the beam waist $w_0(\gamma)$ can then be calculated at this point. This gives the spot sizes at the end mirror, the crystal centre and the beam waist all as functions of γ. Equation 3.25 gives the intracavity power P as a function of γ and so the relationship between the spot size at the cavity end mirror and the intracavity power is described parametrically by γ. The variation of end-mirror spot size with intracavity power in a typical self-modelocked laser cavity is given in Figure 3.10.

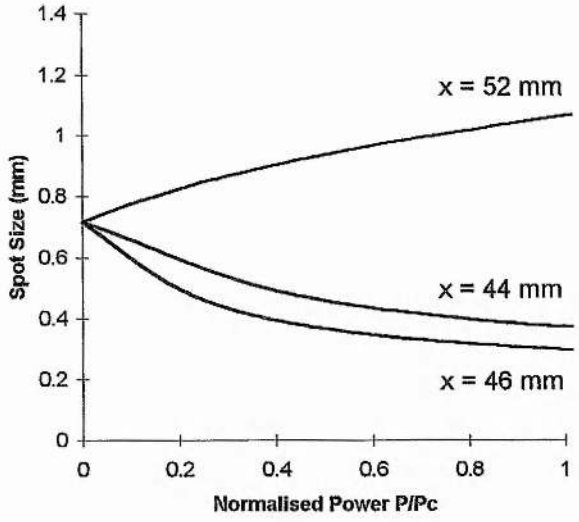

FIGURE 3.10 *The variation with intracavity power of the beam radius on mirror M_1 of Figure 3.9 for different positions of the Kerr medium. The resonator parameters are: L_1 = 700 mm, L_2 = 900 mm, f = 50 mm, z = 107.1 mm and d = 10 mm. The refractive index of the Kerr medium is 1.76. [After Figure 2 of Reference 47]*

Figure 3.10 shows the spot size variation for several values of x, the distance from the crystal face to the folding mirror nearest the end of the cavity at which the spot size is calculated (Figure 3.9). The spot size at the cavity end mirror increases with power for some values of x, whereas for other values it decreases. Clearly, if modelocking is to be achieved by placing a slit at the end of the cavity arm, it is important to work in a regime in which the spot size decreases with increasing intracavity power at this point. A high-peak-power pulse will then slip through the slit whereas low-average-power CW light will be attenuated. As the pulses must evolve from the CW field, an important parameter is the rate of change of the spot size at zero power. This is the small-signal relative spot size variation, defined as

$$\delta = \left(\frac{1}{w} \frac{dw}{dp} \right)_{p=0},$$

EQUATION 3.27

where $p = \frac{P}{P_c}$. If a laser is operating in a configuration for which $\delta < 0$, then noise spikes resulting from mode-beating will see less loss than the CW field at the slit, and will have the potential to build into pulses over several round trips.

The parameter δ can be calculated at any position in the laser cavity, but it reaches its maximum value at the cavity end mirror. An explicit expression may be derived for δ at this point[47]:

$$\delta = -\frac{1}{2}\frac{\alpha_1 + \alpha_2 S}{\alpha_1^2 + \alpha_2^2 + 2\alpha_1\alpha_2 S},$$

EQUATION 3.28

where

$$\alpha_1 = \frac{2B_1D_1}{d_c} - \frac{A_1C_1d_c}{2},$$

$$\alpha_2 = \frac{2B_2D_2}{d_c} - \frac{A_2C_2d_c}{2}$$

and

$$S = A_0D_0 + B_0C_0$$

EQUATION 3.29

A_1-D_1 and A_2-D_2 are defined in Figure 3.11; note that the Kerr element represents the lumped Kerr nonlinearity only, and the two matrices include the effects of propagation through the laser crystal itself. A_0-D_0 are the elements of the matrix describing single pass propagation from mirror M_1 to mirror M_2.

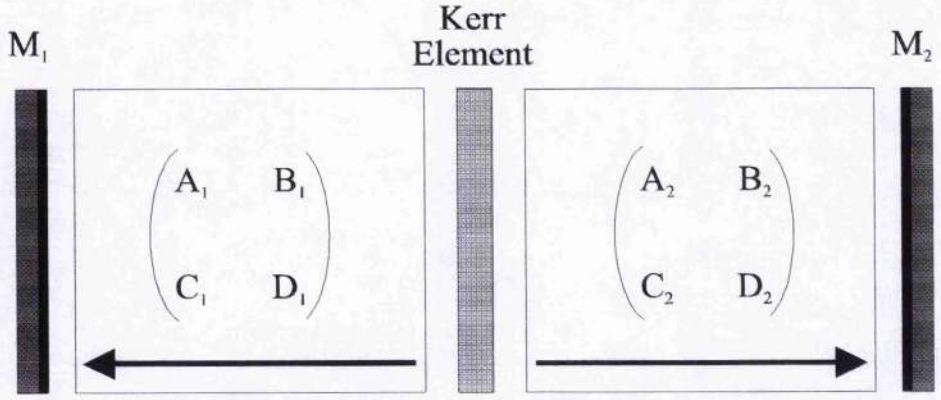

FIGURE 3.11 *Definition of the matrices used in Equation 3.29. The arrows represent the direction of single-pass propagation. Each matrix includes the effect of propagation through one half of the laser crystal, excluding the nonlinear effects which are lumped into the Kerr element.*

3.4.2 Stability in Four-mirror Resonators

The parameter S in Equation 3.28 is related to the laser resonator stability factor g_1g_2[52] by

$$S = 2g_1g_2 - 1$$

EQUATION 3.30

The resonator is stable if $-1 < S < 1$. The cavity stability parameter is an important factor because the extreme values of δ are[47]

$$\delta_{max,min} = \pm\frac{1}{2\sqrt{1-S^2}}.$$

EQUATION 3.31

Note that $\delta_{max,min} \to \pm\infty$ as $S \to \pm 1$; this means that for optimum modelocking the laser must be operating close to a stability limit, as has been reported several times in the literature[53-56]. The stability of X- and Z-cavity lasers depends largely on the geometry of their folding sections. In particular, as the distance between the folding mirrors is increased from a small value, the laser will pass through two stability regions (Figure 3.12). In the region corresponding to smaller mirror separations, the intracavity mode is approximately collimated in the short arm of the laser (L_1 in Figure 3.9) and focused onto the end mirror M_2 in the long arm (L_2). The quasi-collimated arm makes the resonator relatively sensitive to

misalignment of its end mirror, and so this stability region is known as the High Misalignment Sensitivity (HMS) region. In the region corresponding to larger mirror separations, the intracavity mode is approximately focused onto the end-mirrors in both arms. The laser is relatively insensitive to misalignment of its end mirror, and so this stability region is known as the Low Misalignment Sensitivity (LMS) region.

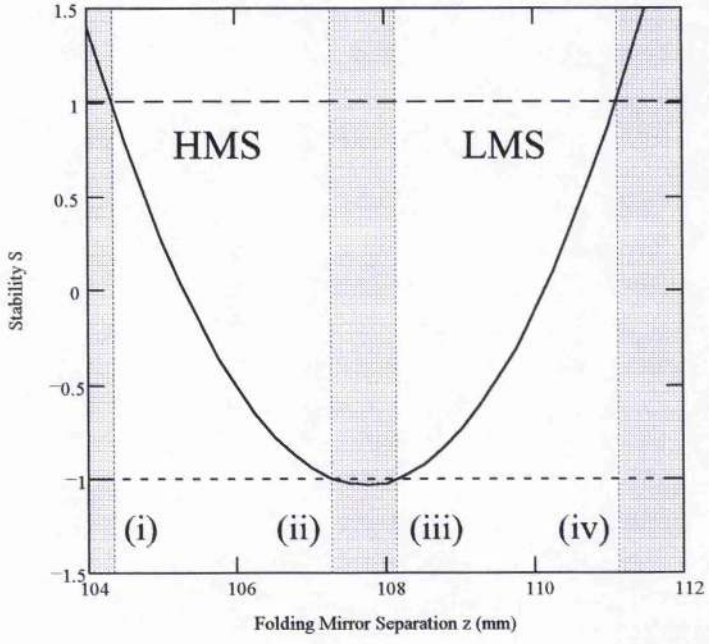

FIGURE 3.12 *Stability as a function of folding mirror separation, for the resonator parameters L_1 = 700 mm, L_2 = 900 mm, f = 50 mm, and d = 10 mm (as defined in Figure 3.9). The laser is stable in the two unshaded regions. In the high misalignment sensitivity (HMS) region the folding mirrors are arranged in an nearly-confocal arrangement; in the low misalignment sensitivity (LMS) region the end mirrors lie in nearly-conjugated planes. Limit (i) corresponds to $C_0 = 0$; (ii) corresponds to $A_0 = 0$; (iii) $D_0 = 0$; and (iv) $B_0 = 0$.*

A detailed analysis of the stability of four-mirror cavities based on the geometric optics of plane wave and spherical wave propagation is given in Appendix B. This analysis leads to analytical expressions for the folding mirror separations corresponding to the four stability limits shown in Figure 3.12. These expressions are summarised in Table 3.1.

Stability Limit	Folding Mirror (Optical) Separation
(i) Planar-Confocal	$2f$
(ii) Weak-Objective	$\frac{(2L_2 - f)f}{L_2 - f}$
(iii) Strong-Objective	$\frac{(2L_1 - f)f}{L_1 - f}$
(iv) Conjugate-Plane	$\frac{(2L_2L_1 - L_2f - L_1f)f}{(L_1 - f)(L_2 - f)}$

TABLE 3.1 *Analytical expressions for the folding mirror separations that bound the two stability regions shown in Figure 3.12. The parameters are f, the focal length of the folding mirrors and L_1 and L_2, the lengths of the short and long cavity arms, respectively. Note that the mirror separations calculated from these formulae are optical distances: to find the equivalent physical distances one must add* $d\left(1-\frac{1}{n}\right)$ *for an AR-coated crystal, or* $d\left(1-\frac{1}{n^3}\right)$ *for a Brewster-angled crystal, to the calculated separations, where d is the length of the laser crystal and n is its refractive index.*

One particularly important stability regime occurs when the lengths of the two cavity arms are equal. In this case, stability limits (ii) and (iii), the weak- and strong-objective limits, coincide. For unequal arm lengths, the intracavity beam is not well behaved at either stability limit because it degenerates into a plane wave in one or other cavity arm, as explained in Appendix B. When the arms are equal, however, the cavity is equivalent to a confocal two-mirror cavity and the beam remains well behaved even though the stability parameter $S \rightarrow -1$. This is important because $\delta_{min} \rightarrow -\infty$ as $S \rightarrow -1$; consequently, enormous changes in spot size can be induced at the cavity end-mirror for only small fluctuations in power. A

symmetric cavity is therefore far more easily modelocked than an asymmetric cavity, in which the S = -1 stability limits cannot be approached because of the intracavity beam degeneration.

3.4.3 Varying The Crystal Position

As well as the stability S, the other significant parameter in determining the magnitude of δ is the position of the laser crystal within the folding section. This variable is characterised in the Cerullo model by the parameter x in Figure 3.9. The Cerullo model predicts that the parameter δ is not well-defined exactly at the centre of the broad confocal stability region of a symmetric resonator, but if the mirror separation z is slightly increased or decreased then the variation of δ with x can be plotted.

Figure 3.13 shows δ(x) with z increased just into the LMS stability region (if z is decreased into the HMS region then Figure 3.13 is reversed). The magnitude of the extreme values of δ becomes arbitrarily large as the confocal limit is approached, and I have predicted that these extrema occur *when the intracavity waist is focused onto an end face of the laser crystal.*

This is easy to understand if we consider the effects of the distributed Kerr lens induced by the intracavity power within the laser crystal. A single lens at the focus of the intracavity beam will have no effect on the spot size at the cavity end mirror. The effect of lenses to either side of the focus increases with the offset of the lens and has opposite signs for lenses on opposite sides of the centre.

If the laser crystal is placed at the exact centre of the folding section then the induced distributed lens will be symmetric about the crystal centre. The net effect will be zero, as equally-sized parts of the beam on either side produce equal and opposite effects. As the crystal is translated towards one side of the focus, the beam will no longer be symmetric within the crystal: a net effect will be produced from the side of the crystal containing the strong Kerr lens associated with the focus. This effect will reach its maximum when the crystal is translated so that the focus sits on the end face of the crystal because, at this point, the change in spot size at the cavity end mirror will have the same sign for all parts of the distributed

lens. If the crystal is translated further then the focus will no longer be within the crystal and so the induced lensing, and hence its effect, will become progressively weaker. The sign of the net induced effect reverses depending upon the direction in which the crystal is translated.

The shape of Figure 3.13 bears a striking resemblance to the shape of a thick-sample Z-scan[57,58], which can be used to determine the nonlinear absorption or nonlinear refraction of a material. In a Z-scan experiment, a Gaussian beam is tightly focused into a nonlinear medium and its transmittance through an aperture is measured as a function of the position of the medium relative to the beam focus. The procedure to which Figure 3.13 relates is indeed closely related to a Z-scan, being a kind of 'intracavity Z-scan', as pointed out by Sheik-Bahae[59].

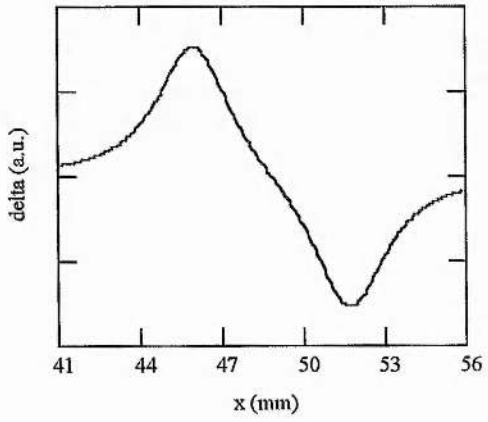

FIGURE 3.13 *The variation of δ with crystal position x, calculated for a mirror separation z close to the confocal limit of the LMS stability region. The magnitude of δ at its extreme values becomes arbitrarily large as the confocal limit is approached.*

3.4.4 The Cerullo diagram

The small-signal spot-size variation δ is, then, most sensitive to variations in the cavity parameters x and z, and a plot of $\delta(x, z)$ summarises the conclusions that can be drawn from the above discussion. Such a plot is shown in Figure 3.14 for an asymmetric and a symmetric cavity.

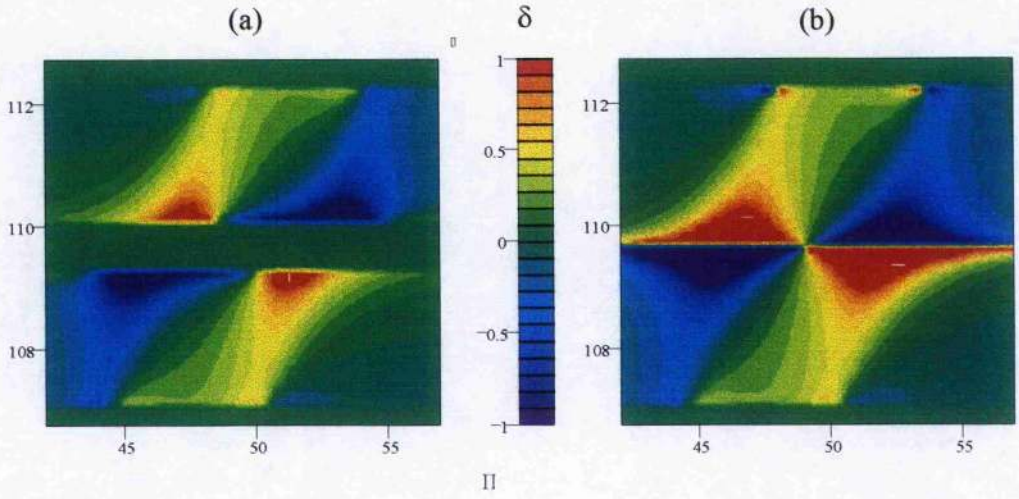

FIGURE 3.14 *Cerullo diagrams showing the variation of the small-signal relative spot-size variation δ with folding-mirror separation z (vertical axis) and Ti:sapphire crystal position x (horizontal axis) for (a) an asymmetric cavity, with L_1 = 700 mm and L_2 = 900 mm; and (b) a symmetric cavity, with $L = L_1 = L_2$ = 800 mm. (N. B. Peaks and troughs have been clipped at $\delta = \pm 1$ for ease of plotting.)*

These plots show that, as predicted, the optimum cavity configuration for hard-aperture modelocking is with the laser operating on the weak- or strong-objective stability limits and with the intracavity mode focused on the face of the crystal. Figure 3.14 shows that in a symmetric laser the two limits join together to give a single, broad region of stability. As this stability limit can be approached arbitrarily closely, $\delta \rightarrow -\infty$ becomes a practical possibility if the intracavity beam is focused on one end surface of the crystal in the tangential plane.

If $\delta \rightarrow -\infty$ then any fluctuations in the field inside the laser cavity will experience significantly less loss at an intracavity slit than that experienced by a CW field and so the laser will modelock preferentially. Most importantly, this modelocking is, theoretically, self-starting: an arbitrarily small fluctuation sees an arbitrarily small loss at the intracavity slit, and so an arbitrarily small fluctuation is distinguished from the CW background field. Prior to the work of Cerullo *et al.*, it was generally assumed that pulse initiation from a CW background would be very difficult to achieve through Kerr lensing, because Kerr lensing depends nonlinearly on field intensity. Techniques such as regenerative-initiation are often employed to introduce into the cavity pulses of sufficiently high peak intensity for Kerr lensing to provide significant loss discrimination at the slit. Cerullo *et al.* show that this is

not essential, however, and have successfully demonstrated true self-starting self-modelocking in a symmetric four-mirror Ti:sapphire laser[49]. It should be recognised, though, that self-starting is very difficult to achieve at low intracavity power levels.

The plots of Figure 3.14 show two regions in which δ is negative; the upper-right region is in the LMS stability region and the lower-left is in the HMS region. It has been found experimentally that self-modelocked laser operation is superior in the upper-right region. In this region, the laser crystal is positioned so that the intracavity focus is near to the face of the crystal nearest to the intracavity slit, as predicted.

3.4.5 Astigmatism

Magni and co-workers have recently developed another model that takes into account the effects of astigmatism on hard-aperture self-modelocking[50]. The beam in the gain crystal of a typical four-mirror resonator is, in general, elliptical and the effects of Kerr lensing in the tangential and sagittal planes are coupled. Magni et al modelled this situation by slicing the nonlinear gain crystal into a sequence of infinitesimally thin segments. They derived an expression for the effect that each of these segments has on the small-signal spot-size variation δ at the cavity end-mirror and then deduced the overall effect of the gain medium by integrating over all the segments. The key assumption here was that the effects of each segment was independent of the effects of the all of the other segments in the crystal. The results of this model were compared with the results of the Cerullo model and the principal conclusion was that δ is enhanced in the tangential plane but greatly diminished in the sagittal plane. This means that only a vertical slit (cutting the horizontal plane) can be used at the cavity end mirror to produce self-modelocking, as had already been observed experimentally[48]. The Magni model will be discussed in more detail in Chapter 5.

3.4.6 Key Conclusions from the Cerullo Model

I have shown that the optimum cavity configuration for hard-aperture self-modelocking is a cavity with arms of equal length, with a folding-mirror separation

on the merged weak-/strong-objective limit, and with the intracavity focus on the face of the crystal nearest to the intracavity slit. The optimum folding-mirror separation is given by (from Table 3.1 and Appendix B)

$$z_{opt} = \frac{(2L-f)f}{L-f} + d\left(1-\frac{1}{n}\right) = \frac{4LR-R^2}{4L-2R} + d\left(1-\frac{1}{n}\right),$$

EQUATION 3.32

where L is the length of the cavity arms and R is the radius of curvature of the folding-section mirrors. It has also been shown, for the first time to my knowledge, that the optimum distance from the folding mirror nearest to the modelocking slit to the surface of the crystal can be written as

$$x_{opt} = \frac{z_{opt} - d\left(1-\frac{1}{n}\right)}{2}.$$

EQUATION 3.33

This is simply the distance to the optical centre of the folding section. Equation 3.32 and Equation 3.33 are correct for an AR-coated crystal; for Brewster-angled crystals n should be replaced by n^3 in both equations.

3.5 Dispersion

Once a pulse is established in a cavity by the self-amplitude modulation of self-modelocking, it will reach a steady-state duration that is determined by the effects of self-phase modulation and the net dispersion seen by the pulse over a round trip[60].

3.5.1 The Soliton Model of Ultrashort Pulse Lasers

Self amplitude modulation can reduce the duration of pulses in a laser to around 1 ps before the effects of positive group-velocity dispersion in the laser crystal become limiting. If sufficient negative GVD is introduced to the cavity, via a prism pair or similar arrangement, pulses in the sub-100 fs regime can be obtained. The relationship between the exact pulse duration that can be expected from a laser and the intracavity power required to produce that duration is a vitally important

consideration in the development of a low-threshold ultrashort-pulse system. To study this relationship, we can take advantage of the fact that pulses see both self-phase modulation and negative GVD during each cavity round trip and experience soliton-like shaping.

The key assumption of the soliton model of pulse propagation in ultrashort-pulse lasers is that the dispersive and non-linear effects seen by a pulse can be treated as being simultaneous and continuous throughout many cavity round-trips. In reality, of course, the pulse sees dispersion only between the prism pair and in intracavity elements such as the gain crystal, and nonlinear effects are seen only in the gain crystal. Despite this, however, the soliton approximation is valid provided that the cavity round-trip length is very much less than both the dispersion length L_D and the nonlinear length L_{NL}. The dispersive and nonlinear lengths must be equal in order for a pulse to propagate as a N=1 soliton, and are given by[61]

$$L_D = \frac{T_0^2}{|\beta_2|} \quad \text{and} \quad L_{NL} = \frac{1}{P_0\gamma} = \frac{2T_0}{E\gamma} \quad (\text{sech}^2 \text{ pulse}),$$

EQUATION 3.34

where P_0 is the peak power of the pulse, E is its energy and T_0 is its 1/e half-width, related to its full-width at half maximum (FWHM) width by

$$T_{FWHM} = 2\ln\left(1+\sqrt{2}\right)T_0 \quad (\text{sech}^2 \text{ pulse}).$$

EQUATION 3.35

The parameter γ in Equation 3.34 is the nonlinearity coefficient (units $m^{-1}\ W^{-1}$) and is related to the nonlinear refractive index n_2 and the effective beam radius w_{eff} by

$$\gamma = \frac{2n_2}{\lambda w_{eff}^2}.$$

EQUATION 3.36

The parameter β_2 in Equation 3.34 is the GVD parameter (units $fs^2\ mm^{-1}$), which we assume to be equal to the net round-trip dispersion divided by the pulse's round-trip path length within dispersive cavity elements, which will typically be of the order of tens of centimetres.

For a typical FWHM pulse duration of 100 fs and 500 fs^2 GVD over a 40 cm round-trip dispersive path length, the dispersion length is L_D = 2.6 m, or about seven times the path length within dispersive elements. Similarly, for P_0 = 100 kW, $n_2 = 1.5 \times 10^{-20}$ m^2 W^{-1} and w_{eff} = 95 μm, we find that again L_{NL} = 2.6 m. Both the dispersive length and the nonlinear length therefore correspond to many round-trips for these parameter values. For very short pulses and/or very low β_2 and/or very tight focusing, however, these characteristic lengths reduce to the order of a cavity length and the discrete nature of the nonlinear and dispersive components of the pulses round-trip then begins to have a destabilising effect on the intracavity pulse[60]. This limits pulse-shortening due to SAM, and makes the use of the soliton model unreliable.

3.5.2 Dispersion, Pulse Duration and Intracavity Power

If the dispersive and nonlinear lengths are sufficiently long, the problem of pulse propagation in a laser cavity reduces to a problem similar to that of pulse propagation in an optical fibre. In the steady state, this is described by the nonlinear Schrödinger equation[62-65], the solutions of which are known as solitons. The order of a soliton is characterised by the parameter N, where

$$N^2 = \frac{L_D}{L_{NL}} = \frac{P_0 T_0^2 \gamma}{|\beta_2|}.$$

EQUATION 3.37

and the fundamental (N=1) solutions u(z,t) have the form[66]

$$u(z,t) = \operatorname{sech}\left(\frac{t}{T_0}\right) \exp\left(\frac{iz}{2L_D}\right).$$

EQUATION 3.38

A pulse of this shape will propagate for arbitrarily long distances in a fibre without changing its shape, provided that N = 1; i.e.,[66]

$$\frac{P_0 T_0^2 \gamma}{|\beta_2|} = 1$$

EQUATION 3.39

A pulse in a *laser cavity* must maintain its shape (or at least have a periodically varying shape) over many cavity round-trips, in a similar way. A pulse in a self-modelocked laser will generally have a profile described by Equation 3.38. For a given γ and β, Equation 3.39 gives us the relationship between pulse duration and pulse peak power (and hence intracavity power).

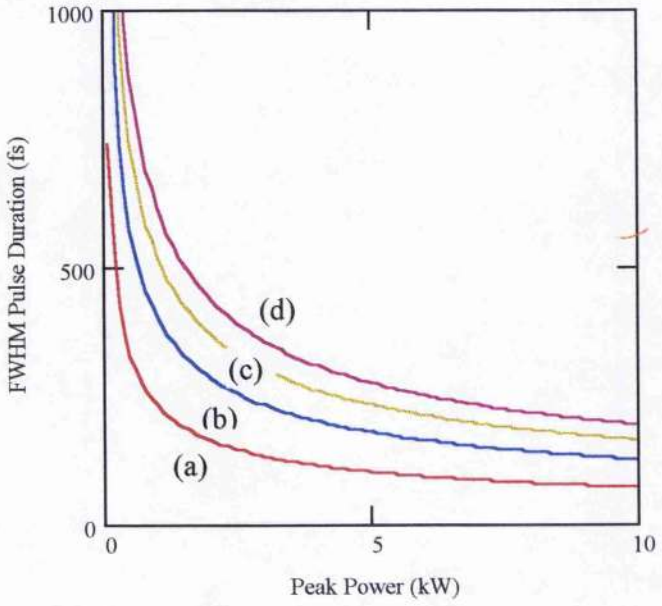

FIGURE 3.15 *Calculated variation of FWHM soliton duration with peak power P_T in an optical fibre. Curves are shown for fixed GVD parameter values (a) $\beta_2 = 0.25$ $fs^2\ mm^{-1}$, (b) $\beta_2 = 0.75\ fs^2\ mm^{-1}$, (c) $\beta_2 = 1.25\ fs^2\ mm^{-1}$ and (d) $\beta_2 = 1.75\ fs^2\ mm^{-1}$. The nonlinear fibre parameter $\gamma = 1.4 \times 10^{-5}\ W^{-1}\ m^{-1}$ throughout.*

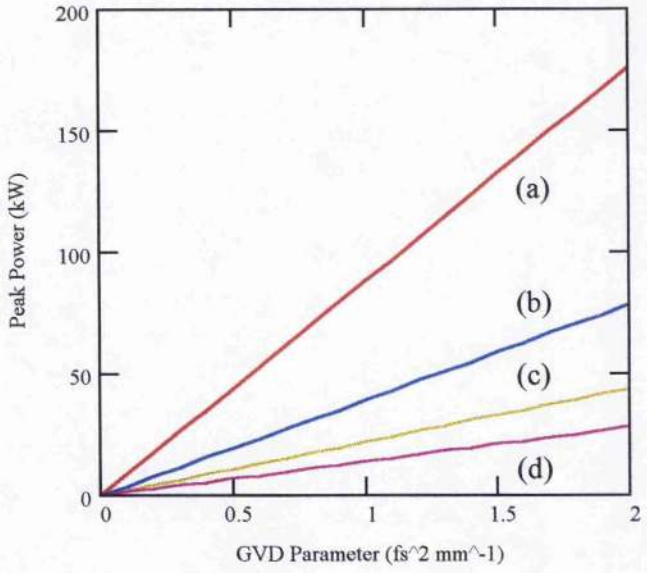

FIGURE 3.16 *Calculated peak power required to support a soliton in a fibre as a function of the dispersion parameter β_2, for solitons of fixed FWHM duration (a) 50 fs, (b) 75 fs, (c) 100 fs and (d) 125 fs. This figure can be obtained from Figure 3.15 by reading off the values of intersections of those curves with a horizontal line drawn at particular pulse durations.*

P_T is the peak power required to support pulses of duration T_0, and this is the relationship we require for our consideration of the factors affecting low-threshold operation. Firstly, this expression and Equation 3.36 together tell us that reducing the effective beam waist w_{eff} will increase γ and hence decrease P_T; in other words, the intracavity beam should be focused as tightly as possible for low-threshold operation. Similarly, reducing $|\beta_2|$ reduces the threshold power required to support pulses of a particular duration. Figure 3.15 shows the variation of T_0 with P_T for fixed values of the GVD parameter β_2. Figure 3.16 shows the variation of P_T with β_2 for fixed pulse durations.

These figures imply that arbitrarily short pulses can be obtained for arbitrarily high intracavity powers, and that $P_T \rightarrow 0$ as $|\beta_2| \rightarrow 0$. The predictions of Equation 3.39 are not physically realistic in these extreme situations, however.

In the extreme of high intracavity power and short pulse durations, the nonlinear length L_{NL} and the dispersive length L_D become comparable to the length of the laser cavity. Consequently, the discrete nature of the dispersive and nonlinear

cavity elements becomes significant and the pulse begins to break up (in the laboratory, this is evidenced by multiple-pulsing effects).

In the extreme of low net round-trip GVD, the effects of third-order dispersion (TOD) become significant. It is well known that, in the sub-100 fs regime, the pulse duration obtainable from a laser for a given intracavity power is limited by TOD. The converse is also true: the threshold power required to sustain pulses of durations in the sub-100 fs regime is, in general, limited by residual TOD.

Third-order dispersion can limit pulse duration because it limits the broadening of the pulse spectrum[60]. The presence of third-order dispersion in a cavity means that group-velocity dispersion is a linear function of wavelength. This means that there will be some wavelength at which the sign of the GVD changes from negative to positive. Pulse shortening is limited near to this wavelength because, as the negative GVD in a cavity is reduced, the wings of the pulse spectrum broaden towards this crossover wavelength. At first, the centre wavelength of the pulse spectrum will be shifted away from the positive GVD region, leading to an asymmetric spectrum. Eventually, however, the spectrum will broaden across the crossover wavelength. A dispersive wave will then be formed that will act as a loss in the pulsed operation, and modelocking will drop out.

The residual third-order dispersion in a cavity has two origins: the laser crystal and the GVD-compensating prism pair which contributes both through material dispersion and through refractive dispersion between the intracavity prisms. Third-order dispersion is given by[67]

$$\frac{d^3\phi}{d\omega^3} = -\frac{\lambda^4}{4\pi^2 c^3}\left(3\frac{d^2P}{d\lambda^2} + \lambda\frac{d^3P}{d\lambda^3}\right),$$

EQUATION 3.40

where P is the optical path length seen by light of wavelength λ. In material dispersion, P is simply the physical path length times the material refractive index n; in refractive dispersion, $\frac{d^2P}{d\lambda^2}$ is given by Equation 2.2 and

$$\frac{d^3P}{d\lambda^3} \cong 4\frac{d^3n}{d\lambda^3}L_p \sin(\beta) - 24\frac{dn}{d\lambda}\frac{d^2n}{d\lambda^2}L_p \cos(\beta)$$

EQUATION 3.41

where, as for the second-order case, L_p is the prism separation, $\cos(\beta) \cong 1$ and $\sin(\beta) \cong 2$ mm.

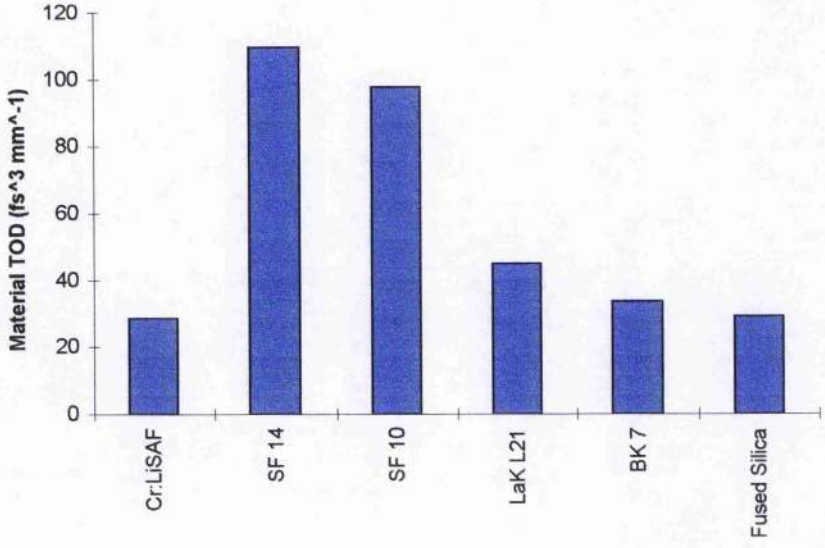

FIGURE 3.17 *Material third-order dispersion in various optical materials.*

The material TOD of various optical materials is shown in Figure 3.17. A comparison with Figure 2.9 shows that the magnitudes of TOD and GVD vary in a similar way between each material. Similarly, the relative position of each of the materials in a plot of refractive TOD versus prism separation (Figure 3.18) is the same as in the refractive GVD case Figure 2.10, and also ties in with the relative magnitudes of the material TOD.

The limiting effect of third-order dispersion on the reduction of P_T is dependent upon the magnitude of the net round-trip TOD, taking into account the effects of refractive dispersion between the intracavity prisms and material dispersion in the laser crystal, AO modulator and in any excess prism glass over and above the 2 mm per prism allowed for in Equation 3.41. The magnitude of the net TOD is calculated by calculating the prism separation needed for GVD compensation, and then summing the various contributions to TOD including the effects of the prism pair at this separation. The result is shown in Figure 3.19 for a cavity typical of that used in the low-threshold experimental work described in the next chapter.

The prism materials can still be broadly divided into the two groups visible in the preceding two figures; namely, the highly-dispersive SF glasses and the others. However, interestingly, the lowest net round trip TOD is achieved with LaK L21 prisms, which exhibit neither the lowest material nor the lowest refractive TOD. This is because, although prisms made of materials such as BK 7 and fused silica introduce less TOD than LaK L21 per millimetre of prism separation, they also introduce less GVD per millimetre of prism separation and must therefore be

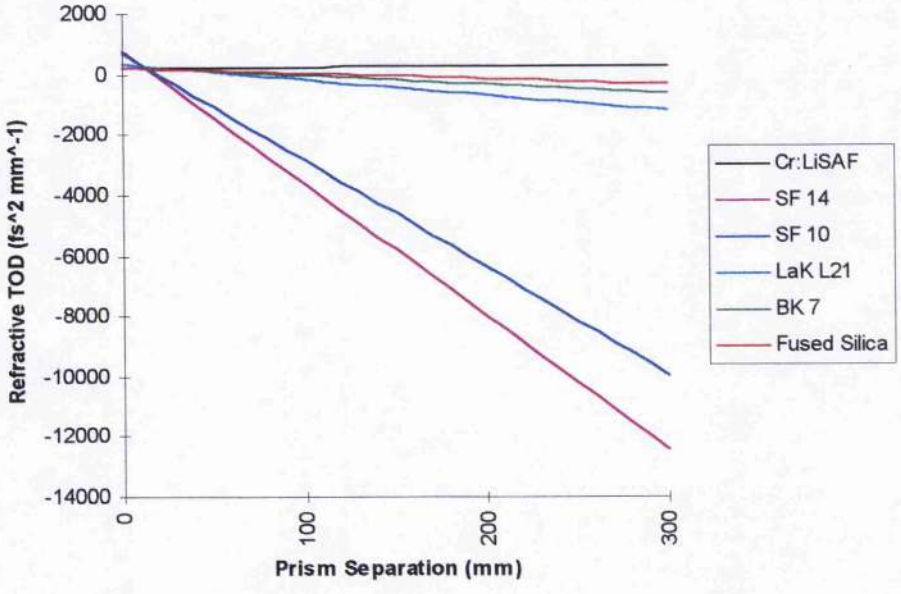

FIGURE 3.18 *Refractive TOD for prism pairs made of various optical materials. Note that the refractive TOD results from both propagation between the prism pair and propagation through 2 mm of material in each prism.*

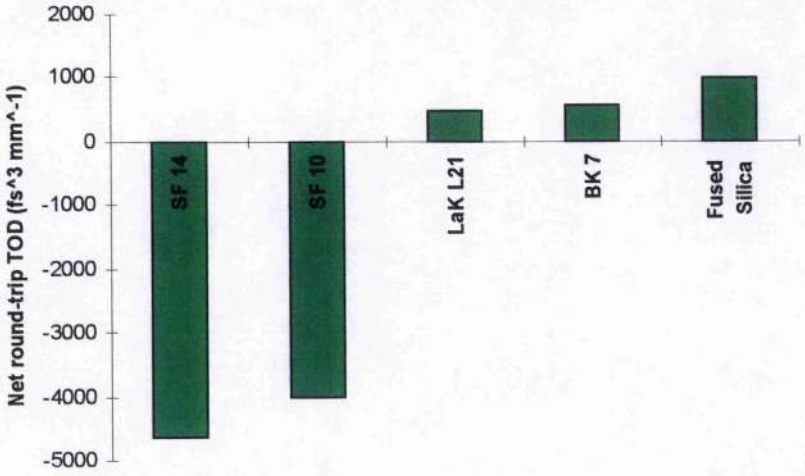

FIGURE 3.19 *The net round-trip TOD in a laser cavity consisting of a 24.1 mm Cr:LiSAF crystal, a 11.6 mm quartz (silica) modulator, 1 mm excess glass per prism and SPM equivalent to 100 fs^2 GVD.*

placed further apart in order to achieve second-order dispersion compensation. This increases the absolute magnitude of the TOD introduced. Of the materials considered and for the laser described in the next chapter, LaK L21 is the best compromise between the need for an intrinsically low-TOD material and the need to compensate for GVD with a prism separation small enough to avoid refractive TOD becoming the dominant source of higher-order dispersion.

Lemoff and Barty showed that complete GVD and TOD compensation with a prism pair is physically possible given the correct choice of prism material, prism separation and intraprism path length[68]; however, the required prism separations and/or path lengths are too large to be practical in our system. Chirped dielectric mirrors[69] or Gires-Tournois mirrors[70,71] could provide complete GVD and TOD dispersion compensation, but introduce additional losses that are undesirable in a low-threshold system.

3.6 Concluding Remarks

In this Chapter I have discussed the various factors that affect the pump power required to generate sub-100 fs pulses in a Cr:LiSAF laser. The motivation for this investigation was the prospect of developing a self-modelocked laser pumped by only a single, narrow-stripe semiconductor laser. Such a system would be significantly less costly than the self-modelocked laser systems currently commercially available.

Cr:LiSAF has a significantly higher $\sigma\tau$ product than Ti:sapphire and therefore an inherently lower CW oscillation threshold. I have derived an analytical expression that predicts the oscillation threshold in a laser in which both pump and cavity modes are focused Gaussian beams. Minimum threshold is obtained in such a system by focusing both beams as tightly as possible; it is important that both pump and cavity beam waists are approximately the same size because otherwise a poor overlap between the modes can result in an increased threshold. Both spots should be focused near to the pumped face of the crystal. Tight focusing of the intracavity beam also results in strong, localised nonlinear lensing, which makes the laser more suitable for self-modelocking, as evidenced by applying the model developed by Cerullo *et al.*

I have also derived another expression that relates the beam overlap efficiency to the brightness of the pump beam (for pump beams of the same output power). This analysis predicts that laser threshold increases significantly for pump beams that are far from diffraction-limited. Self-injection locking is a means of obtaining near-diffraction-limited beams of modest powers from broad-area semiconductor lasers. The behaviour of the self-injection locking technique was discussed in terms of the selection of an array supermode and as the result of interference between multiple outputs from an injected Gaussian beam which undergoes multiple reflections within the gain region of the diode.

The Cerullo model of self-modelocking offers a general prescription for the optimisation of a laser resonator for ultrashort-pulse generation. I have derived analytical expressions that give the exact folding mirror separation and crystal position needed for optimised operation, eliminating the need for the graphical method usually employed in the Cerullo model. Modelling predicts that optimum modelocking will be obtained when the intracavity beam is focused onto the end of the laser crystal in the tangential plane.

Once a pulse has been established in a laser cavity, intracavity dispersion is the principle limitation on the power needed to sustain pulses of a particular duration. If the net intracavity GVD is reduced, third-order dispersion becomes the limiting factor, and so careful choice of prism material becomes vital.

The low-threshold, all-solid-state Cr:LiSAF system described in Chapter 4 is based on the ideas outlined in this chapter. The laser is pumped by a self-injection-locked AlGaInP semiconductor laser that delivers a near-diffraction-limited beam. Use of an AR-coated crystal rather than a Brewster-angled crystal reduces the intracavity beam waist size in the crystal, and the pump and intracavity beams are also tightly focused in order to reduce the CW oscillation threshold still further. The tight cavity mode also increases the strength of the Kerr lens responsible for modelocking. The cavity mode is focused near to the end of the crystal for optimised modelocking. The laser employs LaK L21 prisms, which were calculated in Section 3.5.2 to give low third-order dispersion. The implementation of these key design points leads to the Cr:LiSAF laser producing 100-fs pulses for just 73 mW of pump power.

---

[1] See References 46 - 50

[2] A. J. Alfrey, IEEE J. Quantum Electron. **25**, 760 (1989)

[3] S. A. Payne, L. L. Chase, H. W. Newkirk, L. K. Smith and W. F. Krupke, IEEE J. Quantum Electron **24**, 2243 (1988)

[4] W. K. Koechner, in *Solid-State Laser Engineering* (4th Edn.), Springer-Verlag, Berlin (1996), p94

[5] E. Hecht, in *Optics* (2nd Edn.), Addison-Wesley, Reading, MA (1987), p402

[6] W. K. Koechner, in *Solid-State Laser Engineering* (4th Edn.), Springer-Verlag, Berlin (1996), p99

[7] M. Piché, Opt. Comm. **86**, 156 (1991)

[8] J. Van der Pol, Phil. Mag. **3**, 65 (1927)

[9] R. Adler, Proc. IRE **34**, 351 (1946)

[10] K. Otsuka and S. Tarucha, IEEE J. Quantum Electron. **17**, 681 (1981)

[11] K. Kobayashi, H. Nishimoto and R. Lang, Electron. Lett. **18**, 54 (1982)

[12] C. L. Tang and H. Statz, J. Appl. Phys. **38**, 323 (1967)

[13] R. H. Pantell, Proc. IEEE **53**, 474 (1965)

[14] A. E. Siegman in Lasers, University Science Books, California (1986), Chapter 29

[15] H. L. Stover and W. H. Steier, Appl. Phys. Lett. **8**, 91 (1966)

[16] C. J. Buczek, R. J. Freiberg and M. L. Skolnick, J. Appl. Phys **42**, 3133 (1971)

[17] J. -L. Lachambre, P. Lavigne, G. Otis and M. Noel, IEEE J. Quantum Electron. **12**, 756 (1976)

[18] C. J. Buczek and R. J. Freiberg, IEEE J. Quantum Electron. **8**, 641 (1972)

[19] L. E. Erickson and A. Szabo, Appl. Phys. Lett. **18**, 433 (1971)

[20] G. Magyar and H. J. Schneider-Muntau, Appl. Phys. Lett. **20**, 406 (1972)

[21] J. J. Turner, E. I. Moses and C. L. Tang, Appl. Phys. Lett. **27**, 441 (1975)

[22] I. J. Bigio and M. Slatkine, IEEE J. Quantum Electron. **19**, 1426 (1983)

[23] R. E. Teets, IEEE J. Quantum Electron. **20**, 326 (1984)

[24] J. -I. Nishizawa and K. Ishida, IEEE J. Quantum Electron. **11**, 515 (1975)

[25] R. Lang and K. Kobayashi, IEEE J. Quantum Electron. **12**, 520 (1977)

[26] S. Kobayashi and T. Kimura, Electron. Lett. **16**, 668 (1980)

[27] S. Kobayashi, J. Yamada, S. Machida and T. Kimura, Electron. Lett. **16**, 746 (1980)

[28] S. Kobayashi and T. Kimura, IEEE J. Quantum Electron. **17**, 681 (1981)

[29] R. Lang, IEEE J. Quantum Electron. **18**, 976 (1982)

[30] G. R. Hadley, IEEE J. Quantum Electron. **22**, 419 (1986)

[31] E. Kapon, J. Katz and A. Yariv, Opt. Lett. **4** , 125 (1984)

[32] L. Goldberg, H. F. Taylor, J. F. Weller and D. R. Scifres, Appl. Phys. Lett. **45**, 722 (1984)

[33] C. J. Chang-Hasnain, J. Berger, D. R. Scifres, W. Streifer, J. R. Whinnery and A. Dienes, Appl. Phys. Lett. **50**, 1465 (1987)

[34] J. E. Epler, N. Holonyak, R. D. Burnham, T. L. Paoli and W. Streifer, J. Appl. Phys. **57**, 1489 (1985)

[35] J. E. Epler, N. Holonyak, R. D. Burnham, T. L. Paoli, R. L. Thornton and M. M. Blourke, Appl. Phys. Lett. **47**, 7 (1985)

[36] J. Yaeli, W. Streifer, D. R. Scifres, P. S. Cross and R. L. Thornton, Appl. Phys. Lett. **47**, 89 (1985)

[37] L. Goldberg and J. F. Weller, Electron. Lett. **25**, 112 (1989)

[38] J. -M. Verdiell and R. Frey, IEEE J. Quantum Electron. **26**, 270 (1990)

[39] J. -M. Verdiell, R. Frey and J.-P. Huignard, IEEE J. Quantum Electron. **27**, 396 (1991)

[40] G. R. Hadley, J. P. Hohimer and A. Owyoung, Appl. Phys. Lett. **49**, 684 (1986)

[41] J. -M. Verdiell, H. Rajbenbach and J. -P. Huignard, Appl. Opt. **31**, 1992 (1992)

[42] G. L. Abbas, S. Yang, V. W. S. Chan and J. G. Fujimoto, Opt. Lett. **12**, 605 (1987)

[43] G. L. Abbas, S. Yang, V. W. S. Chan and J. G. Fujimoto, IEEE J. Quantum Electron. **24**, 609 (1988)

[44] Personal communication with David Burns, Institute of Photonics, University of Strathclyde, Wolfson Centre, 106 Rottenrow, Glasgow, G4 0NW, Scotland, UK.

[45] Model implemented by Ian Lindsey, University of St. Andrews.

[46] V. Magni, G. Cerullo and S. De Silvestri, Opt. Comm. **96**, 348 (1993)

[47] V. Magni, G. Cerullo and S. De Silvestri, Opt. Comm. **101**, 365 (1993)

[48] G. Cerullo, S. De Silvestri, V. Magni, and L. Pallaro, Opt. Lett. **19**, 807 (1994)

[49] G. Cerullo, S. De Silvestri, and V. Magni, Opt. Lett. **19**, 1040 (1994)

[50] V. Magni, G. Cerullo, S. De Silvestri, and A. Monguzzi, J. Opt. Soc. Am. B **12**, 476 (1995)

[51] A. E. Siegman in *Lasers*, University Science Books, California (1986), Chapters 15,20,21

[52] E. Siegman in *Lasers*, University Science Books, California (1986), p 746

[53] M. Piché, Opt. Comm. **86**, 156 (1991)

[54] T. Brabec, C. Spielmann, P. F. Curley and F. Krausz, Opt. Lett. **17**, 1292 (1992)

[55] H. A. Haus, J. G. Fujimoto and E. P. Ippen, IEEE J. Quantum Electron **28**, 2086 (1992)

[56] D. Georgiev, J. Herrmann and U. Stamm, Opt. Comm. **92**, 368 (1992)

[57] M. Sheik-Bahae, et al., Opt. Eng. **30**, 1228 (1991)

[58] P. B. Chapple, J. Staromlynska, R. G. McDuff, J. Opt. Soc. Am. B **11**, 975 (1994)

[59] M. Sheik-Bahae, P. Li-Kam-Wa, P. Buck, in *Technical Digest of Conference on Lasers and Electro-Optics* (Optical Society of America, Washington, D. C., 1994), Paper CWA1

[60] C. Spielmann, P. F. Curley, T. Brabec and F. Krausz, IEEE J. Quantum Electron. **30**, 1100 (1994)

[61] G. P. Agrawal, in *Nonlinear Fiber Optics* (Academic Press, London, 1995) p61

[62] V. E. Zakharov and A. B. Shabat, Sov. Phys. JETP **34**, 62 (1972)

[63] A. Hasegawa and F. Tappert, Appl. Phys. Lett. **23**, 142 (1973)

[64] J. Satsuma and N. Yajima, Prog. Theor. Phys. Suppl. **55**, 284 (1974)

[65] R. K. Dodd, J. C. Eilbeck, J. D. Gibbon and H. C. Morris, in *Solitons and Nonlinear Wave Equations* (Academic Press, New York, 1982)

[66] G. P. Agrawal, in *Nonlinear Fiber Optics* (Academic Press, London, 1995) p145

[67] R. L. Fork, O. E. Martinez and J. P. Gordon, Opt. Lett. **9**, 150 (1984)

[68] B. E. Lemoff and C. P. J. Barty, Opt. Lett. **18**, 57 (1993)

[69] R. Szipöcs, K. Ferencz, Ch. Spielmann and F. Krausz, Opt. Lett. **19**, 201 (1994)

[70] D. Kopf, G. Zhang, R. Fluck, M. Moser and U. Keller, Opt. Lett. **21**, 486 (1996)

[71] I. T. Sorokina, E. Sorokin, E. Wintner, A. Cassanho, H. P. Jenssen and R. Szipöcs, in *1996 Conference on Lasers and Electro-Optics Europe* (IEEE Catalog 96TH8161) Paper CWA1

4. A Low-threshold, All-solid-state, Self-modelocked Cr:LiSAF Laser

4.1 Introduction

In Chapter 3, I considered the factors that affect the pump-power requirement of a self-modelocked laser. With these factors in mind, I will now describe a laser arrangement which was designed to have a very low self-modelocking threshold. The system was based around a Cr:LiSAF crystal pumped by a self-injection-locked semiconductor laser. In the first section of this chapter, the characteristics of the semiconductor laser will be reported, both in its free-running and its self-injection-locked configurations. The Cr:LiSAF 'W-cavity' will then be described, with particular attention being paid to the advantages for low-threshold self-modelocking of an AR-coated plane/plane crystal compared with a crystal having Brewster-angled faces.

The CW performance of the laser will be considered briefly, followed by a detailed examination of the mechanisms that caused an unexpected modulation in the tuning curve of the laser. The self-modelocked performance of the laser will then be described, in particular its low power requirements. A short discussion of 'self-starting' regenerative modelocking will be followed by a description of the excellent noise properties of the laser. I will then describe a streak camera evaluation, made possible by the low levels of noise in the laser output, that demonstrated sub-picosecond resolution, a resolution previously only accessible with cavity-locked lasers and shuttered cameras. The chapter concludes with a consideration of further improvements that could be made to the system to bring the threshold for self-modelocking closer to the power available from relatively cheap, narrow-stripe semiconductor lasers.

4.2 The Self-injection-locked Semiconductor Pump laser

4.2.1 The Semiconductor Laser

(a) (b)

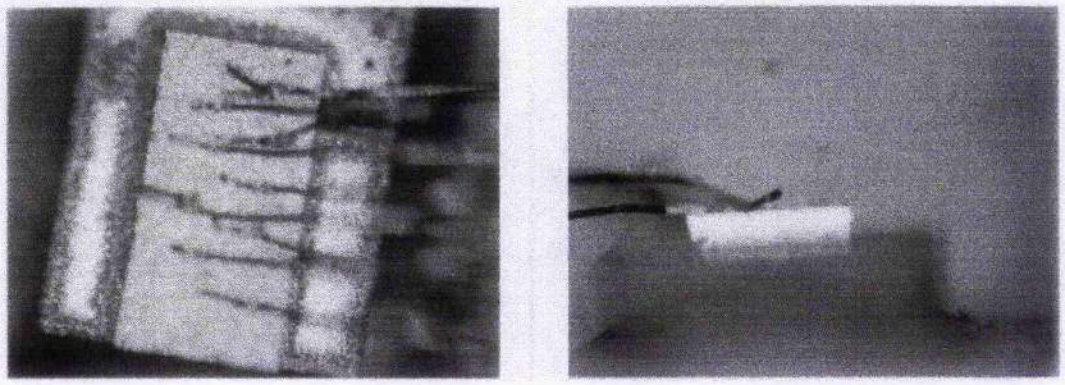

FIGURE 4.1 *The APT-Uniphase HB-067-500-130-C semiconductor laser: (a) top surface (b) back facet. The 25 μm bond wires give an indication of scale.*

The semiconductor laser used as a pump source throughout these experiments was a multiple-quantum well AlGaInP device supplied by APT-Uniphase (Device # HB-067-500-130-C, Figure 4.1). The diode was grown on a diamond substrate and its facets were anti-reflection coated for 670 nm. At room temperature (25 °C), it produced over 500 mW of CW light for a drive current of 1.1 A, and

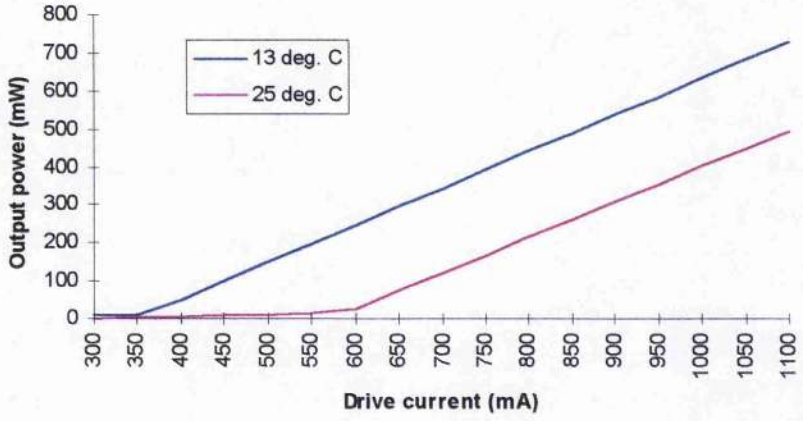

FIGURE 4.2 *The I-P characteristics of the APT-Uniphase semiconductor laser HB-067-500-130-C at 13 °C and 25 °C.*

cooling to 13 °C resulted in output powers of ~750 mW. The current-power (I-P) characteristics of the laser are shown in Figure 4.2.

The semiconductor laser was driven by a Spectra Diode Labs SDL-800 Laser Diode Driver. The laser was mounted, with its active stripe horizontal, on a 35 mm x 45 mm x 5 mm brass plate that was attached to the side of a brass cylinder of height 140 mm and diameter 50 mm. Between the plate and the block was a RS 618-724 Peltier-effect cooler. The aluminium block was cooled by an RS 403-140 heat sink, with a thermal resistance of 2.5 °C/W. In everyday, self-injection-locked use, the laser was driven by 600 mA - 650 mA and the brass plate was maintained at ~ 13 °C by driving the thermo-electric cooler with ~ 400 mA of current.

The laser output spectrum was centred on 668.8 nm ± 0.2 nm at 650 mA drive

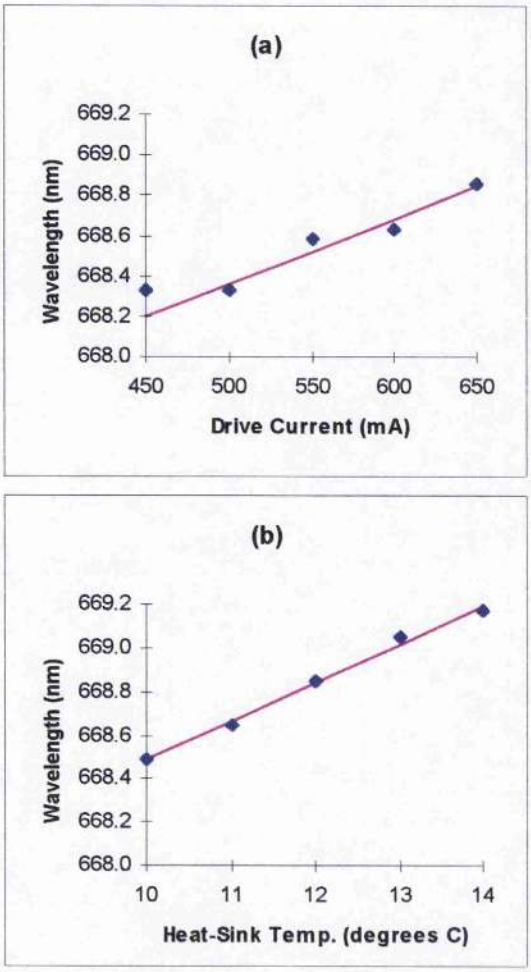

FIGURE 4.3 *Tuning characteristics of the AlGaInP diode laser output with (a) drive current and (b) temperature.*

current for a heat sink temperature of 12 °C. The tuning characteristics are shown in Figure 4.3. The laser wavelength rose by 0.3 nm for every 100 mA increase in drive current and by 0.1 nm for every degree Celsius rise in heat-sink temperature. The drive current to the thermo-electric cooler was adjusted manually to compensate for fluctuations in the temperature of the laboratory. In the latter stages of the experimental work, a Marlow Industries Inc. Temperature Controller Model SE5020 was used to provide feedback control.

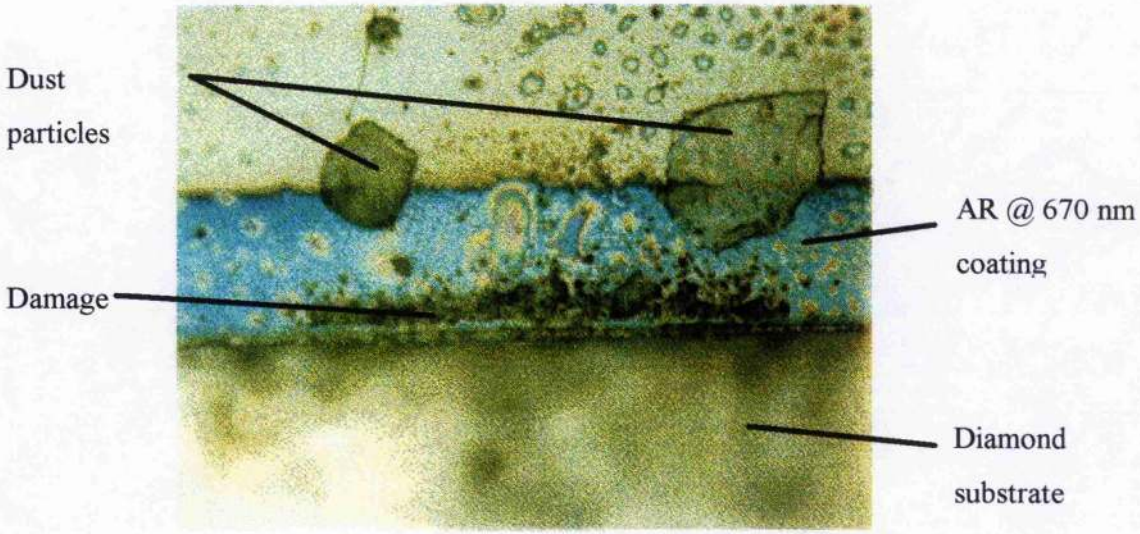

FIGURE 4.4 *Damage to the front facet of the APT-Uniphase laser diode, probably caused by dust.*

The laser diode was not hermetically sealed and was exposed to the laboratory environment. After 12 months of daily operation, the diode was suddenly catastrophically damaged by dust on its facet (Figure 4.4). It was replaced by an identical APT-Uniphase laser. This device was oriented with its active stripe vertical and, as the pumped Cr:LiSAF crystal was mounted with its c-axis horizontal, this meant that the output of the semiconductor laser was polarised in the wrong plane for optimum absorption. In practice, the doping level in the crystal was sufficiently high for this inefficiency to have only a negligible effect on the performance of the Cr:LiSAF laser.

4.2.2 The Self-injection-locking Scheme

Figure 4.5 shows a schematic of the effect of the self-injection-locking optics (minus the feedback mirror) on the semiconductor laser's output beams in the planes parallel and perpendicular to the diode's active stripe. In the plane parallel to the stripe, the beam diverges at an angle of 8.7° from an emitting aperture 100 μm wide. In this plane the feedback mirror is required to phase-lock the lateral modes of the diode laser beam (Section 3.3). To achieve this, the mirror must be positioned so that it reflects back, at the correct angle, spontaneous emission from just outside the "top hat" of the diode's laser emission. The mirror can only be accurately positioned within the emission profile if the diode output is spatially extended when it reaches the feedback mirror. This is achieved by ensuring that the microscope objective and the cylindrical lens (f = 60 mm) together act to focus the beam some distance in front of the feedback mirror, so that by the time the beam reaches the feedback mirror it will have diverged considerably.

In the plane perpendicular to the stripe, the laser beam is diffraction-limited and

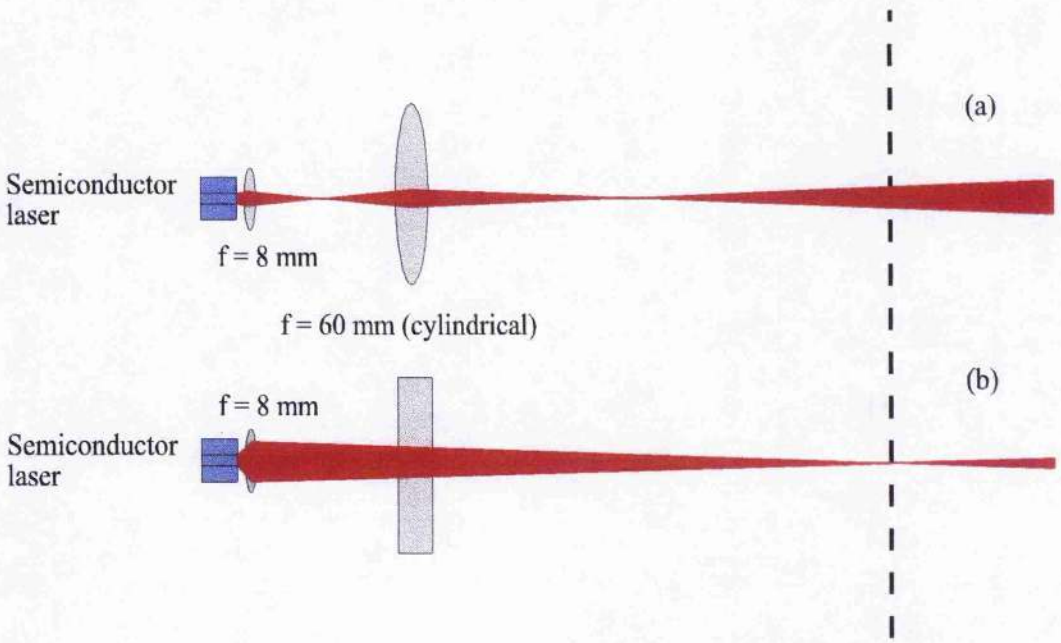

FIGURE 4.5 *A schematic of the effect of the self-injection-locking optics (minus the feedback mirror) on the semiconductor laser output beams, in the planes (a) parallel and (b) perpendicular to the diode active stripe. The dashed line indicates the plane in which the feedback mirror would sit.*

diverges with an angle of 37°. In this plane, the beam does not change when the diode is injection locked. The feedback mirror should therefore reflect the output beam back along the exact path that it takes from the diode. Consequently, the mirror should be placed at a beam focal waist and the microscope objective lens (f = 8 mm) is therefore positioned so that it focuses the output beam onto the middle of the feedback mirror in this plane.

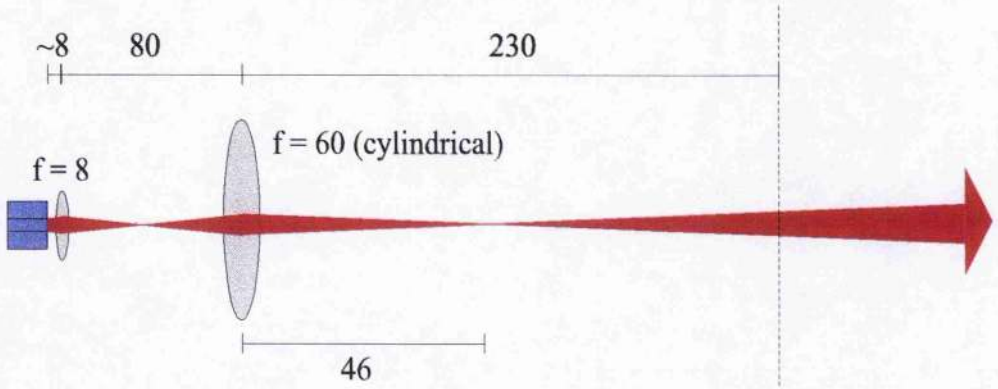

FIGURE 4.6 *Typical dimensions of the self-injection-locked laser system (all lengths are in mm).*

Typical dimensions of the optics used for self-injection-locking feedback are shown in Figure 4.6. It should be noted that the feedback scheme is, in principle, scaleable to any size and so, potentially, the bulk optics could be replaced with micro-optics and the whole self-injection-locked device reduced to match-box size.

In the self-injection-locked laser (Figure 4.7), the light field is concentrated in two lobes that appear on either side of the path formerly taken by the unlocked 'top hat' mode. The cylindrical lens in the self-injection-locked system acts to collimate the light contained in these lobes.

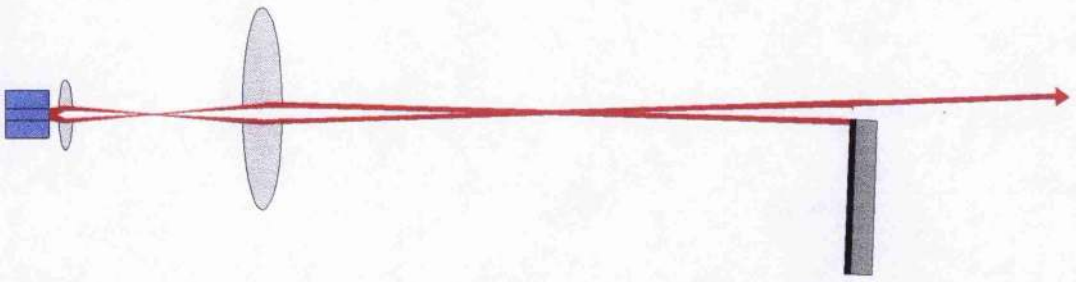

FIGURE 4.7 *Schematic of the beams in the self-injection-locked laser. The two beams sit at the edge of the unlocked beam profile. The output beam is collimated.*

Figure 4.8 shows the far-field beam profiles of the locked and the unlocked laser, together with the corresponding spectra. Self-injection locking reduced the full width at half maximum (FWHM) beam divergence in the far field from 10 ± 1 ° to 1.0 ± 0.1° and the FWHM oscillating spectral bandwidth from 0.5 ± 0.2 nm to 0.3 ± 0.2 nm.

The threshold current for self-injection-locked operation was around 335 mA (c.f. the CW threshold of 350 mA). Near the diode threshold, injection-locked operation was easily obtained. The diode output was monitored visually on a piece of card, and the change from unlocked to locked operation was clearly visible, particularly for currents below the CW threshold. As the current was increased the

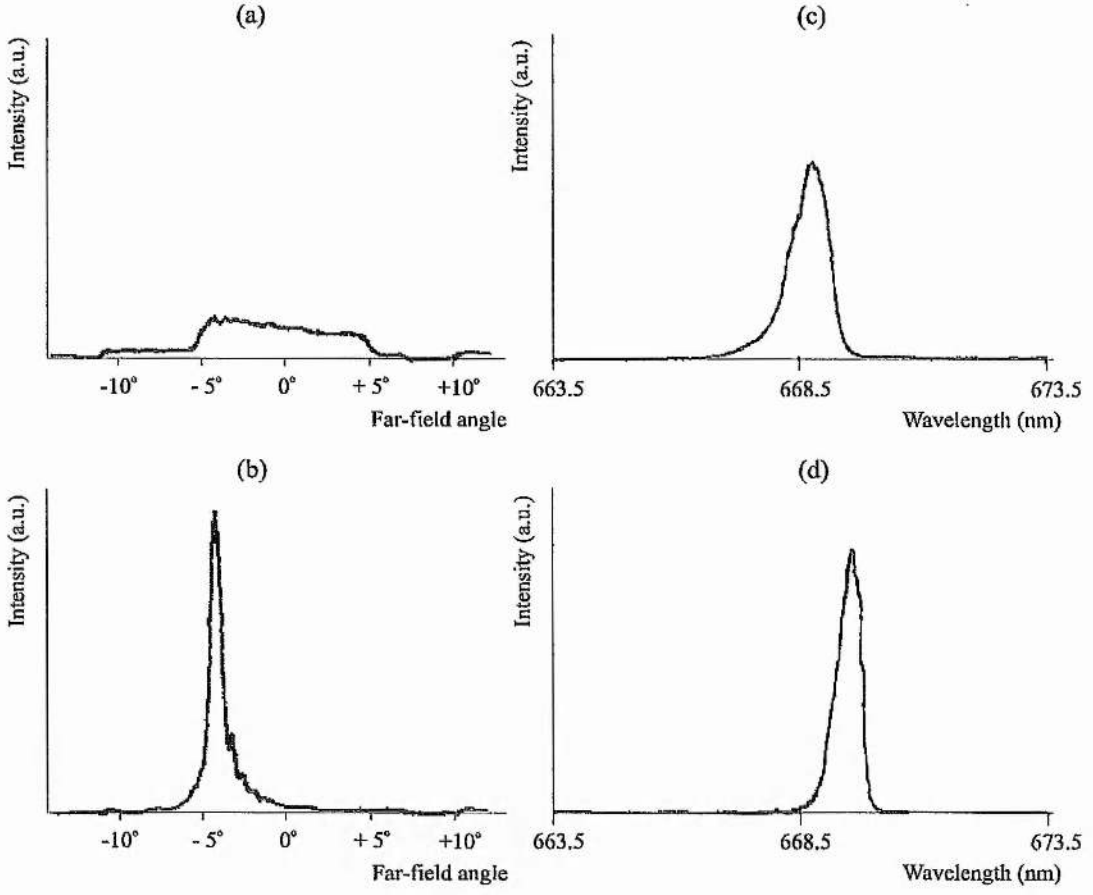

FIGURE 4.8 *Output from the semiconductor laser under unlocked and locked conditions at 657 mA drive current (169 mW output power): (a) far-field beam profile of the unlocked laser with the locking optics in place (minus the feed-back mirror), FWHM 10 ± 1 °; (b) far-field beam profile of the self-injection-locked laser, FWHM 1.0 ± 0.1 °; (c) spectrum of the unlocked laser, FWHM 0.5 ± 0.2 nm; (d) spectrum of the self-injection-locked laser, FWHM 0.3 ± 0.2 nm.*

diode re-tuned slightly, as described above, and this slight increase in wavelength made re-optimisation of the injection locking necessary after every few tens of milliamps current increase. Although far-field beam profiles of the quality of those shown in Figure 4.8 could be obtained at currents of up to 700 mA (300 mW output) by careful optimisation of the injection-locking set-up, it became increasingly difficult to obtain and maintain a diffraction-limited output as the diode drive current was increased. Figure 4.9 shows the change in the output mode with increasing current (a few minutes was spent optimising the system between each reading). At low drive currents, the diffraction-limited lobe was readily maintained, with over eighty-five percent of the beam energy inside a Gaussian profile. At a drive current of about 550 mA a second peak began to appear. It became increasingly difficult to suppress this peak, and the diode output departed increasingly from Gaussian beam characteristics. Then at 650 mA drive current the whole injection-locked beam shifted to another single lobe at a larger angle in the far-field. This lobe contained over seventy percent of the beam energy, but it was approximately 1.7 times wider than the diffraction-limited lobe obtained at lower currents. Although this mode was not diffraction-limited, it was, nevertheless, much closer to the diffraction-limit than the mode of the unlocked laser.

The self-injection-locked system needed re-optimisation on a regular basis, but only at intervals of perhaps a week or so. The Cr:LiSAF laser appeared reasonably tolerant of the quality of the self-injection-locked diode beam: a higher output power could be obtained from a slightly less than diffraction-limited but higher-power pump beam than from a diffraction-limited but lower power beam. The operational diode drive current of 650 mA was chosen as a trade-off between the need to maintain a reliable near-diffraction-limited mode and the need to pump the Cr:LiSAF laser with as much power as possible.

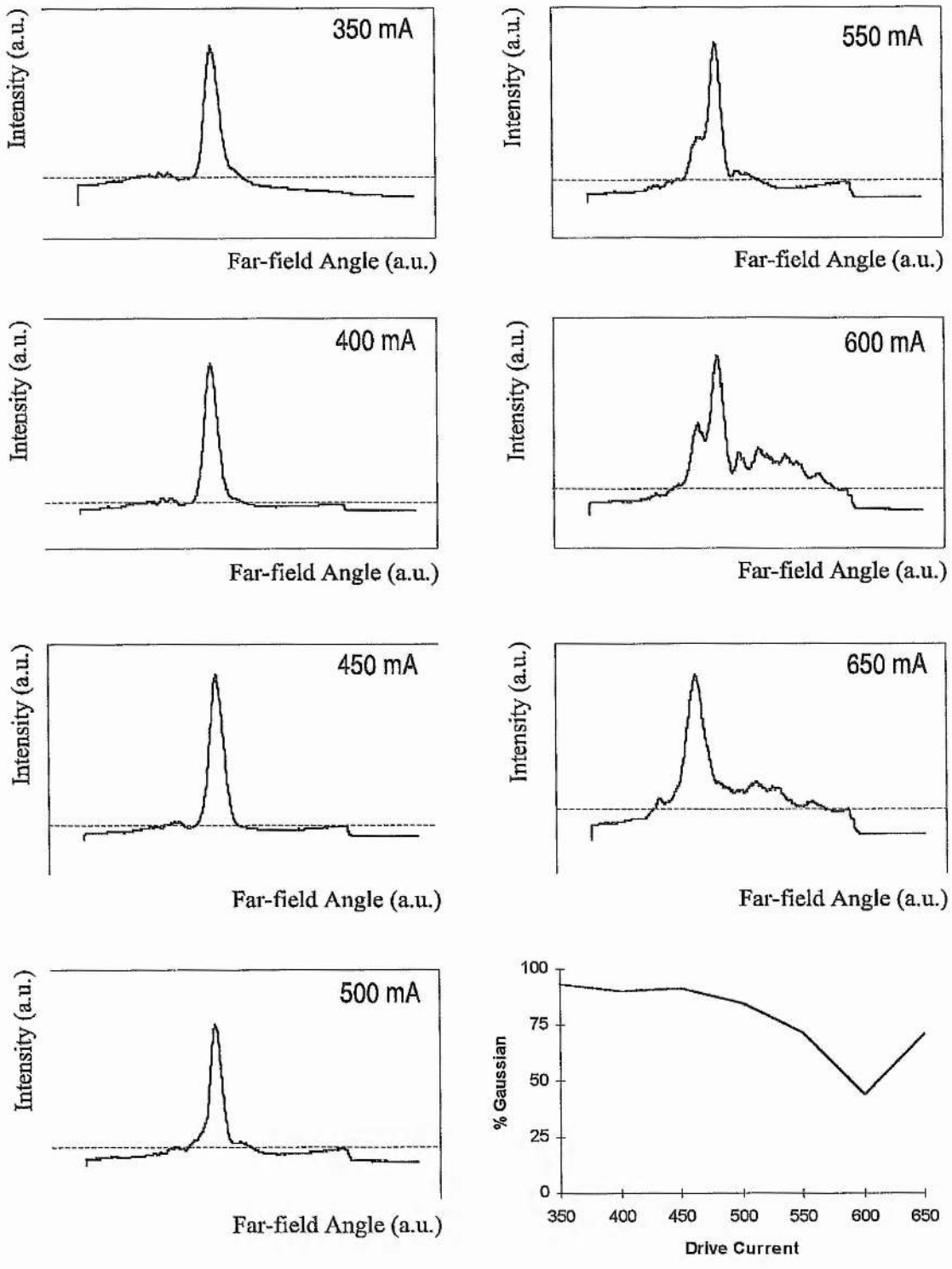

FIGURE 4.9. *Injection-locking vs. drive current. The boxed figures show the deterioration of the locked mode with increasing current. The dashed lines indicate the zero line used to exclude from calculations background signals that result from stray light. The line graph shows the percentage of each of these modes that can be fitted inside a Gaussian profile. The spike in the I = 650 mA figure is approximately 1.7 times wider than the spikes in the other figures.*

4.3 The Cr:LiSAF Laser

4.3.1 The W-cavity

The laser cavity used throughout the low-threshold Cr:LiSAF experiments is shown in Figure 4.10. The gain crystal was a 3 % Cr^{3+} doped LiSAF crystal grown by Lightning Optical Corporation, cut as a 12 mm x 8 mm x 5 mm cuboid. One end of the crystal was coated for high reflectivity at 840 nm and high transmissivity (anti-reflection - AR) at 670 nm; the other end was AR-coated at 840 nm. The cavity mirrors were Laseroptik 2.5 mm diameter BK7 mirrors, coated for high transmissivity at 670 nm and high reflectivity at 840 nm. The transmission loss of the mirrors was measured to be 0.08 % at the laser wavelength. The cavity end-mirrors were planar, and the rear surface of each substrate was cut with a 1° wedge in order to eliminate etalon reflections. The mirrors in the cavity folding section were initially 100 mm radius of curvature (ROC) plano-convex mirrors; these were later replaced with 75 mm ROC mirrors.

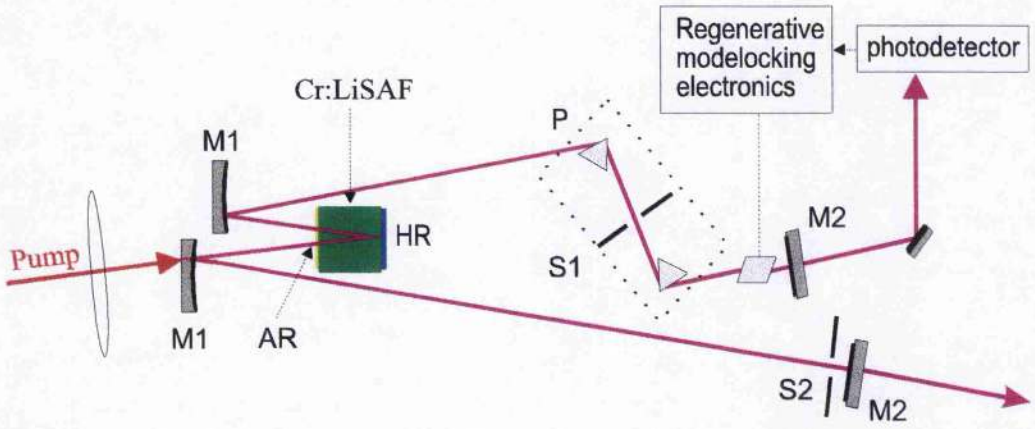

FIGURE 4.10 *The W-cavity: M1 focusing mirrors; M2 plane end mirrors; P dispersion compensation prisms; S1 tuning slit; S2 hard-aperture modelocking slit; also shown is the regenerative-initiation scheme.*

The Cr:LiSAF laser was built approximately 2 m away from the pump laser. A 60 mm cylindrical lens was placed 75 mm beyond the self-injection-locked laser feedback mirror and collimated the pump light in the plane perpendicular to its active stripe. Collimation external to the self-injection-locked laser was necessary

in the unlocked plane because the injection-locking process required that the beam in this plane was focused onto the feedback mirror, as described above.

Light from the pump laser was relayed to the Cr:LiSAF crystal by means of two mirrors, coated for high reflectivity at 666 nm. These mirrors could be used to steer and walk the pump beam to ensure that an optimum overlap with the Cr:LiSAF laser mode was achieved. The pump light was focused into the crystal by means of a 75 mm plano-convex lens. This lens was replaced with a 50 mm plano-convex lens when the cavity folding mirrors were changed to 75 mm ROC mirrors.

The pump light was focused into the crystal through one of the cavity folding mirrors: this acted as a plano-concave (defocusing) lens of focal length

$$f_{mirror} = \left[(n-1)\left(\frac{1}{\infty} - \frac{1}{R}\right) \right]^{-1}$$

EQUATION 4.1

where n = 1.51, the refractive index of the mirror substrate. For R = 100 mm, Equation 4.1 gives f_{mirror} = -196 mm, and for R = 75 mm it gives f_{mirror} = -147 mm. Allowing for this defocusing effect, the effective focal length of the pump optics is given by

$$f_{eff} = \left(\frac{1}{f_{lens}} + \frac{1}{f_{mirror}} - \frac{d}{f_{lens} f_{mirror}} \right)^{-1}$$

EQUATION 4.2

Equation 4.2 gives f_{eff} = 94 mm with the 75 mm lens and 100 mm ROC mirrors, and f_{eff} = 65 mm with the 50 mm lens and the 75 mm ROC mirrors (for the measured lens-mirror separations of d = 35 mm and d = 16.5 mm, respectively).

In the modelocked laser, second-order dispersion compensation was achieved with an intracavity Brewster-cut prism pair. Initially, SF14 prisms were used, but these were later replaced with LaK L21 prisms. LaK L21 prisms introduce less third-order dispersion into the cavity than prisms made from SF14 (Section 3.5.2). Tuning was achieved by means of an intracavity slit placed between the prisms. A second slit was placed in the arm of the cavity nearest to the curved mirror through which pump light was focused; this acted as a hard-aperture modelocking slit, in

according with the Magni, Cerullo and de Silvestri prescription discussed in the previous chapter (Section 3.4). Regenerative-initiation of the modelocking process was achieved by monitoring the light leaking through one cavity end mirror with a fast photodetector and then feeding the processed RF signal back to the intracavity acousto-optic modulator in the manner described in Chapter 2. The AO modulator was a Brimrose model FQM442, based on a 12 mm long Brewster-angled block of quartz.

The Cr:LiSAF laser cavity arms were of equal length (i.e., the cavity was symmetric). They were 810 mm with the 100 mm ROC. mirrors and 820 mm long with the 75 mm ROC. mirrors. The dimensions of the folding section are shown in Figure 4.11.

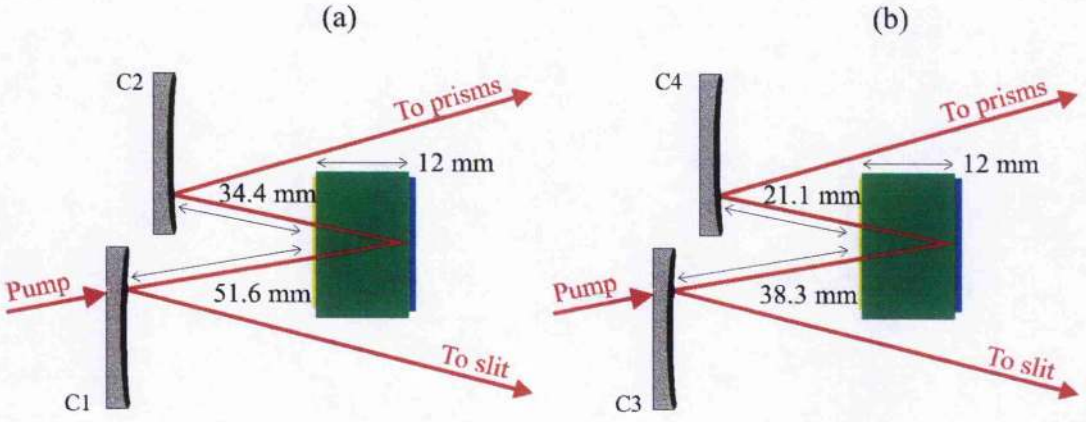

FIGURE 4.11 *The dimensions of the cavity folding section, with (a) 100 mm ROC mirrors (C1 & C2), and (b) 75 mm ROC mirrors (C3 & C4).*

4.3.1.1 W-cavity Pumping Options

The W-cavity shown in Figure 4.10 is optically similar to the conventional Z-cavity used in the green-pumped Cr:LiSAF experiments described in Chapter 2. It is essentially a Z-cavity folded about the HR coating on the rear surface of the crystal, as can be seen from Figure 4.12(a). The original motivation for choosing this cavity design was that it would allow the use of a very short focal length lens to tightly focus a pump beam through the crystal's HR coating. This would lead to a very small pump spot size in the crystal and would permit the use of an high-power, poor-quality pump beam. Such intimate coupling is possible in a three-mirror V-cavity, such as that of Figure 4.12(b), but the W-cavity offers a novel

means to combine intimate coupling with a Cerullo-style four-mirror cavity configuration.

A V-cavity can be unfolded to form a symmetric four-mirror X-cavity, as shown in Figure 4.12(a). As will be explained in Chapter 5, hard-aperture Cerullo-style modelocking is not possible in a three-mirror laser in which one of the mirrors is an HR-coating on the crystal itself. This results from the reduced number of degrees of freedom of adjustment available in a three-mirror laser compared with a four-mirror laser. In a four-mirror laser, the length of the two cavity arms, the separation of the folding mirrors and the position of the crystal in the folding section can all be varied independently. In a three-mirror laser, only the length of the single arm and the position of the crystal are independent variables.

Optimum hard-aperture modelocking demands a symmetric cavity in so far as both

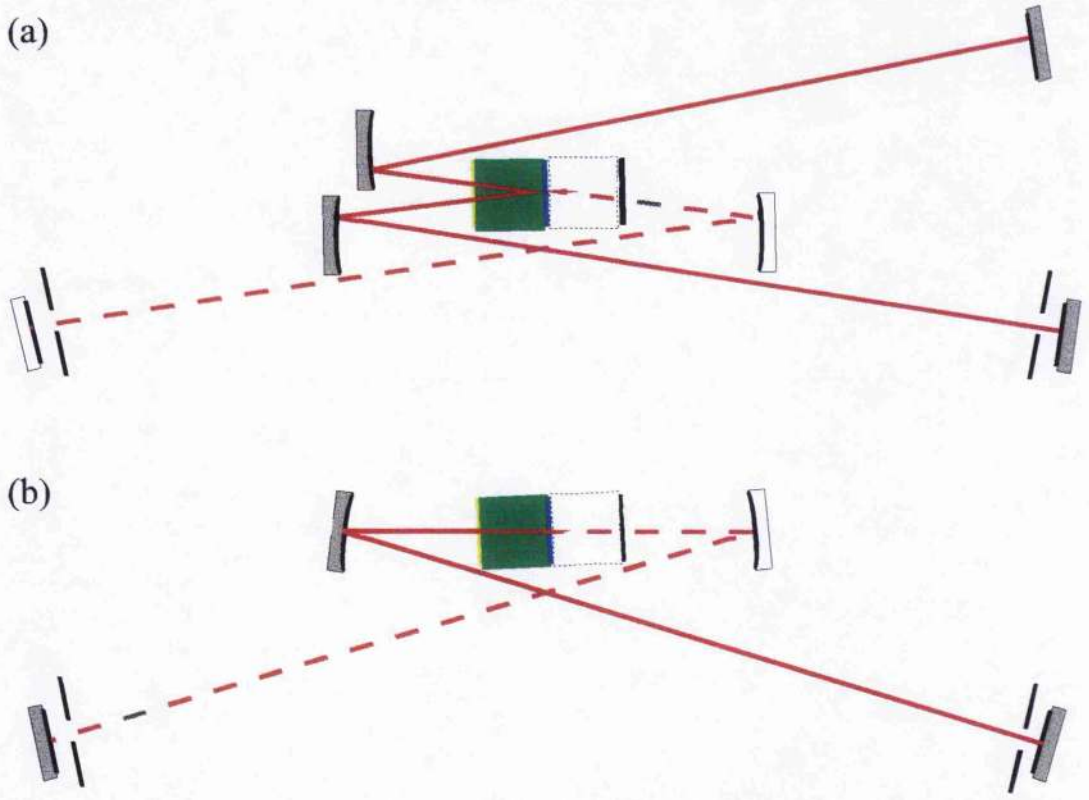

FIGURE 4.12 *(a) A four-mirror W-cavity based around a crystal coated HR on one side. This cavity can be seen to be identical to a symmetric conventional z-cavity if it is folded out at the HR coating.*

(b) A three-mirror V-cavity based around a crystal coated HR on one side. This cavity can be seen to be identical to a completely-symmetric conventional X-cavity if it is folded out at the HR coating.

of the cavity arms should be of the same length, but a Cerullo analysis predicts that a large negative $\delta = \frac{1}{w}\frac{dw}{dp}\Big|_{p=0}$ (the small signal relative change in spot size at the end of a cavity arm) is not possible for an *exactly* symmetric cavity. δ reaches a maximum when the intracavity focus is on the face of the crystal, and positioning the crystal at the centre of the folding section results in a very low δ.

Another problem is that the V-cavity is equivalent to a four-mirror X-cavity with slits at *both* end mirrors. The contraction of the intracavity mode at the end of one arm of an hard-aperture modelocked laser is accompanied by an expansion of the mode in the other arm. This again makes the V-cavity unsuitable for Cerullo-style modelocking. Modelocked V-cavity lasers have recently been demonstrated[1,2], but these devices rely on the soft-aperture modelocking technique; i.e. modelocking that improves pump-cavity mode overlap within the gain crystal.

The W-cavity offers the possibility of intimate pumping combined with the freedom of adjustment of a z-cavity that makes hard-aperture modelocking possible. The W-cavity is therefore a novel solution to the problems associated with trying to introduce a very tightly focused pump beam into a hard-aperture modelocked laser. Despite this, however, intimate pumping was not the pumping technique used in our Cr:LiSAF laser system. Preliminary experiments showed that, although it is a perfectly viable scheme for a CW laser, intimate coupling into a W-cavity is not the optimum method of pumping a modelocked laser. According to the Cerullo model, optimum modelocking occurs when the intracavity mode of the laser is focused at the end of the nonlinear crystal. In the case of a W-cavity, this means at the AR coating; i.e. at the opposite end of the crystal from the entrance point of an intimately-coupled pump beam. If the intracavity mode is focused at the AR coating then the most efficient pumping scheme is to pump the device through one of the cavity focusing mirrors. This approach is equivalent to the conventional pumping scheme used in a typical Z-cavity.

Although the potential for intimately pumping a W-cavity cannot be exploited efficiently in a single-diode-pumped modelocked laser, this cavity geometry still provides an additional route for the implementation of multiple-diode pumping

schemes. A self-modelocked cavity could be envisaged in which a single, self-injection-locked diode laser was used to provide just enough power to achieve self-modelocking. One or two high power, non-diffraction-limited diode lasers could then be intimately-coupled into the larger intracavity mode at the HR end of the crystal in order to greatly enhance the output power of the modelocked laser

4.3.1.2 AR-coatings versus Brewster Angles

The crystal used in the W-cavity was especially suitable for low-threshold self-modelocking because it had flat, AR-coated faces. (In fact, it has only one AR-coated face, but for the purposes of this discussion we can regard the crystal as being 24 mm long with two AR coated surfaces; i.e. we can 'unfold' the crystal at the HR coating). In conventional self-modelocked-laser cavities, the gain crystal is Brewster-angled in order to eliminate reflection losses to the intracavity beam as it passes through the crystal. However, the Brewster-angles reduce the effective length of the laser crystal by a factor of n^2 in the tangential plane; this means that the intracavity beam is focused at different points inside the crystal in the sagittal and tangential planes (Figure 4.13(a)). This has two consequences: firstly, the effective beam waist is distributed over several millimetres of crystal and, secondly, the effective area of the waist is more than doubled.

In the light of Section 3.2, we can see that the tight, localised spot that is obtained

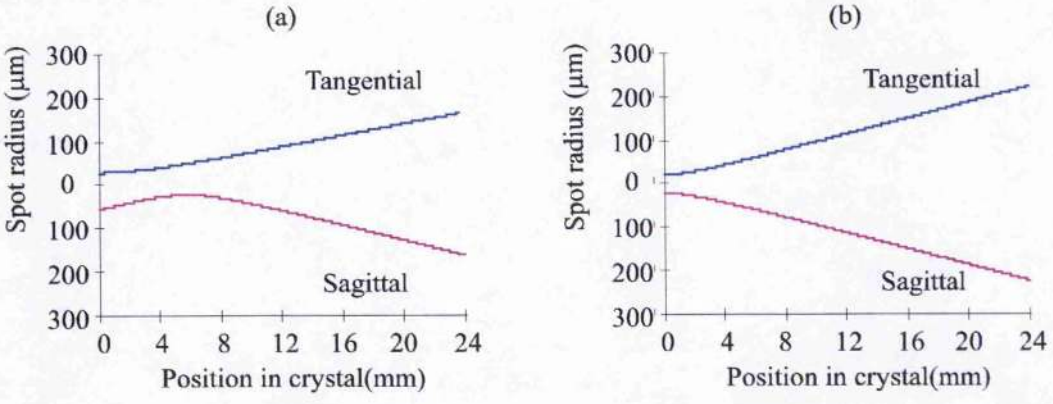

FIGURE 4.13 *Spot sizes inside a 24 mm Cr:LiSAF crystal whose end faces are (a) Brewster-angled and (b) plane and AR-coated. The cavities are optimised for Cerullo modelocking in each case. Calculating the effective focal areas* $\pi r_{tan} r_{sag}$ *gives an average focal waist radius (area) of 32 μm (3280 μm²) for the Brewster-angled rod and 21 μm (1390 μm²) for the plane AR-coated rod.*

in the AR-coated crystal is advantageous for low-threshold operation because a tight spot gives a low CW threshold. It also produces a stronger Kerr lens and so reduces the self-modelocked threshold. The highly localised nature of the spot is also advantageous for both CW and modelocked operation. Most of the available pump light is absorbed in the first few millimetres of the Cr:LiSAF crystal, and so positioning the intracavity beam waist as closely as possible to the crystal end face maximises the efficiency of the pump-cavity mode overlap. In addition to this, a Cerullo analysis of the modelocked laser predicts that optimum modelocking is again obtained by focusing at the end face of the crystal. The intracavity spot can be positioned precisely in the AR-coated crystal but this is more difficult to achieve in a Brewster-angled crystal because the effective beam waist is distributed over several mm.

Although an AR-coated crystal is superior to a Brewster-angled crystal in a low-threshold laser, the performance enhancements resulting from a tightly-focused and highly-localised intracavity waist are cancelled out at higher pump powers by the

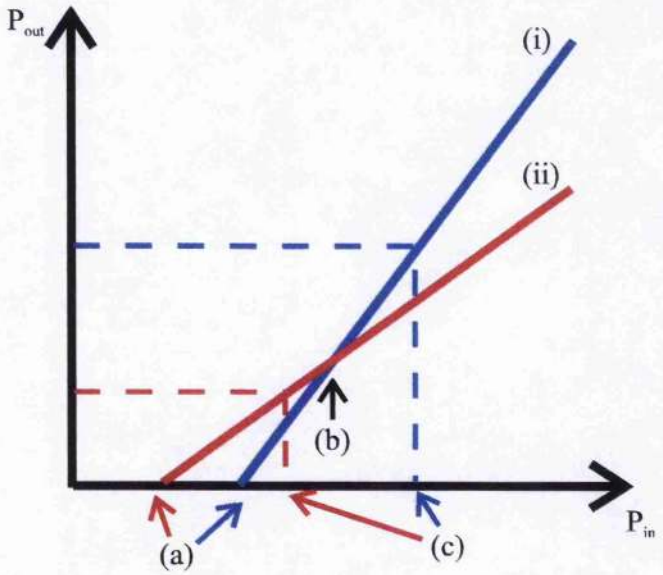

FIGURE 4.14 *P_{in}-P_{out} curves for a laser based around (i) a Brewster-angled crystal and (ii) an AR-coated crystal. The AR-coated crystal gives a lower CW threshold (a), but also a lower slope because of losses introduced by the AR coatings. The AR-coated crystal gives a superior performance to the Brewster-angled crystal at powers below the crossover point (b). The AR-coated crystal is to be preferred for femtosecond systems in which the available pump power is limited, as long as the femtosecond laser modelocking threshold (c) is lower than the crossover point.*

losses introduced by the AR-coating itself. This problem is illustrated in Figure 4.14, which shows a schematic of the output power versus pump power curve that would be expected from lasers utilising AR-coated and Brewster-angled crystal. Brewster angles (which are virtually loss-free) will always permit higher output powers than AR coatings at some pump power well above threshold. AR-coated rods are clearly not suitable for use in lasers pumped by powers greater than this "cross-over" value. However, an AR-coated crystal will be superior in a system operating near threshold, for example in a system in which pump powers are limited, such as a laser pumped by a narrow-stripe semiconductor laser.

4.3.1.3. Output Astigmatism

In a conventional four-mirror laser system utilising a Brewster-angled crystal a circular output beam is obtained by balancing the astigmatic effects of the Brewster angles against the astigmatic effects of the curved mirrors in the cavity folding section. Clearly, this balance cannot be achieved in a laser based around an AR-coated crystal, as the only source of astigmatism will be the mirrors. However, as Figure 4.15 shows, this causes no significant astigmatism at the output coupler provided that the angle of incidence of the intracavity beam on the curved mirrors is kept below a half-angle of ~8°. The minimum half-angle possible in our Cr:LiSAF laser was ~3° with the 100 mm ROC mirrors and ~4° with the 75 mm ROC mirrors. Further reduction of this angle was limited by the width of the laser

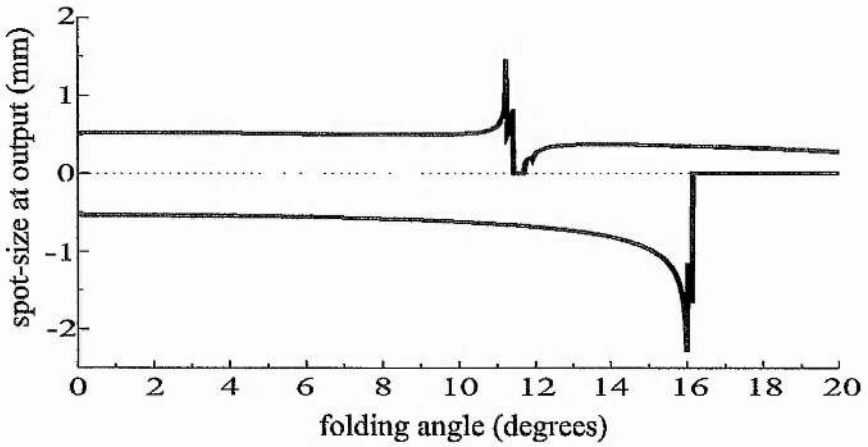

FIGURE 4.15 *Astigmatism at the laser output coupler as a function of the angle of incidence of the intracavity beam on the folding-section mirrors.(Upper curve: tangential plane, lower curve: sagittal plane)*

crystal.

4.3.2 CW Performance

With 100 mm ROC mirrors in the folding section, the Cr:LiSAF laser had a CW threshold of 45 mW and a slope efficiency of 1.1 % (Figure 4.16). With the 75 mm ROC mirrors it had a CW threshold of 35 mW and a slope efficiency of 1.0 %. In both cases, the maximum output power at 150 mW pump power was ~1.2 mW.

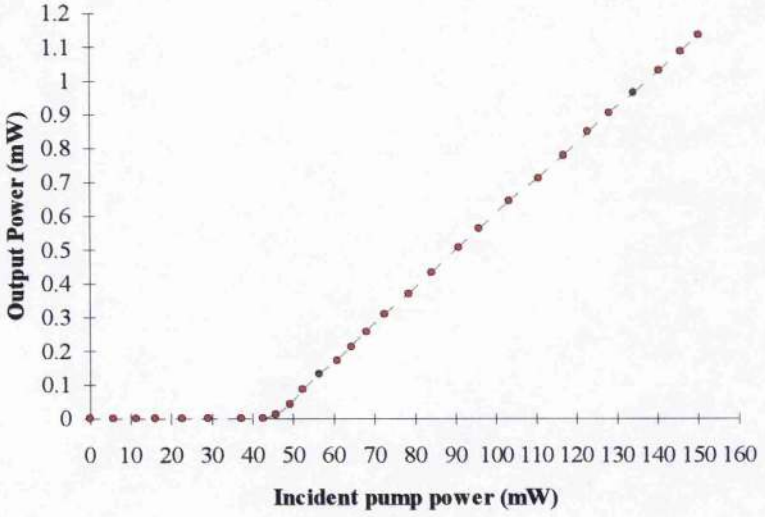

FIGURE 4.16 *The power transfer characteristics of the CW diode-pumped Cr:LiSAF system with 100 mm ROC folding-section mirrors.*

4.3.2.1 Tuning - Birefringence Effects

In a low-threshold laser system it is desirable to eliminate as many sources of loss as is practicably possible. An unexpected source of loss was revealed when the Cr:LiSAF laser was tuned: the tuning curve (Figure 4.17) was modulated with a period of 4.6 nm. This phenomenon can be shown to result from birefringence effects caused by a small misalignment of the c-axis of the Cr:LiSAF crystal.

Ideally, a Cr:LiSAF laser should generate light that is polarised in a plane parallel to the c-axis of the crystal at the output of the laser and at all points within the

laser cavity. The gain crystal and any Brewster surfaces such as those of the dispersion-compensation prisms or the AO modulator can all affect the polarisation of the intracavity field. In 1992 it was observed that if a Ti:sapphire laser was set up with its c-axis rotated slightly from the horizontal then the laser tuning curve exhibited a modulation[3] that was similar to that seen in our laser. This phenomenon was explained by the realisation that the combined effects of the misaligned gain crystal and the intracavity Brewster-surfaces acted like an intracavity birefringent filter.

Horizontally polarised light that enters a misaligned birefringent crystal emerges with a slightly elliptical polarisation. Most of the vertical component of this elliptical field will be lost if the light subsequently passes through Brewster-angled interfaces such as those of the intracavity prism pair. The eccentricity of the induced polarisation ellipse depends on the laser wavelength. At certain wavelengths, the net effect of the crystal birefringence will be zero and the light will emerge entirely horizontally polarised. These are the wavelengths of the transmission peaks of Figure 4.17, because at these wavelengths the field will see no loss at the prisms.

That is the basic mechanism behind the observed modulation, although in a laser cavity the situation is a little more complicated. The polarisation state of a laser's intracavity field must reproduce itself in amplitude and phase at all points in the laser cavity after every round trip. The polarisation states that will satisfy this condition can be found by determining the eigenvectors of the round-trip Jones matrix[4]. The polarisation state of a laser field can be described by a vector of the form

$$\begin{pmatrix} A_1 \exp(i\phi_1) \\ A_2 \exp(i\phi_2) \end{pmatrix},$$

EQUATION 4.3

where A_1, A_2 and ϕ_1, ϕ_2 are the amplitudes and phases of the components of the intracavity field obtained when the field is resolved onto two orthogonal reference axes.

FIGURE 4.17. *The tuning curve of the Cr:LiSAF laser, showing a modulation which is due to birefringence effects resulting from the misalignment of the c-axis of the crystal.*

A birefringent crystal of length d can be described by the matrix

$$X(\lambda) = \begin{bmatrix} \exp\left(\frac{\Gamma(\lambda)\cdot i}{2}\right) & 0 \\ 0 & \exp\left(-\frac{\Gamma(\lambda)\cdot i}{2}\right) \end{bmatrix},$$

EQUATION 4.4

where

$$\Gamma(\lambda) = \frac{2\pi\left(n_c(\lambda) - n_a(\lambda)\right)d}{\lambda}$$

EQUATION 4.5

is the relative phase delay between the orthogonally polarised components which see refractive indices $n_c(\lambda)$ and $n_a(\lambda)$, respectively (n_c being the refractive index seen by light polarised parallel to the c-axis, and n_a being the refractive index seen by light polarised parallel to the a-axis - see Figure 4.18). A Brewster-angled interface between air and a dielectric of refractive index n can be described by the matrix

$$B(\lambda) = \begin{bmatrix} 1 & 0 \\ 0 & \frac{4\cdot n^2}{\left(n^2+1\right)^2} \end{bmatrix}.$$

EQUATION 4.6

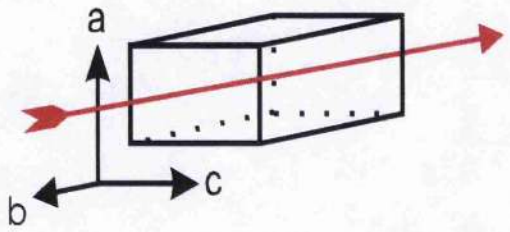

FIGURE 4.18 *The principal axes of Cr:LiSAF, with the crystal oriented as it was in the laser.*

To calculate the polarisation of light at the laser output coupler we must first calculate the net round-trip Jones matrix

$$T(\lambda) = R' \cdot X(\lambda) \cdot R \cdot B(\lambda)^{12} \cdot R' \cdot X(\lambda) \cdot R,$$

EQUATION 4.7

where R is the matrix that rotates the reference polarisation directions from the planes parallel and perpendicular to the Brewster angles to the planes parallel and perpendicular to the crystal c-axis, and R' is the matrix that rotates them back again. R and R' are given by

$$R = \begin{bmatrix} \cos(\phi) & \sin(\phi) \\ -\sin(\phi) & \cos(\phi) \end{bmatrix} \qquad R' = \begin{bmatrix} \cos(-\phi) & \sin(-\phi) \\ -\sin(-\phi) & \cos(-\phi) \end{bmatrix},$$

EQUATION 4.8

where ϕ is the angle between the plane of the c-axis and the plane of the Brewster surfaces (taken to be 3° in the following calculations unless otherwise stated).

The matrix $B(\lambda)$ appears twelve times in Equation 4.7 because there are twelve passes through Brewster-angled surfaces in the laser cavity in each round trip: 2 on each of 2 prisms and 2 on the AO modulator, doubled by the return leg of the round trip. These twelve reflections more-or-less destroy any vertically polarised light generated by the birefringent crystal and are the physical source of the loss modulation observed in the laser.

The round-trip transmissivity seen by the intracavity field is related to the eigenvalues $s_1(\lambda)$, $s_2(\lambda)$ of $T(\lambda)$ by

$$t(\lambda) = \left| s_{1,2}(\lambda) \right|^2.$$

EQUATION 4.9

The variation of $t(\lambda)$ with wavelength for each eigenstate is shown in Figure 4.19.

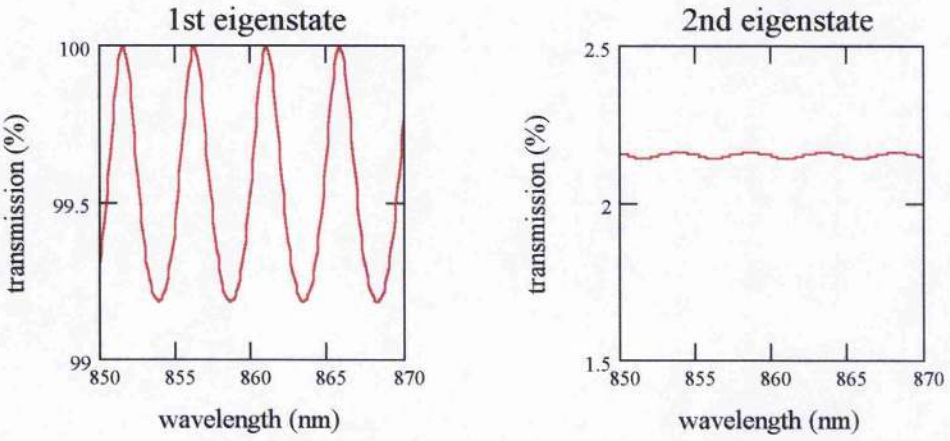

FIGURE 4.19 *The round-trip transmissivity seen by the eigenstates of T(λ), calculated at the laser output coupler.*

The first eigenstate in Figure 4.19 sees substantially less loss than the second eigenstate and consequently it is the first eigenstate that oscillates. The variation of transmission with c-axis misalignment angle is shown in Figure 4.20.

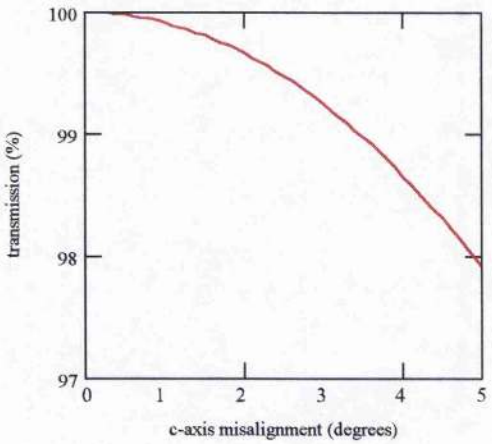

FIGURE 4.20 *The variation of round-trip transmissivity with the angle of rotation of the crystal c-axis from the horizontal. The transmissivity is calculated for λ=868.8 nm which is a minimum in the first eigenstate transmission curve shown in Figure 4.19.*

The modulation of the transmission seen in Figure 4.19 has a period of 4.7 nm, which agrees with the modulation period of 4.6 nm observed on the Cr:LiSAF laser output (Figure 4.17). In order to achieve this good agreement it is necessary to use full Sellmeier expressions to determine the refractive indices of LiSAF for use in Equation 4.5. In the analysis of birefringence-induced loss modulation in

Ti:sapphire carried out by Pan *et al.*[3] the variation of n with λ was ignored and n_o-n_e was taken to be a constant. If this approximation is made when analysing the LiSAF system then the calculated modulation period is too long by a factor of two. The reason for this can be seen in Figure 4.21: the variation of n_o-n_e with wavelength is significantly smaller in sapphire than it is in LiSAF.

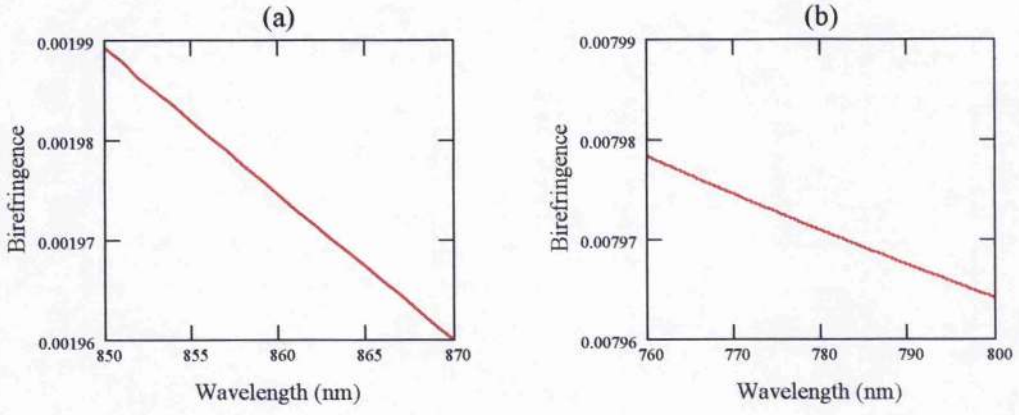

FIGURE 4.21 *Birefringence (n_e-n_o) in (a) LiSAF and (b) sapphire.*

The first eigenstate in Figure 4.19 corresponds to light that is predominately horizontally polarised at the laser output coupler, but that has a small wavelength-dependent vertical component (i.e. it is slightly elliptically polarised); the second eigenstate corresponds to light that is predominantly vertically polarised at the laser output coupler, but which has a small wavelength-dependent horizontal component. The fractions of these elliptically-polarised fields that resolve into horizontally and vertically polarised components are related to the eigenvectors of $T(\lambda)$,

$$S_{1,2}(\lambda) = \begin{pmatrix} E_1(\lambda) \\ E_2(\lambda) \end{pmatrix},$$

EQUATION 4.10

by

$$H(\lambda) = |E_1(\lambda)|^2 \qquad V(\lambda) = |E_2(\lambda)|^2 .$$

EQUATION 4.11

$H(\lambda)$ and $V(\lambda)$ are plotted in Figure 4.22 for the first eigenstate.

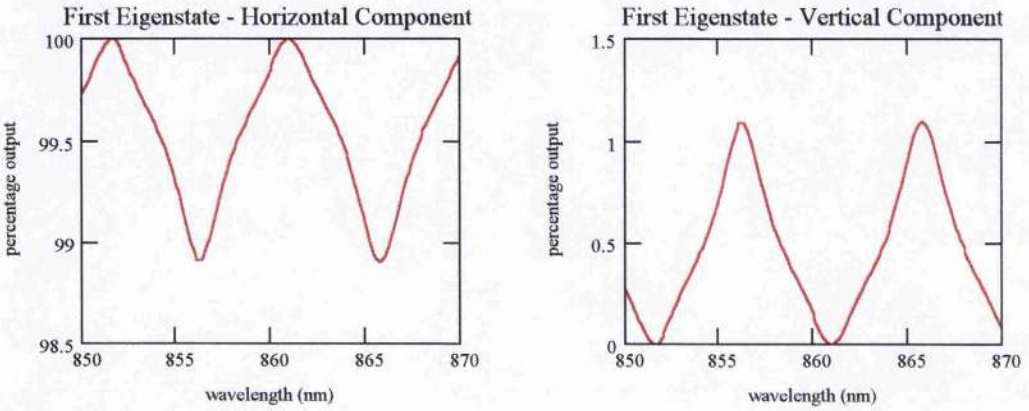

FIGURE 4.22 *The variation with wavelength of the elliptical polarisation of the predominantly horizontally-polarised eigenstate, calculated at the laser output coupler.*

The polarisation of the oscillating eigenstate varies as the field sweeps around the laser cavity. Figure 4.23 shows the size of the vertical component of the elliptically-polarised field at various points in the cavity. The vertical component reaches both its largest and smallest values between the laser crystal and the first prism (locations (2) and (8)). At location (8), as the field makes its round-trip it sees the crystal; then the crystal again; then two prisms; the modulator; the modulator again; and the prisms again. The field therefore sees two passes of the birefringent crystal and then twelve Brewster surfaces. The Brewster surfaces remove almost all the vertical component of the field, which is why this parameter is at a minimum at location (8). Conversely, at location (2) the field sees twelve Brewster surfaces and *then* two passes of the birefringent crystal, so the vertical component is at a maximum at this point because the Brewster angles do not filter out the vertical polarisation generated by the birefringent crystal.

The phase lag between the horizontal and vertical components of the oscillating eigenstate is also shown in Figure 4.23. This is the same at all points in the cavity, with the exception of the output coupler at location (1). The two passes of the birefringent crystal that occur in a round trip can be treated as being one pass of a long crystal. Location (1) is half-way through the 'long crystal', and so the field at this point has seen a different phase shift to the field at all other locations, which see the phase shift due to the whole crystal.

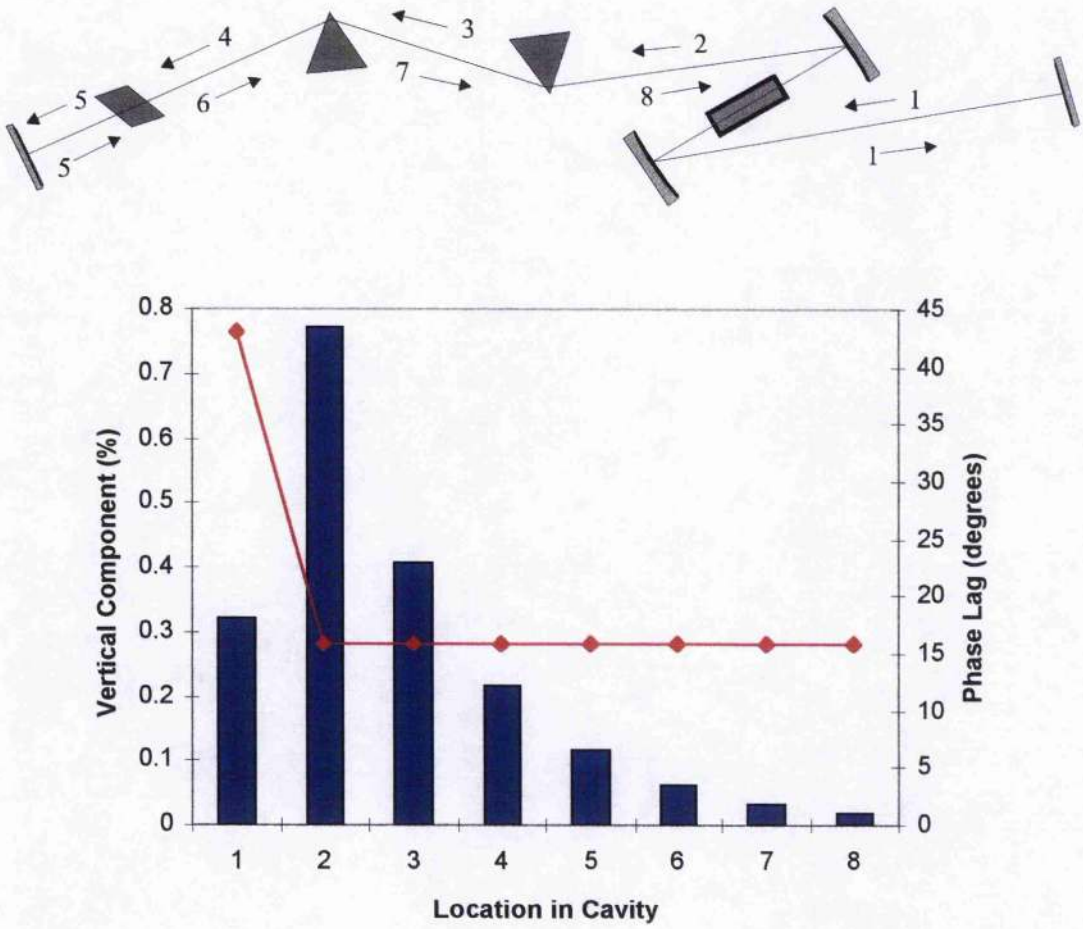

FIGURE 4.23 *The elliptical polarisation of the intracavity field (λ=868.8 nm) at various points in the cavity round-trip. The bar chart gives the magnitude of the vertically polarised component of the oscillating eigenstate at the points indicated in the cavity schematic; this gives an indication of the tilt of the major axis polarisation ellipse from the plane of the intracavity prisms. The line graph gives the phase lag of the horizontal component behind the vertical component; this gives an indication of the eccentricity of the polarisation ellipse (it is minimum with a phase lag of 0 °, maximum with a phase lag of 90 °).*

4.3.2.2 Birefringence and modelocking

In a low-threshold *modelocked* laser birefringence losses are particularly undesirable because the loss seen by pulses does not vary sinusoidally with wavelength but is constant for all wavelengths and equal to the maximum loss seen in the CW case.

Consider a pulse, plane-polarised in the plane of the Brewster-angled prisms, that enters a misaligned Cr:LiSAF crystal. In the co-ordinate axes of the crystal there are two pulse components: one component polarised parallel to the crystal c-axis and another, much smaller, component polarised parallel to the crystal a-axis. As the pulse components propagate through the crystal, the phase difference between them grows and, as before, the polarisation of the resultant field becomes elliptical. However, the smaller pulse also begins to walk away from the larger pulse as the two pulses propagate, because the pulses see different refractive indices. The resultant field therefore corresponds to a longer pulse that is plane-polarised parallel to the a-axis at its front, elliptically polarised in its middle and plane-polarised parallel to the c-axis at its rear. As the component parallel to the a-axis walks further away, the proportion of the resultant pulse that is elliptically polarised diminishes. By the end of the crystal, the component polarised parallel to the a-axis has walked ahead of the other component by a time

$$\Delta t = \frac{(n_c - n_a)L}{c}.$$

EQUATION 4.12

For a wavelength of $\lambda = 860$ nm and a crystal of length $L = 24$ mm, this delay is $\Delta t = 158$ fs. A pulse of less than ~100 fs duration will therefore have split into two independent orthogonally-plane-polarised pulses by the time it reaches the end of the crystal. In the co-ordinate axes of the prisms, one of these independent pulses will be plane polarised at a slight angle to the vertical and the other will be plane polarised at a slight angle to the horizontal. All vertical components will be almost entirely lost on reflection at the twelve Brewster surfaces found in the laser cavity.

The loss seen by a pulse is not modulated with wavelength. The orthogonally polarised pulses will walk away from each other at all wavelengths in the laser tuning range, and so there will be no wavelength at which the crystal can act as a full-wave plate. The loss seen by a pulse will therefore be equal to the maximum loss seen by the CW laser, because all of the vertically polarised component generated in the crystal will be lost at every wavelength.

This constant loss in pulsed operation makes self-modelocking difficult at wavelengths corresponding to peaks in the CW transmission spectrum. In order to modelock the laser at these wavelengths, it is necessary to introduce an additional loss into the CW mode to ensure that pulsed operation is preferred over CW operation. In the diode-pumped Cr:LiSAF laser system, we found that self-modelocking was impossible at wavelengths coinciding with CW transmission peaks. When the laser modelocked, its spectrum was centred between two CW peaks; if it was tuned towards either peak then the self-modelocking dropped out. As one of the principal attractions of Cr:LiSAF as a laser material for self-modelocking is its wide tuneability, this behaviour was particularly unfortunate.

Thus, although birefringence-induced loss is an interesting phenomenon, it is not desirable in a low-threshold laser, and it is particularly unwelcome in a self-modelocked low-threshold device. The obvious way to eliminate the effect is to rotate the crystal by the small angle (1 ° to 2 °) by which its c-axis is misaligned. Unfortunately, the rectangular cross-section of the Cr:LiSAF crystal used in the W-cavity and the design of the crystal mount made this rotation very difficult to achieve in practice. The low-threshold laser system described in Chapter 5, however, was engineered so that its crystal mount could be rotated about the long axis of the crystal. This enabled us to completely eliminate the modulation effects from the laser tuning curve, as will be discussed in the Chapter 5.

4.3.3 Modelocked Performance

4.3.3.1 Self-modelocking the W-cavity

Despite the effects of residual crystal birefringence, the W-cavity Cr:LiSAF laser still performed remarkably well as a low-threshold, ultrashort pulse device. Self-modelocking was initially achieved with R = 100 mm ROC. folding mirrors and SF14 prisms. The first step towards low-threshold self-modelocking was the minimisation of the CW threshold of the laser: this was achieved by maximising the laser output power at lower and lower pump powers. The positions of the mirrors in the cavity folding section at minimum CW threshold were very close to the

predictions of the Cerullo diagram (introduced in Section 3.4) obtained for the W-cavity (Figure 4.24), as expected.

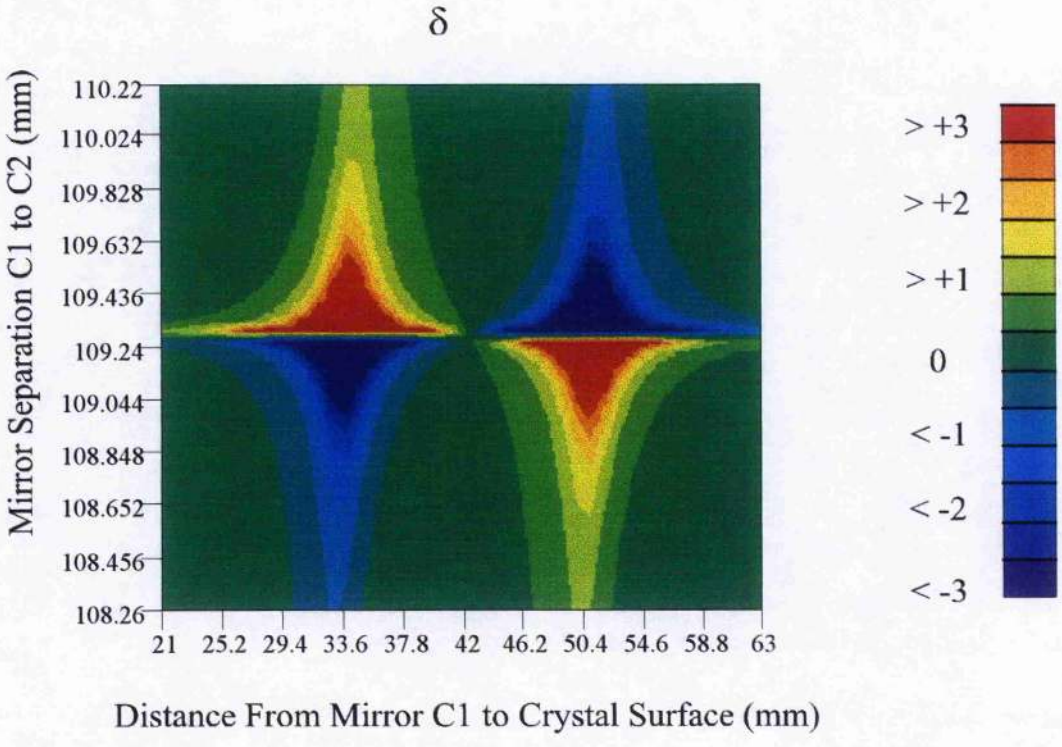

FIGURE 4.24 *The Cerullo diagram for the Cr:LiSAF W-cavity with 100 mm ROC folding-section mirrors (see Figure 4.11(a)).*

Once the minimum CW threshold had been achieved, the pump power was returned to maximum. The laser output from the cavity end mirror nearest to the dispersion-compensation prisms was steered onto the fast photodiode of the regenerative-initiation system (Figure 4.10). A second signal from the photodiode was monitored on an RF-spectrum analyser. With the regenerative-initiation system switched on, the length of the cavity arm containing the KLM slit was adjusted until regenerative modelocking was optimised (the RF power signal was maximised). When it was optimised, regenerative-modelocking could be reliably regained after the pump beam, intracavity beam or beam to the fast photodiode was blocked and then unblocked.

Output from the KLM slit arm of the laser was steered into a SHG autocorrelator. From the first time the second-harmonic of the laser output was observed, it was exhibiting the large fluctuations that are characteristic of near-self-modelocked

operation. Small adjustments of the alignment of the cavity mirrors and the positions of the folding mirrors and crystal were sufficient to induce full self-modelocking.

The ease with which modelocking was achieved in this system was notable, and all the more remarkable considering that no more than 150 mW pump power was used. This performance can be attributed to a number of factors. The use of the Cerullo prescription, which has led to self-starting in other higher-pump-power systems, must be regarded as significant. The plane-plane rod geometry enhanced the benefits of the Cerullo approach because the cavity configurations for low CW threshold and optimised self-modelocking were identical and sharply defined. The reliability of the self-modelocking was closely linked to the reliability of the regenerative modelocking, which was, as far as possible, optimised. Finally, the diode pump source was reliable and stable, without the fluctuations that would hamper modelocking that might be found in mainframe ion lasers.

4.3.3.2 Pulse Characteristics and Pump Power Requirements

The laser produced 93 fs duration pulses at 150 mW pump power and 140 fs duration pulses at 100 mW pump power. Replacing the SF14 prisms with LaK L21 prisms produced 60 fs pulses at 150 mW pump and 99 fs pulses at 100 mW pump. A pulse autocorrelation and spectrum are shown in Figure 4.25 for the 100 mm ROC mirrors and LaK L21 prisms. All pulses were transform-limited, as would be expected from a laser operating in a soliton-like shaping regime.

The prism separations calculated to give GVD compensation were 175 mm for SF14 prisms and 134 mm for LaK L21 prisms. The prism separations actually used, however, were 200 mm and 493 mm respectively, with the extra separation compensating for ~470 fs^2/round-trip of quasi-positive chirp generated by self-phase modulation of the pulses in the Cr:LiSAF crystal. The net third-order dispersion in the cavity was -5510 fs^3/round-trip for the SF14 prisms and 97 fs^3/round-trip for the LaK L21 prisms.

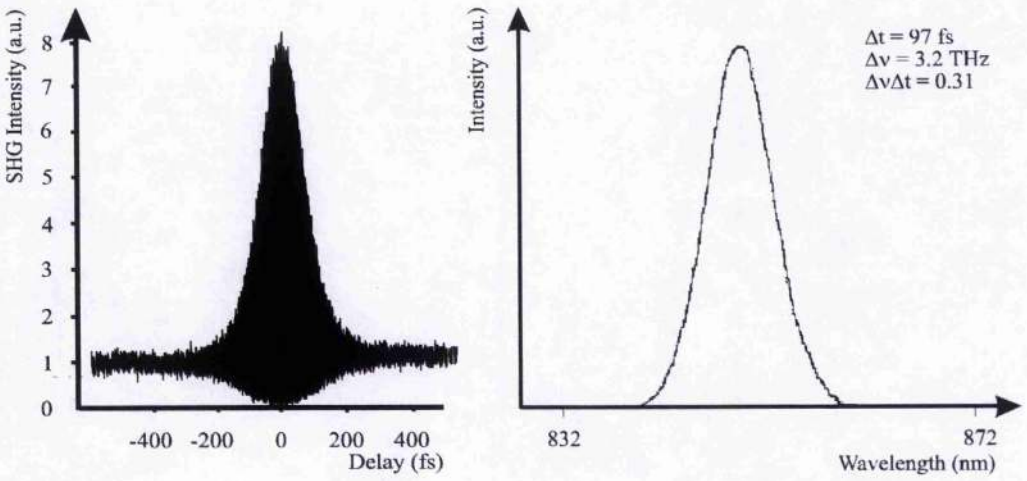

FIGURE 4.25 *An autocorrelation and spectrum of a transform-limited 99 fs pulse obtained from the Cr:LiSAF laser with 100 mm ROC mirrors for 100 mW pump power.*

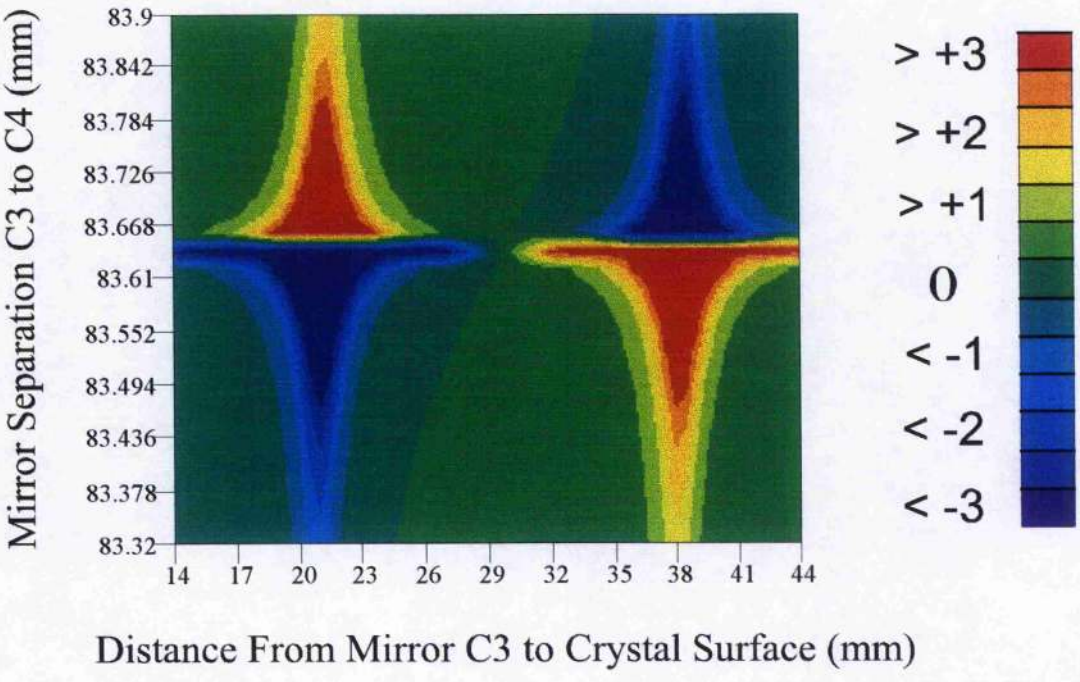

FIGURE 4.26 *The Cerullo diagram for the Cr:LiSAF W-cavity with 75 mm ROC folding-section mirrors (see Figure 4.11(b)).*

It was predicted in Chapter 3 that reducing the sizes of the spots in the Cr:LiSAF crystal would decrease both the CW and modelocked thresholds. Consequently, the 100 mm ROC mirrors in the cavity folding section were replaced with 75 mm ROC mirrors. The cavity was again optimised for a low CW threshold, and the behaviour of the resulting configuration again agreed with the predictions of the Cerullo analysis of this revised cavity (Figure 4.26). The pulse repetition rate was 86 MHz for both mirror sets.

The pulse durations obtained from all laser configurations are summarised in Table 4.1. Comparing the values that have been underlined shows that pulses of approximately the same duration can be obtained for less pump power by either reducing the size of the laser waist in the crystal or reducing the net round-trip third-order dispersion, as predicted.

	Pump power 100 mW	Pump power 150 mW
100 mm ROC. mirrors		
SF14 prisms	140 fs	93 fs
LAK L21 prisms	99 fs	<u>60 fs</u>
75 mm ROC. mirrors		
SF14 prisms	77 fs	<u>65 fs</u>
LAK L21 prisms	<u>65 fs</u>	54 fs

TABLE 4.1 *Pulse durations at 100 mW and 150 mW pump power for 100 mm ROC mirrors and 75 mm ROC. mirrors, and for SF14 and LaK L21 prisms.*

The threshold pump powers for self-modelocking were 88 mW - 90 mW with the 100 mm ROC mirrors, and 70 mW - 73 mW with the 75 mm ROC mirrors. For comparison, the lowest modelocking threshold reported for a similar laser system elsewhere is ~ 207 mW incident power (160 mW absorbed)[5]. Dymott and Ferguson[5] also suggest that sub-100 fs duration pulses were achieved for an incident pump power of over 250 mW (193 mW absorbed). The incident pump power required for sub-100 fs pulses from our system was 73 mW (a pulse

autocorrelation and spectrum for these pulses are shown in Figure 4.27), obtained with the 75 mm ROC mirrors and LaK L21 prisms; this therefore represents a three-fold reduction on the lowest previously-reported result. A low-threshold Ti:sapphire laser has been reported with a modelocking threshold of 500 mW[6], nearly seven times higher than the W-cavity threshold (the higher $\sigma\tau$ product of Cr:LiSAF accounts for a factor of about three in this improvement).

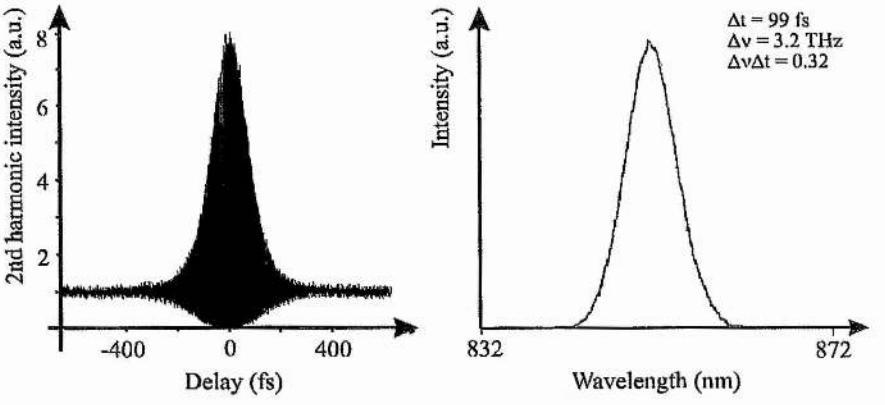

FIGURE 4.27 *An autocorrelation and spectrum of transform-limited 99 fs pulses obtained from the Cr:LiSAF laser for 73 mW pump power. This pump power is a three-fold reduction on the previous lowest pump power requirement for sub-100-fs pulses.*

4.3.3.3 Power-Transfer Characteristics of the Self-Modelocked Laser

Figure 4.28 shows the power-transfer characteristics of the self-modelocked laser. This figure was obtained by reducing the pump power from 150 mW to 0 mW by rotating an ND wheel in front of the self-injection-locked semiconductor laser. As the wheel was rotated, the output power of both the pump and the Cr:LiSAF laser were monitored on photodiodes connected (respectively) to the X- and Y- inputs of an HP 54603B oscilloscope with its 'Storage' mode set to 'Auto-Store'.

The figure clearly shows the various operating regimes that exist at different pump powers, and it also shows the transitions between these regions. The laser begins to oscillate at 48 mW pump power and operates CW, with a slope of 8.0 μW/mW, until the power reaches 84 mW. The feedback electronics of the regenerative-initiation system then begins to trigger, but there is insufficient signal for true regenerative modelocking and the resulting output is extremely noisy. At 95 mW, full regenerative modelocking takes over. In this region, the laser is passively AO modelocked with a slope of 9.7 μW/mW (extrapolating back from this line gives a 'threshold' of 55 mW at P_{out} = 0 mW). At 102 mW, the laser self-modelocks. The self-modelocked laser has a slope of 10.9 μW/mW (the extrapolated 'threshold' is 58 mW). Note that the output power rises by about 20 μW when self-modelocking occurs; this is because the laser experiences less loss at the intracavity slit when it

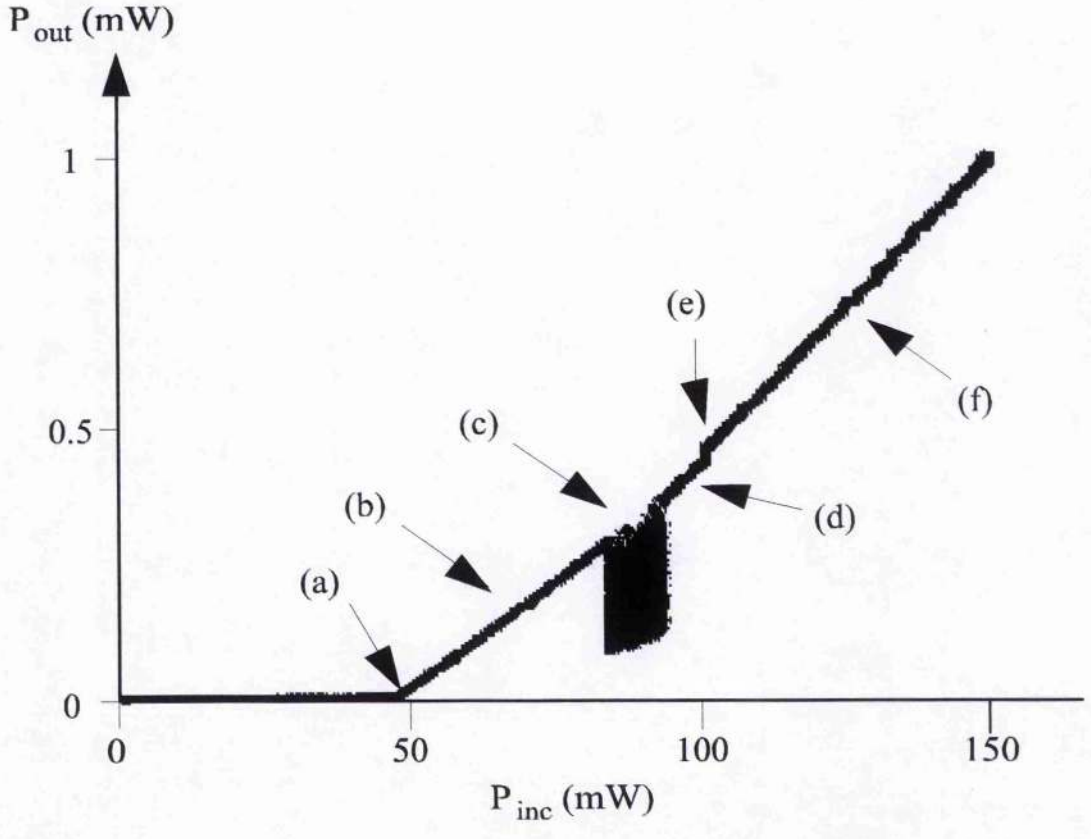

FIGURE 4.28 *The power-transfer characteristics of the self-modelocked Cr:LiSAF laser. The labels indicate (a) the CW oscillation threshold; (b) CW operation; (c) instability in the regenerative modelocking feedback electronics; (d) regenerative modelocking; (e) the self-modelocking threshold; and (f) self-modelocking.*

is modelocked than when it is CW, and so it requires less gain and so excess pump power is converted into output power.

4.3.3.4 The Nature of the Modelocking

Although the design of the laser was based around the Cerullo prescription for hard-aperture modelocking, and the cavity configuration at which it modelocked agreed with that prediction, the laser actually seemed to run in hard-aperture, soft-aperture and perhaps even mixed regimes. On some occasions, adjustments to the modelocking slit had very significant effects on the pulsed output; on others, it seemed to be to have little or perhaps no effect. In general, the most stable pulses were produced when the slit appeared to be doing nothing, contrary to expectation. It seems that the Cerullo prescription leads to a cavity geometry that is good for both types of modelocking. Introducing a Kerr lens in the end of a crystal in a symmetric cavity produces the largest possible change in the intracavity mode at the end of the long cavity arms. It seems reasonable to suppose that it also produces a large change in the mode inside the crystal. The behaviour of the laser suggests that this mode change produces a better overlap with the pump beam than is possible with a CW field. This may not occur at the exact configuration which gives the best hard-aperture modelocking, but the laser needed little adjustment to get from one regime to the other. However, because soft-aperture modelocking was significantly more stable than hard-aperture modelocking, it was very difficult to get from the soft-aperture regime to the hard-aperture regime, once soft-aperture modelocking was established.

4.3.3.5 'Self-starting' Ultrashort Pulse Generation

Self-starting self-modelocking has recently been demonstrated in Cerullo-style hard-aperture-modelocked lasers[7]. A 'self-starting' laser is generally defined to be one in which self-modelocked operation restarts after the pump or intracavity beam is interrupted. Our laser was not self-starting in this sense, because the intracavity power was too small for noise fluctuations to evolve into pulses through self-focusing. Indeed, if the regenerative-initiation circuit was disconnected from the laser then it was not possible to induce modelocking at all, even by tapping mirrors or by any other similar method. However, with the regenerative-initiation circuit in

place, self-modelocking could be reliably regained even if the pump beam or intracavity beam was chopped. Figure 4.29 was obtained by monitoring the second-harmonic output of the autocorrelator in real-time, and demonstrates 'self-starting' regenerative operation. Given the low intracavity power (~ 1 W) in this laser, this self-starting ultrashort-pulse generation demonstrates the reliability and stability of pulse generation in the femtosecond Cr:LiSAF laser.

It is possible to use Figure 4.29 to estimate an upper limit on the time it takes for pulses to build up in the laser. The frequency of the chopper was increased until the pump temporal windows were too narrow to allow pulsing to start in one window out of a significant number (15 - 20). It can be deduced that the pulse build-up time in this particular window must have been longer than the window duration. As self-starting occurred in all the other windows, it is reasonable to assume that this build-up time is in the long-duration wing of a statistical distribution. It therefore provides a reasonable upper limit on the pulse build-up time. Other methods of estimating the build-up time are, of course, available. It could be observed directly by measuring the fraction of a pump window for which the second-harmonic signal is not present. Taking repeated measurements would give a good estimate of the mean build-up time, but this method requires a good knowledge of the duration of the pump window, and this is difficult to obtain without a narrow pump beam and a fast chopping speed. An alternative approach would be to use a fast photodetector to observe the pulses directly, but in our laser the femtosecond pulses would be preceded by longer, regeneratively-modelocked pulses, and so this method would probably require an unfeasibly high photodetector temporal resolution.

The pulse start-up times were calculated to be < 4.5 ms when the pump beam was chopped and < 6.6 ms when the intracavity beam was chopped. The first figure is shorter than the second because chopping the pump beam leads to perturbations in the laser crystal, for example in the amount of thermal lensing seen by the intracavity field. Self-starting is therefore enhanced in this case because these perturbations give pulse build-up a 'kick' similar to that obtained by tapping a cavity mirror. The figure of 6.6 ms is therefore a more accurate estimate of the upper-limit of the pulse build-up time.

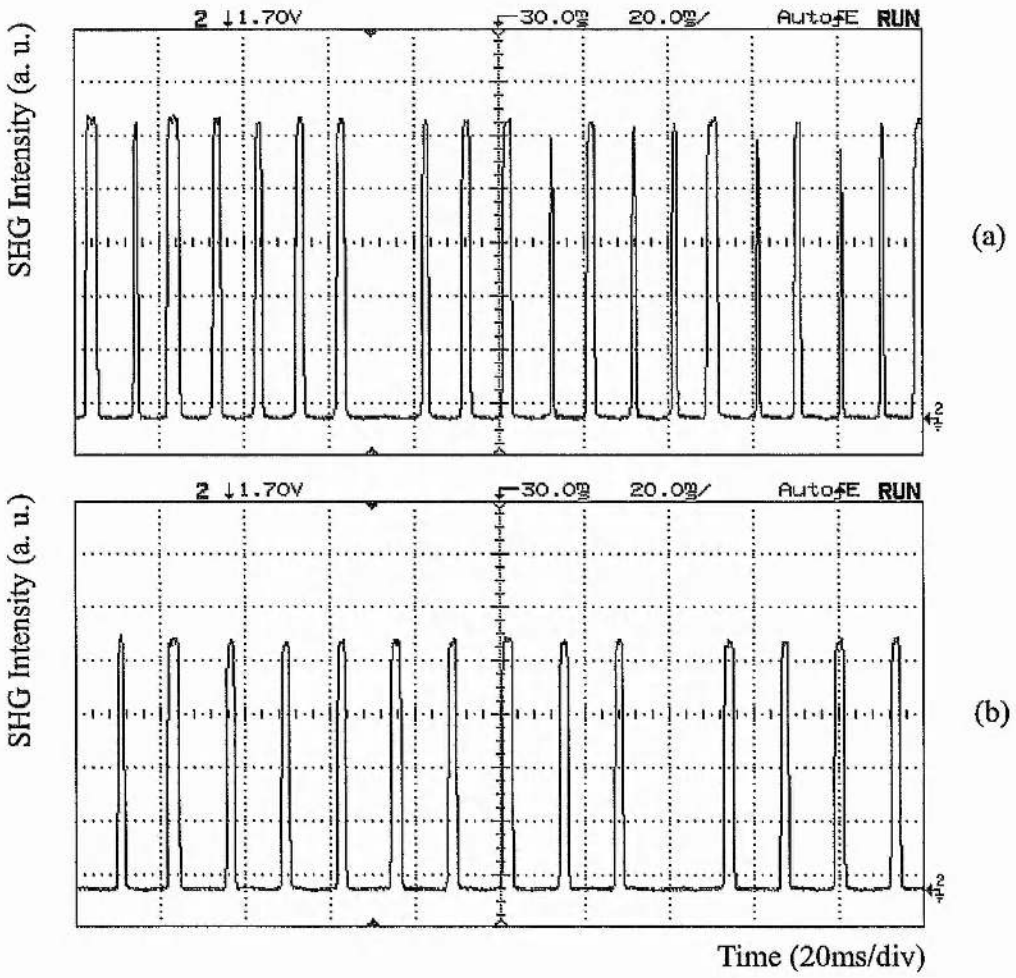

FIGURE 4.29 *'Self-starting' ultrashort pulse generation: (a) chopping the pump beam leads to a single incident of self-starting failure at a chopping frequency of 110 Hz, implying a pulse build-up time of < 4.5 ms; (b) chopping the intracavity beam leads to a single incident of self-starting failure at a chopping frequency of 76 Hz, implying a pulse build-up time of < 6.6 ms.*

4.3.3.6 Pulse Train Noise

The output from a modelocked laser will never be an ideal train of identical pulses. Random influences will lead to random variations in pulse durations, amplitudes and repetition rates. These random variations are characterised as noise. Noise is an unwanted effect that can limit the temporal resolution of, for example, pump-probe experiments, electro-optic sampling experiments and pulse duration measurements made with synchroscan streak cameras.

In ultrashort pulse lasers most noise fluctuations will occur on time scales much longer than the duration of the pulses, or even their repetition rate. The shape of

the pulses will therefore remain approximately constant and the principal types of noise seen on the laser output will be random fluctuations in pulse intensity and in pulse repetition rate, known as amplitude noise and phase noise, respectively. The intensity of a noisy ultrashort pulse train of this type can be written[8]

$$F(t) = F_0(t) + F_0(t)A(t) + \dot{F}_0(t)TJ(t)$$

EQUATION 4.13

Where $F_0(t)$ represents the noise-free modelocked pulse train, $\dot{F}_0(t)$ is its time derivative T is the average pulse repetition time and A(t) and J(t) are random functions representing fluctuations in the average pulse intensity and the average pulse repetition time, respectively.

Von der Linde[8] showed that the noise properties of a pulse train could be extracted from its power spectrum because the power spectrum is the Fourier transform of the pulse train autocorrelation. He shows that the power spectrum can be written

$$P_F(\omega) = \left(\frac{2\pi}{T}\right)^2 \left|\tilde{f}(\omega)\right|^2 \sum_{n=-\infty}^{n=+\infty} \left[\delta(\omega_n) + P_A(\omega_n) + (2\pi n)^2 P_J(\omega_n)\right]$$

EQUATION 4.14

where $\dot{f}(\omega)$ is the Fourier transform of the pulse profile. The first term in Equation 4.14 is a delta function representing the perfectly modelocked pulse train and $P_A(\omega)$ and $P_J(\omega)$ are the power spectra of the amplitude noise and the phase noise respectively. Note particularly that the phase noise term increases with harmonic number n, whereas the amplitude noise is constant at all harmonics (Figure 4.30). It is therefore possible to separate the effects of amplitude- and phase-noise by comparing the laser power spectra at the fundamental repetition frequency and at a high harmonic.

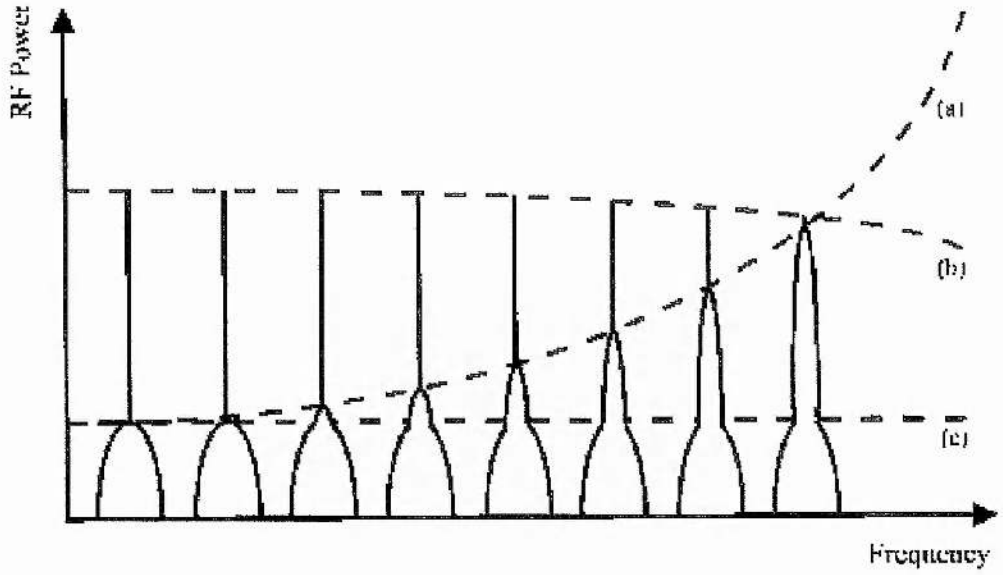

FIGURE 4.30 *A representation of the power spectrum of a train of pulses with fluctuating amplitude and pulse repetition rate. The amplitude noise is constant (c) at all harmonics but the phase noise increases quadratically (a) with harmonic number. The response of the photodiode/spectrum-analyser system (b) tails off at high frequencies.*

Specifically, the power spectra at the fundamental repetition frequency and at a high (n^{th}) harmonic are measured and the single-sideband noise power spectral densities $L_1(f)$ and $L_n(f)$ are calculated. Single-sideband power spectral density is defined as the ratio of power in one phase modulation sideband, in a 1 Hz integration bandwidth, to the total spectral power, at an offset *f* Hz away from the carrier frequency[9]. The single-sideband phase-noise power spectral density $L_j(f)$ and the single-sideband amplitude-noise power spectral density $L_A(f)$ can then be calculated from $L_1(f)$ and $L_n(f)$[10]. The rms timing jitter in a bandwidth from f_l to f_h is then given by

$$\sigma_J = \frac{\phi_{rms}}{2\pi f_0} = \frac{1}{2\pi f_0}\left(2\int_{f_l}^{f_h} 10^{\frac{L_J(f)}{10}}\,df\right)^{\frac{1}{2}}$$

EQUATION 4.15

(where ϕ_{rms} is the phase noise) and the rms amplitude fluctuation is given by

$$\sigma_J = \left(2\int_{f_l}^{f_h} 10^{\frac{L_A(f)}{10}} df \right)^{\frac{1}{2}}.$$

EQUATION 4.16

The limit f_l is set by the acquisition time of the power density data and f_h is set by the bandwidth of the measurement system.

The noise properties of the Cr:LiSAF laser were measured by focusing its output onto a silicon avalanche photodiode that was biased at 130 V using a power supply with a high degree of electrical smoothing. The diode had a 3 dB bandwidth of ~2 GHz. The output from the diode was fed into a RF spectrum analyser that was linked to a PC, and a software package was used to determine the phase and amplitude noise of the laser. The package extracts five power spectra ranging from a 1 kHz span with a 10 Hz resolution bandwidth to a 10 MHz span with a 30 kHz resolution bandwidth, at both the pulse repetition frequency and the 10^{th} harmonic. The single-sideband phase and amplitude noise spectra were calculated from this data, as were the rms timing jitter figures for the frequency ranges 100 Hz -500 Hz, 500 Hz - 5 kHz and 5 kHz - 50 kHz. Measurement of the phase noise below 100 Hz was limited by the resolution bandwidth of the spectrum analyser and measurement above 50 kHz by the noise floor of the detection system.

Noise can arise from several sources. Previous investigations[11] revealed, for example, that a resonance in the top of an optical bench led to a noise component at 200 Hz, and that vibrations in laser mirror mounts led to a component at 1 kHz. Noise on the pump laser, cavity length fluctuations and acoustic fluctuations are also all significant sources of noise.

Work previously carried out at the University of St. Andrews successfully reduced the noise contribution from cavity length fluctuations[12]. A piezo-electric transducer-controlled cavity mirror mount was used to reference the cavity frequency of a self-modelocked Ti:sapphire laser to an ultrastable crystal oscillator signal. This technique successfully reduced the phase noise of the Ti:sapphire almost to the quantum-limited value[13]. The only active step taken to reduce the noise in the Cr:LiSAF laser described in this chapter was an attempt to eliminate

the effects of air turbulence. Disturbances in the air caused, for example, by people walking past the laser, or even by moving a hand to adjust some part of the laser, caused serious instability in the laser's pulsed output. To counter this effect, the laser cavity was covered with polythene sheeting stretched over metal hoops. This shielding was not air-tight but it successfully prevented most air disturbances from affecting laser operation.

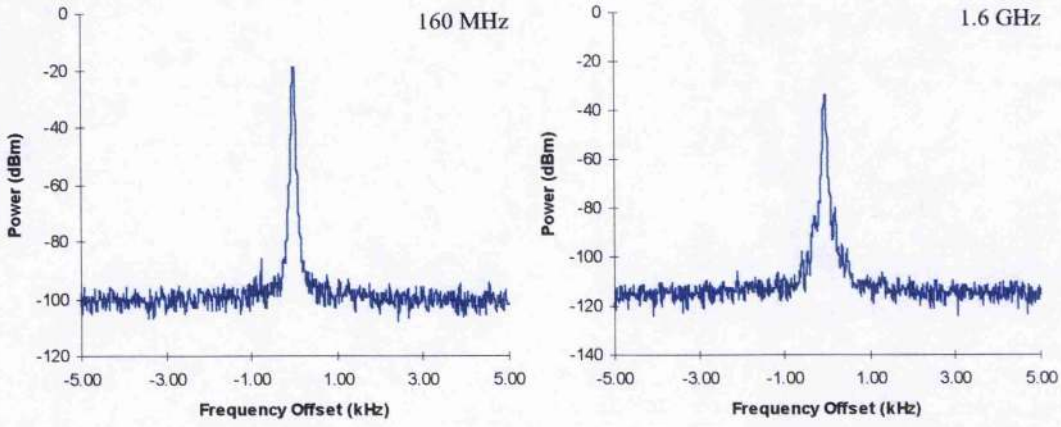

FIGURE 4.31 *RF power spectra of the (a) 2nd harmonic and (b) 20th harmonic for a 10 kHz frequency span.*

Figure 4.31 shows the power spectra of the Cr:LiSAF laser recorded for a 10 kHz frequency span at the 2nd and 20th harmonics. The increase in phase noise on the 20th harmonic spectrum near the central spike is clearly visible. The background power level is lower at the 20th harmonic because 1.6 GHz is near the bandwidth of the fast photodiode. The single-sideband phase-noise power spectrum and amplitude-noise power spectrum are shown in Figure 4.32 and Figure 4.33, respectively. The dotted line in Figure 4.32 indicates the limit for the small signal deviation criterion: if the recorded power exceeds this line then the calculated phase-noise is unreliable because there is sufficient power to excite higher-order phase-noise sidebands at high harmonics.

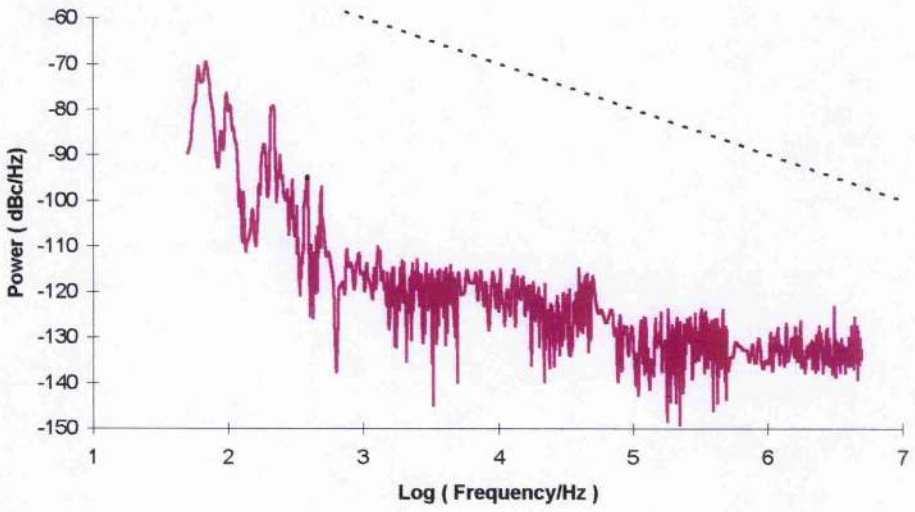

FIGURE 4.32 *The single-sideband phase-noise power spectrum of the self-modelocked Cr:LiSAF laser, calculated using the fundamental and 10th harmonic Fourier components. The dotted line indicates the limit for the small-signal deviation criterion.*

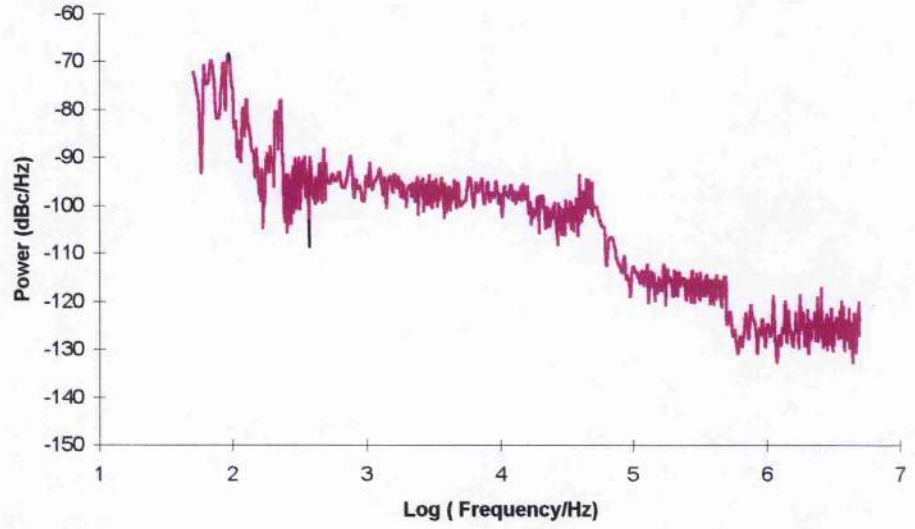

FIGURE 4.33 *The single-sideband amplitude-noise power spectrum of the self-modelocked Cr:LiSAF laser, calculated using the fundamental and 10th harmonic Fourier components.*

The RMS timing jitter figures for the free-running Cr:LiSAF laser are presented in Figure 4.34, together with the corresponding figures for an Ar^+-ion-pumped Ti:sapphire laser that was specifically developed for low-noise operation[12]. The figures for the Cr:LiSAF laser are superior in all frequency ranges. These results

demonstrate the stability of modelocked operation in the Cr:LiSAF laser system, as well as the advantage of using as a pump source a semiconductor laser rather than a relatively high-noise mainframe ion laser.

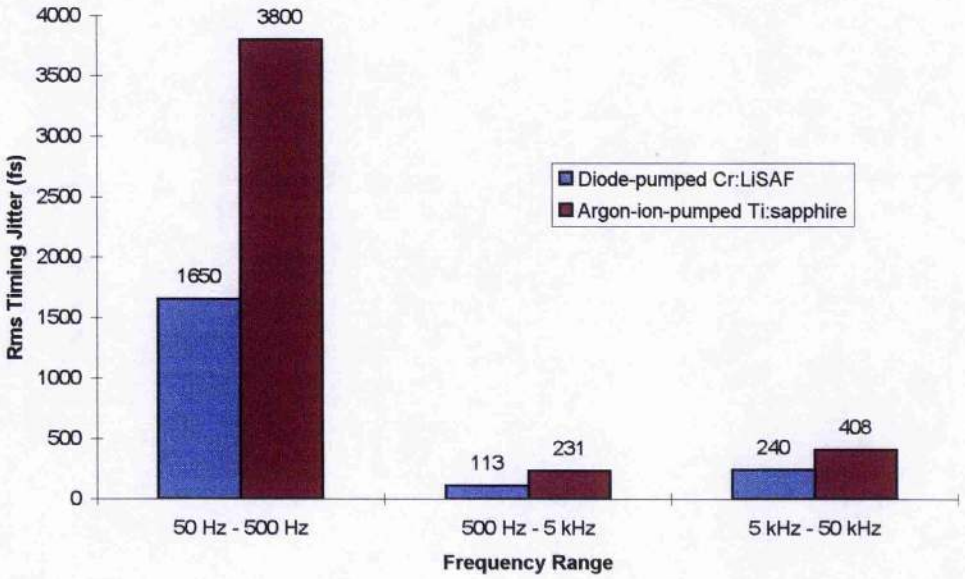

FIGURE 4.34 *Rms timing jitter (fs) in the self-modelocked Cr:LiSAF laser. The figures for a self-modelocked Ti:sapphire laser designed for low-noise operation are given for comparison.*

4.3.3.7 An Application: The Evaluation of a Synchroscan Streak Camera

The superior noise properties of the Cr:LiSAF laser allowed us to perform an evaluation of a streak camera in the sub-picosecond regime. That had previously only been possible with a cavity-locked Ti:sapphire laser. In the Ti:sapphire experiments, the streak camera was also shuttered to reduce the streak integration time, but that was not necessary with the Cr:LiSAF system.

Synchroscan streak cameras are attractive diagnostic tools because they can give direct measurements, over a wide spectral range, of the intensity profiles of pulses of durations of the order of picoseconds. Commercially available cameras give resolutions of the order of a few picoseconds, and sub-picosecond resolution has been reported with the cavity-locked Ti:sapphire laser system[12]. That result was

achieved with the Photochron V streak camera, which was designed at the University of St. Andrews[14] and which is illustrated schematically in Figure 4.35.

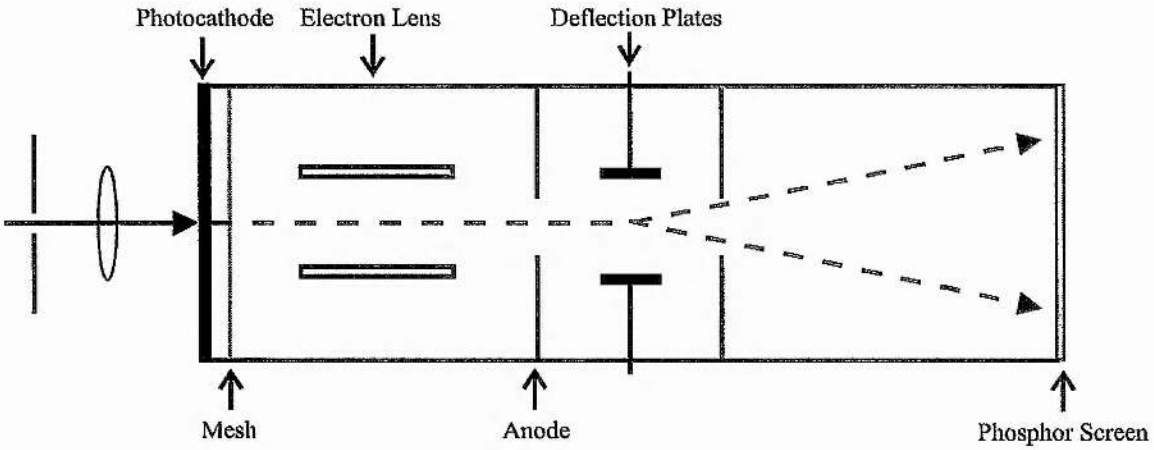

FIGURE 4.35 *A schematic diagram of the Photochron V streak camera.*

The basic operation of a synchroscan streak camera is as follows. Photons arriving at the entrance slit are imaged onto the photocathode where they liberate electrons. These photoelectrons are accelerated by the mesh electrode which is at a potential of 10 kV. The electrons are then focused by the electron lens onto the phosphor screen where they are converted back into photons. This final optical signal was monitored with a vidicon-based optical spectrum analyser (B & M Type OSA 500).

An image of the pulse intensity profile is obtained by applying a time-varying voltage to the deflection plates of the camera. This is a high-frequency sinusoidal signal that is synchronised with the arrival of pulses at the photocathode so that the temporal profile of the pulse is converted into a spatial profile on the phosphor screen. The frequency of this deflection signal is derived from the laser pulse repetition frequency via a fast-photodiode with heavily smoothed power supply, filtering and amplification circuitry.

The limiting temporal resolution of the streak camera is not reached in practice because of amplitude and phase noise on the laser pulse train, electronic noise in the deflection drive circuitry, group-velocity dispersion of the electron pulses and the limited maximum sweep speed of the camera.

The streak image observed on the OSA results from the superposition of many individual pulse images with an integration time of 32 ms. Consequently, noise on the laser pulse train can limit the resolution of the camera because variations in the time of arrival of pulses at the photocathode (i.e., phase noise or timing jitter) will result in a smearing of the streak image. Amplitude noise will result in a variation in the amplitude of the signal reaching the deflection plates, and hence in the rate of deflection of electrons, and will therefore again lead to a smearing of both the pulse profile and the pulse calibration separation (see below). Nonlinearities in the camera electronics can also lead to amplitude- to phase-noise conversion.

A glass slide was used as an optical delay to calibrate the streak camera. The slide was 1.1 mm thick, giving a delay of 11 ps between the pulses reflected from the front and back surfaces. A resolution of 0.97 ps was achieved with the Cr:LiSAF laser (see Figure 4.36), which was the smallest resolution that has been reliably achieved with a synchroscan streak camera to date. Sub-ps pulse durations had been obtained with the Ti:sapphire laser, but this required cavity-locking and the use of a 1 ms shutter to limit the integration time of the streak image.

An explanation of how it was possible to achieve this result with the free-running Cr:LiSAF laser may be inferred from Figure 4.37 which shows the rms timing jitter of the free-running Cr:LiSAF laser, the free-running Ti:sapphire laser and the cavity-locked Ti:sapphire laser in the 50 Hz - 500 Hz and the 500 Hz - 5 kHz frequency ranges. The figure for the Cr:LiSAF laser in the lower frequency range is less than half that of the free-running Ti:sapphire laser, but it is still large relative to the figure for the cavity-locked Ti:sapphire laser. However, in the higher frequency range the Cr:LiSAF laser has the smallest rms timing jitter of the three systems. Phase-noise limits the resolution of the streak camera because timing jitter results in an imperfect overlap of pulses on the phosphor screen of the camera. However, the camera's streak deflection signal is derived from the repetition rate of the laser pulses, and so it is reasonable to expect that the camera will be able to track low frequency variations in pulse repetition rate. The resolution of the camera is therefore not affected by the low-frequency timing jitter on the Cr:LiSAF output. However the high-frequency timing jitter is intrinsically small and so that should not have a significant effect either.

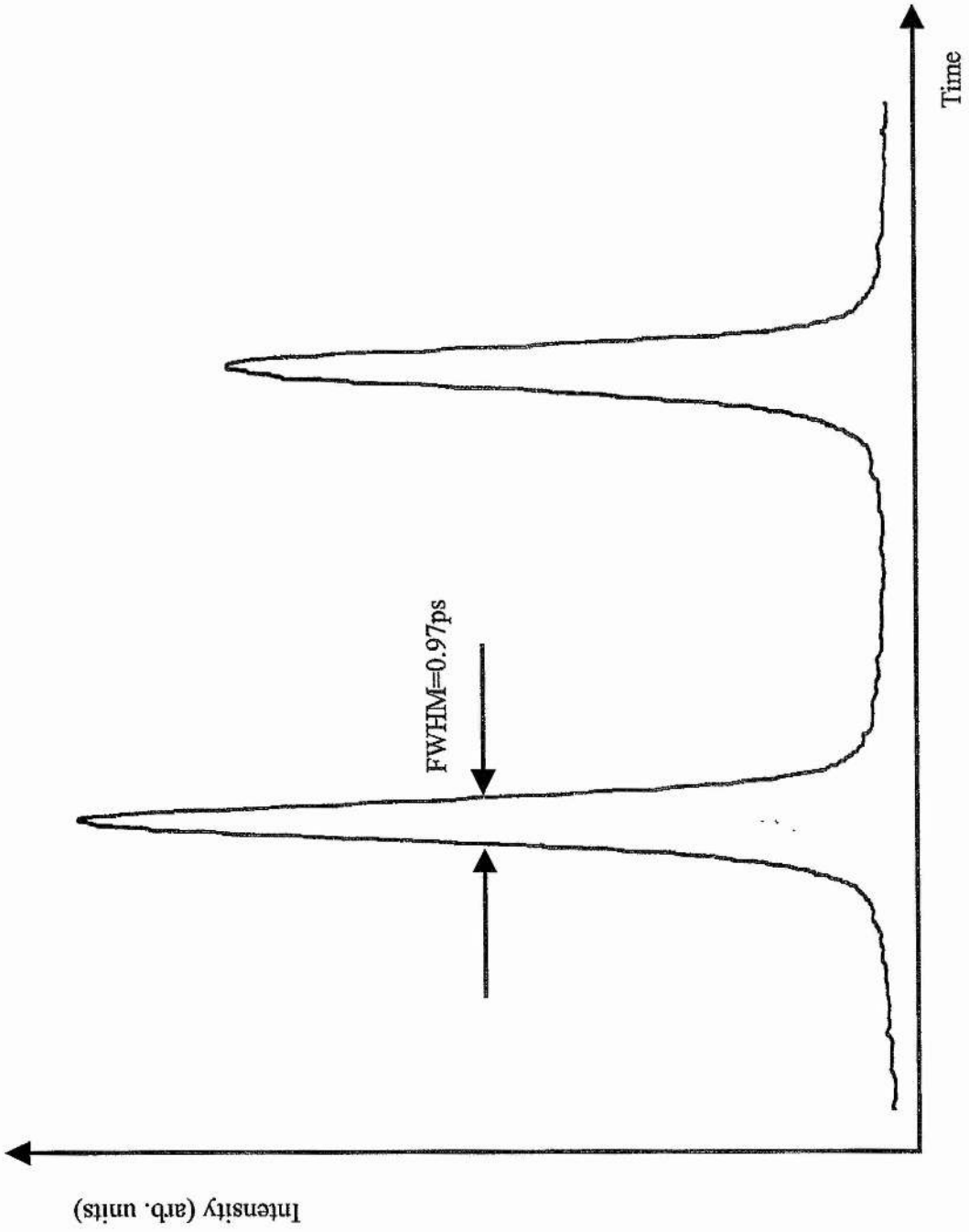

FIGURE 4.36. *Temporal intensity distribution of the free-running, self-modelocked Cr:LiSAF laser recorded using an unshuttered Photochron V synchronously-operating streak camera.*

It is possible that, as far as streak camera measurements are concerned, the effect of cavity-locking on the amplitude noise of a Ti:sapphire laser is, at low frequencies, more significant than its effect on the phase noise. That is because a streak camera cannot track low-frequency amplitude noise, and it suggests that the Cr:LiSAF laser system had intrinsically low amplitude noise. Unfortunately, the amplitude noise of neither the Cr:LiSAF laser nor the Ti:sapphire lasers was characterised in sufficient detail to draw any concrete conclusions about this suggestion.

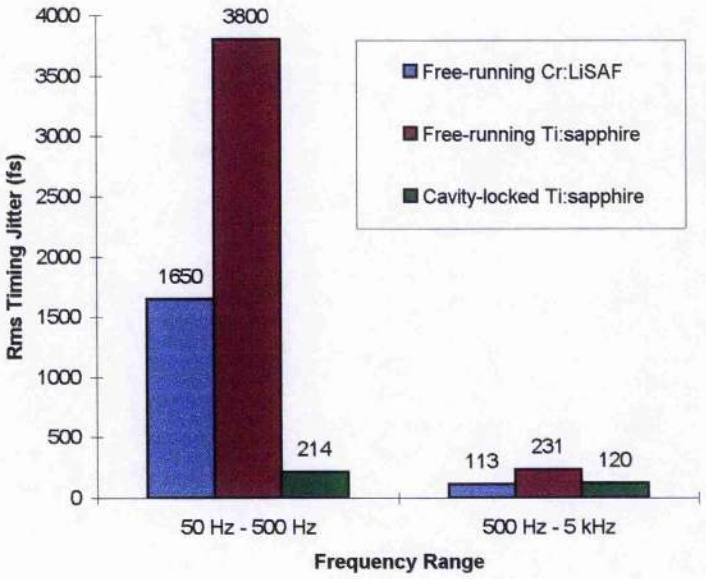

FIGURE 4.37 *Rms timing jitter (fs) in the free-running Cr:LiSAF laser, the free-running Ti:sapphire laser and the cavity-locked Ti:sapphire laser. Note that the Cr:LiSAF laser has the lowest figure in the 500 Hz - 5 kHz range.*

Calculations suggest that the streak camera is not limited by pulse train noise at sub-picosecond resolutions[12]. In this regime, electron group-velocity dispersion and the maximum limit of the camera streak speed are the most significant factors affecting camera resolution. The camera streak speed limits the camera resolution to ~ 700 fs (higher speeds result in distortions in the streak image). Group velocity dispersion occurs because electrons are ejected from the photocathode with a range of velocities, and the velocity spread decreases with voltage. This effect was significant in the Cr:LiSAF laser because it was observed that reducing the voltage on the mesh caused the temporal resolution of the camera to deteriorate. Another

factor in explaining the Cr:LiSAF system's superior performance may be that its output is at 860 nm, which is closer to the cut-off of the cathode at around 890 nm than the 800 nm output from the Ti:sapphire laser. This means that photons from a Cr:LiSAF laser eject electrons over a narrower range of energies than photons from a Ti:sapphire laser. The velocity spread of the ejected photons will therefore be narrower for the Cr:LiSAF laser.

4.4 Concluding Remarks

By implementing the routes to low-threshold self-modelocking described in Chapter 3, a Cr:LiSAF laser has been constructed that produced sub-100 fs pulses for just 73 mW incident pump power. This represents a three-fold reduction on the lowest previously reported pump power requirement. The laser was pumped by a self-injection-locked AlGaInP diode laser. Self-infection locking transformed the far-field output pattern of the diode from a top-hat profile with a width of ~ 10° to a Gaussian lobe of width ~1°. This lobe contained 70 - 80 % of the diode output power.

The resonator of the Cr:LiSAF laser was based around a 'W-cavity' configuration. This arrangement was advantageous for low-threshold operation because it used AR-coated plane/plane crystal surfaces to reduce reflection losses rather than the conventional Brewster-angled surfaces. This led to reduced spot sizes in the gain crystal and hence to a reduced CW and modelocking threshold. It also resulted in a highly localised beam waist in the crystal, and this waist could be positioned very accurately in the optimum position for self-modelocking. This position was near to the optimum position for low-threshold CW operation, which further enhanced the performance of the laser. It was predicted, however, that an AR-coated crystal would be inferior to a Brewster-angled crystal in a higher-power laser system because of losses resulting from the AR coatings. The novel W-cavity design also offers the potential for the intimate coupling of a tightly focused pump beam into the gain crystal of a conventional Z-cavity, although this approach was not exploited in this work.

The laser had a CW threshold of 45 mW and a slope efficiency of 1.1 % with 100 mm ROC folding mirrors and a CW threshold of 35 mW and a slope efficiency of

1.0 % with the 75 mm ROC mirrors. In both cases, the maximum output power at 150 mW pump power was ~1.2 mW. The CW tuning curve of the laser was modulated with a period of 4.6 nm. This phenomenon was found to result from a slight misalignment of the c-axis of the Cr:LiSAF crystal, which caused the crystal and the dispersion-compensation prisms to act in combination to form an intracavity birefringent filter. The birefringent Cr:LiSAF crystal introduced an elliptical polarisation into the laser field, and the vertical component of this was lost at the intracavity prisms. In the modelocked laser, pulses saw a continuous loss at all wavelengths, rather than a loss modulation, because orthogonally polarised pulses walked away from each other in the birefringent crystal and became de-coupled and unable to recombine to give horizontally-polarised light at any wavelength. This severely impeded the tuning of the modelocked laser, and although the effect could be easily removed by rotating the misaligned crystal, this was not practical in our particular system.

	Pump power 100 mW	Pump power 150 mW
100 mm ROC. mirrors		
SF14 prisms	140 fs	93 fs
LAK L21 prisms	99 fs	60 fs
75 mm ROC mirrors		
SF14 prisms	77 fs	65 fs
LAK L21 prisms	65 fs	54 fs

TABLE 4.1 *Pulse durations at 100 mW and 150 mW pump power for 100 mm ROC mirrors and 75 mm ROC. mirrors, and for SF14 and LaK L21 prisms.*

Despite these problems, the laser produced sub-100 fs at remarkably low pump powers. Reducing the intracavity third-order dispersion and reducing the intracavity waist both lowered still further the power required for the generation of such pulses, as expected. The pulse durations obtained from various laser configurations are presented again in Table 4.1.

The threshold pump powers for self-modelocking were 88 mW - 90 mW with the 100 mm ROC mirrors, and 70 mW - 73 mW with the 75 mm ROC mirrors. Characterisation of the various steps in the transition from CW to self-modelocked operation was achieved by monitoring the power-transfer characteristics of the laser. Although the design of the laser was optimised for self-modelocking by considering the Cerullo model of hard-aperture self-modelocking, there was some doubt as to whether the laser was operating in a hard-aperture, soft-aperture or a hybrid regime.

Although self-modelocking in the laser was not self-starting in the conventional sense, regenerative feedback circuitry restarted pulsed operation if the pump or intracavity beams were blocked. Given the low pump powers involved, this was an indication of the reliability of the modelocked operation. The laser also had very good free-running noise properties, comparable to those of a cavity-locked Ti:sapphire. This permitted the evaluation of a streak camera in the sub-picosecond regime, previously only accessible with a cavity-locked Ti:sapphire laser and a shuttered camera.

Despite the low pump-power self-modelocking achieved in this laser, further improvements could be made to the system in order to reduce pump-power requirements still further. The principal advantage of the W-cavity for low-threshold operation, namely the use of AR coatings rather than Brewster angles, could easily be exploited in a conventional Z-cavity and this would eliminate one cavity mirror and hence reduce round-trip losses. Eliminating the birefringence effects caused by the misaligned crystal would further enhance modelocked operation. Replacing the Brewster-rod AO modulator with a combined prism-modulator would reduce round-trip losses, and optimisation of the regenerative-initiation circuitry would also reduce the pump power required for modelocking. Taken together, these improvements would be likely to bring the pump power requirement for sub-100 fs pulses closer to perhaps 50 mW; and a power requirement around this level would make a self-modelocked laser pumped by one or two narrow-stripe, diffraction-limited diode lasers a practical possibility. As such lasers are available for about $300, rather than the several thousand dollars

purchase price of broad-stripe 500 mW devices, this would represent a major advance with exciting prospects for more cost-competitive commercial systems.

---

[1] M. Ramaswamy-Paye and J. G. Fujimoto, Opt. Lett. **19**, 1756 (1994)

[2] B. E. Bouma and J. G. Fujimoto, Opt. Lett. **21**, 134 (1996)

[3] C. L. Pan, C. D. Hwang, J.-C. Kuo, J.-M. Shieh and K.-H. Wu, Opt. Lett. **17**, 1547 (1992)

[4] Personal communication with C. Yelland, University of St. Andrews

[5] M. J. P. Dymott and A. I. Ferguson, Opt. Lett. **19**, 1988 (1994) and M. J. P. Dymott and A. I. Ferguson, Opt. Lett. **20**, 1157 (1995)

[6] K. Oppo, Ph.D. thesis, University of St. Andrews, 1996, Chapter 2

[7] G. Cerullo, S. De Silvestri and V. Magni, Opt. Lett. **19**, 1040 (1994)

[8] D. von der Linde, Appl. Phys. B **39**, 201 (1986)

[9] M. J. W. Rodwell, D. M. Bloom, K. J. Weingarten, IEEE J. Quantum Electron. **25**, 817 (1989)

[10] D. R. Walker, D. W. Crust, W. E. Sleat and W. Sibbett, IEEE J. Quantum Electron. **28**, 289 (1992)

[11] J. M. Evans, Ph.D. Thesis, University of St. Andrews, 1993, Chapter 5

[12] K. Oppo, Ph.D. Thesis, University of St. Andrews, 1996, Chapter 3

[13] D. E. Spence, J. M. Dudley, K. Lamb, W. E. Sleat and W. Sibbett, Opt. Lett. **19**, 481 (1994)

[14] Y. Liu, Ph.D. Thesis, University of St. Andrews, 1992

5. Low-threshold, All-solid-state, Self-modelocked Cr:LiSGaF Lasers

5.1 Introduction

In this Chapter, I describe two laser systems that are refinements of the low-threshold, all-solid-state Cr:LiSAF laser described in Chapter 4. These systems are based on another member of the colquiriite family, Cr^{3+}-doped $LiSrGaF_6$ (Cr:LiSGaF). This laser crystal is closely related to Cr:LiSAF but has attracted attention recently because it has been reported to have superior thermal properties and exhibit lower scattering losses.

The first system described below is a self-modelocked laser based on a Cr:LiSGaF gain crystal placed in a Z-cavity. This system is an improvement on the Cr:LiSAF W-cavity because the Cr:LiSGaF crystal exhibits lower losses than the Cr:LiSAF crystal, and the superfluous HR coating on the gain crystal of the W-cavity has been eliminated. The system was developed to give a higher output power than the W-cavity rather than a lower modelocking threshold. The performance of the laser suggests, however, that a lower modelocking threshold would have been demonstrated if optimisation of threshold had been attempted.

The second system is a self-modelocked laser based on a Cr:LiSGaF gain crystal in a three-mirror cavity in which a prism-modulator is utilised for regenerative initiation of the modelocking process. This system was developed with a view to demonstrating a still lower modelocking threshold. In going from the first Cr:LiSGaF laser to this system two mirror reflections and two passes of a discrete modulator have been eliminated from each cavity round trip. This system represents the logical conclusion of the process of simplifying low-threshold self-modelocked laser cavities. Before the three-mirror cavity itself is described, I will consider models of the stability and modelocking properties of three-mirror resonators. In particular, I will consider the similarities and differences between the stability properties of four-mirror resonators and two distinct forms of three-

mirror resonator, paying particular regard to the implications of these properties for self-modelocking. I will also present the results of Cerullo-style modelling of the two forms of three-mirror resonator.

5.2 Cr:LiSGaF Lasers

A laser based on Cr:LiSGaF was first demonstrated shortly after the crystal was grown in 1992[1] and a diode-pumped, self-modelocked device was demonstrated in 1995 [2]. Cr:LiSGaF attracted attention as a laser material because it was reported to exhibit optical properties that were similar to those of Cr:LiSAF, and thermal properties that were superior (see Appendix A). Specifically, the two crystals have similar intrinsic efficiencies of ~ 52 % (the intrinsic efficiency is the slope efficiency in the idealised case of zero passive loss), similar peak emission wavelengths (835 nm for Cr:LiSGaF, 846 nm for Cr:LiSAF) and closely matched absorption bands. Thermally, the coefficients of expansion are of a lower magnitude for Cr:LiSGaF than for Cr:LiSAF, they are also more isotropic and Cr:LiSGaF exhibits a lower melting point.

The thermo-mechanical properties of a crystal are important factors in determining the scattering losses that will be introduced during its growth. The superior thermal properties of Cr:LiSGaF would consequently be expected to lead to lower scattering losses than those of Cr:LiSAF, and initial experiments have suggested that this is indeed the case[3].

Cr:LiSGaF lasers have generated significantly higher powers than those obtained from typical self-modelocked Cr:LiSAF laser crystals. This reinforces the suggestion that Cr:LiSGaF is a superior laser material to Cr:LiSAF. For example, a Cr:LiSGaF laser pumped by a Kr^+-ion mainframe laser produced 900 mW of CW output power and self-modelocked output powers of 50 - 200 mW, while the use of an additional intracavity nonlinear element increased the modelocked output power to 300 mW [4]. Another self-modelocked Cr:LiSGaF laser utilising low-loss Gires-Tournois structured-dielectric mirrors for dispersion control produced 44-fs pulses at 200 mW [5]. The laser of Reference 4 was pumped with over 2 W of 670 nm light, and this suggests that the thermally-induced roll-off effects that plagued Cr:LiSAF are less significant in Cr:LiSGaF.

Because Cr:LiSGaF can be grown with very low scattering losses it is an ideal gain crystal for a diode-pumped, low-threshold self-modelocked laser systems. Two such systems will now be described.

5.3 The Low-threshold, All-solid-state, Self-modelocked Cr:LiSGaF Z-cavity Laser

The Cr:LiSGaF laser described in this section performed similarly to the Cr:LiSAF system described in Chapter 4. However, the improved optical quality of the crystal permitted the use of an output coupler in the laser. The Cr:LiSGaF system was therefore able to give output powers that were an order of magnitude higher than those of the Cr:LiSAF system.

The Cr:LiSGaF laser cavity is shown in Figure 5.1. It incorporates similar elements to those of the W-cavity used in the Cr:LiSAF experiments, but it is based around a more conventional Z-cavity; the loss associated with the additional HR coating on the crystal in the W-cavity has therefore been eliminated. The LiSGaF crystal was 10 mm long and it was 3 % doped with Cr^{3+} ions. Both crystal facets were anti-reflection coated for 850 nm, and their reflectivity was ~ 0.1 % at this wavelength. The cavity mirrors were the same as those previously, with the exception of the end-mirror in the arm that did not contain the prisms; that mirror was a 1.5 % output-coupler rather than a high-reflector. The pump focusing lens had a focal length of 50 mm and the folding mirrors had radii of curvature of 75

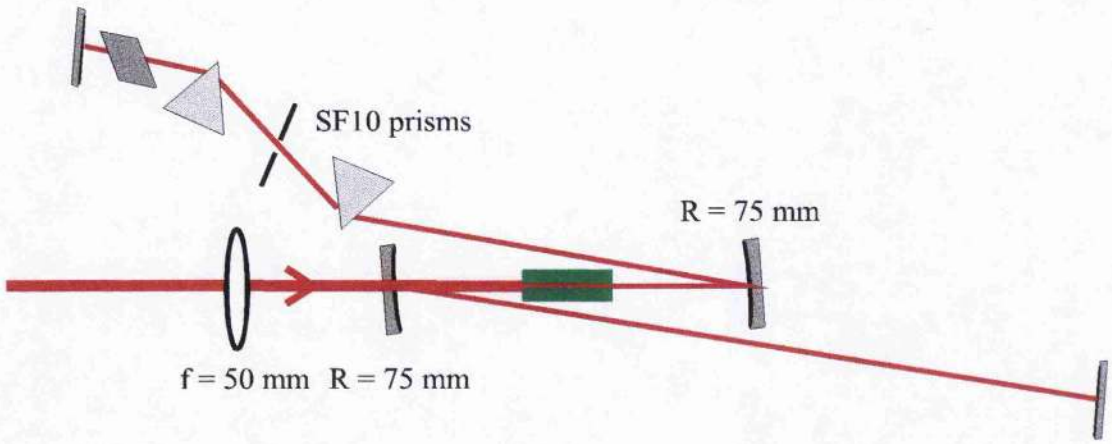

FIGURE 5.1 *The Cr:LiSGaF laser cavity.*

mm. The folding angles at the folding mirrors were approximately 3°. The intracavity prisms were made from SF 10 glass and a tuning slit was placed between them, but there was no hard-aperture self-modelocking slit. The modulator was the Brimrose model FQM442 AO modulator used previously. The pump laser was the self-injection-locked AlGaInP semiconductor laser described in Section 4.2.

The power-transfer characteristics of the Cr:LiSGaF laser - without intracavity prisms or modulator - are shown in Figure 5.2 for a highly reflecting end-mirror, a 1.5 % output-coupler and a 3 % output coupler. The slopes of the 1.5 % output-coupler and 3 % output-coupler lines are almost identical, confirming that the losses introduced by the Cr:LiSGaF crystal are very much less than 1.5 %. With all intracavity elements in place, the laser had a CW threshold as low as 30 mW and a slope efficiency of 9 %.

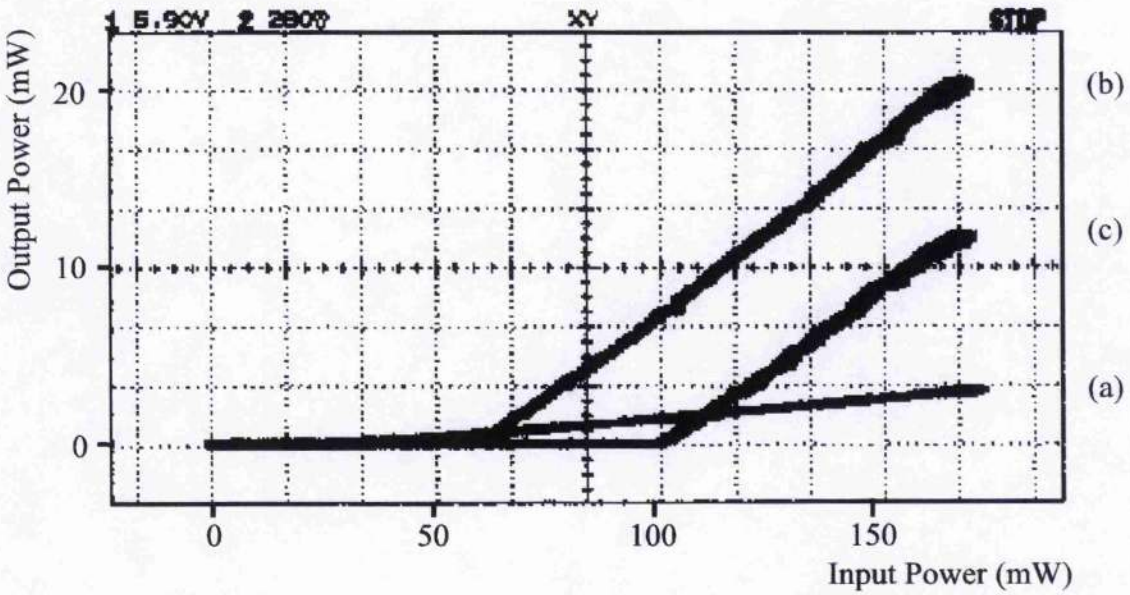

FIGURE 5.2 *The power-transfer characteristics of the Cr:LiSGaF laser, without intracavity prisms or modulator, with (a) a highly reflecting end-mirror, for which T = 0.08 % (b) a 1.5 % output-coupler and (c) a 3 % output-coupler.*

The Cr:LiSGaF crystal was mounted on a goniometer in order to investigate the birefringence effects that were previously observed in Cr:LiSAF (Section 4.3.2.1). As the Cr:LiSGaF laser was tuned, its output was monitored via a monochromator and CCD array. A modulation of the tuning curve was observed that was similar to

that seen in Cr:LiSAF (Section 4.3.2.1). The Cr:LiSGaF crystal was then rotated until the laser could be tuned smoothly across the whole of its range. Figure 5.3 shows tuning curves for the crystal in the optimised position and rotated 3° away from this position, the rotation being in a plane perpendicular to the axis of the intracavity beam. The separation of the two peaks of Figure 5.3 was ~ 50 nm. If the crystal had been made from Cr:LiSAF, the model described in Section 4.3.2.1 would have predicted a modulation with a period of 11 nm. The modulation of the Cr:LiSGaF tuning curve is not as clean as that of the Cr:LiSAF curve, but this difference in modulation period suggests that there are differences in the Sellmeier expressions of Cr:LiSGaF and Cr:LiSAF. (Sellmeier equations for Cr:LiSGaF were not available at the time of writing because most researchers appear to have assumed that they would be the same as those of Cr:LiSAF.)

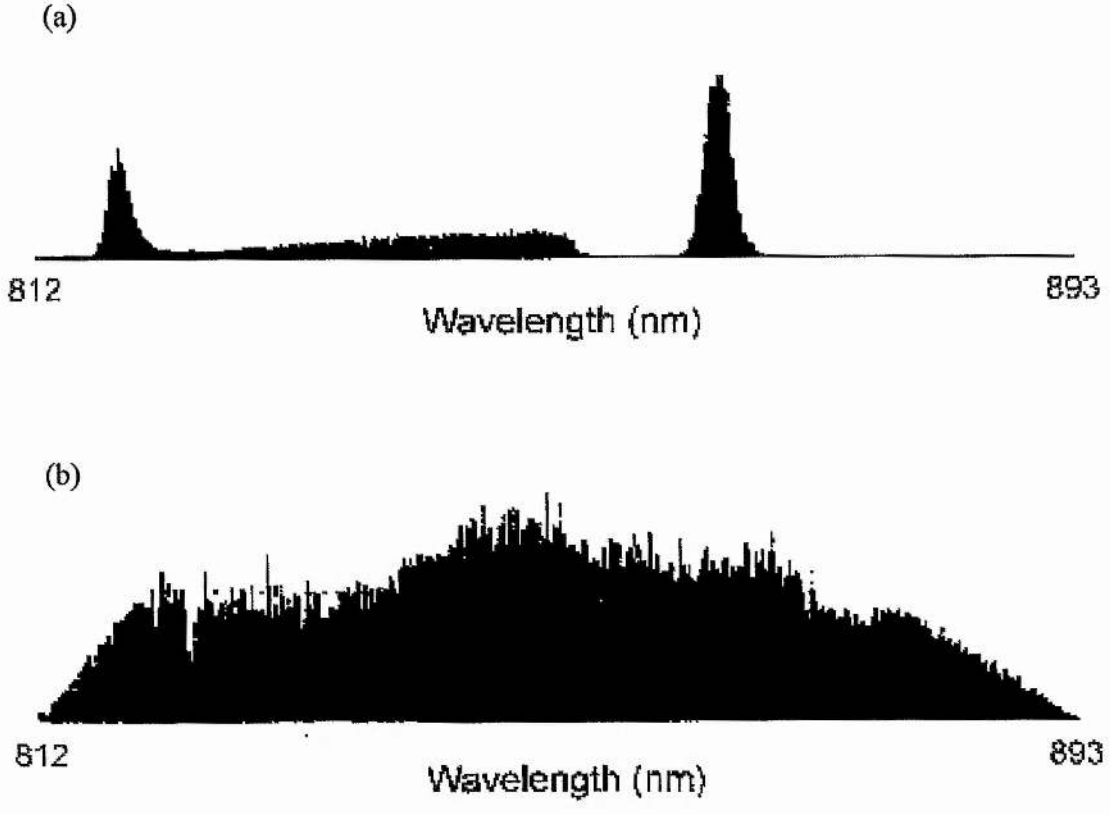

FIGURE 5.3 *The CW tuning curve of the Cr:LiSGaF laser with the crystal c-axis (a) rotated ~ 3° from the plane of the intracavity prisms and (b) parallel to the plane of the intracavity prisms.*

The results in Figure 5.3 demonstrate that, as predicted in Chapter 4, modulation effects due to crystal birefringence can be completely eliminated by careful alignment of the crystal c-axis.

When self-modelocked, the Cr:LiSGaF laser gave transform-limited pulses of 87 fs duration (Figure 5.4). The modelocked output power was 11.5 mW through a 1.5 % output-coupler, for a pump power of 170 mW. In comparison, the Cr:LiSAF laser described in the previous chapter gave 93 fs pulses (with SF14 prisms) and the output power was 1 mW through a high-reflector, for a pump power of 150 mW.

This result demonstrates that useable output powers can be obtained from a low-threshold self-modelocked Cr:LiSAF laser pumped with relatively modest pump

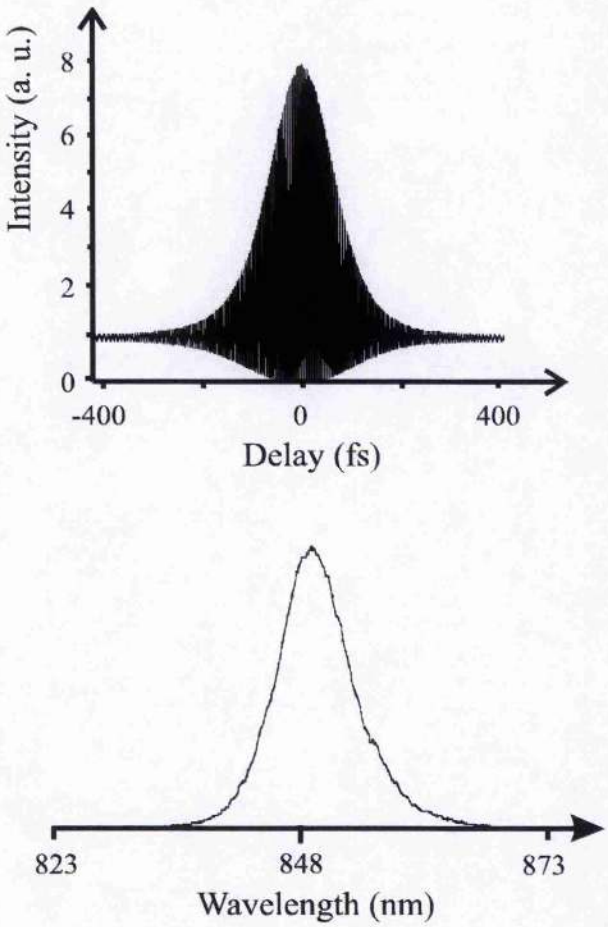

FIGURE 5.4 *Interferometric autocorrelation and spectrum for pulses from the Cr:LiSGaF laser. The average output power of the pulses was 11.5 mW for 170 mW pump power and* $\Delta\tau = 87$ *fs,* $\lambda = 850$ *nm,* $\Delta\lambda = 8.3$ *nm and* $\Delta\nu\Delta\tau = 0.30$.

powers (170 mW is below the CW threshold of many Cr:LiSAF systems). More significantly, if the output-coupler of the Cr:LiSGaF laser were replaced with a high-reflector then the intracavity power would be significantly higher in the Cr:LiSGaF laser than it was in the Cr:LiSAF laser for the same pump power. One would expect this to result in shorter pulses or, equivalently, in a lower pump-power requirement for pulses of a particular duration. Replacing the SF10 prisms with fused-silica prisms would have the same effect. One would therefore expect to obtain sub-100 fs pulses at still lower pump powers. (NB: for a cavity utilising a 10 mm crystal, fused-silica prisms lead to a lower net round-trip third-order dispersion than LaK L21 prisms. However, LaK L21 prisms lead to lower third-order dispersion for a 24 mm crystal such as that used in the W-cavity of Chapter 4).

5.4 Low-threshold, All-solid-state, Self-modelocked Operation of a Three-mirror Cr:LiSGaF Laser

The performance of the laser described above is superior to that of the laser described in the previous chapter. The improvement can be attributed to the reduction in round-trip loss that results from the lower scattering loss of the Cr:LiSGaF crystal and the elimination of the superfluous HR coating on the laser crystal of the W-cavity. The elimination of other sources of round-trip loss would again reduce the pump power required to obtain a particular intracavity power, and hence a particular pulse duration.

In one round trip, the field inside a Z-cavity experiences reflection losses from several surfaces: six mirror reflections, four reflections from the crystal facets, four reflections from the modulator facets and eight reflections from the surfaces of the dispersion-compensation prisms. Eliminating any of these sources of loss would be advantageous. Other methods of achieving dispersion compensation are available, such as Gires-Tournois interferometers and chirped-dielectric mirrors, but these devices have relatively high insertion losses and involve multiple passes that would introduce still more loss. The losses associated with the modulator, however, can be minimised by using a combined prism-modulator, in which the piezo-electric transducer of the modulator is deposited onto a dielectric block cut as a prism rather than a Brewster slab[6].

Intracavity losses can also be reduced by reducing the number of mirrors in the resonator. Self-modelocked lasers based on three-mirror resonators have recently been demonstrated[7-9]. These lasers have only four mirror reflections per round-trip, and if the back surface of the crystal is HR-coated to form one of these mirrors then two reflections from the crystal surface are also eliminated. The rest of this chapter is devoted to a consideration of the self-modelocking properties of three-mirror resonators.

5.4.1 The Magni Model

The model used to study three-mirror resonators was an implementation[10] of the most complete form of the Cerullo model introduced in Chapter 3 [11]. This form of the model, referred to as the 'Magni model' henceforth, is capable of making accurate predictions of spot-size variations in both the sagittal and tangential planes of the cavity because it takes into account effects resulting from astigmatism in the intracavity beam. It can be used to predict the cavity-mode spot sizes at both the cavity end mirror and the pumped surface of the laser crystal itself. The suitability of the cavity for both hard- and soft-aperture self-modelocking can therefore be studied.

In the Magni model, the Kerr medium is divided into thin slices, each of which behaves as a nonlinear lens with a dioptric power ϕ_x in the x-plane given by

$$\phi_x = p\left(\frac{\lambda}{n\pi}\right)^2\left(\frac{w_x}{w_y}\right)^{1/2}\frac{1}{w_x^2}dz$$

EQUATION 5.1

where w_x and w_y are the spot sizes in orthogonal planes and p is the intracavity beam power P normalised to the critical power for self-trapping P_c. The subscripts x and y are reversed in the expression for the dioptric power in the y-plane, ϕ_y. P_c is given by the expression

$$P_c = \frac{\lambda^2}{2\pi n n_2}.$$

EQUATION 5.2

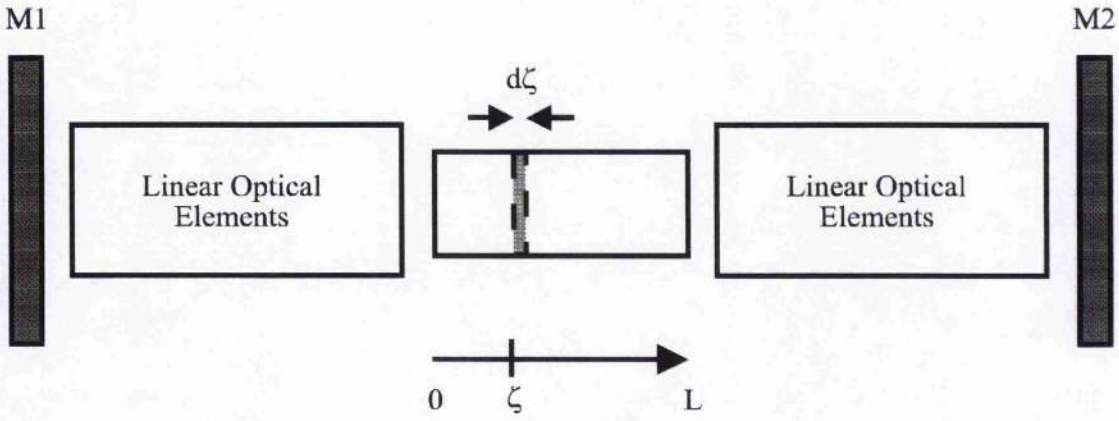

FIGURE 5.5 *The general resonator considered in the Magni model. M1 and M2 are plane mirrors; if a cavity has a curved end mirror then that curvature is included in the matrix of linear optical elements of the appropriate cavity arm.*

The general resonator considered in the Magni model is shown in Figure 5.5. The round-trip propagation matrix is denoted

$$\begin{pmatrix} \tilde{A}(\zeta) & \tilde{B}(\zeta) \\ \tilde{C}(\zeta) & \tilde{D}(\zeta) \end{pmatrix}.$$

EQUATION 5.3

The matrix describing propagation from M1 to M2 is denoted

$$\begin{pmatrix} A & B \\ C & D \end{pmatrix}$$

EQUATION 5.4

and the matrices representing propagation from the nonlinear slice at ζ to mirror M1 and mirror M2 are denoted

$$\begin{pmatrix} A_1 & B_1(\zeta) \\ C_1 & D_1(\zeta) \end{pmatrix} \text{ and } \begin{pmatrix} A_2 & B_2(\zeta) \\ C_2 & D_2(\zeta) \end{pmatrix},$$

EQUATION 5.5

respectively. In order to calculate δ_{1x}, the small-signal spot-size variation at M1 in the x-plane, Magni integrates the effects of each nonlinear slice in the Kerr medium. To do this, he makes the key assumption that, for intracavity powers

much less than the critical power P_c, the spot sizes in each slice of the crystal are not affected by lensing in the other slices. The final expression for δ_{1x} is

$$\delta_{1x} = \left(\frac{1}{2w_x}\frac{dw_x}{dp}\right)_{p=0} = -\frac{1}{n}\left(\frac{1-S_y^2}{1-S_x^2}\right)^{\frac{1}{4}}\int_0^L \left|\frac{\tilde{B}_x}{\tilde{B}_y}\right|^{\frac{1}{2}} \frac{B_{2x}D_{2x}S_x + B_{1x}D_{1x}}{\tilde{B}_x^2}\,d\zeta$$

EQUATION 5.6

where the stability parameters S_x and S_y take the form

$$S_x = \frac{\tilde{A}_x + \tilde{D}_x}{2} = A_x D_x + B_x C_x .$$

EQUATION 5.7

The value of δ at an arbitrary plane between M1 and the nonlinear crystal is given by

$$\delta_x = \frac{A_x'^2 - \left(\frac{\lambda B_x'}{\pi w_{1Lx}}\right)^2}{A_x'^2 + \left(\frac{\lambda B_x'}{\pi w_{1Lx}}\right)^2}\delta_{1x}$$

EQUATION 5.8

where A_x' and B_x' are elements of the matrix describing propagation from mirror M1 to the plane of interest.

5.4.2 Stability Properties of Three-mirror Resonators

Before discussing the results of the modelling of three-mirror lasers using the Magni model, I will consider briefly the stability properties of these cavities. Stability is an important factor in the self-modelocking of a laser cavity because the propensity of a laser to modelock can increase near a stability limit, as highlighted in Chapter 3. Figure 5.6 shows the variation of the stability parameter S with folding mirror separation z.

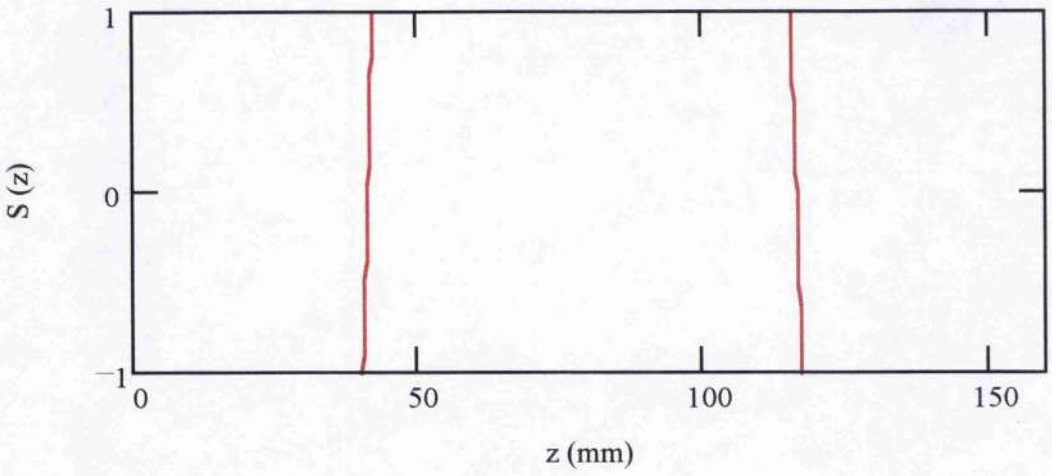

FIGURE 5.6 *The variation of the stability parameter S with folding mirror separation z for a three-mirror cavity employing folding-mirrors of radii of curvature 75 mm. The cavity is stable for -1 < S < +1. In the leftmost stability region one of the folding-mirrors is ~ 20 μm from the intracavity focus, whereas in the rightmost stability region the mirror is 75 mm from the focus.*

For a resonator that has end mirrors of finite radii of curvature, the two expressions given in Equation 5.7 will only agree if the radii of curvature are taken to be twice their actual value when calculating the single-pass matrix elements A_x, B_x, C_x and D_x. This can be understood if we consider the infinite waveguide equivalent of a laser resonator (Figure 5.7). It appears that curved mirrors should be considered equivalent to bi-convex lenses in such a system. If a resonator end-mirror is curved then single pass propagation through the resonator involves passing through only half of the lens equivalent to this end-mirror. The mirror is, therefore, equivalent to a plano-convex lens of twice the actual focal length of the mirror.

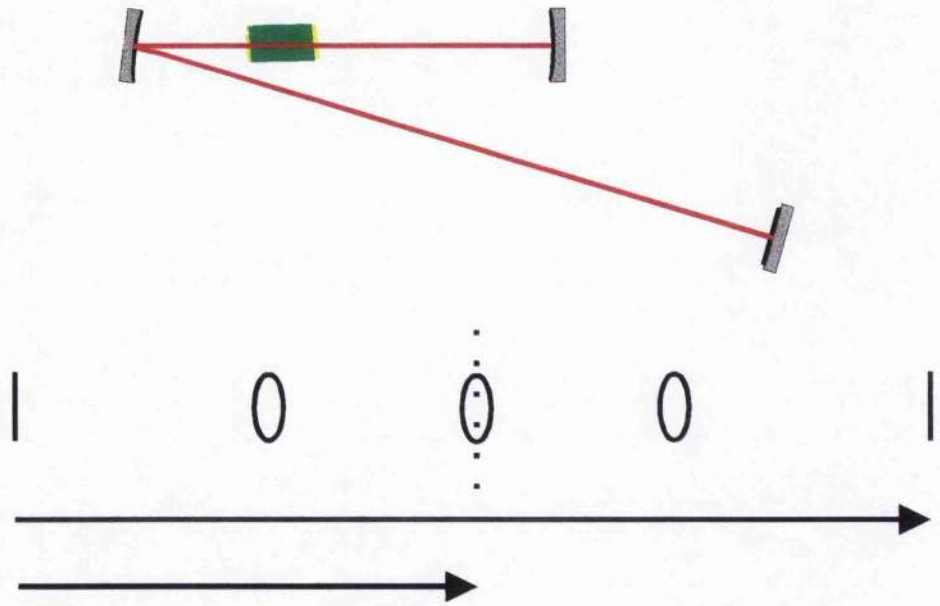

FIGURE 5.7 *A laser with one end mirror that has a finite radius of curvature, together with a segment of its associated infinite periodic waveguide. If we consider a complete trip around the cavity then each bounce from a curved mirror can be treated as passage through a lens of the same focal length as that of the mirror. However, a single pass through the cavity starting at the plane end mirror will end on the curved end mirror. In the waveguide model, this is equivalent to propagation through half a lens. If we treat the equivalent lens as being a bi-convex lens of focal length f, then we can consider propagation through half the lens to be equivalent to propagation through a plano-convex lens of focal length 2f.*

Figure 5.6 shows that, in general, a three-mirror resonator will have two stability regions when z is varied. However, these regions do not correspond to the two regions that are obtained in a four-mirror resonator (see Appendix B, Figure 3.12). In a four-mirror resonator, the two stability regions correspond to cavity configurations in which the resonator is stable to plane-wave and spherical-wave imaging, respectively. In three-mirror resonators, the two stability regions result from the fact that there are, in general, two distances from an intracavity waist at which the radius of curvature of a curved mirror matches the radius of curvature of the optical wavefront. The radius of curvature of the optical wavefront of a focused Gaussian beam is at a maximum (infinity) at its waist and at an infinite distance from its waist. It reaches a minimum at a distance

$$x_R = \frac{\pi w_0^2}{\lambda}$$

EQUATION 5.9

from its waist, where w_0 is the waist radius and λ is the wavelength. The parameter x_R is the Rayleigh range[12]. The radius of curvature at this point is given by

$$R_{min} = x_R\left[1+\left(\frac{\pi w_0^2}{\lambda x_R}\right)^2\right] = \frac{2\pi w_0^2}{\lambda}.$$

EQUATION 5.10

All radii of curvature greater than R_{min} are therefore reached at two distances from the waist, one closer than x_R and one further away. A stable resonator can therefore be constructed with a mirror with a matching radius of curvature placed at either of these points. I will now consider the stability and modelocking properties of two important three-mirror resonator configurations (see Figure 5.8).

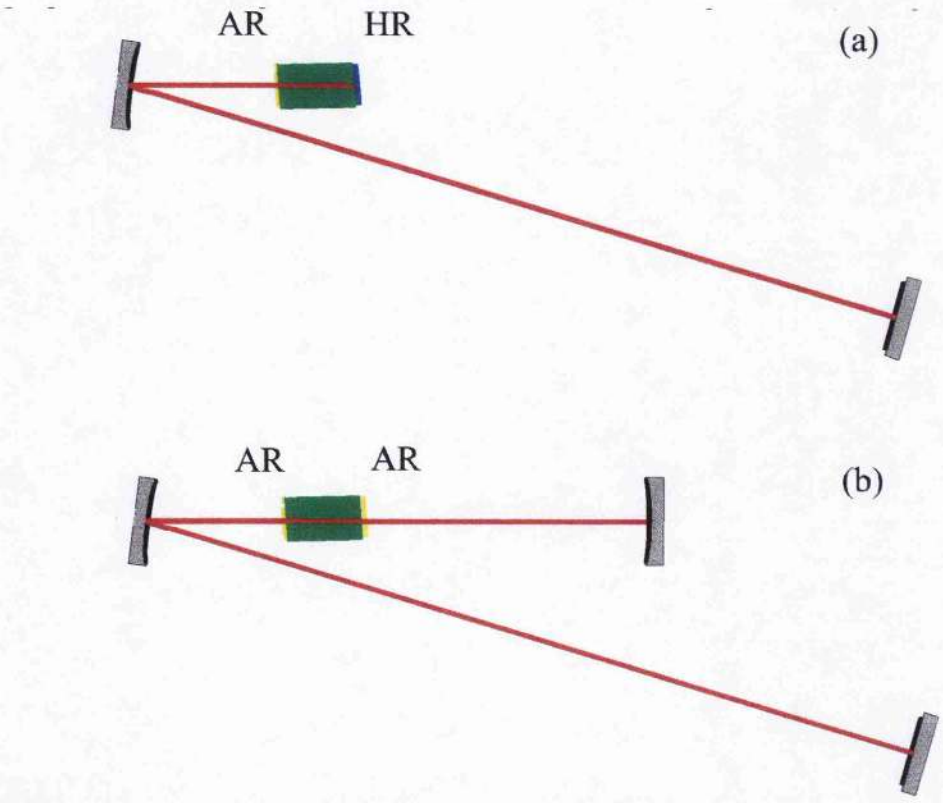

FIGURE 5.8 *Two three-mirror cavities: (a) semi-monolithic (b) retro-reflecting.*

One of these configurations, the semi-monolithic configuration, operates in the x-less-than-x_R stability region. The other, dubbed the retroreflector configuration, operates in the x-greater-than-x_R stability region.

5.4.2.1 The Semi-monolithic Laser

The semi-monolithic laser is important historically because the first three-mirror laser to be self-modelocked was based upon this geometry[7]. In the semi-monolithic laser, a plane mirror is coated onto the rear surface of the crystal itself. A plane mirror has an infinite radius of curvature, and a three-mirror resonator utilising a plane mirror in its folding section can therefore only be stable if the mirror is placed at infinity (x-greater-than-x_R, but somewhat impractical) or at the intracavity beam waist (x-less-than-x_R). Conversely, the intracavity beam waist of a stable three-mirror semi-monolithic laser will always be positioned at the plane mirror at the end face of the crystal. That is not the case for the beam waist in a four-mirror resonator, which can be positioned anywhere within the laser crystal.

Because the intracavity waist must always be on the rear surface of the laser crystal, the number of degrees of freedom of adjustment of a semi-monolithic resonator is reduced when compared with a four-mirror resonator. In fact, two degrees of freedom are lost, because in a four-mirror resonator we can

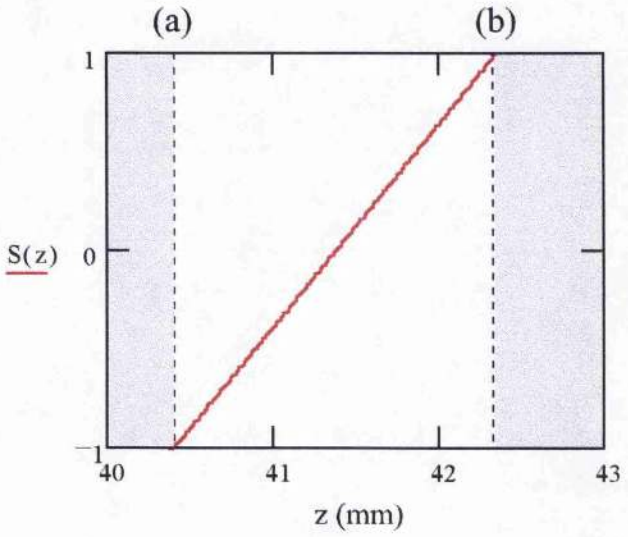

FIGURE 5.9 *The variation of S with z in the semi-monolithic laser. The planar-confocal stability limit (a) and the conjugate-plane stability limit (b) are marked.*

independently adjust the two arm lengths, the folding mirror separations and the position of the laser crystal, whereas in a semi-monolithic resonator we can independently adjust only one arm length and the folding mirror separation (*or* the crystal position). As will shortly become apparent, this reduction in the number of degrees of freedom of adjustment is significant in the self-modelocking of a semi-monolithic laser.

The variation of stability S with separation z in the semi-monolithic laser is shown in Figure 5.9. A comparison with the equivalent diagram for a four-mirror laser (Figure 3.12) shows an important difference: the variation is quadratic in the four-mirror case, but it is linear in the three-mirror case (to the first order in z). However, the stability limits (a) and (b) correspond directly to the four-mirror stability limits (i) and (iv); that is at stability limit (a) the intracavity beam degenerates into a plane wave in the arm of the resonator, and at stability limit (b) it degenerates into a spherical wave. Four-mirror stability limits (ii) and (iii), on the other hand, correspond to degeneration into a plane wave in one arm of the resonator and into a spherical wave in the other arm and *vice versa*, and clearly this has no analogy in a resonator with only one arm.

However, the symmetric-confocal stability limit does have an analogy in a three-mirror laser. Stability limits (ii) and (iii) become degenerate in a four-mirror laser when the cavity arm lengths are equal (see Appendix B). The symmetric-confocal condition occurs when the length of the cavity arms is equal to the effective focal length of the folding section. This condition can also occur in a three-mirror resonator but, crucially, in a three-mirror laser the symmetric-confocal configuration is not at a stability limit. In a four-mirror laser the symmetric-confocal configuration is ideal for self-modelocking because it is a critically stable configuration (S = -1) with a well-behaved intracavity beam. In a three-mirror laser, the intracavity beam is still well-behaved - indeed, it is has an identical profile to the beam in half of the four-mirror resonator - but it is maximally stable (S = 0). A laser in such a configuration cannot self-modelock, as we shall shortly see.

Although equivalent symmetric-confocal four- and three-mirror lasers have identical intracavity beam profiles, they have very different stability properties. This is a direct consequence of the reduction in the number of degrees of freedom of

adjustment that results from the change from four to three mirrors. The four-mirror symmetric-confocal resonator is critically stable because a small adjustment in the length of one of its arms will make it asymmetric and therefore unstable. The three-mirror confocal resonator is maximally stable because it cannot be made asymmetric in the same way; it only has one arm and so the 'two' arms seen on a round-trip will always be of the same length.

In the Cerullo model of four-mirror resonators, the propensity of a laser to self-modelock was characterised as a function of z, the folding mirror separation, and x, the distance from one of the folding mirrors to the face of the crystal. In a semi-monolithic three-mirror resonator, these parameters are degenerate because $z = x + L$, where L is the length of the crystal. Figure 5.10 therefore shows δ_x as a function of z only, both at the cavity end-mirror and at the coated face of the crystal. Note that Equation 5.8 cannot be used to calculate the variation of δ_x at the face of the crystal from its variation at the end mirror because these two positions are on

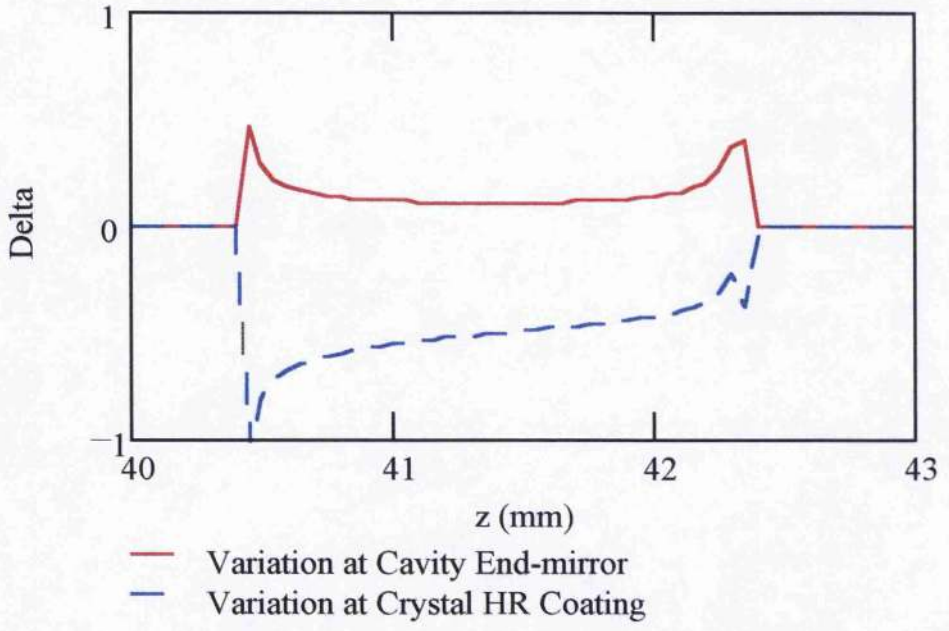

FIGURE 5.10 *Small-signal relative-spot-size variation δ_x as a function of z (= x + L) in the semi-monolithic laser at the cavity end-mirror (M1) and at the HR-coated face of the crystal (calculated by treating HR coating as M1; i.e. reversing subscripts 1 and 2 in the Magni model), for a constant cavity length of 800 mm. The modelocking parameter is arbitrarily set to zero for unstable cavity configurations.*

opposite sides of the nonlinear crystal. Instead, the Magni model must be re-worked by treating the coated face of the crystal as M1.

It is clear from Figure 5.10 that the semi-monolithic cavity cannot be made to self-modelock by using a slit at the end of the cavity arm, because δ_x is positive here for all values of z for which the cavity is stable. At the HR coated face of the crystal, on the other hand, δ_x becomes increasingly negative as stability limit (a) is approached. The laser is likely to be pumped through the HR coating, and it would therefore be possible to exploit the spot-size variation at this face by ensuring that the decrease in spot size resulted in an improved overlap with the pump beam. This was the approach taken by Fujimoto and co-workers[7,8].

5.4.2.2 The Retroreflector Laser

The other three-mirror cavity configuration that is of interest is the 'retroreflector' configuration, and the practical operation of a self-modelocked laser based upon this design is described below. In the retroreflector cavity, a curved mirror is placed at a distance from the intracavity beam focus that is approximately equal to its radius of curvature. The variation of stability S with folding mirror separation z is shown in Figure 5.11.

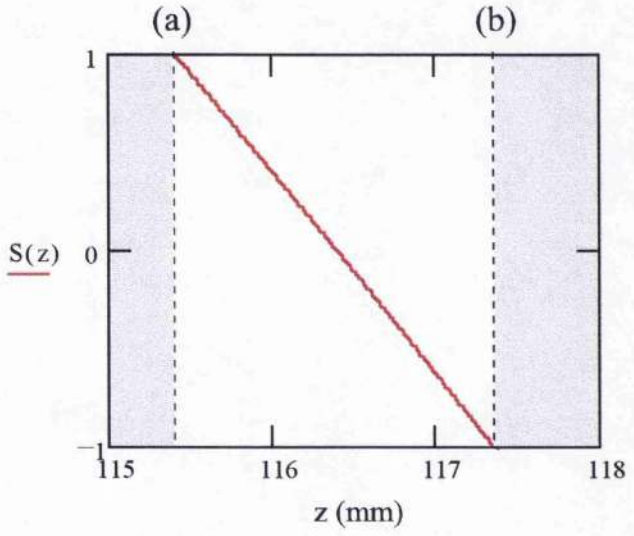

FIGURE 5.11 *The variation of S with z in the retroreflector laser. The planar-confocal stability limit (a) and the conjugate-plane stability limit (b) are marked.*

The stability properties of the retroreflector configuration are very similar to those of the semi-monolithic configuration. There are two points to note, however.

Firstly, the distance from the intracavity beam waist to the mirror is 'dead space' as far the geometric model of stability is concerned. That is to say, limits (a) and (b) occur at values of z that are equal to the corresponding values of z in the semi-monolithic laser plus the radius of curvature of the retroreflector. Secondly, given this first point, the only effect of the retroreflector is that it changes the sign of the slope of S in the stability diagram. All that this means is that a ray leaving an end mirror on one side of the cavity axis will return after one round trip to the same side in a retroreflector laser and to the other side in a semi-monolithic laser. As the beam inside a laser resonator is symmetric about the cavity axis this change has no physical effect.

As far as stability is concerned, then, the semi-monolithic and retroreflector cavities are effectively identical. However, a crystal can be positioned anywhere within the folding section of the retroreflector cavity, which means that retroreflector cavity has one more degree of freedom of adjustment than the semi-monolithic cavity, although it still has one less than a four-mirror cavity. Thus, in the retroreflector cavity, the arm length, folding mirror separation and the position of the crystal can all be adjusted.

This implies that we can plot a full Cerullo-style diagram for a retroreflector cavity. Figure 5.12 shows the variation of the small-signal relative-spot-size variation δ_x as a function of folding mirror separation z and crystal position x in the retroreflector laser at the face of the crystal nearest to the long cavity arm and at the end-mirror at the end of that arm (Figure 5.12).

Figure 5.12 shows that the plots pertinent to hard- and soft- aperture modelocking are 'photographic negatives' of each other. In both plots, δ_x reaches its extreme values at the edges of stability, as expected. It also reaches its extreme values when the intracavity mode is focused near to the end surfaces of the crystal, as was the case in a four-mirror resonator. But in the hard aperture plot, δ_x is positive when the intracavity mode is focused just inside the laser crystal and negative when it is focused just outside whereas, in the soft aperture plot, the reverse is true. These results imply that self-modelocking should be possible in both hard- and soft-aperture configurations, but it is likely to be more easily achieved in a soft-aperture configuration because in this case the intracavity mode is focused inside the laser

crystal and hence a good pump-cavity mode overlap is possible. This would certainly be preferred in a low-threshold laser, for the reasons discussed in Section 3.2.

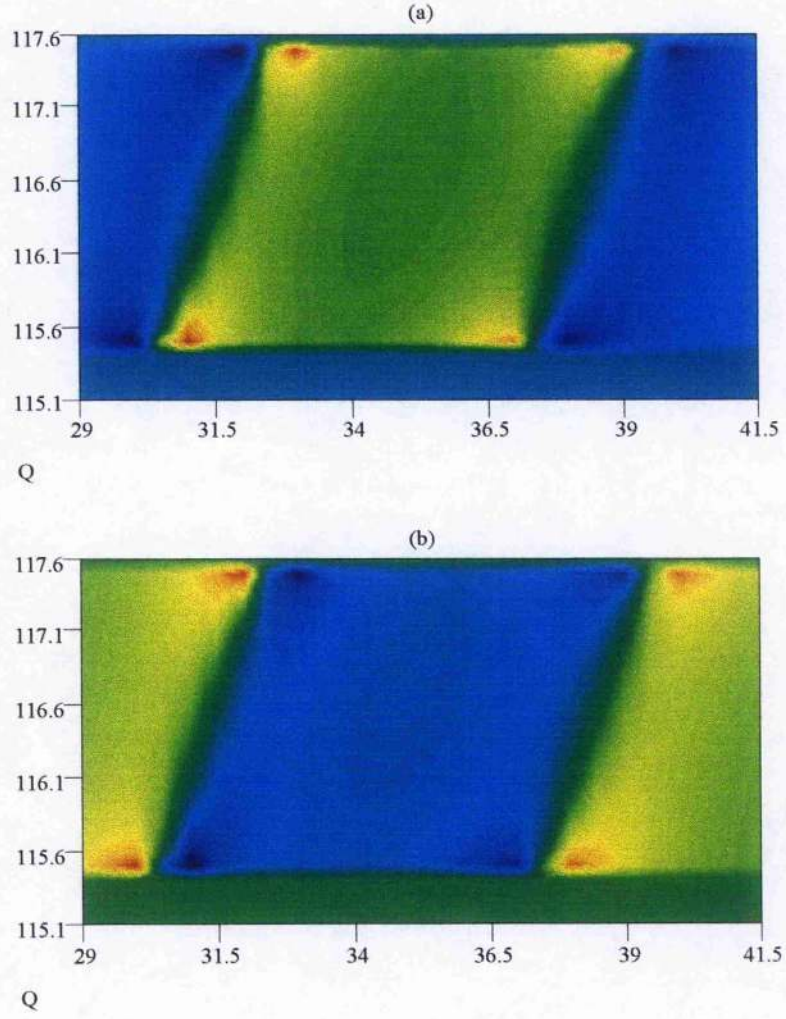

FIGURE 5.12 *Small-signal relative-spot-size variation δ_x as a function of folding mirror separation z (vertical axis, in mm) and crystal position x (horizontal axis, in mm) in the retroreflector laser (a) at the end-mirror at the end of the long cavity arm (M1) and (b) at the face of the crystal nearest to that arm (calculated using Equation 5.8), for a constant cavity length of 800 mm. The plots have been capped at δ_x = +1 (red peak) and δ_x = -1 (blue peak), and δ_x has been arbitrarily set to zero (green) for unstable cavity configurations.*

5.4.2.3 A Practical Retroreflector Laser

The three-mirror Cr:LiSGaF laser that was constructed in the laboratory is shown in Figure 5.13. The Cr:LiSGaF crystal was the same crystal as that used in the 4-

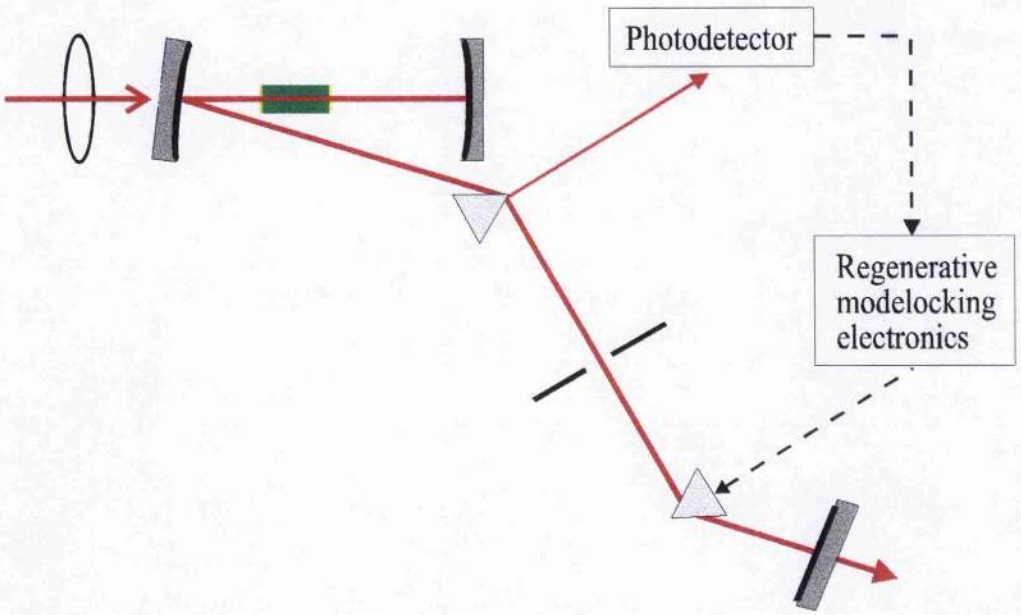

FIGURE 5.13 *The three-mirror Cr:LiSGaF laser.*

mirror cavity described in Section 5.3 and the mirrors were the same as those used in previous Cr:LiSGaF/Cr:LiSAF systems. The pump lens was of focal length 50 mm. In this three-mirror retroreflector configuration, the optical distance between the folding section mirrors was initially set up to be approximately equal to the focal length of one of the mirrors plus the radius of curvature of the other (75 mm / 2 + 75 mm = 112.5 mm = 115.4 mm physical length). The final separation that gave self-modelocking was approximately 117 mm physical length, which was near to the outer (quasi-concentric) limit of laser stability at 117.4 mm. The angle of incidence of the intracavity beam at the folding-section mirror was ~ 3°.

The three-mirror laser had a CW threshold of 14 mW without intracavity prisms and 31 mW with the prisms in place. This relatively large increase in threshold suggests that the prisms were rather lossy. The laser (with prisms) gave 890 μW output power for 134 mW pump power, a slope efficiency of 0.9 %.

In self-modelocked operation, intracavity GVD was compensated for with a fused-silica prism and a Spectra Physics Model 342A Mode Locker (which was a fused-silica prism with a piezo-electric transducer on its top surface, and came originally from a modelocked krypton ion laser). The prism separation was 56 cm, implying SPM balanced by ~600 fs^2 of positive GVD. The residual third-order dispersion

was -71 fs^3 (had LaK L21 prisms been used in this laser, the corresponding figure would have been -442 fs^3) The laser was modelocked in a regenerative-initiation configuration similar to that described in previous chapters. However, the cavity length of this laser was only 870 mm, corresponding to a pulse repetition rate of 173 MHz, and so the divide-by-four circuitry used in the regenerative set-up in previous experiments was replaced with a divide-by-two circuit. The modelocker resonances were very weak around 90 MHz, and so it was necessary to operate near to a resonance in order to obtain sufficient modulation for modelocking. In the previous systems, the modulator had been operated between resonances; operating on a resonance makes modelocking more difficult to achieve because the resonances are shifted upwards in frequency as the modulator heats up. However, when the modelocking was fully optimised, these effects did not affect pulsed operation in the Cr:LiSGaF laser.

When modelocked, the laser produced transform-limited 84 fs pulses at 116 mW pump power, with an output power of 470 μW through the highly reflecting end-mirror (Figure 5.14). Transform-limited 100 fs pulses were obtained for a pump power of just 93 mW. This was higher than the 73 mW threshold achieved with the W-cavity, but this was attributed to losses associated with the particular prism modelocker used in these experiments. The beams reflected from the surface of this prism contained over twice as much power as the beam passing through the highly reflecting end mirror; this suggested that the prism was not correctly aligned in its mount. Work is currently underway to correct this problem, and preliminary results have included CW output powers of 2.5 mW through the HR end-mirror, a three-fold increase on the previous value and twice the power obtained from the four-mirror device. It is hoped that this improvement in CW performance will translate into a reduction in the threshold for self-modelocking. In the meantime, the demonstration of self-modelocked sub-100-fs operation of this laser at sub-100 mW pump powers, at twice the pulse repetition frequency of the Cr:LiSAF laser (and therefore at half the pulse peak power), and using less-than-ideal optical components, demonstrates the potential of the three-mirror laser design for ultra-low-threshold self-modelocking.

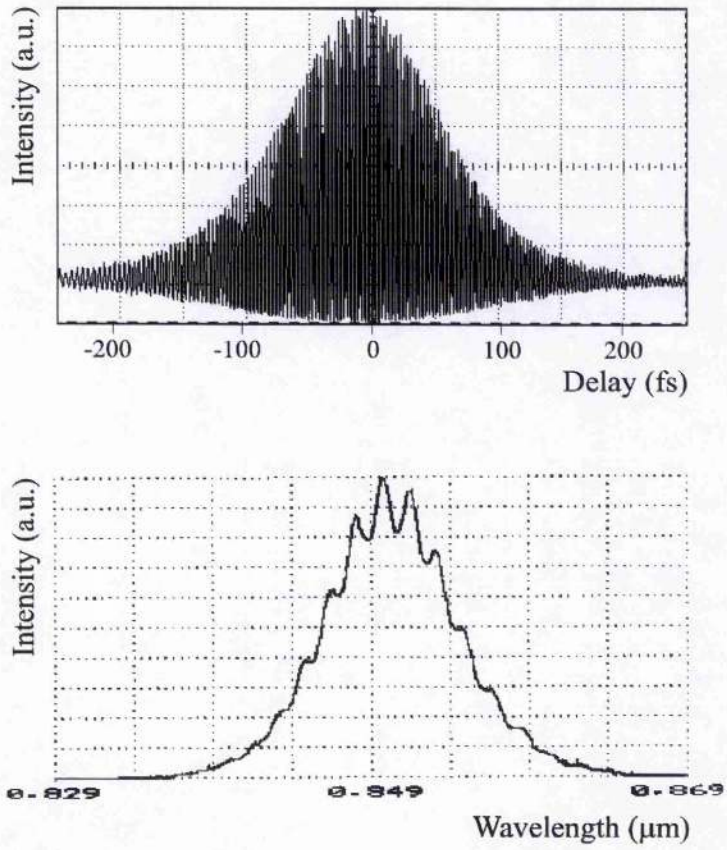

FIGURE 5.14 *Interferometric autocorrelation and spectrum of the output of the three-mirror Cr:LiSGaF laser at 116 mW pump power ($\Delta\tau$ = 84 fs, $\Delta\lambda$ = 9.1 nm, $\Delta\nu\Delta\tau$ = 0.32) pulses.*

5.5 Concluding Remarks

I have described in this chapter two low-threshold, all-solid-state, self-modelocked laser systems based upon the gain crystal Cr:LiSGaF. The first of these utilised a conventional Z-cavity. The low material scattering loss of Cr:LiSGaF, combined with an implementation of the steps towards low-threshold self-modelocked operation outlined in Chapter 3, enabled the production of transform-limited pulses of 87 fs duration at output powers of 11.5 mW for 170 mW pump power. These figures should be compared with the performance of the Cr:LiSAF laser described in Chapter 4, which produced 93 fs pulses at 1 mW output power for 150 mW pump power. The order-of-magnitude increase in output power was possible because the reduction in scattering losses from the gain crystal permitted the use of a 1.5 % output-coupler instead of an highly reflecting end-mirror. Self-

modelocking was achieved without the use of an intracavity modelocking aperture. The laser was not optimised for low-threshold operation, but it is reasonable to expect that replacing the 1.5 % output-coupler with an high reflector and using fused-silica prisms instead of SF 10 prisms would result in sub-100-fs pulses at pump powers still lower than those achieved in the optimised Cr:LiSAF laser.

In addition to these modelocking results, it was also confirmed that the birefringence effects observed in Cr:LiSAF and Cr:LiSGaF can be eliminated by rotating the plane of the crystal c-axis, as was predicted in the previous chapter.

The second laser described in this chapter was an all-solid-state, self-modelocked Cr:LiSGaF laser based around a novel three-mirror resonator configuration. Before introducing the experimental results obtained from this laser, the stability and modelocking properties of three-mirror resonators were considered. Either one or two degrees of freedom of adjustment are removed in going from a conventional four-mirror laser to three mirror lasers, depending upon the exact three-mirror configuration. This reduction in the degrees of freedom results in significantly different stability properties. Most significantly in terms of self-modelocking, the symmetric-confocal configuration leads to an identical beam profile in three- and four-mirror resonators, but very different stability properties. In a four-mirror resonator, the symmetric-confocal configuration is critically stable and is the optimum configuration for self-modelocking. In a three-mirror resonator, on the other hand, the symmetric-confocal configuration is optimally stable, and is therefore not suitable for modelocking.

Three-mirror resonators exhibit two stability regions, one closer to the intracavity focus than the Rayleigh range and one further away. An important example of a resonator operating in the first region is the 'semi-monolithic' cavity configuration, in which a plane mirror is coated directly onto the rear surface of the crystal. The 'Magni model', a model of self-modelocking similar to the Cerullo model introduced previously, was used to investigate the self-modelocking properties of three-mirror resonators. This modelling showed that hard-aperture modelocking is not possible in a semi-monolithic resonator. Soft-aperture modelocking is possible, on the other hand, as has been demonstrated by other workers[7,8].

The second three-mirror configuration considered is the 'retroreflector' cavity configuration, in which a curved mirror is placed at a distance from the intracavity focus that is approximately equal to the mirror radius of curvature. In terms of stability, this laser can be considered to be similar to the semi-monolithic laser if the distance between the intracavity focus and the retroreflecting mirror is treated as 'dead space'. This resonator has one more degree of freedom than the semi-monolithic laser and consequently the intracavity beam waist can be positioned anywhere within the gain crystal (rather than just at the HR coating of the semi-monolithic crystal). A full Cerullo-style plot can therefore be produced for both hard- and soft-aperture modelocking using the Magni model. These plots predict that, while hard- and soft-aperture modelocking are both possible in this cavity configuration, soft-aperture modelocking is likely to be more easily achieved.

A compact self-modelocked Cr:LiSGaF laser based on a retroreflector three-mirror cavity configuration was constructed. The laser utilised a prism-modulator, and the intracavity beam experienced two fewer mirror reflections per round-trip than it would in a four-mirror laser. The retroreflector laser produced transform-limited 84-fs pulses at 0.5 mW output power, for a pump power of 116 mW. Pulses of sub-100-fs duration were produced for 93 mW pump power. The laser was not optimised at this stage, but its performance approached that of the optimised W-cavity Cr:LiSAF laser, which gave sub-100-fs pulses at 73 mW pump power. Initial attempts to improve the retroreflector laser have resulted in a three-fold increase in CW output power - to 2.5 mW through a high-reflector - and we are confident that this increase in intracavity power can be translated into a significant reduction in the power required for sub-100-fs pulses. The pulse repetition rate was 173 MHz, corresponding to a cavity length of 870 mm, which is half the length of the z-cavity Cr:LiSGaF laser described above.

The retroreflector configuration is a simple and compact cavity configuration that is highly suitable for low-threshold, self-modelocked operation. When optimisation of the cavity is complete, work will commence on building a retroreflector laser that is pumped by only one or two 50 mW, narrow-stripe, semiconductor lasers. As explained in previous chapters, these pump sources are inexpensive and require only the simplest of optics for coupling into the laser cavity. A compact three-

mirror Cr:LiSGaF laser pumped by narrow-stripe diode lasers would thus represent an attractive low-cost source of sub-100-fs pulses tunable in the near-infrared spectral region.

---

[1] L. K. Smith, S. A. Payne, W. L. Kway, L. L. Chase and B. H. T. Chai, IEEE J. Quantum Electron. **28**, 2612 (1992)

[2] V. P. Yanovsky, F. W. Wise, A. Cassanho and H. P. Jensenn, Opt. Lett. **20**, 1304 (1995)

[3] Kristin Lewotsky, Laser Focus World, April 1995

[4] I. T. Sorokina, E. Sorokin, E. Wintner, A. Cassanho, H. P. Jenssen and M. A. Noginov, Opt. Lett. **21**, 204 (1996)

[5] I. T. Sorokina, E. Sorokin, E. Wintner, A. Cassanho, H. P. Jenssen and R. Szipöcs, Opt. Lett. **21**, 1165 (1996)

[6] J. R. Lincoln, M. J. P. Dymott and A. I. Ferguson, Opt. Lett. **19**, 1210 (1994)

[7] M. Ramaswamy-Paye and J. G. Fujimoto, Opt. Lett. **19**, 1756 (1994)

[8] B. E. Bouma and J. G. Fujimoto, Opt. Lett. **21**, 134 (1996)

[9] G. J. Valentine, G. T. Kennedy and W. Sibbett, in *1996 Conference on Lasers and Electro-Optics Europe*, (IEEE Catalog 96TH8161) Paper CFF6

[10] Model implemented in conjunction with G. J. Valentine, University of St. Andrews.

[11] V. Magni, G. Cerullo, S. De Silvestri and A. Monguzzi, J. Opt. Soc. Am. B **12**, 476 (1995)

[12] P. Das, in *Lasers and Optical Engineering* (Springer-Verlag, New York, 1990) p206

6. Conclusions

6.1 A Summary of the Thesis

This thesis is concerned with the design and assessment of all-solid-state self-modelocked Cr:LiSAF and Cr:LiSGaF lasers. Diode-pumped self-modelocked colquiriite lasers are attractive for several reasons. They are compact, reliable and efficient sources of ultrashort pulses with excellent noise properties, and in these respects compare favourably with the Ar^+-laser-pumped Ti:sapphire laser which now dominates the market for ultrashort-pulse lasers operating around 800 nm. However, several problems were encountered in the development of all-solid-state self-modelocked colquiriite laser systems. These stem from the conflicting requirements made by self-modelocking and direct diode-pumping with broad-area semiconductor lasers. Self-modelocking is a nonlinear process, and consequently it requires that the intracavity beam be tightly focused in the laser crystal. Diode-pumping with a broad-area semiconductor laser, on the other hand, requires the matching of a non-diffraction-limited pump beam to a diffraction-limited intracavity beam, which is difficult to achieve with a tightly focused beam. In addition, a poor pump-cavity mode overlap can lead to large amounts of excess pump power being deposited in the laser crystal as heat. This is a particular problem in Cr:LiSAF because there is a thermally activated non-radiative decay route that leads to a depopulation of the upper laser level at modest crystal temperatures. Two alternative solutions were proposed, one based on the indirect diode pumping of highly doped crystals via frequency-doubled minilasers, and the other based on the direct diode pumping of low-threshold laser systems by diffraction-limited beams.

6.1.1 Indirect Diode-pumping of Cr:LiSAF Lasers Via Frequency-doubled Minilasers

Firstly, an indirectly diode-pumped Cr:LiSAF system was developed, using LiSAF crystals doped with very high levels of Cr^{3+} ions (Chapter 2). This enabled the construction of Cr:LiSAF lasers that were pumped by frequency-doubled

minilasers operating in the green spectral region, where there is a trough in the absorption of Cr:LiSAF. Frequency-doubled minilasers offer diffraction-limited beams at several watts of power, much higher than that currently available from single-element AlGaInP semiconductor lasers.

Two minilaser-pumped Cr:LiSAF lasers were constructed as described in Chapter 2 of this thesis. The first system utilised an AR-coated LiSAF crystal doped with 10 % Cr^{3+}. It could be pumped by either an Ar-ion mainframe laser or a frequency-doubled Nd:YLF ring minilaser. The laser produced transform-limited 90 fs pulses at 859 nm at a repetition rate of 86 MHz. The output power was 30 mW at 320 mW absorbed pump power and self-modelocked operation was achieved for absorbed pump powers as low as 280 mW. Minilaser-pumped operation was impeded, however, by stability problems associated with the pump laser.

The second system utilised a Brewster-angled crystal doped with 22 % Cr^{3+}. Again it could be pumped both by either an Ar-ion mainframe laser or a frequency-doubled Nd:YAG minilaser. The performance of the Cr:LiSAF laser was similar with both pump sources, although the minilaser suffered from periodic bursts of amplitude fluctuations due to a second-harmonic generation instability (the 'green problem', Section 2.3.1). This laser produced over 120 mW of output power through a 1.5 % output coupler when pumped by 1.1 W absorbed pump power. When self-modelocked, the laser gave 72 fs pulses at 76 mW output power. At pump powers greater than ~1.2 W, the laser suffered from thermally induced roll-off which was attributed to non-radiative decay routes from the upper laser level. 160 mW of output power was obtained by pumping the Cr:LiSAF laser from both ends, thus distributing the thermal load. The 'green problem' plagued both frequency-doubled minilaser pump sources. However, multi- and single-longitudinal mode minilaser systems have recently become commercially available that offer stable outputs at powers of up to several watts. The relatively low threshold of Cr:LiSAF lasers means that they can be pumped by lower power minilasers and could therefore be lower-cost alternatives to higher-power minilaser-pumped Ti:sapphire lasers.

6.1.2 Direct Diode-pumping of Low-threshold Cr:LiSAF and Cr:LiSGaF lasers

6.1.2.1 Low-threshold Cr:LiSAF Lasers

An alternative technique to direct diode-pumping with broad-area semiconductor lasers is the low-threshold approach outlined in Chapter 3. The high $\sigma\tau$ product of Cr:LiSAF can be expected to lead to an inherently low laser threshold. Consideration was therefore given to ways in which the laser threshold and the power required for self-modelocking could be reduced still further, to bring the pump power requirement down to the low levels that are within the operating range of diffraction-limited narrow-stripe semiconductor lasers. Narrow-stripe diodes are attractive pump sources because they are significantly less expensive than broad-area diodes, and because they require less complicated pump optics to achieve a good pump-cavity mode overlap.

The factors affecting the pump power required to self-modelock a diode-pumped laser were also considered in Chapter 3. The oscillation threshold of a laser in which both pump and cavity modes are focused Gaussian beams is minimised by focusing both beams into as tight a waist as possible, at a point near to the pumped face of the crystal. Tight focusing also results in pronounced, and strongly localised, nonlinear lensing which is advantageous for 'Cerullo-style' self-modelocking. Oscillation threshold increases significantly for pump beams that are far from being diffraction limited. Self-injection locking is a means of obtaining near-diffraction-limited beams of modest powers from broad-area semiconductor lasers.

The Cerullo model of self-modelocking offers a general prescription for the optimisation of a laser resonator for ultrashort-pulse generation. Consideration of the empirical properties of this model and the geometric optics of four-mirror resonators led to two simple analytical expressions for the optimum modelocking configuration of a four-mirror resonator. These two equations eliminate the need for the graphical method normally employed in a Cerullo model of this kind of resonator.

Once a pulse is established in a laser cavity, intracavity dispersion is the principal limitation on the power needed to sustain a particular duration of pulse. If the net intracavity GVD is reduced, third-order dispersion becomes the limiting factor. Careful choice of prism material is therefore vital if the modelocking threshold for a laser is to be minimised.

By implementing these routes to low-threshold self-modelocking, a Cr:LiSAF laser was constructed that produced sub-100 fs pulses for just 73 mW incident pump power (Chapter 4). This represented a three-fold reduction on the lowest previously reported pump power requirement. This laser was pumped by a self-injection-locked AlGaInP diode laser. Self-infection locking transformed the far-field output pattern of the diode from a top-hat profile with a width of ~ 10° to a Gaussian lobe of width ~1°, and this lobe contained 70 % - 80 % of the diode output power. The Cr:LiSAF laser had a CW threshold of 45 mW and a slope efficiency of 1.1 % with 100 mm ROC folding mirrors and a CW threshold of 35 mW and a slope efficiency of 1.0 % with the 75 mm ROC mirrors. In both cases, the maximum output power at 150 mW pump power was ~1.2 mW.

The CW tuning curve of the laser exhibited a modulation with a period of 4.6 nm. The origin of this phenomenon was identified as a slight misalignment of the c-axis of the Cr:LiSAF crystal. This resulted in the combination of the crystal and the dispersion-compensation prisms having the effect of an intracavity birefringent filter.

The laser had very good free-running noise properties which were comparable to those of a cavity-locked Ti:sapphire. This permitted the evaluation of a streak camera in the sub-picosecond regime, which had previously only been accessible with a cavity-locked Ti:sapphire laser and a shuttered camera.

6.1.2.2 Low-threshold Three- and Four-mirror Cr:LiSGaF Lasers

The performances of two low-threshold, all-solid-state, self-modelocked laser systems based upon the gain crystal Cr:LiSGaF were described in Chapter 5. The first of these utilised a conventional Z-cavity. The low material scattering loss of Cr:LiSGaF, combined with an implementation of the steps towards low-threshold self-modelocked operation outlined in Chapter 3, enabled the production of

transform-limited pulses of 87 fs duration at output powers of 11.5 mW for 170 mW pump power. An order-of-magnitude increase in output power was possible compared with the Cr:LiSAF system because the reduction in scattering losses from the gain crystal permitted the use of a 1.5 % output-coupler instead of an highly reflecting end-mirror. It was also confirmed that the birefringence effects observed in Cr:LiSAF and Cr:LiSGaF can be eliminated by rotating the plane of the crystal c-axis.

The second laser described in Chapter 5 was an all-solid-state, self-modelocked, Cr:LiSGaF laser based around a novel three-mirror resonator configuration. Before introducing experimental results obtained from this laser, the stability and modelocking properties of three-mirror resonators were considered. The number of degrees of freedom of adjustment is reduced results in going from four- to three-mirror resonators, and this results in significantly different stability properties. Three-mirror resonators exhibit two stability regions, one closer to the intracavity focus than the Rayleigh range and one further away. An important example of a resonator operating in the first region is the 'semi-monolithic' cavity configuration, in which a plane mirror is coated directly onto the rear surface of the crystal. The 'Magni model', a model of self-modelocking similar to the Cerullo model introduced previously, was applied to the self-modelocking properties of three-mirror resonators. This showed that soft-aperture modelocking is possible in a semi-monolithic resonator but hard-aperture modelocking is not possible. Another important three-mirror resonator is the 'retroreflector' cavity configuration. In this configuration a curved mirror is placed at a distance from the intracavity focal that is approximately equal to the mirror radius of curvature. An analysis based on the Magni model predicts that, while hard- and soft-aperture modelocking are both possible in this cavity configuration, soft-aperture modelocking is more easily achieved.

A compact self-modelocked Cr:LiSGaF laser based on a retroreflector three-mirror cavity configuration utilising a prism-modulator was constructed. The retroreflector laser produced transform-limited 84-fs pulses at 470 μW output power, for a pump power of 116 mW. The pulse repetition rate was 173 MHz, corresponding to a cavity length of 870 mm. Pulses of sub-100-fs duration were

produced for 93 mW pump power. The laser has not yet been optimised, but initial attempts at improvement have resulted in a three-fold increase in CW output power. It should be possible to translate this increase in intracavity power into a significant reduction in the power required for sub-100-fs pulses, bringing this requirement down to the level where pumping by one or two narrow-stripe, diffraction-limited diode lasers would be a practical possibility.

The retroreflector configuration is a simple and compact cavity configuration that is highly suitable for low-threshold, self-modelocked operation. A compact three-mirror Cr:LiSGaF laser pumped by narrow-stripe diode lasers would form an attractive low-cost source of sub-100-fs pulses in the near-infrared.

6.2 Suggestions for the Future

The three-mirror laser described in the previous section is something close to the logical conclusion of the low-threshold self-modelocking work which is described in the latter parts of the thesis. Switching to a semi-monolithic geometry would remove from the round trip two further passes of the laser crystal, although this would probably not be particularly significant in terms of threshold. The regenerative-initiation system adds most to the complexity of the laser. Some form of passive initiation technique is, however, essential to self-modelocked operation in such a low-intracavity-power system, and regenerative initiation with a prism AO modulator has the advantage that it does not require any additional intracavity elements.

A further possible simplification would be to adopt an unconventional dispersion-compensation scheme, paralleling the approach of Bouma in his three-mirror semi-monolithic Ti:sapphire laser cavities[1]. In these lasers, dispersion compensation is achieved by using a single Brewster-angled prism in conjunction with a semi-monolithic gain crystal with one Brewstered face and one plane AR-coated face. In a round trip, an intracavity pulse sees the equivalent of three prisms, and it is possible to achieve a net negative dispersion that permits soliton-like pulse shaping into the sub-100-fs regime. The second-order dispersion properties of this kind of cavity can be easily modelled with the extended-ABCD-matrix model developed by Kostenbauder[2]. A potential problem with this laser system is that both the use of

two prisms made from different materials and the use of a Brewster-angled crystal will result in an elliptical intracavity beam which will lead to an increased CW and/or modelocking threshold.

What factors will affect the development of Cr:LiSAF (or Cr:LiSGaF) lasers in general? To date, the principal constraint on development has been the need to trade off beam power against beam quality in AlGaInP pump lasers. The problem has been compounded by the poor thermal properties of Cr:LiSAF. The approach in this thesis has been to circumvent these problems. In the first systems described, this was achieved by using indirect diode pumping via minilasers. The minilasers act to convert non-diffraction-limited AlGaAs pump diode outputs at 800 nm into diffraction-limited beams at a wavelength that are suitable for pumping Cr:LiSAF lasers. The second approach was to bring the power requirements of a self-modelocked system down to a level that could be obtained from inexpensive diffraction-limited diodes.

What other approaches are available? The limited output power of broad area devices means that multiple diodes or diode arrays are required for higher power outputs. All-solid-state self-modelocked Cr:LiSAF lasers have now been reported that offer output powers of over 200 mW[3]. The performance of the green-pumped laser described in Chapter 2 suggests, however, that their outputs will be limited by thermal problems at some point. Of course, there is always the possibility that other colquiriites such as Cr:LiCAF and Cr:LiCGaF will be developed to the point where they offer similar loss properties and better thermal behaviour than that offered by Cr:LiSAF or Cr:LiSGaF.

Assuming that no such miracle crystal appears, how can Cr:LiSAF lasers be developed to offer still higher powers? It is important that the thermal load in the laser crystal is distributed over as large a volume as possible. The crystal in any heavily pumped system must therefore have a long absorption length and be cooled effectively. Beyond this, it may be instructive to look to higher power *CW* lasers for possible ideas. In particular, CW frequency-doubled minilasers may suggest possibilities for self-modelocked lasers. These lasers are pumped by high-power, far-from diffraction limited pump beams that are coupled into a large intracavity mode. This ensures a good overlap between the cavity mode and the far-from-

diffraction-limited pump beams, and also reduces the thermal loading of the laser crystal. However, self-modelocked lasers require tightly-focused waists in order to enhance the non-linear effects that are required for pulsed operation. But *frequency-doubled* minilasers also require tightly-focused waists for efficient frequency doubling. This is achieved by focusing the intracavity beam into a nonlinear crystal whilst maintaining a large waist in the gain crystal in another part of the cavity, and this scheme could usefully be adapted to the problem of higher-power ultrashort-pulse generation.

A self-modelocked laser has already been demonstrated that utilised a highly nonlinear glass rod in a second cavity folding section[4]. This approach was adopted because the relatively low intracavity powers and short gain crystal used in this laser did not alone provide a sufficient nonlinear effect for modelocking. However, it should be possible to directly copy proven CW frequency-doubled minilaser cavity designs. Replacing the frequency-doubling crystal with a crystal with a high nonlinear refractive index (for example, Schott SF59 glass) would permit the use of a large intracavity mode in the Cr:LiSAF crystal because the crystal would then only be required to provide gain. Alternatively, the nonlinear crystal could also be Cr:LiSAF, so that laser operation could be achieved at low pump powers in the tight-focusing section of the cavity. A second Cr:LiSAF crystal could then be pumped with high power beams in a weak-focusing section. In this kind of scheme, the two functions of the laser crystal in a conventional cavity - achieving threshold gain and converting pump power into output power - are achieved in two separate crystals, each positioned at a point in the cavity best suited to its function.

As an example of this kind of adoption of CW laser designs, one could envisage Cr:LiSAF lasers based upon the frequency-doubled Nd:YLF ring cavity described in Section 2.3.2, or upon the 3-mirror Nd:YAG cavity described in Section 2.3.5. (Indeed, the Nd:YAG laser is simply a semi-monolithic 3-mirror cavity with a nonlinear crystal at the intracavity beam waist and the gain crystal at the end of the long cavity arm). The large intracavity waist in the Cr:LiSAF gain crystal in either system could be pumped, for example, by one or more high-power fibre-coupled diode array, each of which would offer several watts of red pump light.

Another alternative future Cr:LiSAF system might be based on a combination of some of the ideas of Chapters 2 and 3. The laser described in Chapter 2 utilised a highly doped Cr:LiSAF crystal pumped in the green wing of the Cr:LiSAF absorption peak centred at 670 nm. Payne *et al.* demonstrated that highly doped Cr:LiSAF could be pumped at 792 nm; i.e., on the other IR wing of this peak[5]. Broad-stripe (500 μm) AlGaAs diodes are available that offer powers of up to 4 watts at around 800 nm. Direct pumping of a frequency-doubled minilaser-style cavity would be one possibility, but another alternative would be to self-injection lock the AlGaAs diode and pump a simple three-mirror cavity, in a scheme analogous to that described in Chapter 5. Although this would result in a reduction in the pump power available from the diode, it would be hoped that the improved beam quality would compensate for this in the Cr:LiSAF laser performance.

Whatever method is used to obtain an increase in the pump power, the maximum output power available from a self-modelocked laser will, in general, be limited by intracavity third-order dispersion. It was demonstrated in Chapter 2 that TOD limits both the minimum pulse duration available from a laser and also the minimum pump power necessary to maintain pulses of a particular duration. Clearly, it will also limit the maximum output power available from a self-modelocked system. As the intracavity power in a laser is increased, the duration of circulating pulses decreases until the third-order limited duration is reached. If the intracavity power is increased beyond this point, the pulse cannot shorten any further and instabilities will result. It is thus essential to eliminate third-order dispersion as far as possible, and this would probably be best achieved with chirped-dielectric mirrors or Gires-Tournois interferometers, particularly in a high power system in which intracavity losses are relatively unimportant.

The work describes in this thesis has been an attempt to develop femtosecond lasers that are more user-friendly than the Ar-ion-pumped Ti:sapphire laser. User-friendly femtosecond lasers have a recognisably higher profile nowadays, in the

world at large and, in the future, compact and ultraquiet femtosecond systems will have increasingly wide applicability to many branches of science and technology.

Post Script

In the two months that have passed since I left St. Andrews, work has continued on the optimisation of the three-mirror retroreflector laser described in Chapter 5. That laser has now produced sub-100 fs pulses at pump powers of less than 40 mW, and self-modelocked operation has been demonstrated at pump powers as low as 21 mW.

---

[1] B. E. Bouma and J. G. Fujimoto, Opt. Lett. **21**, 134 (1996)

[2] A. G. Kostenbauder, IEEE J. Quantum Electron. **26**, 1148 (1990)

[3] Announced by U. Keller in a question at the *1996 Conference on Lasers and Electro-optics,* Hamburg.

[4] G. P. A. Malcolm and A. I. Ferguson, Opt. Letters **16**, 1967 (1991)

[5] S.A.Payne, W.F.Krupke, L.K.Smith, W.L.Kway, L.Davis DeLoach and J.B.Tassano, IEEE J.Quantum Electron. **28**, 1188 (1992)

Appendix A - Physical Properties of the Colquiriite Crystals

A.1 Summary of Known Thermo-optic and Thermo-mechanical Constants of the Colquiriites

Property	Symbol	Unit	LiSAF	LiSGaF	LiCAF	LiCGaF
Expansion coefficient	α_a	10^{-6}/°C	25	12	22	
	α_c		-10	0	3.6	
Melting point		°C	766	716	810	762
Density		g/cm^3	3.45	3.892	2.988	3.517
Heat capacity at 25 °C	C_p	J/(g°C)	0.842		0.935	
Thermal diffusivity	λ_a	10^{-6} m^2/s			1.64	
	λ_c		1.08		1.84	
Thermal conductivity	k_a	W/(m°C)	3.0	3.4	4.58	
	k_c		3.3 (3.09)	3.6	5.14	
Thermal expansion at 25 °C	α_a	10^{-6}/°C	18.8 (24)	13	22.0	
	α_c		-10.0 (-10)	-6	3.6	
Fracture toughness	K_a	MPa/m$^{1/2}$			0.37	
	K_c		0.40		0.18	
dn/dT	$\perp c$	10^{-6}/°C	-2.5		-4.2	
	$\parallel c$		-4.0		-4.6	
Elastic constants	c_{11}	GPa	117		118	
	c_{33}		94		107	
Youngs modulus	E	GPa	109		96	

A.2 Summary of Known Optical and Laser Properties of the Colquiriites

Property	Symbol	Unit	LiSAF	LiSGaF	LiCAF	LiCGaF
Intrinsic efficiency	η_0	%	53	52	67	
Quantum intrinsic efficiency	η_q	%	67	66	82	
Emission peak		nm	846	835	763	770
π emission cross section	σ_e	10^{-20} cm^{-2}	4.8	3.3	1.3	
Emission lifetime	τ	μs	67	88	170	200
Zero-phonon line		nm	699	699	678	
$\sigma\tau$ product	$\sigma\tau$	10^{-24} cm^{-2} s	3.22	2.90	2.21	
Refractive index at 850 nm	n_a n_c		1.4054 1.4074		1.3890 1.3877	
Nonlinear refractive index	n_2	10^{-14} esu	2.9±0.9	4.3±0.9		

Data supplied by Lightning Optical Corporation.

Sources

Smith *et al.*, IEEE J. Quantum Electron. **28**, 2612 (1992)

Woods *et al.*, J. Opt. Soc. Am. B **8**, 970 (1991)

Y. Yin and D. A. Keszler, Chem. Mater. **4**, 645 (1992)

Payne *et al.*, Appl. Optics **33**, 5526 (1994)

H. P. Jenssen, University of Central Florida CREOL

Appendix B - Four-mirror Resonator Stability

To understand more clearly the Cerullo model of self-modelocking - and four-mirror resonators, in general - we develop in this Appendix a model for four-mirror resonators (Figure B.1) based on an extension of the geometric optics treatment of resonator stability. Conventionally, resonator stability is analysed by considering the passage of a ray of light around the resonator: if the ray remains within the resonator after an infinite number of round-trips then the cavity is stable; if it 'walks away' from the cavity axis then it is unstable[1]. In the model described here, consideration is given to the behaviour of plane and spherical waves as they pass through the cavity folding section. The folding mirrors behave as if they are a single lens with a focal length that is a function of the mirror separation.

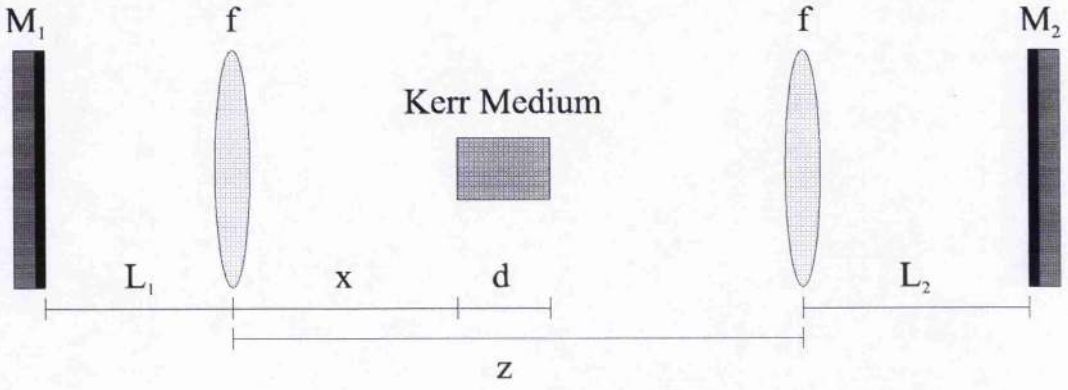

FIGURE B.1 *Representation of a four-mirror resonator: M_1, M_2 - plane mirrors; f - lenses corresponding to the curved mirrors of the folding section).*

The figure given in Chapter 3 to illustrate four-mirror resonator stability is repeated as Figure B.2 below. It is instructive to look in more detail at the behaviour of the cavity mode in each of the regions shown in Figure B.2. As described in Chapter 3, in the high misalignment sensitivity (HMS) stable region the intracavity mode in the short cavity arm L_1 is approximately collimated and the mode in the long cavity arm L_2 is approximately focused. In the low misalignment sensitivity (LMS) region the mode is approximately focused in both arms. These two configurations can be investigated using the approximation of geometric optics by considering the effect of a single pass of the resonator on a plane wave or a

spherical wave travelling from one of the end mirrors. In an actual resonator, of course, the intracavity mode is a Gaussian beam that is self-reproducing over many round trips; i.e., it is an eigenmode of the round-trip ABCD matrix. However, this single pass geometric approximation accurately describes the stability properties of a resonator if we interpret a stable resonator configuration as one in which a plane or spherical wave is focused to a point at or beyond the plane of the cavity end mirrors. In other words, a resonator can support a stable Gaussian eigenmode if either plane waves or spherical waves emanating from one end mirror *converge* onto the other end mirror.

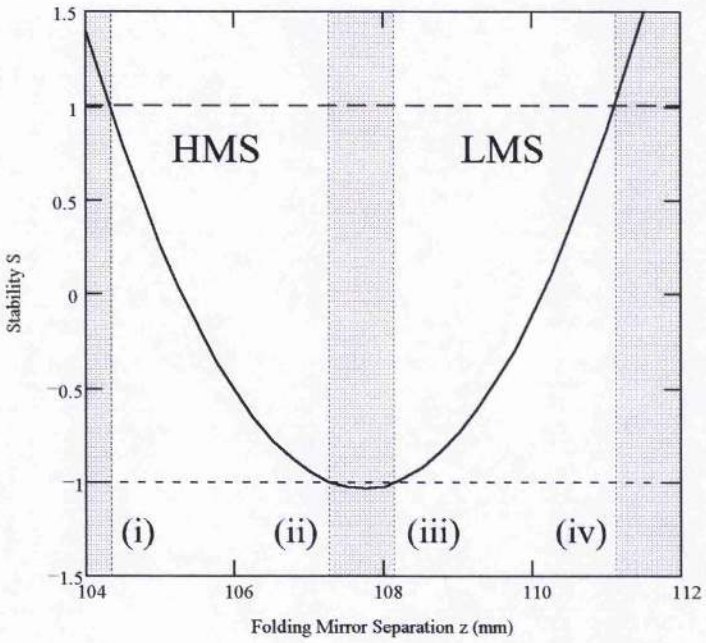

FIGURE B.2 *Stability as a function of folding mirror separation, for the resonator parameters L_1 = 700 mm, L_2 = 900 mm, f = 50 mm, and d = 10 mm (as defined in Figure B.1). The laser is stable in the two unshaded regions. In the high misalignment sensitivity (HMS) region the folding mirrors are arranged in an nearly-confocal arrangement; in the low misalignment sensitivity (LMS) region the end mirrors lie in nearly-conjugated planes. Limit (i) corresponds to $C_0 = 0$; (ii) corresponds to $A_0 = 0$; (iii) $D_0 = 0$; and (iv) $B_0 = 0$ (see page 98).*

B.1 The HMS Region

We can approximate behaviour in the HMS region by considering the effects of the resonator on a plane wave travelling from end-mirror M_1 to end-mirror M_2 in Figure B.1. This analysis applies equally well to a plane wave travelling from M_2 to

M_1, but in an asymmetric resonator the intracavity mode is approximately collimated in the short arm L_1, and so a plane wave travelling from M_1 to M_2 is more physically realistic.

In geometric optics terms, a four-mirror resonator consists of a pair of identical lenses of focal length f (in reality curved folding-section mirrors) separated by a distance z. Such an optical system is equivalent to a single lens if we consider the front (or back) focal length[2]

$$f' = \frac{f(z-f)}{z-2f}$$

EQUATION A

In the region to the left of limit (i) in Figure B.2, f' is negative. This means that a plane wave travelling from M_1 will diverge when it reaches the folding section mirrors: clearly, this is an unstable cavity.

B.1.1 Limit (i) - the Planar-Confocal Limit

If we increase the mirror separation to limit (i), we find that $f' \to \infty$ as $z \to 2f$. This means that a plane wave travelling from M_1 is focused an infinite distance beyond M_2. In other words, the resonator is optically equivalent to a 1:1 telescope.

In the language of laser resonators, we can also consider this cavity configuration to be an infinite periodic waveguide consisting of segments that are alternately equivalent to planar and confocal ($z = 2f$) two-mirror laser cavities (Figure B.3).

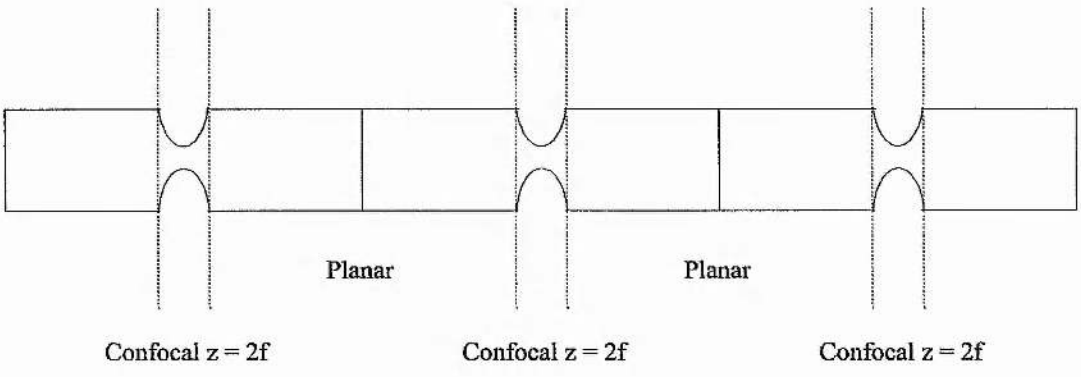

FIGURE B.3 *The eigenmode of the infinite periodic waveguide corresponding to a four-mirror cavity on stability limit (i) in Figure B.2. Note that alternate segments are equivalent to two-mirror planar and symmetric confocal resonators.*

Although a confocal resonator is insensitive to misalignment of its mirrors, the planar segments of this resonator mean that overall the laser mode is not well behaved.

B.1.2 The Stable HMS Region Between Limits (i) and (ii)

Between stability limits (i) and (ii) the front/back focal length of the lens pair is in the range $L_2 \leq f' \leq \infty$. This means that a plane wave emanating from mirror M_1 is converging when it reaches M_2, and so this configuration meets our criterion for a stable resonator. Although we approximate this region by assuming a collimated beam in one arm, Figure B.4 shows that the beam is, in fact, well behaved at the peak of the HMS region. Figure B.4 also shows, however, that our geometric approximation is legitimate for determining the behaviour of the mode at the limits of the stability region.

B.1.3 Limit (ii) - the Weak-Objective Limit

As the mirror separation is increased, the front/back focal length of the resonator

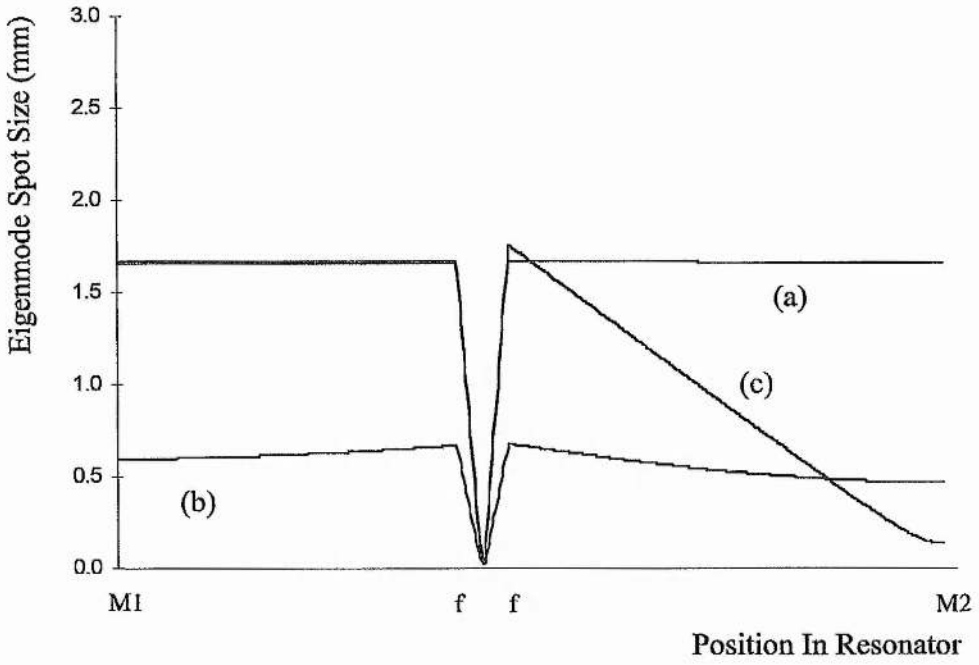

FIGURE B.4 *The resonator eigenmodes corresponding to (a) limit (i), the planar-confocal stability limit; (b) the peak of the HMS region; and (c) limit (ii), the weak-objective stability limit.*

decreases until, at limit (ii), it is equal to the length of the long cavity arm L_2. In this configuration, the folding section acts as an objective lens of focal length L_2. If we consider the resonator to be an infinite periodic waveguide then it consists of alternating planar and confocal two-mirror segments separated by regions containing a waist (corresponding to propagation in the laser folding section, Figure B.5). Note that in this laser the confocal two-mirror laser region occurs on a double pass of the long cavity arm, rather than in the folding section as is the case at limit (i); in other words, it is a confocal laser with a focal length of $f' = L_2$ rather than $f = \frac{z}{2}$. The planar segments of this waveguide ensure that at this stability limit, as at limit (i), the laser mode is not well behaved.

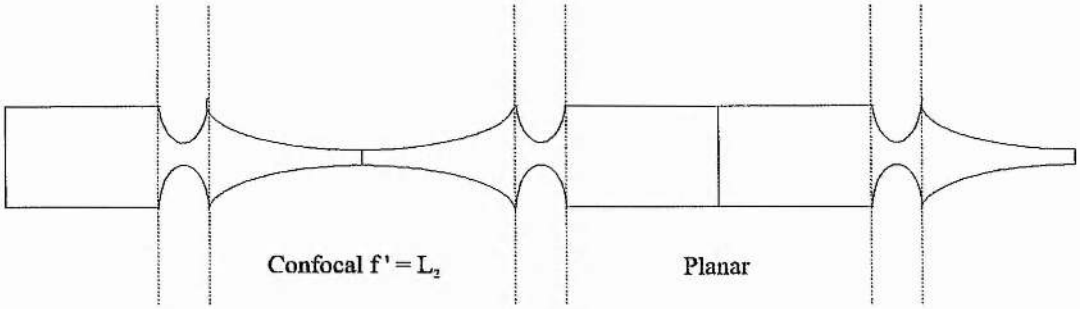

FIGURE B.5 *The infinite periodic waveguide corresponding to a four-mirror cavity on stability limit (ii) in Figure B.2. Note that this waveguide consists of alternating planar and confocal two-mirror segments (with* $f' = L_2$*) separated by a region containing a waist (corresponding to propagation in the laser folding section).*

B.2 The LMS Region

If the folding mirror separation is increased beyond limit (ii), then a plane wave emanating from mirror M_1 will be focused short of mirror M_2, and so the resonator cannot support a stable HMS-type mode. The alternative possible stable mode structure would be LMS-type modes, in which the mode is approximately focused on both end mirrors. We can investigate this stability region by considering the effect of a resonator on a spherical wave emanating from M_1. An object placed at M1, a distance L1 behind the back surface of the lens pair, forms an image at a distance[3]

$$s_i = \frac{fz - \frac{f^2 L_1}{L_1 - f}}{z - f - \frac{L_1 f}{L_1 - f}}$$

EQUATION B

For mirror separations z of less than stability limit (iii), s_i is negative; i.e., the image is virtual, and the lens pair causes a spherical wave from M_1 to diverge. Between stability limits (ii) and (iii) the laser is therefore incapable of supporting either plane-wave- or spherical-wave-type modes.

B.2.1 Limit (iii) - the Strong-Objective Limit

At limit (iii) a spherical wave emanating from M_1 is imaged at infinity; i.e., the lens pair behaves like an objective lens of focal length L_1. The intracavity mode at this stability limit is similar to that at limit (ii), as can be seen from Figure B.6. The planar segments of this waveguide again ensure that the laser mode is not well behaved at this limit.

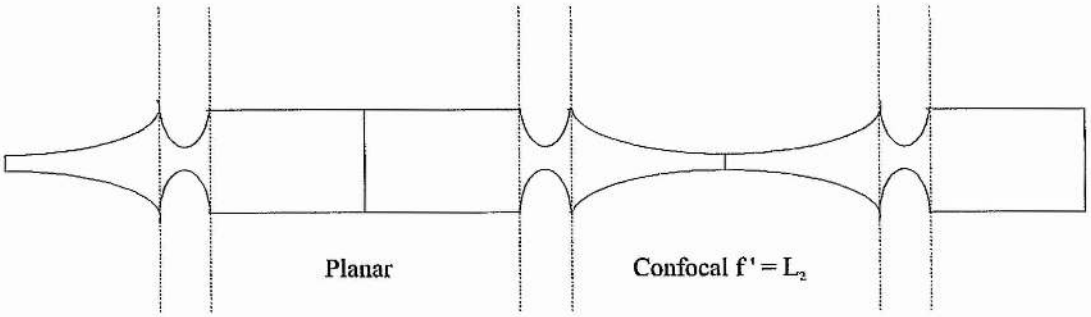

FIGURE B.6 *The infinite periodic waveguide corresponding to a four-mirror cavity on stability limit (iii) in Figure B.2. This waveguide is similar to that shown in Figure B.5.*

B.2.2 The Stable LMS Region Between Limits (iii) and (iv)

Between stability limits (iii) and (iv), a spherical wave emanating from M_1 will be focused a distance s_i beyond the front surface of the folding-section lens pair, where $L_2 \leq s_i \leq \infty$. The light will therefore be converging when it reaches M_2, and the resonator is able to support stable eigenmodes. Figure B.7 shows that, again,

our model is a good approximation to the resonator eigenmodes at the stability limits. Comparing Figure B.7 with Figure B.4 shows that, although the geometric optics model gives a much less accurate picture of the resonator eigenmodes at the peak of the stability regions (curves (b) in the figures), the LMS mode is indeed significantly more focused at M_1 than the HMS mode. This is in keeping with our use of LMS spherical-wave and HMS plane-wave approximations.

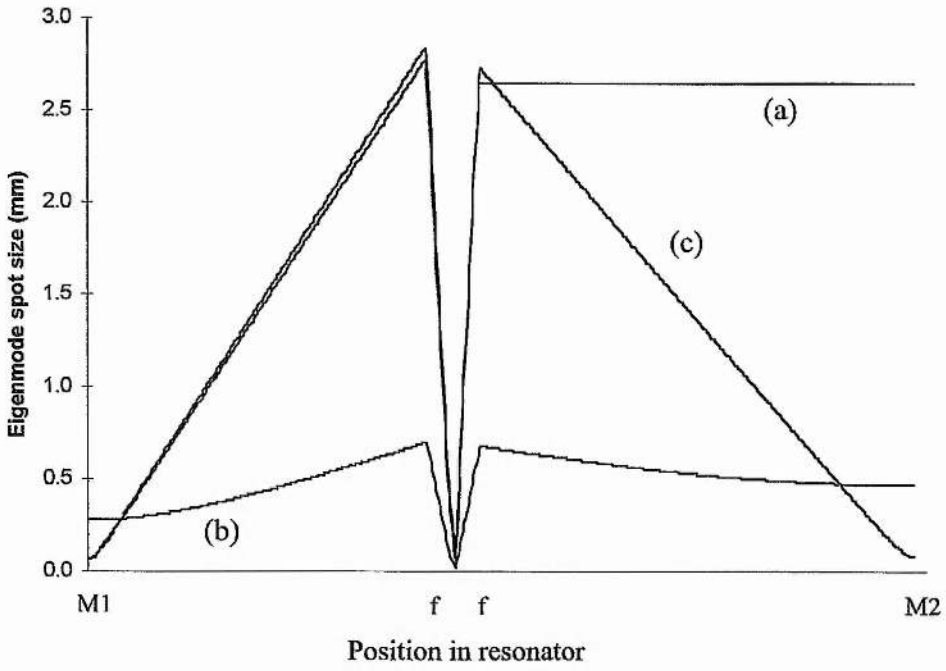

FIGURE B.7 *The resonator eigenmodes corresponding to (a) limit (iii), the strong-objective stability limit; (b) the peak of the LMS region; and (c) limit (iv), the conjugate-plane stability limit.*

B.2.3 Limit (iv) - the Conjugate-Plane Limit

As the mirror separation is increased still further, the image distance s_i decreases until, at limit (iv), a spherical wave emanating from mirror M_1 is focused exactly onto mirror M_2. An object at M_1 is therefore imaged onto M_2 and *vice versa*; M_1 and M_2 are therefore in conjugate planes. The laser resonator in this configuration is qualitatively similar to a two-mirror concentric resonator; f' is of the order of half the resonator arm lengths. The eigenmode on this limit is not well-behaved as the spot size on each end mirror is vanishingly small (Figure B.8).

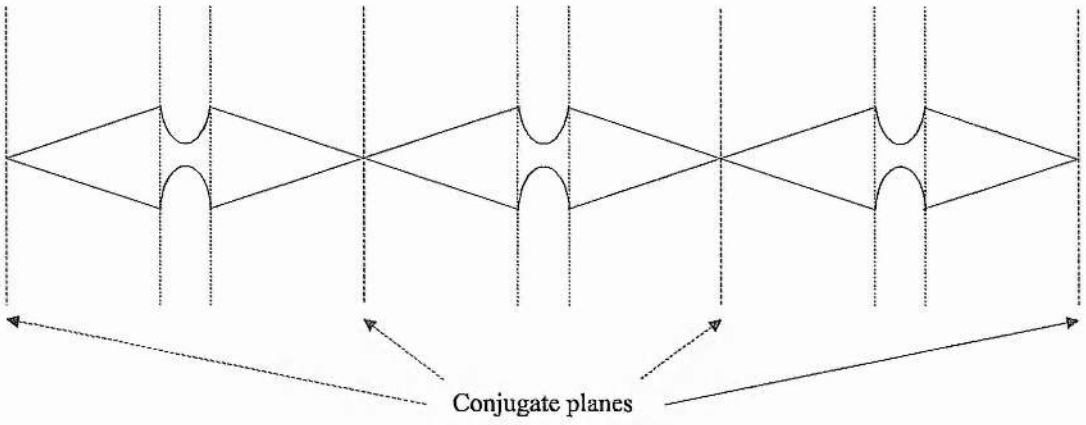

FIGURE B.8 *The infinite periodic waveguide corresponding to a four-mirror cavity on stability limit (iv) in Figure B.2. This resonator is qualitatively similar to a two-mirror concentric resonator.*

Stability Limit	Folding Mirror (Optical) Separation
(i) Planar-Confocal	$2f$
(ii) Weak-Objective	$\frac{(2L_2 - f)f}{L_2 - f}$
(iii) Strong-Objective	$\frac{(2L_1 - f)f}{L_1 - f}$
(iv) Conjugate-Plane	$\frac{(2L_2L_1 - L_2f - L_1f)f}{(L_1 - f)(L_2 - f)}$

TABLE B.1 *Mathematical expressions for the folding mirror separations that bound the two stability regions shown in Figure B.2. The parameters are f, the focal length of the folding mirrors and L_1 and L_2, the lengths of the short and long cavity arms, respectively. Note that the mirror separations calculated from these formulae are optical distances: to find the equivalent physical distances one must add* $d\left(1-\frac{1}{n}\right)$ *for an AR-coated crystal, or* $d\left(1-\frac{1}{n^3}\right)$ *for a Brewster-angled crystal, to the calculated separations, where d is the length of the laser crystal and n is its refractive index.*

At mirror separations larger than limit (iv), a spherical wave emanating from M_1 forms an image that is short of M_2 and *vice versa*. The resonator will support neither near-plane nor near-spherical modes and is unstable.

Expressions for the mirror separations that correspond to each of the four stability limits discussed here can be derived from Equation A and Equation B. They are summarised for convenience in Table B.1.

B.3 Symmetric Resonators

The mirror separation at which the effective focal length f' drops below a distance L is the same separation as that at which an object placed at L is just able to form a real image at infinity. Spherical wave imaging therefore 'takes over' from plane wave imaging at some critical separation $z_0(L)$. In a stable resonator, an image must be formed for either a spherical wave or a plane wave travelling both from M_1 to M_2 and from M_2 to M_1. But the critical separation for an arm of length L_1 is different from that for an arm of length L_2, and so for an asymmetric resonator there will be an unstable region where $z_0(L_1) < z_0(L) < z_0(L_2)$; this is the region between limits (ii) and (iii) discussed above. If, however, the resonator is symmetric with arms of length $L_1 = L_2 = L_0$ then the critical separation $z_0(L_0)$ is the same for both arms. This means that plane waves *and* spherical waves travelling in either direction in the resonator will form images at the end mirrors. This special case resonator occurs when both arm lengths are equal to the folding section effective focal length f', and so this resonator is equivalent to a symmetric confocal two-mirror resonator (Figure B.9). The HMS and LMS regions of Figure B.2 join together to form a single broad stability region, with the stability parameter $S = -1$ at its centre ($z = z_0(L_0)$). Although the resonator is critically stable at this point, the intracavity mode is well-behaved, with end-mirror spots that are neither vanishingly small nor excessively large, as can be seen from Figure B.10.

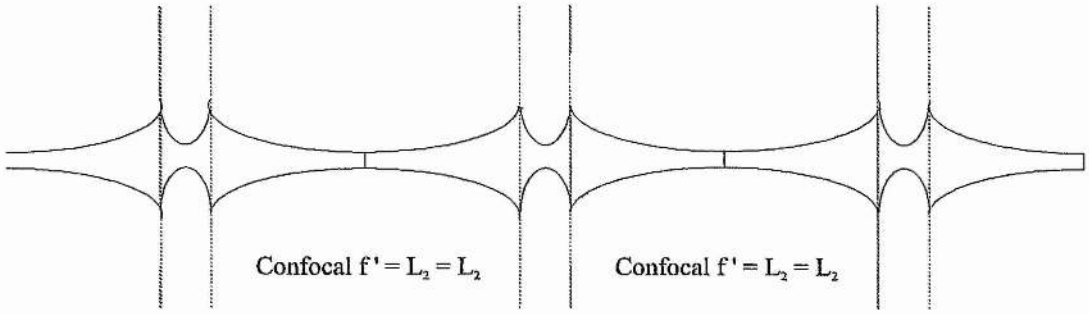

FIGURE B.9 *The infinite periodic waveguide corresponding to a symmetric four-mirror cavity on the S = -1 stability limit. This resonator is equivalent to a two-mirror symmetric confocal resonator.*

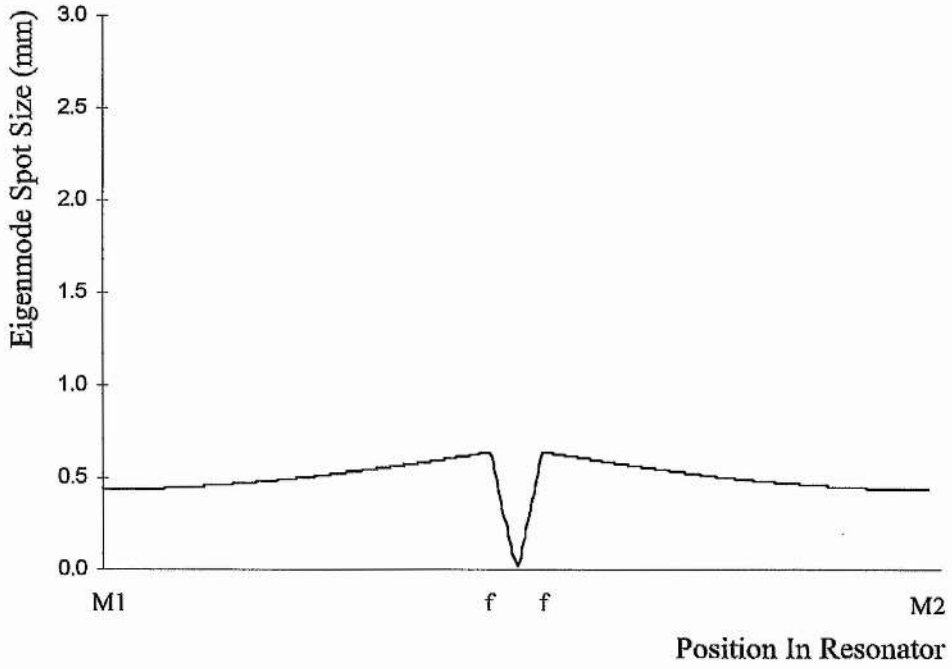

FIGURE B.10 *The resonator eigenmodes corresponding to the centre of the single stability region of a symmetric resonator. Although the stability parameter S = -1 at this point, the eigenmode is well behaved compared with its behaviour at limits (ii) and (iii) in Figure B.4 and Figure B.7, respectively.*

B.4 Varying The Crystal Position

The four stability limits discussed in the preceding section are important in the Cerullo model because for any given X - or Z- cavity configuration the maximum attainable value of the small-signal spot size variation δ tends to infinity at these points (Equation 3.31). Symmetric cavities are particularly important because even

when S = -1 the intracavity mode in a symmetric cavity remains well behaved as the stability 'limit' is approached. This means that this configuration can be realised in practice, whereas the intracavity mode in an asymmetric cavity is too critically sensitive to cavity alignment for an asymmetric cavity to be a practical possibility.

As well as the stability S, the other significant parameter in determining the magnitude of δ is the position of the laser crystal within the folding section. This variable is characterised in the Cerullo model by the parameter x in Figure 3.9, and relates to the positioning of the distributed Kerr lens induced by the intracavity beam. A comprehensive analysis of the effects of adding a Kerr lens to a laser cavity clearly requires something along the lines of the full nonlinear ray-transfer matrix approach of the Cerullo model. However, we can tentatively pursue our geometric model a little further. In a real laser, the induced Kerr lens is distributed throughout the crystal, but we can predict the key conclusions of the Cerullo model by considering the effects of a simple lens placed between the two curved mirrors of the cavity folding section. In a laser with a tightly-focused intracavity waist this is a reasonable approximation to reality, as is demonstrated in Section 3.2.4.

The properties of a compound lens consisting of three lenses can be deduced in the same way as those of a compound lens consisting of two lenses are calculated. The first folding mirror and the Kerr lens are first treated as a single compound lens; an object placed at a distance L_1 from the folding mirror results in an image at s_{12}, where

$$s_{12} = \frac{f_K d_1 - \dfrac{f_k L_1 f}{L_1 - f}}{d_1 - f_K - \dfrac{L_1 f}{L_1 - f}},$$

EQUATION C

and f_K is the focal length of the induced Kerr lens with d_1 its distance from the first folding mirror. (Equation C is merely Equation B for lenses of unequal focal length). We then treat this image as the object for the second folding-section mirror and calculate the final image position s_i using

$$\frac{1}{s_i} = \frac{1}{f} - \frac{1}{d_2 - s_{12}}$$

EQUATION D

which is the Gaussian Lens Equation[4] (d_2 is the distance from the Kerr lens to the second folding mirror). The back focal length of this three-lens combination is then determined by calculating the image position of an object placed at the back focal plane of the folding-mirror/Kerr-lens combination; that is, by setting s_i equal to the two-lens back focal length (which is found by letting $L_1 \rightarrow \infty$ so that $L_1 - f \rightarrow L_1$ in Equation C). The front focal length of the three-lens combination is calculated by calculating the object position L_1 that results in the two-lens combination forming an image at the (front) focal plane of the third lens; that is, by setting $d_2 - s_{12} = f$ and using Equation C to calculate the corresponding L_1.

The most important effect of adding a lens to a symmetric cavity is the breaking of the cavity symmetry. If the additional lens is positioned off-centre in the folding section then the effective back focal length and front focal length will no longer be equal. If the folding-mirror separation is set so that the laser is exactly on the confocal limit then the predictions of geometric optics are not well behaved; if, however, the mirror separation is slightly increased or decreased from this value then geometric optics makes predictions that can be interpreted meaningfully.

If the mirror separation is reduced to just inside the HMS region then the resonator becomes stable to plane waves emanating from either mirror. However, the front and back focal lengths are no longer equal and so the intracavity beam will tend to be collimated (giving a larger spot size) in the arm associated with the longer focal length and focused in the arm associated with the shorter focal length (giving a smaller spot size). These arms are equivalent to the shorter and longer arms of an asymmetric resonator, respectively. A plot of the difference between the back and front focal lengths against the position of the lens is shown in Figure B.11.

Similarly, if the mirror separation is increased to just inside the LMS region then the resonator becomes stable to spherical waves emanating from mirrors M_1 and M_2, but the image distances for waves from each end mirror are no longer equal. The spot size will be larger in the arm in which the image is formed at a longer

distance and smaller in the arm in which the image is formed at a shorter distance. A plot of the difference between these image distances against the position of the lens is again shown in Figure B.11.

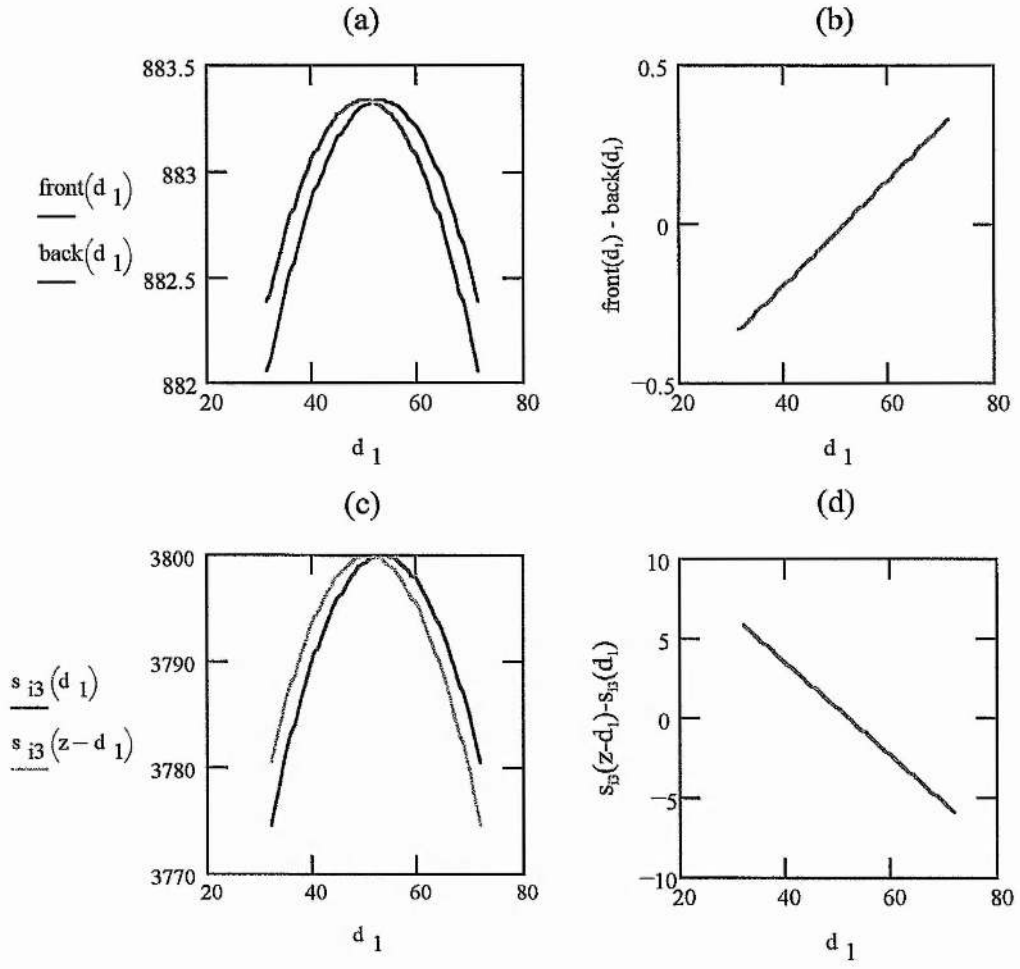

FIGURE B.11 *Three-lens combinations: (a) front and back focal lengths in the HMS region, and (b) the difference between the front and back focal lengths; (c) image distances for objects at M_1 and M_2 in the LMS region, and (d) the difference between those distances. The figures are calculated for f_K = 100 m. All distances are given in mm in both abscissae and ordinates.*

The principal difference between this geometric approach and the predictions of the Cerullo model is that this approach predicts that the spot sizes decrease in both arms, whereas Cerullo predicts an decrease in one arm and an increase in the other. We are considering the behaviour of the intracavity beam near to the central stability limit, however, where the beam is far from being either a plane or spherical wave, as shown in Figure B.10. In this region we must take the results of the full

self-consistent Gaussian beam approach as being true and discard the geometric optics results.

However, both approaches are in agreement on how we optimise the fundamental design parameter x. Figure B.11 parts (b) and (d) show that the change in spot-size increases the further the Kerr lens is offset from the centre of the folding section. This is in agreement with the Cerullo model, which indicates that δ is maximised when the intracavity waist is at either end of the crystal (the furthest offset possible). Furthermore, Figure B.11 predicts that the beam will shrink at mirror M1 for small offset x in the HMS region and for large x in the LMS region, in agreement with the Cerullo model (see Figure 3.14). Thus our geometric optics approach appears to predict the correct trends in spot-size variations due to a Kerr lens but to be inappropriate for predicting the spot-sizes themselves.

It is also interesting to note that the predictions of our geometric optics model agrees with numerical simulations carried out by Piché and Salin[5] for the case of asymmetric cavities. Piché and Salin report that self-focusing in the gain crystal pushes a laser that is operating on Limit II into the region of instability between the HMS and LMS regions, whereas a laser that is operating on Limit III is pushed further into the LMS stability zone. The geometric optics model predicts that adding a lens between the cavity folding mirrors makes the cavity stable to neither plane nor spherical waves if it is operating on Limit II, and makes it more stable to spherical waves (s_i increases) if it is operating on Limit III. Cerullo *et al* do not consider this behaviour in their model, but it is consistent with their observation that self-modelocked operation is more difficult to achieve near Limit II than near Limit III[6].

B.5 Conclusions

The geometric-optics model of resonator stability developed in this Appendix provides a useful insight into the nature of the stability regions and the stability limits of four-mirror resonators. Each stability limit corresponds to a degeneration of the intracavity mode to either a plane or a spherical wave, and at each limit the laser becomes equivalent to some combination of planar, confocal or pseudo-concentric two-mirror resonators. Analytic expressions can be derived for the

folding mirror separations that correspond to each of these limits. The end-mirror misalignment sensitivity of the resonator in each region can also be deduced from the model: the resonator is sensitive to misalignment in the 'plane-wave' region and insensitive to misalignment in the 'spherical wave' region.

Extension of the model to modelocked operation meets with mixed success. Treating the folding mirror/Kerr lens combination as a single lens fails to predict the correct spot-size change in the cavity arms, as might be expected in a regime far from the stability limits where degeneration into plane or spherical waves occurs. However, the geometric optics approach does predict that changes can be maximised by putting the Kerr lens as far off-axis as possible, in agreement with the full eigenmode analysis of Cerullo. It also predicts that the direction in which the lens must be displaced for an optimised change reverses between the HMS and LMS regions, in agreement with Cerullo.

Overall, the model provides a reliable insight into the optics of four-mirror cavity stability regions, but its predictions must be treated with caution when it is extended to include the effects of a Kerr lens.

---

[1] see, for example, P. Das in *Lasers and Optical Engineering, Springer-Verlag*, New York (1991), p198

[2] E. Hecht, in *Optics,* (2nd Edn., Addison-Wesley, Reading, Ma., 1987) p148

[3] E. Hecht, in *Optics,* (2nd Edn., Addison-Wesley, Reading, Ma., 1987) p147

[4] E. Hecht, in *Optics,* (2nd Edn., Addison-Wesley, Reading, Ma., 1987) p138

[5] M. Piché and F. Salin, Opt. Lett. **18**, 1041 (1993)

[6] G. Cerullo, S. De Silvestri, V. Magni and L. Pallaro, Opt. Lett. **19**, 807 (1994)

Appendix C - Publications

C.1 Journal Publications

'All-solid-state femtosecond Cr^{3+}:LiSAF lasers pumped at 532 nm and 670 nm'
M. P. Critten, D. Burns, J. M. Evans, K. Lamb, C. Yelland and W. Sibbett
Journal of Modern Optics **43**, 919 (1996)

'Low-threshold diode-pumped femtosecond Cr^{3+}:$LiSrAlF_6$ laser'
D. Burns, M. P. Critten and W. Sibbett
Optics Letters **21**, 477 (1996)

C.2 Conference Publications

'An all-solid-state, femtosecond Cr:LiSAF laser pumped at 532.5 nm'
K. Lamb, M. P. Critten, C. Yelland, J. Hong, D. Burns and W. Sibbett
in *Technical Digest of the 1994 Conference on Lasers and Electro-Optics Europe*, IEEE, 1994, paper CPD1.1

'All-solid-state femtosecond Cr^{3+}:LiSAF lasers pumped at 532 nm and 670 nm'
M. P. Critten, D. Burns, J. M. Evans, K. Lamb, C. Yelland and W. Sibbett
in *Technical Digest of the Twelfth UK National Quantum Electronics Conference*, Southampton, 1995, poster P1-1

'A low phase-noise, all-solid-state, self-modelocked Ti:sapphire laser'
K. Lamb, D. Burns, M. P. Critten, C. Yelland, W. E. Sleat and W. Sibbett
in *Technical Digest of the Twelfth UK National Quantum Electronics Conference*, Southampton, 1995, paper 4-4

'Low-threshold low-noise all-solid-state femtosecond Cr^{3+}:LiSAF lasers'
M. P. Critten, D. Burns and W. Sibbett
in *Conference on Lasers and Electro-Optics*, Vol. 9, 1996 OSA Technical Digest Series (Optical Society of America, Washington, D. C., 1996) p 65, paper CMK6

'Low-threshold, all-solid-state femtosecond Cr^{3+}:LiSAF and Cr^{3+}:LiSGaF lasers'
M. P. Critten, D. Burns and W. Sibbett
in *Technical Digest of the 1996 Conference on Lasers and Electro-Optics Europe*,
IEEE Catalog No. 96TH8161, p 337, paper CFF1

'Novel resonator designs for low-threshold self-modelocking'
G. J. Valentine, M. P. Critten, G. T. Kennedy, J.-M. Hopkins, P. Loza-Alvarez
and W. Sibbett
Accepted for 1997 *Conference on Lasers and Electro-Optics*

Acknowledgements

I would like to thank my supervisor Professor Wilson Sibbett for his support, guidance and unflappable optimism throughout this project. I am indebted to David Burns for all of his inestimably large input. I would also like to thank

Derryck Reid for teaching me about non-linear optics,

Johnny Evans for his early work on Cr:LiSAF,

Karen Oppo (neé Lamb) for teaching me how to self-modelock a laser,

Gordon Kennedy for passing on his knowledge of solitons and other matters,

Gareth Valentine for our idea-bouncing sessions regarding three-mirror lasers

(and both Gordon and Gareth for graciously lending me all their equipment - sometimes voluntarily),

Carl Yelland for building and operating the frequency-doubled minilasers (with Hong) and teaching me about birefringence,

Bill Sleat for everything electronic, and teaching me about noise and streak cameras,

Jimmy Lindsey and everyone else in the workshop for making everything I needed,

John-Mark Hopkins and Pablo Loza-Alvarez for carrying the torch forward, and

Cate McGowan for keeping me organised.

Finally, I would like to thank Jane Nelson for her support throughout these last three years, and Wilson, David and my father for proof-reading this thesis.